University of Southampton

Mass Modelling in X-/γ-ray astronomy

by

Colin Ferguson

A thesis submitted for the degree of
Doctor of Philosophy

Department of Physics and Astronomy
Faculty of Science

September 2000

UNIVERSITY OF SOUTHAMPTON

ABSTRACT

FACULTY OF SCIENCE

DEPARTMENT OF PHYSICS AND ASTRONOMY

Doctor of Philosophy

Mass Modelling in X-/γ-ray astronomy

by Colin Ferguson

The current status of hard X-ray/γ-ray astronomy is briefly reviewed. The next large ESA γ-ray observatory, INTEGRAL, is reviewed both in terms of its instrumentation and its scientific goals. All γ-ray observations are made against a background noise that is large compared with the signal to be measured, which makes understanding of the background crucial. Mass Modelling is currently being developed to enable observatories to better understand their background, improving the quality of data obtained from observations and the sensitivity of the telescope. Much of the current local development of Mass Modelling is driven by the INTEGRAL mission. Mass Modelling within the context of INTEGRAL is reviewed concentrating on The INTEGRAL Mass Model (TIMM).

The background within INTEGRAL is composed of three main components: the prompt cosmic rays, the diffuse γ-rays and the induced radioactivity within the satellite and detectors. To model the third component has required the development of a new code (DECAY). The development and testing of the DECAY code is presented. Testing is carried out using three practical examples: bombardment of a crystal by protons in a high-energy beam; modelling of the background within a low Earth orbit satellite; and, modelling of the background within a high altitude balloon. Having introduced TIMM, and the GGOD software suite used to carry out modelling, the results of recent TIMM simulations are presented and discussed.

The sensitivity of a telescope is a function of its background and its observing time. The IBIS instrument suffers from a large dead time ($\sim 20\%$). By reducing the dead time, with a minimal increase in the background count rate, the sensitivity of IBIS could be further improved. Two suggested ways for doing this, segmenting (or zoning) the veto and raising the low-energy thresholds of the veto crystals, are investigated using TIMM.

Finally, X-ray observations are presented of the globular cluster 47 Tucanae.

Contents

List of Figures

List of Tables

Preface

The work presented in this thesis has been carried out by the author, in collaboration with others, at the University of Southampton between October 1996 and October 1999. Chapter 3 initially reviews mass modelling, however the author has worked on various versions of The INTEGRAL Mass Model (TIMM) mentioned, from v2.0 - v3.4, and the author was solely responsible for upgrading v3.3 to v3.4 and for running the v3.4 model. The results presented in this thesis are from the v3.4 run. Earlier versions of TIMM were worked on by Dr. Andy Green (v1.0a) and Dr. Fan Lei (v1.0a - v3.3).

The DECAY code presented in chapter 4 was created solely by the author, though Dr. Fan Lei helped integrate this code into the GGOD software suite, and provided routines to calculate the beta particle energy spectra. The simulations of the beam test and HEAO-1 were solely the author's work. The model used to simulate the GRIS balloon payload was created by Dr. Juan Naya of Goddard Space Flight Centre, integrated into GGOD by the author, and all simulations and analysis were carried out solely by the author.

Chapter 5 presents results and analysis of v3.4 of TIMM. As mentioned previously, this was created by upgrading v3.3, which was done solely by the author. The running and analysis of the v3.4 model was carried out solely by the author.

The model used to study zoned vetoing in chapter 6 was an earlier version of TIMM and not built by the author. The running of this model, the veto schemes chosen, and all of the analysis was carried out solely by the author.

The data used in chapter 7 was obtained by proposals submitted by Dr. Fan Lei. This was reduced and analysed by the author.

Acknowledgements

I am greatly indebted to my supervisor, Prof. Tony Dean, for his continual guidance and support throughout these long years.

I should also like to thank Dr. Fan Lei for his daily help and advice throughout the majority of my PhD time, and Dr. Andy Green for his guidance in the early days. Drs. Anthony Bird, Rodolfo Gurriarian, and, Jon Lockley also deserve thanks for their many interesting comments.

I would also like to thank the other members of the Southampton INTEGRAL group for all of their help - Angela Malizia, Chris Lawton, Charlotte Perfect, Matt Westmore, Nene Diallo, Dave Willis, and, Simon Shaw.

Special thanks must go to Matt & Linda, Ian & Helen, Grant & Luisa, Rachel & Gareth, Cor & Terri, Jeno (especially for this last year), Debs, Willoughby, Paul and Rob for the many good times, some of which I remember. All of those that have played(?) for the astro group football team also deserve thanks. I thank everyone else in the Astronomy group over the last few years for the many interesting shenanigans.

Outside of the Astronomy group i would like to thank all of my family - mum, dad, Del, Gav and my grandad. I should also very much like to thank my gran who sadly passed away during my time here.

I would finally like to thank all of my friends from university and school who i see from time to time, and email far more often. Without all of those people to talk to i am sure i would've gone mad by now.

List of Acronyms

AGN Active Galactic Nuclei

ART-P Instrument on-board the GRANAT satellite

ASCA The Advanced Satellite for Cosmology and Astrophysics

BATSE Burst And Transient Source Experiment

BeppoSAX The Italian/Dutch X-ray Astronomy Satellite

BGO Bismuth Germanate

BHCs Black Hole Candidates

BHXB Black Hole X-ray Binary

BL Lacs BL Lacertae type AGN

BNL Brookhaven National Laboratory

CAD Computer Aided Design

CDB Cosmic Diffuse gamma-ray Background

CDG Cosmic Diffuse Gamma-rays

CdTe Cadmium telluride

CGRO Compton Gamma Ray Observatory

COMPTEL Compton Telescope

COSSC Compton Observatory Science Support Centre

CsI(Tl) Caesium iodide with a thalium dopant

CVs Cataclysmic Variables

DECAY The code created to process radioactive decays

DFEE Detector Front End Electronics

DSID Data set Identification

EC Electron Capture

EGRET Energetic Gamma Ray Experiment Telescope

ESA European Space Agency

FCFOV Fully Coded Field Of View

FWHM Full Width at Half Maximum

GCDE Galactic Central radian Deep Exposure

Ge Germanium

GEANT/GCALOR Software used to simulate photons, electrons, neutrons and protons.

Geant4 Version 4 of the GEANT package

GGOD GEANT/GCALOR ORIHET DECAY software suite

GOF Guest Observer Facility

GPS Galactic Plane Survey

GRBs Gamma Ray Bursts

GRIS Gamma Ray Imaging Spectrometer

GSFC Goddard Space Flight Centre

GTI Good Time Interval

HEAO-1 High-Energy Astrophysical Observatory number 1

HEAO-3 High-Energy Astrophysical Observatory number 3

HED High-Energy Detector (on HEAO-1)

HEO High-Earth Orbit

HEXE High-Energy X-ray Experiment

HEXTE High-Energy X-ray Timing Experiment (on RXTE)

HMXB High Mass X-ray Binary

HPGSPC High Pressure Gas Scintillation Proportional Counter

HRI High Resolution Imager (on Einstein or ROSAT)

HURA Hexagonal Uniformly Redundant Array

IBAS INTEGRAL Burst Alert System

IBDR Instrument Baseline Design Review

IBIS The Imager on-Board the INTEGRAL Satellite

ICDR Instrument Critical Design Review

IHDR Instrument Hardware Design Review

INTEGRAL INTErnational Gamma Ray Astrophysical Laboratory

IPC Imaging Proportional Counter (on Einstein)

IPR Incident Pixel Reconstruction

ISDC INTEGRAL Science Data Centre

ISGRI Cadmium telluride detector plane in IBIS

ISWT INTEGRAL Science Working Team

IT Isomeric Transition

JEM-X Joint European X-ray Monitor

LADs Large Area Detectors (part of BATSE)

LECS Low-Energy Concentrators (on BeppoSAX)

LED Low-Energy Detector (on HEAO-1)

LEO Low-Earth Orbit

LMXB Low Mass X-ray Binary

MECS Medium-Energy Concentrators (on BeppoSAX)

MED Medium-Energy Detector (on HEAO-1)

MEM Maximum Entropy Method

MSP Millisecond pulsar

Mpc Mega-parsec = 1 million parsecs

NaI Sodium iodide

NFI Narrow Field Instruments

NNDC National Nuclear Decay Centre

OMC Optical Monitoring Camera

ORIHET Code used to compute the decay rates of isotopes using their production rates and radiation history.

OSSE Oriented Scintillation Spectrometer Experiment

PCA Proportional Counter Array (on RXTE)

PCFOV Partially Coded Field Of View

PDS Phoswich Detection System

PDU Power Distribution Unit

PENSDF2 Database of Nuclear Structure and Decay cross-sections held at LNL/BNL. The P denotes data stored by parent nuclide.

PICsIT Pixellated caesium iodide detector in IBIS

PLM Payload Module

PMTs Photomultiplier tubes

PSD Pulse-Shape Discrimination

PSLA Point Source Location Accuracy

PSPC Position Sensitive Proportional Counter

QPOs Quasi-Periodic Oscillations

QSOs Quasi-Stellar Objects (aka Quasars)

ROSAT Röntgen Satellite

RTU Remote Terminal Unit

RXTE Rossi X-ray Timing Explorer

SAA South Atlantic Anomaly

SATURNE A proton beam facility located in France

SDC Science Data Centre

SGR Soft Gamma Repeater

SIGMA A French/Russian coded-aperture γ-ray imaging telescope

SMM Solar Maximum Mission

SN(e) Ia Type Ia Supernova(e)

SN(e) II Type II Supernova(e)

SNR Supernova(e) remnants

SPI SPectrometer on INTEGRAL

SSSA/S3A Supervised Standard Scientific Analysis

SVD Singular Value Decomposition

SVM Service Module

TIMM The INTEGRAL Mass Model

TGRS	Transient Gamma Ray Spectrometer
WFC	Wide Field Camera

Chapter 1

Recent advances in γ-ray astronomy

1.1 Introduction

The field of γ-ray astronomy is a relatively new one. This is mainly because the Earth's atmosphere stops hard X-rays and γ-rays from reaching the surface. Only in the last 30 years, with the advent of high-altitude balloons and satellites, has it become possible to detect astronomical γ-rays. At high altitudes, and especially outside the atmosphere, γ-ray telescopes are subject to particle and photon bombardment that creates background noise against which observations have to be made. In many cases the background noise is very large compared with the astronomical signal to be measured. This has meant that detectors have been required to have large areas to attain good sensitivity, and even though many missions have been launched in the past, only in the last decade has a clearer picture of the γ-ray sky begun to emerge. One mission which has contributed greatly to the recent dramatic increase in information and data available is the Compton Gamma Ray Observatory (CGRO). At launch in 1991 this was the heaviest object NASA had put into orbit. CGRO carried four instruments covering a total energy range of 20 keV - 30 GeV: the Burst And Transient Source Experiment (BATSE); the Oriented Scintillation Spectrometer Experiment (OSSE); the Compton Telescope (COMPTEL); and, the Energetic Gamma Ray Experiment Telescope (EGRET). These instruments provided imaging and spectrometry over six decades of photon energy.

In this chapter CGRO will be discussed, starting with the instruments and moving on to the scientific results, and used to introduce many of the concepts and theories relevant to this thesis and γ-ray astronomy in general. This thesis considers mainly the 10 keV - 10 MeV energy band and so less emphasis will be placed on EGRET than on the other CGRO instruments.

1.2 Burst And Transient Source Experiment (BATSE)

BATSE is an all-sky monitoring instrument covering the energy range 20 keV - 1 MeV (Paciesas et al. 1993; Gehrels et al. 1993; COSSC web site). BATSE is composed of eight separate detectors that are mounted on the corners of the CGRO satellite. This allows BATSE to view all of the sky that isn't obscured by the Earth. The individual detector modules of BATSE use a Large Area Detector (LAD) made of sodium iodide to record the γ-ray energies (fig. 1.1). Each of the LAD's has a thin plastic scintillator in front of the NaI crystal to veto charged particles. Each module also contains a smaller detector which is optimised for spectral resolution. Though single modules have no position resolution, the combination of several elements can, via triangulation, determine the position of any source. BATSE monitors many sources using the Earth's atmosphere to occult them. By looking at the steps in the count rate, one can determine the direction and strength of a source.

BATSE's primary objective is the detection, location and study of Gamma Ray Bursts. BATSE has also provided much useful data on variable or transient sources, produced a map of the γ-ray sky, and has been used to study the effects of solar flares.

An all-sky map from the BATSE data that has been accumulated is currently being worked on at Southampton University and hopefully will be published in the near future (Shaw et al. 2000). This will be the most sensitive all-sky map in the energy range 20 - 120 keV ever obtained. BATSE also contributed to the study of solar flares by using the same triggering techniques as used for bursts for flares. When a flare was detected, other instruments on CGRO such as OSSE and COMPTEL could be used to study the flares.

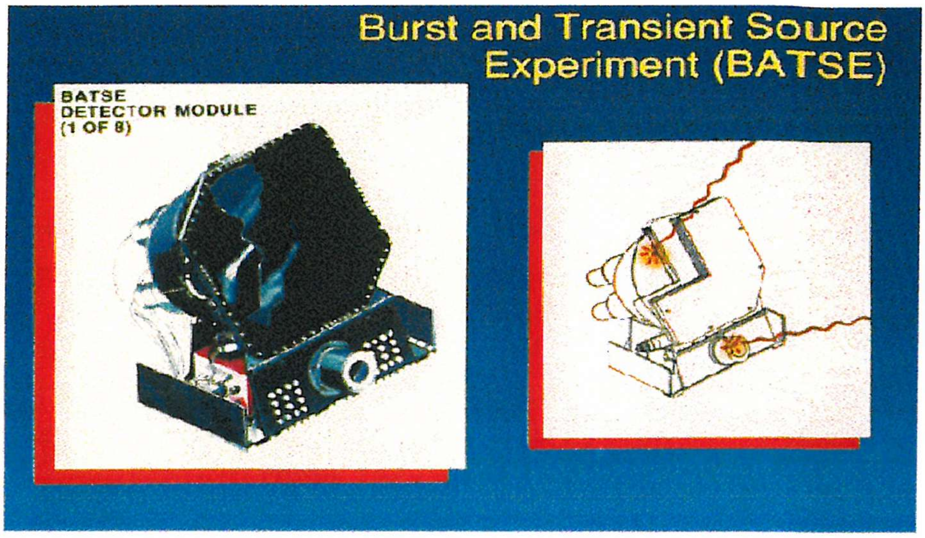

Figure 1.1: *The Large Area Detectors (LADs) of BATSE, taken from the Compton Observatory Science Support Center (COSSC) web pages..*

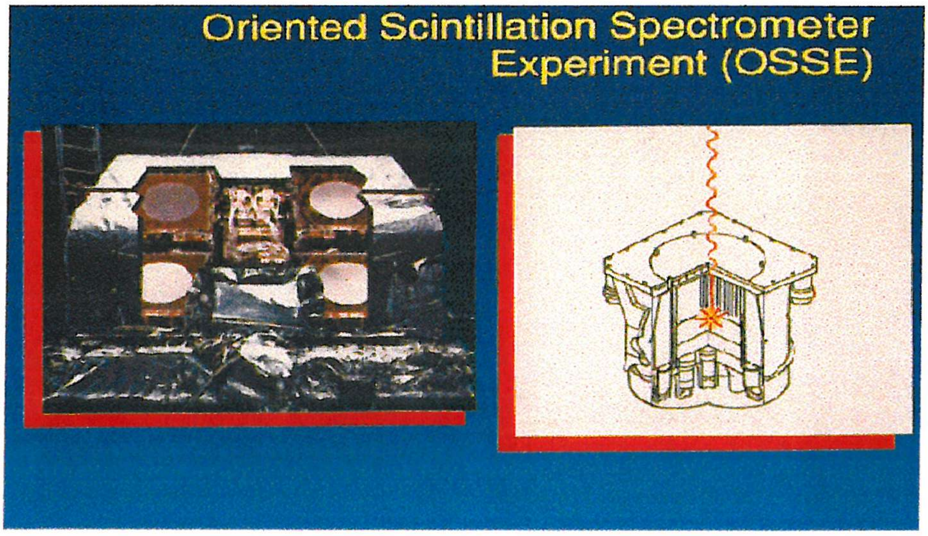

Figure 1.2: *The OSSE detectors, taken from the Compton Observatory Science Support Center (COSSC) web pages.*

1.3 Oriented Scintillation Spectrometer Experiment (OSSE)

OSSE consists of four collimated NaI scintillation detectors, sensitive to energies from 50 keV to 10 MeV (fig. 1.2). Each of these detectors can be individually pointed. This allows observations of a γ-ray source to be alternated with observations of nearby background regions. An accurate subtraction of background contamination can then be made. A detailed description of OSSE is given by Johnson et al. (1993).

The high spectral resolution of OSSE has allowed it to map matter-antimatter (electron-positron) annihilation in the galaxy, radioactive decay of nuclei in supernova remnants and study magnetic fields using cyclotron lines.

1.4 Compton Telescope (COMPTEL)

The imaging Compton Telescope (COMPTEL) utilizes the Compton Effect and two layers of γ-ray detectors to reconstruct an image of a γ-ray source in the energy range 1 - 30 MeV. COMPTEL's upper layer of detectors are filled with a liquid scintillator which scatters an incoming γ-ray photon according to the Compton Effect. This photon is then absorbed by NaI crystals in the lower detectors. The instrument records the time, location, and energy of the events in each layer of detectors. From this information a circle on which the direction of the photon lies can be constructed. The intersection of many of these circles gives the photon's origin. Gamma-rays from active galaxies, radioactive supernova remnants, and diffuse γ-rays from giant molecular clouds can be studied with this instrument. The energy range of COMPTEL complements that of OSSE, and the same type of astronomical phenomena can be studied with both. A detailed description of COMPTEL is given by Schönfelder et al. (1993).

1.5 Energetic Gamma Ray Experiment Telescope (EGRET)

EGRET is the highest energy experiment on board CGRO, giving coverage over the range 20 MeV - 30 GeV (Thompson et al. 1993). Like COMPTEL, EGRET is an imaging instrument. The EGRET instrument produces images using high-voltage gas-filled spark chambers. High-energy γ-rays enter the chambers and produce an electron-positron pair. As this pair travels through the gas filled

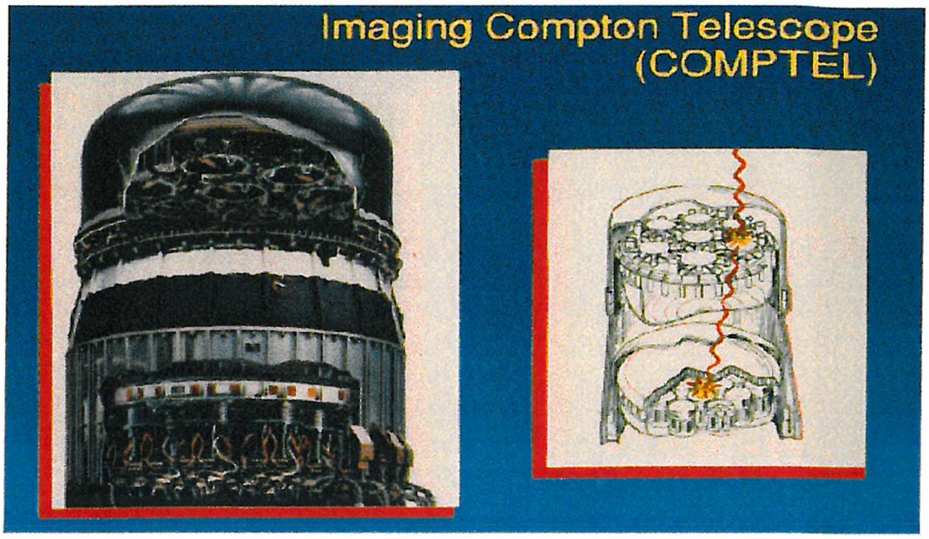

Figure 1.3: *COMPTEL, taken from the Compton Observatory Science Support Center (COSSC) web pages.*

chamber, sparks are detected in electrified wires which criss-cross the chamber. The spark chamber essentially takes a picture of the trail of the pair as they pass through the instrument. These tracks lead back to the incident direction of the cosmic γ-ray, allowing EGRET to image the sky. Once the pair exit the chamber, they are absorbed by a scintillator which gives a good estimate of the total pair energy, and hence the energy of the incident photon. EGRET is 10 to 20 times larger and more sensitive than previous detectors operating at these high energies and has made detailed observations of high-energy processes associated with diffuse γ-ray emission, γ-ray bursts, cosmic rays, pulsars, and active galaxies known as blazars.

1.6 The Galactic Plane and Centre

The Galactic X/γ-ray background, particularly from the galactic ridge (i.e. the narrow region centered on the plane of the galaxy covering approximately $\pm 60^o$ in longitude), has been studied with every major X-ray and γ-ray observatory. The spectrum of emission is reasonably well measured and understood above ~ 1 MeV. At energies above 100 MeV, the dominant emission processs is the decay of π^0 meson produced in the interaction of cosmic-ray nucleons with the interstellar matter (Bertsch

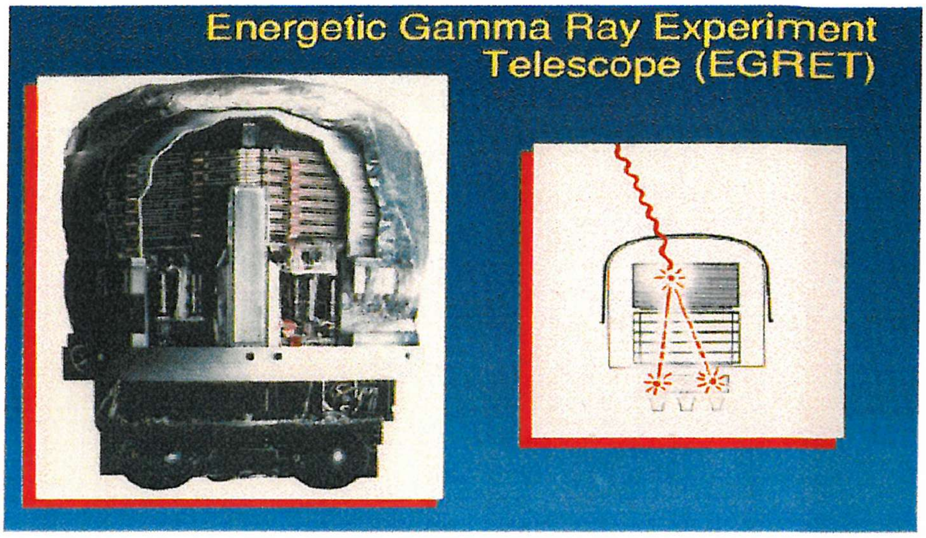

Figure 1.4: *EGRET, taken from the Compton Observatory Science Support Center (COSSC) web pages.*

et al. 1993). Between ~ 1 and 70 MeV, electron bremsstrahlung and inverse Compton scattering appear to dominate over discrete soures (Strong et al. 1996). At soft γ-ray energies (below 1 MeV), multiple components are believed to contribute to the total emission (Purcell et al. 1997; Kinzer et al. 1999). These include transient discrete sources, positron annihilation line and three-photon positronium continuum radiation, and a soft γ-ray component dominant up to about 300 keV of unknown origin.

Recent simultaneous measurements using OSSE and the Rossi X-ray Timing Explorer (RXTE) by Valinia et al. (2000) have indicated that a substantial component of the 40 - 100 keV flux from the Galactic ridge is due to discrete sources. Valinia et al. (2000) have measured the spectrum from 3 keV to 1 MeV and have found this can be modelled by four components: a high-energy continuum dominating above 500 keV; a positron annihilation line and positronium continuum; a hard X-ray/soft γ-ray component between 10 keV and 200 keV; and, a thermal plasma model of solar abundance and temperature 2.6 keV. It is suggested that temporal variability seen within the 40 - 100 keV band is due to the presence of discrete sources. The remaining emission could then be due either to more discrete sources or could be truly diffuse in nature (Valinia et al. 2000).

The inner Galactic disk (within ±60° longitude) emits γ-rays with spectra made up of a number of distinct components. Understanding the spectral characteristics and spatial distribution of these components in the 50 keV - 10 MeV range provides information about nucleosynthesis in the Galaxy, about the cosmic-ray electron spectrum, and about the interstellar medium in which the cosmic rays propagate. Much of the observed γ-ray emission below 10 MeV appears to be distributed over a ridge along the Galactic plane.

The principal components of the central Galactic ridge spectrum in the 0.05 - 10 MeV range are (1) a variable soft low-energy component, important below $\sim$ 300 keV, known to contain contributions from discrete sources; (2) a positronium annihilation continuum; (3) a 511 keV positron annihilation line; (4) a 1.809 MeV ^{26}Al line; and (5) a component resulting from cosmic rays interacting with the interstellar gas and photon fields (Kinzer et al. 1999). OSSE has been used to measure the spectrum of the Galactic plane at several different longitudes by Kinzer et al. (1999), and the spectra obtained are shown in figure 1.5.

The soft low-energy component has a variable discrete source contribution concentrated toward the centre, but also has an underlying stable component broadly distributed in longitude about the centre with a latitude width of about 5° FWHM toward the centre (Purcell et al. 1996). The Galactic centre region positron annihilation line and continuum components appear to come principally from a central bulge that is sharply peaked toward the centre in both latitude and longitude, and a ridge component extending to at least $\sim \pm 35^{\circ}$ in longitude. There also appears to be broadly distributed positron annihilation emission underlying these narrow components. The narrow 1.809 MeV ^{26}Al line follows a broad longitude distribution which is consistent with the carbon-oxygen distribution (Diehl et al. 1995).

The hard continuum, measured well only above $\sim$30 MeV, is by extrapolation expected to be principally from a ridge along the plane with an $\sim 80^{\circ}$ wide, roughly flat, maximum in longitude about the centre. The low-energy part of this cosmic ray induced component is thought to result principally from cosmic ray electron bremsstrahlung and inverse Compton electron scattering on interstellar photons and will likely have a spatial distribution differing from that of the nucleon-interaction component dominant above $\sim$ 70 MeV. The latitude distribution of these soft γ-ray components is not currently well known and it may be a combination of broad and narrow spatial components. Since it is not possible to measure the cosmic-ray electron spectrum directly below $\sim$1 GeV, the γ-ray measurements provide one of the best ways to determine the Galactic electron spectrum and distribution at lower energies.

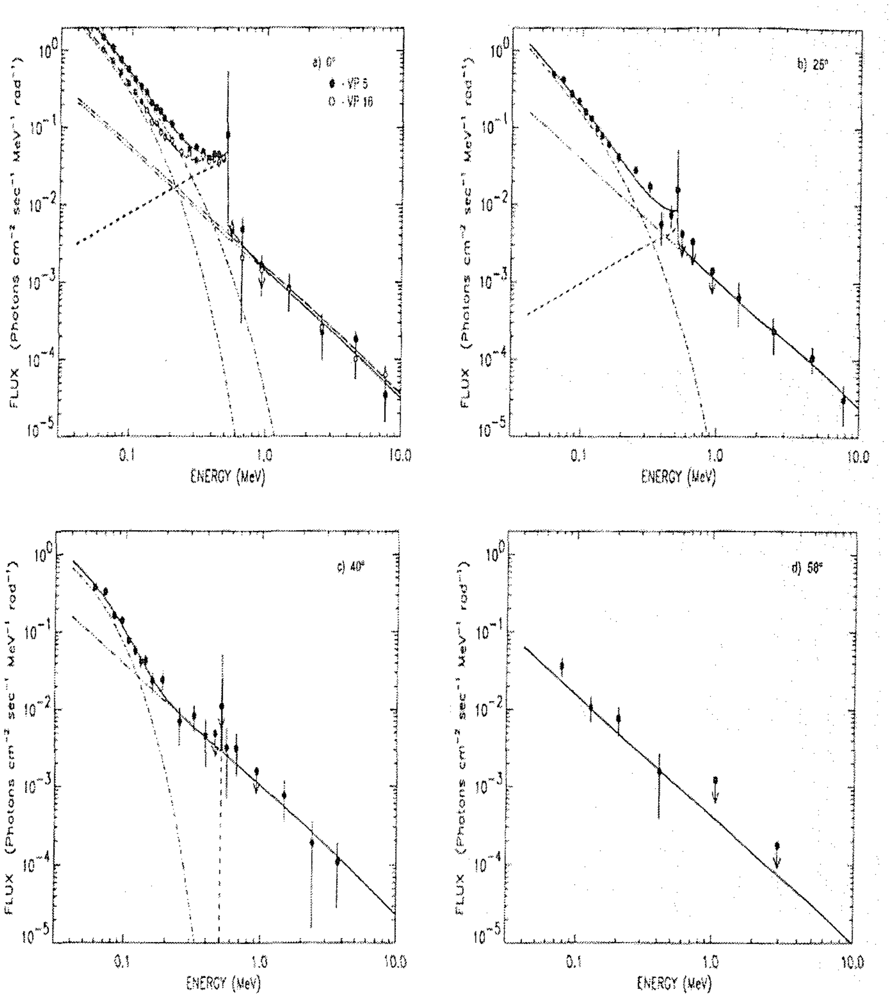

Figure 1.5: *The OSSE "apparent" photon spectra of the Galactic plane at four different longitudes for an assumed 5° wide (FWHM) Galactic ridge distribution and a flat longitude distribution. Best-fit composite models are shown by the solid lines or by a long-dashed line. The dash-dotted line is an exponentially absorbed power-law component; the dashed line is a positronium continuum component and a 2.5 keV FWHM narrow line at 511 keV; the dash-triple-dotted line is the cosmic-ray interaction continuum model. Two results at 0°, and one at 25°, at 40°, and at 58° are given in (a), (b), (c), and (d), respectively (Kinzer et al. 1999).*

1.6.1 Galactic electron-positron annihilation

Recently OSSE has provided new insight into the Galactic 511 keV line emission (Purcell et al. 1997). From the late 1970's the existence of a Galactic 511 keV line (and Positronium Continuum) has been known, however the location and distribution has not been well studied. It was thought the 511 keV line intensity may be variable and it was suggested that the source was a combination of a steady state diffuse Galactic component and a time variable point source near the Galactic centre (Lingenfelter & Ramaty 1989). Possible sources of the diffuse galactic component include cosmic ray interactions in the interstellar medium, γ-ray bursts, pulsars, and β^+ decay products from radioactive nuclei produced by supernovae, novae or Wolf-Rayet stars. Photon-photon pair production in the vicinity of an accreting black hole has been suggested as a possible source of time variable annihilation emission (Ramaty et al. 1992).

Purcell et al. (1997) combined OSSE observations (taken up to Jan 5 1997) with Transient Gamma Ray Spectrometer (TGRS) and Solar Maximum Mission (SMM) data to produce detailed galactic 511 keV emission maps. They used 2 different mapping methods, Singular Value Decomposition (SVD) and Maximum Entropy (MEM), which gave the same features: (1) a central bulge, (2) emission in the Galactic plane, and (3) a probable enhancement or extension of emission at positive latitudes above the galactic centre (figure 1.6). No evidence of time variability was found (Purcell et al. 1997).

Purcell et al. (1997) also placed a point source at the location of 1E1740.7-2942 in their models to search for emission. They obtained a 3σ upper limit to the 511 keV line emission from this source of 1.6×10^{-4}photons cm^{-2}s^{-1}.

Supernovae are found to be capable of producing positrons at the required rate to account for the intensity and morphology of the observed 511 keV line emission (Purcell et al. 1997; Chan & Lingenfelter 1993). The positive latitude feature is suggestive of an asymmetric positron outflow from the galactic nucleus, which may be associated with a fountain of radioactive debris ejected from the galactic centre region by enhanced supernovae activity in the region (Dermer & Skibo 1997) or with jet activity from one or more black holes residing near the galactic centre (Purcell et al. 1997). Alternatively, nearly all of the observed positrons might also have been produced in a single explosive γ-ray burst-like event occuring near the galactic centre $\sim 10^6$ years ago (Purcell et al. 1997).

With high resolution spectroscopy, the phases of the interstellar gas in which positrons annihilate

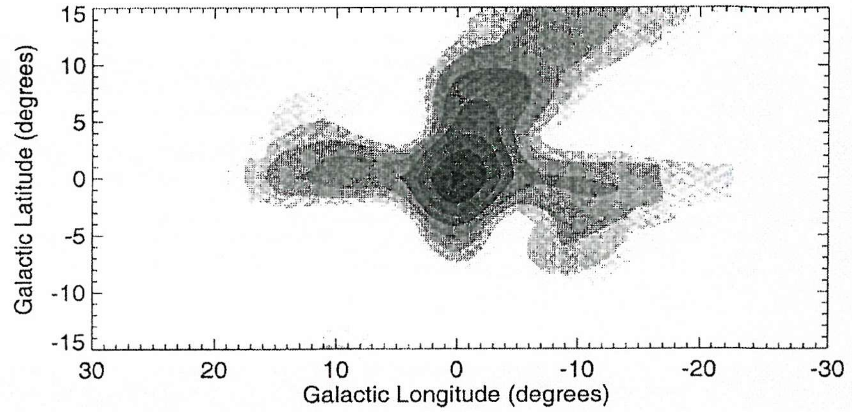

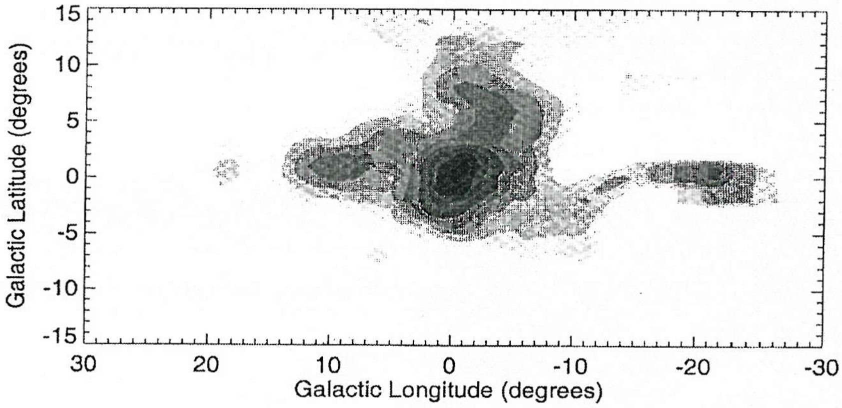

Figure 1.6: *OSSE maps of the Galactic 511 keV emission as given by Purcell et al. (1997). The top map shows the result obtained using the Singular Value Decomposition method and the bottom figure shows the result obtained using Maximum Entropy (in both maps the contours are exponentially spaced).*

can be determined from spectral decompositions of the positron annihilation radiation. Guessoum et al. (1991) have studied several scenarios important to astrophysics. The 511 keV line emitted from a cold (10^2 K) HI gas consists of two components, a very narrow feature with a FWHM of ~1.5 keV resulting from direct annihilation with atomic electrons and a broader feature with FWHM of ~6.5 keV resulting from annihilation of singlet positronium. The broad width of the positronium line results from the motion of the positronium atoms formed in flight by charge exchange with neutral hydrogen. In warm ($\sim 10^6$ K) plasmas, the annihilation line is thermally broadened to a FWHM of ~10 keV. In cold and warm media, the annihilation line should be accompanied by characteristic emission resulting from triplet positronium annihilation, while in the hot plasma this continuum is significantly suppressed. Consequently observations of both the shape of the 511 keV line and the triplet-continuum to line ratio can determine in what phase material the positrons annihilate and thus permit the various phases to be mapped. Balloon-borne high-resolution spectrometers have resolved the annihilation line obtaining widths of 1 keV to 3 keV (Leventhal et al. 1993). These results indicate that the width of the line may be variable, which would require a variable point source component.

1.6.2 Lines from cosmic ray - interstellar matter interactions

A variety of lines with narrow and broad profiles are expected to be produced by cosmic ray - instellar matter interactions (Ramaty et al. 1979), the most prominent ones being those of $^{12}C^*$ at 4.44 MeV and $^{16}O^*$ at 6.13 MeV. The narrow lines, or line components, result from dust grains, where recoiling excited nuclei come to rest before they de-excite, while the broad lines, or line components, originate from the interstellar gas. Detection of these narrow lines can provide a direct determination of the composition, size and galactic distribution of interstellar dust grains, as well as the intensity and distribution of low-energy cosmic rays.

1.7 Nucleosynthesis - Explosive and Hydrostatic

Observations of γ-ray lines from nuclear transitions of decaying radionuclei and the annihilation of positrons produced in various nucleosynthetic sites provides the most direct method of studying current models and rates of nucleosynthesis. The most important decay chains from nucleosythetic

Decay Chain	Half-life	Emission (MeV)
$^7Be \rightarrow^7 Li$	53.29 d	0.478
$^{22}Na \rightarrow^{22} Ne$	2.6 yr	0.511, 1.275
$^{24}Na \rightarrow^{24} Mg$	14.96 hr	1.369, 2.754, 3.866
$^{26}Al \rightarrow^{26} Mg$	7.4×10^5 yr	0.511, 1.809
$^{44}Ti \rightarrow^{44} Sc \rightarrow^{44} Ca$	49 yr; 3.93 hr	0.511, 0.068, 0.078; 1.157
$^{56}Ni \rightarrow^{56} Co \rightarrow^{56} Fe$	5.9 d; 77.3 d	0.511, 0.847, 1.238, 2.599
$^{57}Co \rightarrow^{57} Fe$	271.8 d	0.014, 0.122, 0.136
$^{60}Fe \rightarrow^{60} Co \rightarrow^{60} Ni$	1.5×10^6 yr; 5.3 yr	0.059; 1.173, 1.332

Table 1.1: *Key isotopic decay chains from nucleosynthetic processes.*

processes yielding γ-ray lines are summarised in Table 1.1.

1.7.1 Supernova 1987A

Despite occuring before the launch of CGRO, there was a surprising amount of data accumulated for this event by other γ-ray missions. The detection of γ-ray lines (0.847, 1.238 and 2.599 MeV) from ^{56}Co provided, for the first time, direct diagnostics of nucleosynthesis in a Type II SN explosion (Tueller et al. 1990). In all three cases the lines were redder than expected and had higher line-widths than expected. The large widths ($\sim$1% @ 847 keV) suggest the ^{56}Co emission region is in a high velocity part of the expanding supernova shell. From the line fluxes a significant optical depth is required to explain the bolometric light curve, which is primarily powered by the radioactive decays. However, the fact that the lines are red-shifted implies one can see to the receding part of the supernova shell, and hence would suggest an optically thin shell. These apparent paradoxes, which show the need for further more detailed investigation, could possibly be solved if the expanding shells contain knots or filaments which are optically thick within a more transparent medium (Tueller et al. 1990).

1.7.2 Other Supernovae

Because of obstruction by the massive ejecta, and the small amount of ^{56}Ni synthesized, the γ-ray line fluxes expected from Type II supernovae (massive star explosions) are much lower than for Type

Ia supernovae (explosions of white dwarfs).

It is widely accepted that Type Ia Supernovae (SNe Ia) are thermonuclear explosions of carbon-oxygen white dwarfs; however, Höflich et al. (1998) distinguish three groups of progenitor models. The first group consists of carbon-oxygen white dwarfs, close to the Chandrasekhar mass, that accrete mass through Roche lobe over-flow from an unevolved or evolved companion star. In these accretion models, the explosion is triggered by compressional heating. From the theoretical standpoint, the two key issues are the conditions under which the thermonuclear explosion starts and how the burning front propagates through the white dwarf, these determine whether there is detonation, deflagration or delayed detonation. The ignition and propagation may be affected by the rotation and mass accretion rate of the white dwarf, which will in turn be affected by the metallicity, age, and population of the progenitor system (Höflich et al. 1998). The second group of progenitor models features two low-mass white dwarfs in a close orbit that decays as a result of the emission of gravitational radiation. This eventually leads to the merging of the two white dwarfs. In this scenario, the total mass of the merged object may exceed the Chandrasekhar mass and rotation may play an especially significant role (Höflich et al. 1998). A third class of models are those involving helium detonations, i.e. double detonation of a C-O white dwarf triggered by the detonation of an outer helium layer in low-mass white dwarfs (Höflich et al. 1998).

Gamma-rays allow direct observation of the radioactive isotopes that power the observable light curves and spectra of SNe Ia and thus are a powerful diagnostic tool. One of the most important decay chains expected to be visible is that of ^{56}Ni→^{56}Co→^{56}Fe. Observations of SNe Ia are very limited, and one of the few to have been observed is SN 1991T. This was observed by CGRO, both with OSSE and COMPTEL, though none of the expected lines were observed (Leising et al. 1995). While the lack of any evidence of ^{56}Co emission poses problems for SNe Ia models, SN 1991T was rather unusual (Leising et al. 1995). SN 1991T was one of the brightest Type Ia supernovae at maximum light and its light curve evolves slower than most other SNe Ia. It is unclear whether its faintness in the γ-rays is because it was unusually bright in the optical or because the models over predicted its γ-ray luminosity (Leising et al. 1995).

1.7.3 Novae

A classical nova outburst is caused by rapid, non equilibrium, thermo-nuclear burning of hydrogen on the white dwarf's surface. During this process many light elements (i.e. $A \leq 30$) may be synthesised. Aside from short-lived β unstable nuclei, which might be detectable via their positron annihilation γ-rays, the lines most likely to be detectable appear to be the 1275 keV line from ^{22}Na ($t_{1/2} = 2.6$ years) and the 478 keV line from ^{7}Be ($t_{1/2} = 53.3$ days) (Gómez-Gomar et al. 1998).

Very few searches have taken place for these lines thus far, and those that have taken place have been unsuccessful. Iyudin et al. (1995) used COMPTEL to search for ^{22}Na emission. They set 2σ upper limits to the 1275 keV line emission for 11 novae of $2\text{-}6\times10^{-5}$ photons cm^{-2} s^{-1}. These upper limits reduce the mass of ^{22}Na created in the outburst and pose some questions for theories.

The Transient Gamma Ray Spectrometer (TGRS) has also been used to search for novae. In this case Harris et al. (1999) were looking for blue-shifted electron-positron annihilation features, which would be expected to occur during the early evolution of the novae, possibly before the maximum in the visible lightcurve. However, like COMPTEL no positive results were obtained, though TGRS proved to be sensitive enough to detect ONeMg novae within about 1 kpc. Clearly, if models of novae evolution and isotope production are to be tested then more sensitive searches of the whole sky will be necessary.

1.7.4 ^{26}Al and ^{60}Fe

The formation of ^{26}Al occurs in nucleosynthesis sites such as novae, supernovae, and the interior of massive stars (for a recent review of ^{26}Al in the Galaxy see Prantzos & Diehl 1996). The 1.809 MeV γ-ray line originating from the decay of radioactive ^{26}Al was discovered by HEAO-3 (Mahoney et al. 1984), with a total galactic flux of $3 - 4 \times 10^{-4}$ ph cm^{-2} s^{-1}, and confirmed by SMM (Share et al. 1985). The line width appeared to be very little broadened which indicates that the ^{26}Al decay takes place in the interstellar medium (Mahoney et al. 1984).

Mapping of the 1.809 MeV emission would help identify ^{26}Al sources and was one of the aims of CGRO. The COMPTEL imaging telescope produced the first Galactic map using the 1.809 MeV line from ^{26}Al (Diehl et al. 1995). In general the maps produced using this line show emission along the Galactic plane, at the Galactic centre and at the Galactic anti-centre (fig. 1.7).

Knödlseder (1999) noted a correlation between microwave radiation and the 1.809 MeV γ-ray

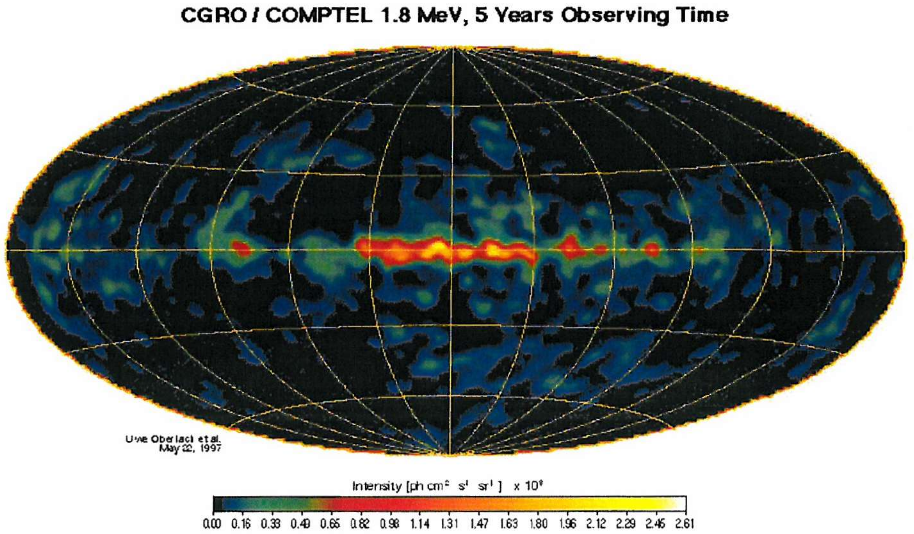

Figure 1.7: *COMPTEL all-sky map using the 1.809 MeV line produced in the decay of* ^{26}*Al, taken from the COSSC web pages.*

line distribution that may be due to massive stars creating the Galactic ^{26}Al. Knödlseder (1999) derived a total Galactic ^{26}Al mass of $3.1 \pm 0.9 M_{\odot}$. It is suggested that $\sim \frac{2}{3}$ of the ^{26}Al originates in Wolf-Rayet stars and that $\sim \frac{1}{3}$ originates in Type II supernovae. It is further predicted that the Galactic metallicity gradient should produce a difference in the relative 1.809 MeV to microwave ratios in the inner and outer galaxy, but this is at the limit of COMPTEL's sensitivity and so is undetectable.

Another possible diagnostic tool that could be used to understand nucleosynthesis within the Galaxy is the distribution of ^{60}Fe. The lifetime of ^{60}Fe ($t_{1/2} = 1.5 \times 10^6$ yr) is slightly larger than that of ^{26}Al ($t_{1/2} = 7.2 \times 10^5$ yr) and ^{60}Fe is expected to be produced in Type II supernovae. Potentially therefore, the instellar medium should contain both of these isotopes, and their ratio is indicative of their formation mechanism. If both are produced mainly in supernovae then their ratio will be equivalent to their production ratios, if on the other hand ^{26}Al is produced mainly in Wolf-Rayet stars, where ^{60}Fe is not produced, then their ratios will be much less than that expected for supernovae. Naya et al. (1998) used GRIS to observe the Galaxy and look for 1.809 MeV (^{26}Al), 1.173 MeV (^{60}Fe) and 1.332 MeV (^{60}Fe) γ-rays. They detected the 1.809 MeV line, but could only set upper limits on the other two. The 2σ upper limit set to the ^{60}Fe/^{26}Al flux ratio is 0.14, which is slightly lower than predictions, but still compatible. Clearly if the 1.173 and 1.332 MeV lines could be detected and the flux ratio derived then this would provide an important discriminant between the possible sources of ^{26}Al and ^{60}Fe. The GRIS results also suggest that the width of the ^{26}Al line is 3 times higher than expected, which may indicate that the ^{26}Al is moving with a velocity above 400 km/s, and tends to support origin within supernovae and Wolf-Rayet stars (Naya et al. 1996).

1.8 Galactic variable and transient sources

There are many transient or variable X-/γ-ray sources within our Galaxy. The transient sources, that are usually located in the Galactic plane, flare on timescales less than a day with the outburst persisting for several weeks. There are at least two different types of Galactic transient sources: those that are believed to be X-ray pulsars in which the neutron star accretes from a stellar Be companion, and, black hole binary systems in which enormous outbursts are due to either instabilities in the mass transfer from the binary companion or in the structure of the accretion disc.

1.8.1 Black Hole Candidates (BHCs)

An X-ray source is classified as a black hole X-ray binary (BHXB) if the inferred mass of the compact object is greater than 3 $M_{\odot}$. Five distinct X-ray spectral states have been noted in BHXB systems (Esin et al. 1998): the low/hard state, high/soft state, intermediate state, very high state, and the quiescent/off state.

Systems in the low/hard state have power-law spectra (index ~1.4 - 1.9), an exponential cut-off around 100 keV and very little evidence of a soft thermal component. The high/soft state spectra are dominated by a black-body component with temperature ~1 keV. At higher energies, high-state spectra show a power-law tail (index ~2.2 - 2.7) that often extends to over 500 keV without an obvious turnover. For some systems an intermediate state has been observed, this is intermediate in both spectral shape and luminosity between the high and low states. A few systems have also been observed in a very high state, with luminosities close to the Eddington limit. This state has similar spectral properties to the high state, but is characterised by higher bolometric luminosity, more prominent hard tail, stronger variability, and the presence of 3 - 10 Hz Quasi-Periodic Oscillations (QPOs). All transient black hole systems spend some time in the quiesent/off state, which naturally is characterised by very low X-ray luminosity.

Esin et al. (1998) suggest that BHXB systems can be explained as consisting of an inner advection dominated accretion flow (ADAF) surrounded by an outer thin disk. In the low and quiesent states the mass accretion rate is low. Thus the accretion disc consists of an inner ADAF and an outer thin disk. When the accretion rate increases, the radius at which the ADAF can be maintained decreases, and the thin discs inner edge is closer to the black hole. This is the intermediate state. At higher accretion rates, the thin disc extends all the way down to the last stable orbit. This is the high state.

Grove et al. (1998) used OSSE to study the spectral states of 7 transient black hole candidates: GRO J0422+32, GX 339-4, GRS 1716-249, GRS 1009-45, 4U 1543-47, GRO J1655-40 and GRS 1915+105. It is found that the X-ray low/hard state seems to be correlated with a γ-ray exponentially cut-off power-law, which is consistent with thermal comptonisation of soft photons from the accretion disc. The X-ray high/soft state is correlated with a γ-ray power-law state, which is due to bulk motion comptonisation.

The first state appears to be the γ-ray extension of the X-ray low, hard state where the majority of luminosity is carried by photons of energy ~100 keV. The power-law γ-ray state is associated with the presence of a strong ultrasoft X-ray excess (kT ~1 keV), the signature of the X-ray high, soft (or perhaps very high) state (Grove et al. 1998; fig. 1.8).

Grove et al. (1998) also searched for emission lines (narrow and broad) at 170 keV (backscatter from 511 keV), ~480 keV (line seen by SIGMA from Novae Muscae) and at 511 keV. They set 5σ daily flux upper limits of between 5 and 15×10^{-4} photons $\mathrm{cm}^{-2}\ \mathrm{s}^{-1}$.

It should be noted however, that the number of truly simultaneous X-ray and γ-ray observations of BHCs is small, and so further simultaneous broad band observations are necessary to confirm the possible correlation between the X-ray and γ-ray states (Grove et al. 1998).

1.8.2 Neutron star systems

Low Mass X-ray Binaries (LMXB)

In these systems the companion star is of low mass ($\leq 1\,M_{\odot}$). If the neutron star has a weak magnetic field ($< 10^{11}$ G) then accretion from the companion onto the neutron star surface can occur, and this may lead to a build up of helium. Eventually, when the mass of helium accreted is

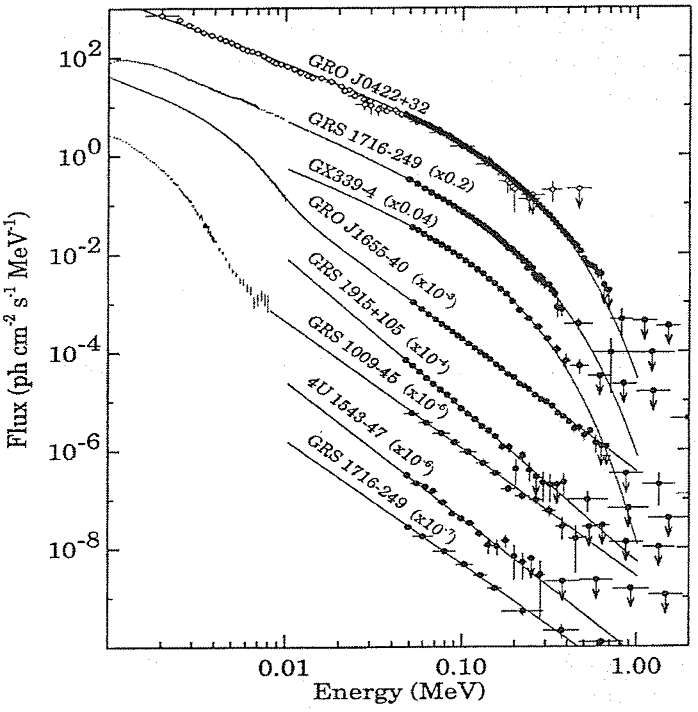

Figure 1.8: *Photon spectra measured for 7 black hole candidates by Grove et al. (1998). The spectra have been arbitrarily scaled for clarity. The black dots are the OSSE data, the other symbols are contemporaneous or near contemporaneous data from HEXE (diamonds) and ASCA (crosses). The upper three spectra show exponentially cut-off power-laws and are from the X-ray low/hard state. The lower set of spectra have gamma-ray power-laws and are from the X-ray high/soft state.*

too much, there will be runaway thermonuclear burning of the helium. These sources are known as X-ray bursters. When the magnetic field is higher ($\sim 10^{12}$ G) accretion onto the surface is channelled down the magnetic poles. The X-ray emission tends to be pulsed at the rotation frequency of the neutron star. See Bildsten et al. (1997) for a review of 5 years worth of BATSE observations of these type of systems.

High Mass X-ray Binaries (HMXB)

In these systems accretion from a high mass companion star occurs, in some special cases this star is a Be type star. In normal supergiant - neutron star systems, accretion occurs from the stellar wind, and the X-ray luminosity is proportional to the mass loss rate from the companion. In Be X-ray binaries the neutron star is often in a highly eccentric orbit, and mass loss from the companion occurs in the form of a circumstellar disc, when the neutron star impacts this a strong X-ray outburst occurs. See Bildsten et al. (1997) for a review of 5 years worth of BATSE observations of both types of HMXB systems.

Soft Gamma Repeaters (SGR)

At least three of the four currently known soft gamma repeaters (SGRs) are associated with slowly rotating, extremely magnetized neutron stars ($> 10^{13}$ G) located within young supernova remnants (Kouveliotou et al. 1998, 1999). They are characterized by the recurrent emission of γ-ray bursts with relatively soft spectra and short durations (~ 0.1 s). It has been suggested that these bursts are due to neutron star crust fractures driven by the stress of an evolving, ultrastrong magnetic field.

1.8.3 White Dwarf systems

AM Her type systems (aka Polars) with their strong magnetic fields ($10^7 - 10^8$G) are able to prevent formation of an accretion disc and channel the accretion flow directly down to the white dwarf surface, resulting in shock temperatures approaching 100 keV. The strong shocks present in the accretion funnel in these systems are undoubtedly capable of accelerating particles to relativistic energies and perhaps also producing electron-positron pairs.

1.9 Extragalactic variable sources

Gamma-rays and hard X-rays provide an exciting spectral band for the study of Active Galactic Nuclei (AGN). Gamma-ray observations could prove critical to the overall understanding of these objects for several reasons:

- Gamma-ray photons are extremely penetrating, thus providing a direct view of the innermost regions of the sources, where the basic energy sources and radiation mechanisms reside.
- The X-ray and γ-ray data currently available on AGN indicate that a substantial fraction of the total luminosity in these sources is emitted in the X-/γ-ray band. The γ-ray spectral emission characteristics, however, appear to depend on AGN type: objects which exhibit beaming characteristics such as QSOs and BL Lacs emit a hard spectrum up to GeV energies, which is also probably beamed, whereas Seyferts and radio galaxies show a clear cut-off in the spectral emission, the value of which can vary from a few tens of keV to possibly MeV energies in a similar manner to that observed in galactic black hole candidates such as Cyg X-1 and 1E1740.7-2942.
- The extremely high luminosity and short variability timescale observed in the X-ray band indicates the emission regions have a very high photon density. Under these conditions, electron-positron pairs are created by collisions between photons. Emission and absorption processes by these pairs strongly affect the overall emergent γ-ray spectra, both in terms of continuum and any 511 keV line emission.
- The intensity and the measured spectral shape of the high-energy cosmic diffuse background imply that AGN spectra cannot extend into the γ-ray range with the hard "canonical" photon power-law slope (1.7) observed in the 2 - 100 keV band. The exact determination of the energy where the spectra steepen has important consequences, not only to constrain the physical models of these sources, but also to assess their contribution to the extragalactic diffuse background.

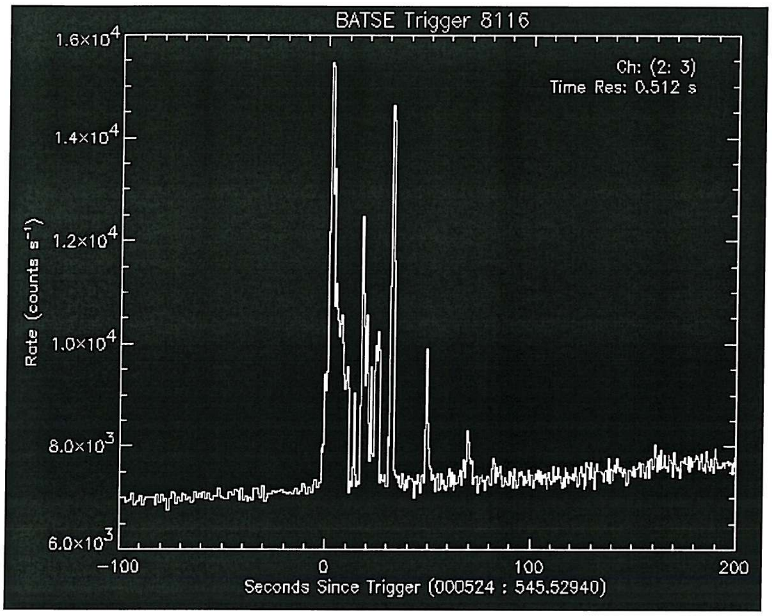

Figure 1.9: *Light curve of GRB 000524 taken from the BATSE online archive.*

1.10 Gamma Ray Bursts (GRBs)

BATSE's prime aim was to improve understanding of the Gamma Ray Burst phenomena. In the 8 or so years of CGRO's operation BATSE has observed over 2000 GRBs. The profiles of GRBs are very variable, BATSE has observed GRBs which rise and fall on timescales of order 20 seconds with very simple structures, however most bursts have many spikes, on timescales of ~0.1 s, and/or numerous well defined sub-pulses (Fishman 1999, fig. 1.9 shows the light curve of a GRB picked randomly from the BATSE archive). The duration of GRBs spans over five decades, from a few milliseconds to over a thousand seconds. When the distribution of the GRB durations is plotted there appear to be two peaks, at ~0.5 s and at ~34 s. Mukherjee et al. (1998) have recently suggested a third peak at 2 - 5 s. A correlation between the hardness and duration of GRBs has also been found and confirmed over the years.

The general spectral form of GRBs is well described by the Band function (Band et al. 1993), where the GRB spectrum can be fit with one power-law at low energies and a steeper (i.e. more negative index) power-law at higher energies with a smooth break joining the two. Many GRBs do not appear to emit photons above ~300 keV. Those that show emission up to and above 10 MeV can be fit with power-laws of index ~-2. Over the BATSE energy range νF_ν plots have been used to determine the peak energy (E_p) for the GRB spectra. Mallozzi et al. (1995) compared the GRB intensity and E_p and found that the resultant correlation is consistent with a redshift of the continuum spectrum with distance. Spectral softening is usually seen throughout a GRB, and also within the sub-pulses of burst. In many cases the peaks are usually offset, with the softer peak delayed by a few seconds from the harder peak, and lasting much longer than the harder peak. The distribution of GRBs as seen by BATSE is consistent with an isotropic source population, though there is evidence that GRBs are not homogeneous, and possibly current observations are sampling to the very edge of the source distribution in space.

In the last two years, since the discovery of GRB 980425, and its coincidence with the position of SN 1998bw (Galama et al. 1998), there has been discussion regarding their possible association. GRB 980425 had a peak photon flux 30 times less than that of the largest peak seen by BATSE in the energy range 50 - 300 keV. It is however not an unusual event, and the possible linking of an under-luminous GRB like this one, with an explosive supernova would enhance understanding of both phenomena.

On February 28, 1997, the BeppoSAX spacecraft detected and rapidly localized a burst with the Wide Field Camera (WFC), and, pointing the Narrow Field Instruments (NFI) at the location, discovered the first fading X-ray counterpart (Costa et al. 1997, fig. 1.10). After this Van Paradijs et al. (1997) observed the area with optical telescopes and discovered the first fading optical counterpart associated with a GRB. Since then it has been discovered that most GRBs have fading X-ray counterparts, and that approximately 50% of them also have fading optical counterparts (Hurley 1998). Fading can often be described by a power-law with index ~-1.5. The redshift of a GRB was first constrained by Metzger et al. (1997), who determined the redshift to GRB 970508 was > 0.8 and < 2.2.

Two different theories that have been proposed for GRBs are neutron star mergers (Paczyński 1991) and hypernovae (Paczyński 1998). Neutron star merger requires the neutron star to be in a binary with either another neutron star or a black hole. Such a merger could liberate 10^{52} erg of energy. If this scenario were true then the burst rate should follow that of star formation, which is thought to peak at around $z \sim 1.25$. The evolution of the system would be: (1) first star goes supernova 10^7 yrs after formation, leaving behind a high mass X-ray binary system; (2) this would

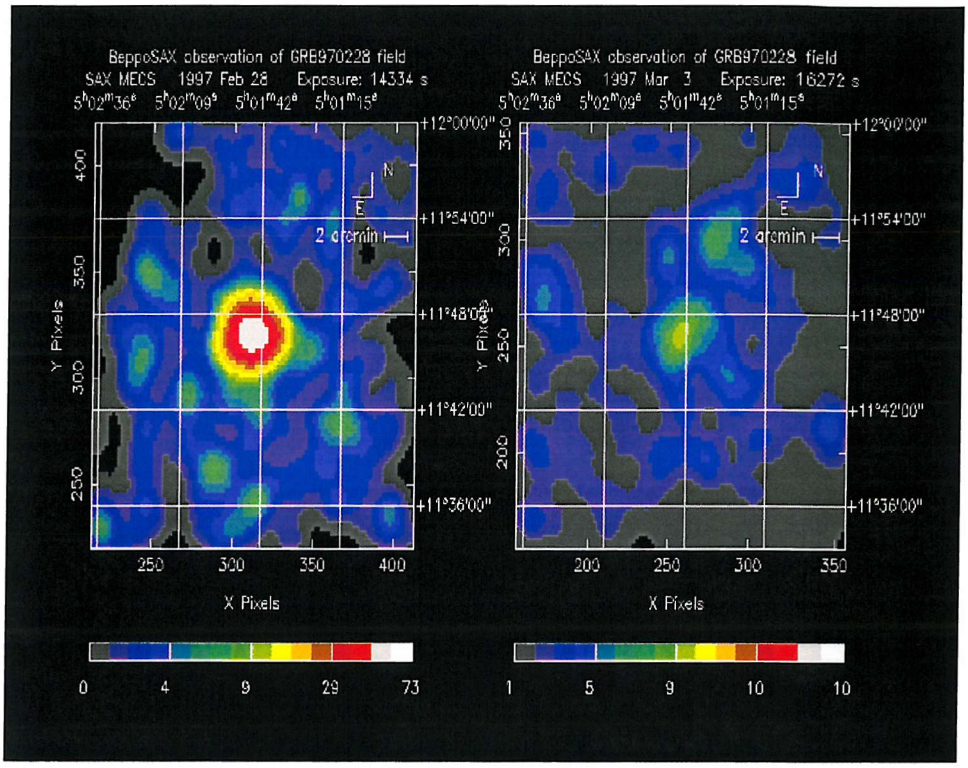

Figure 1.10: *The first X-ray afterglow observed for a Gamma Ray Burst, GRB 970228, taken from the BeppoSAX web site.*

have a short lifetime (10^5 yr) before the second star explodes as a supernova, leaving behind a binary neutron star system; (3) this system will radiate its orbital energy away as gravitational radiation in several times 10^9 yr, resulting in a merger. If the resulting γ-rays are not beamed then only about one event is required every 10^6 years in every galaxy. It is possible that, due to kicks on the binary from supernovae explosions, these sources may be a long way from their birthplaces.

There is however a limited amount of energy that can be liberated from the merger of neutron stars, which will of course not all go into observable radiation. There has been suggested therefore a model which starts with a larger available energy budget, and that is hypernovae. Hypernovae are extremely energetic supernovae which result from the collapse of a 10-15 $M_\odot$ star to a black hole with an accretion disk which produces the energy for the burst. The progenitors of hypernovae only live for about 10^6 yrs, and consequently will not travel far from their birthplaces. This provides a test between the two models, hypernovae will be inside their host galaxies, whereas a lot of neutron star merger sources would be expected to have escaped from their host galaxies.

1.11 Cosmic Diffuse Background (CDB)

Recent measurements of the cosmic diffuse gamma-ray background have eliminated the presence of the MeV bump (Kinzer et al. 1997; fig 1.11). Below a few hundred keV the observed cosmic diffuse background (CDB) is believed to be due to the superposition of unresolved Seyfert Galaxies, whereas for photon energies above 3 MeV Blazars are the dominant source population (Zdziarski 1996). There is no known galaxy type that can fill the gap between the Seyfert galaxies and blazars. However, the CDB around photon energies ~1 MeV could be partly, or even completely, due to cumulative γ-ray production in supernovae (Watanabe et al. 1999). In particular, γ-ray lines from the reaction chain $^{56}Ni \rightarrow ^{56}Co \rightarrow ^{56}Fe$ are abundant enough to generate a detectable signal. Although iron synthesis occurs in all types of supernovae, the contribution to the background is dominated by type Ia events due to their higher photon escape probabilities. Supernovae cannot contribute to the CDB above 3.5 MeV, simply because they do not produce radioactive isotopes that emit γ-ray lines above that energy. The presence of strong lines would lead to steps in the spectrum that might be observable with future γ-ray instruments. The currently favoured scenarios of SN I progenitors and their cosmic rate of evolution underpredict the CDB (Watanabe et al. 1999).

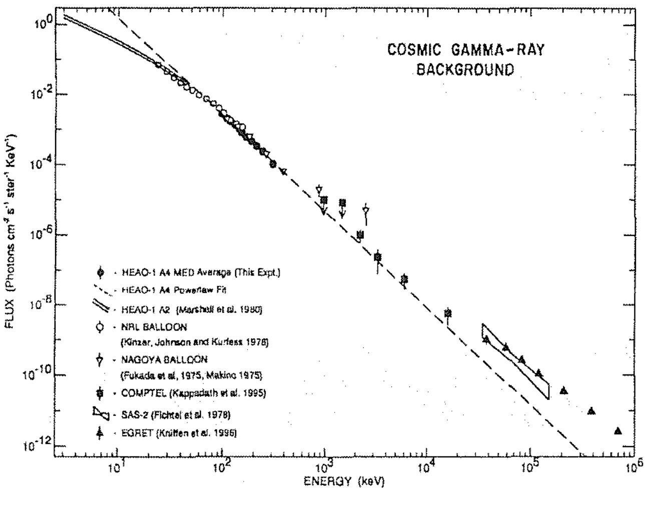

Figure 1.11: *Selected measurements of the cosmic diffuse gamma-ray background as given by Kinzer et al. (1997). The spectral shape of the background can be explained by emission from AGN and SNe Ia (Zdziarski 1996).*

1.12 Summary

As can be seen from fig. 1.12 the number of known γ-ray sources has increased dramatically since the launch of CGRO. Before the launch of CGRO the γ-ray sky was relatively unknown, but now there are many known sources, some of which are as yet unidentified with objects at other wavelengths. In the future, missions are required to build on the progress made by CGRO, to observe sources with higher spectral and positional resolution, and to provide more and higher quality data. CGRO has also demonstrated the usefulness of multi-instrument satellites, with payloads optimised to complement each other and to provide wide spectral coverage.

One of the near-future missions which aims to build on the recent progress is the INTErnational Gamma Ray Astrophysics Laboratory (INTEGRAL). This ESA lead mission will contain several complementary instruments to provide coverage over the energy range from a few keV - 10 MeV with simultaneous optical monitoring. With this payload INTEGRAL will extend much of the work done by BATSE, OSSE and COMPTEL.

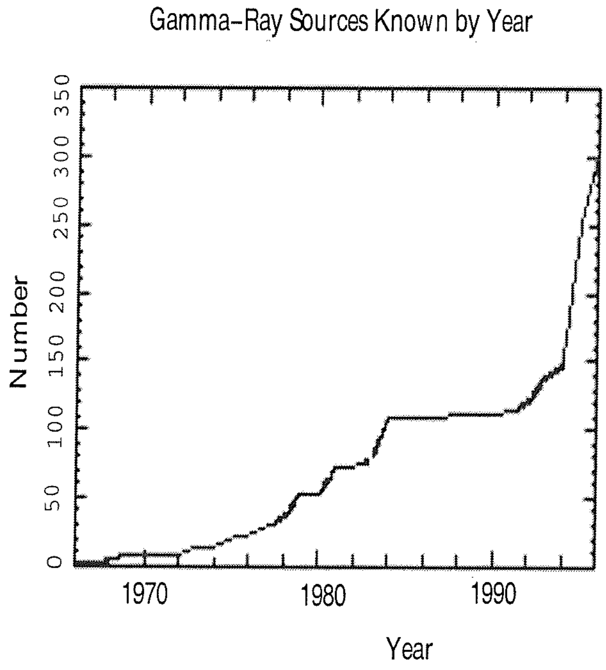

Figure 1.12: *The number of known γ-ray sources against year (Macomb & Gehrels 1999).*

Chapter 2

The INTEGRAL Mission

2.1 Overview

INTEGRAL was selected by the ESA science programme committee as an ESA medium-size mission of the Horizon 2000 programme to be launched in 2001. The mission is led by ESA but will have contributions from Russia (PROTON launcher) and NASA (Deep Space Network ground station).

INTEGRAL (The INTErnational Gamma-Ray Astrophysics Laboratory) is dedicated to the fine spectroscopy ($E/\Delta E = 500$) and fine imaging (angular resolution = $12'$ FWHM) of celestial γ-ray sources in the energy range 15 keV - 10 MeV with concurrent source monitoring in the X-ray (3 - 35 keV) and optical (V-band, 550 nm) energy ranges.

INTEGRAL uses the same service module as the X-ray Multi-mirror Mission (XMM). It will be launched using a Russian PROTON rocket, into a highly eccentric 72-hour orbit, though it is designed to also be compatible with an ARIANE 5 launcher. The nominal life time of the observatory is 2 years, though there is a possible extension to 5 years. Most of the observing time will be made available to the worldwide scientific community. The INTEGRAL core programme (the time guaranteed for the INTEGRAL Science Working Team) consists of 3 parts: (i) Frequent scans of the Galactic Plane (Galactic Plane Survey, GPS) (ii) Deep Exposure of the Galactic central radian (Galactic Central Radian Deep Exposure, GCDE) (iii) Pointed observations of selected sources. A schematic of the INTEGRAL satellite is shown in figure 2.1. A brief outline of the key scientific objectives and instrumentation is provided in this chapter.

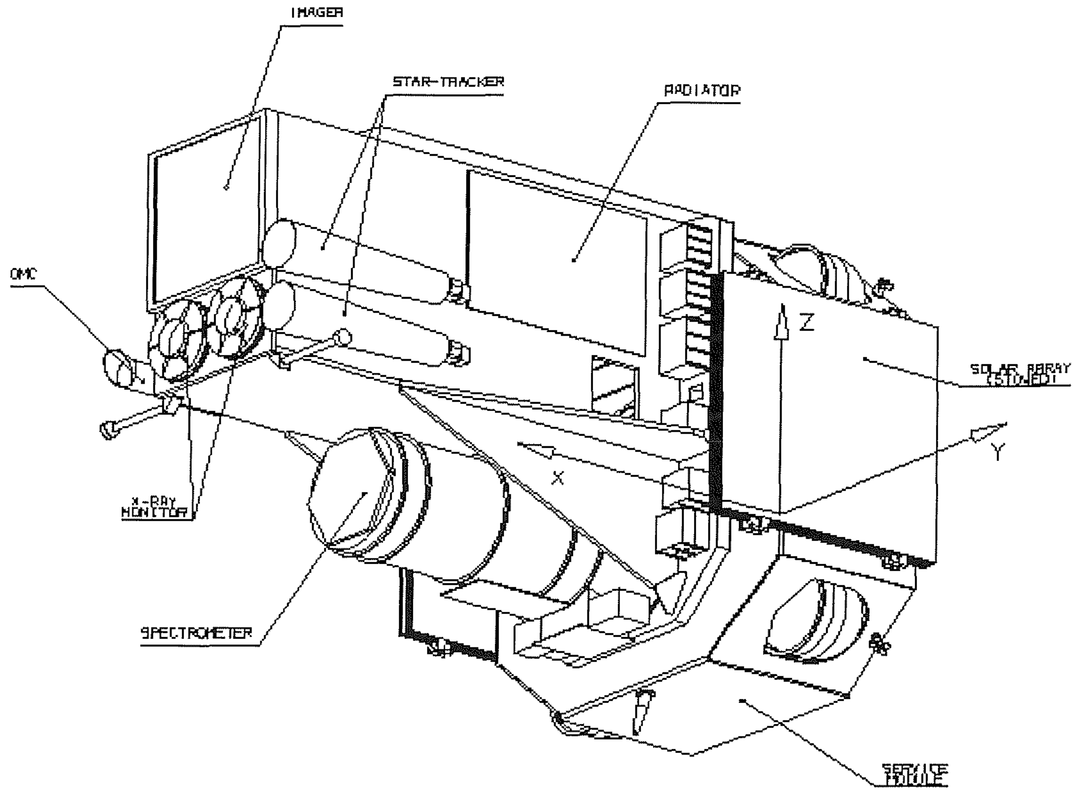

Figure 2.1: *Schematic of INTEGRAL (Picture taken from ESA web pages).*

2.2 Scientific Payload

The INTEGRAL payload consists of two main γ-ray instruments:

- SPI (SPectrometer on INTEGRAL) - A cryogenically cooled germanium spectrometer providing high spectral resolution (2 keV @ 1 MeV), high line sensitivity, degree resolution mapping of diffuse source emission and degree imaging capability.
- IBIS (Imager on-Board the INTEGRAL Satellite) - A high angular resolution telescope ($12'$ FWHM) providing accurate source positioning, high continuum and broadline sensitivity and medium spectral capability.

These are supported by two monitor instruments, which will provide observations in the X-ray and optical energy bands:

- JEM-X (Joint European X-ray Monitor) - An X-ray monitor which will extend the spectral coverage down to a few keV, enabling INTEGRAL to associate γ-ray and X-ray sources, and provide coverage of the Fe line at $\sim$ 6 keV.
- OMC (Optical Monitoring Camera) - An optical camera which will search for, locate and study the optical counterparts of γ-ray bursts.

As an example of the complementary nature of the instruments, SPI and IBIS will simultaneously be able to study a particular line emission, the former investigating the detailed line shifts and shape, the latter locating the source of the emission to better than $1'$. Simultaneously the X-ray Monitor will provide information on the emission at lower energies, down to and including the $\sim$6 keV line of highly ionised iron, and the Optical Monitor will observe in the 500 - 850 nm waveband. All 4 instruments are co-aligned.

SPI, IBIS and JEM-X share a common principle of operation - they are all coded mask telescopes. The coded mask technique is the key which allows imaging, which is all important in separating and locating sources. It also provides near perfect background subtraction because for any particular source direction the detector pixels can be considered to be split into two intermingled subsets, those capable of viewing the source and those for which the flux is blocked by opaque mask elements. Effectively the latter subset provide an exactly contemporaneous background measurement for the former, made under identical conditions.

2.2.1 SPectrometer on INTEGRAL (SPI)

SPI will perform spectral analysis of γ-ray point sources and extended regions in the 20 keV - 8 MeV energy range with an energy resolution of 2 keV (FWHM) @ 1 MeV. The instrument uses an array of 19 hexagonal high purity Germanium detectors (thickness 7 cm, side length 3.2 cm) cooled by a Stirling cooler system to an operating temperature of 85 K. A hexagonal coded mask, with 127 elements, is located 1.71 m above the detection plane in order to image large regions of the sky (FCFOV = 16°) with an angular resolution of $\sim 2^\circ$. The mask has 63 opaque elements, made of 3 cm thick tungsten, and 64 transparent elements. In order to reduce background radiation, the detector assembly is shielded by a veto (anticoincidence) system, which extends around the bottom and side of the detector almost completely up to the coded mask. The veto shields are made of Bismuth Germanate (BGO) scintillation crystals and provide an effective shielding thickness of 5 cm. The aperture (and hence contribution by cosmic diffuse radiation) is limited to ~30°. A plastic veto is provided below the mask to further reduce the 511 keV background. Figure 2.2 shows a cut away view of SPI. Table 2.1 summarise SPI's characteristics.

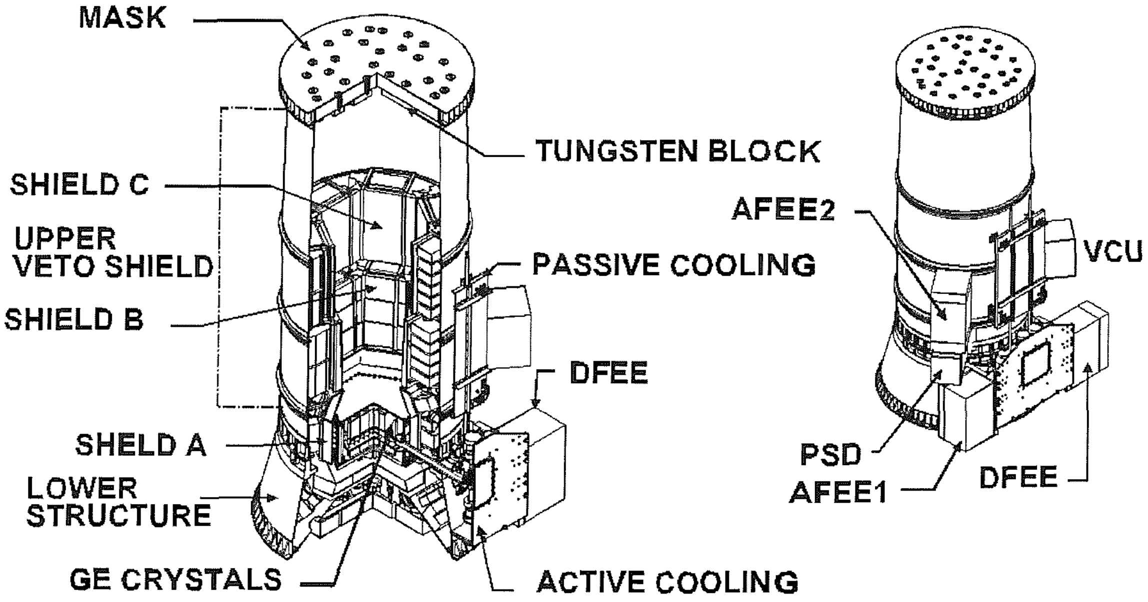

Figure 2.2: *Cut away view of the Spectrometer on board INTEGRAL (SPI). Picture taken from ESA web pages.*

For long observations SPI is background limited, and it is critical to maintain the overall instrument background at the lowest possible level. The suppression of the internal germanium detector background is aided by the use of on-board pulse shape discrimination (PSD). In the energy range 0.2 - 1.5 MeV the dominant component of the background results from β-decays in the germanium detectors induced primarily by secondary neutrons. These β-decays go primarily into the ground state (i.e. no accompanying photon). Since the range of the β in germanium is short (< few mm) the energy deposition of these events is localised to a small region. This is in contrast to the primary photons that constitute the signal. Most of these photons undergo multiple Compton scattering before either losing all of their energy or departing the detector. The current pulse generated by an interaction in the germanium detector depends on the location and multiplicity of the interactions in that detector. By analyzing this pulse (with the PSD) one can distinguish between single and multiple site events. It is estimated that the background in the range 0.2 - 1.5 MeV can be reduced by as much as a factor of 10 (Teegarden et al. 1997).

2.2.2 Imager on-Board the INTEGRAL Satellite (IBIS)

IBIS provides fine imaging (12′ FWHM), source identification and spectral sensitivity to both continuum and broad lines over a broad (15 keV - 10 MeV) energy range. The imager will exploit, simultaneously with the other instruments on INTEGRAL, celestial objects of all classes ranging from the most compact Galactic systems to extragalactic objects. A tungsten coded-aperture mask (located at 3.2 m above the top detector plane) is optimised for high angular resolution. As diffraction is negligible at γ-ray wavelengths, the angular resolution obtainable with a coded mask telescope is limited by the spatial resolution of the detector array. The imager design takes advantage of this by utilising a detector with a large number of spatially resolved pixels, implemented as physically distinct elements. The detector uses two planes, one a 2600 cm^2 layer of CdTe (16384 pixels, each 4×4×2 mm (width × depth × height)), and the other a 3100 cm^2 layer of CsI (4096 pixels, each 9×9×30 mm). The detector provides the wide energy range and high sensitivity continuum spectroscopy required for INTEGRAL. The CdTe array is used in order to achieve a good spectral resolution in the lower end of the detector energy range. The CsI array, placed 10 cm below the CdTe array, gives good stopping power up to several MeV while maintaining high spatial resolution and good spectral resolution. The large sensitive area (> 3000 cm^2) is designed for optimal performance at 511 keV (Ubertini 1997). The division into two layers allows the paths of photons to be tracked in 3D, as they scatter and interact with more than one element. Events can be categorised and the signal-to-noise ratio improved by rejecting those which are unlikely to correspond to real (celestial) photons, e.g. towards the high end of the energy range. The detector aperture is restricted by a thin tungsten passive shield, covering the distance between the mask and the position sensitive detector, and is shielded in all other directions by an active BGO scintillator veto system (Ubertini 1997). Figure 2.3 shows a cut away view of the IBIS detector planes. Simulations have shown that assuming no error in pointing axis reconstruction and/or other systematic effects, IBIS will locate in the sky strong pointlike sources (30σ) with an accuracy of better than $30''$ (Ubertini 1997). The characteristics of IBIS are summarised in table 2.1.

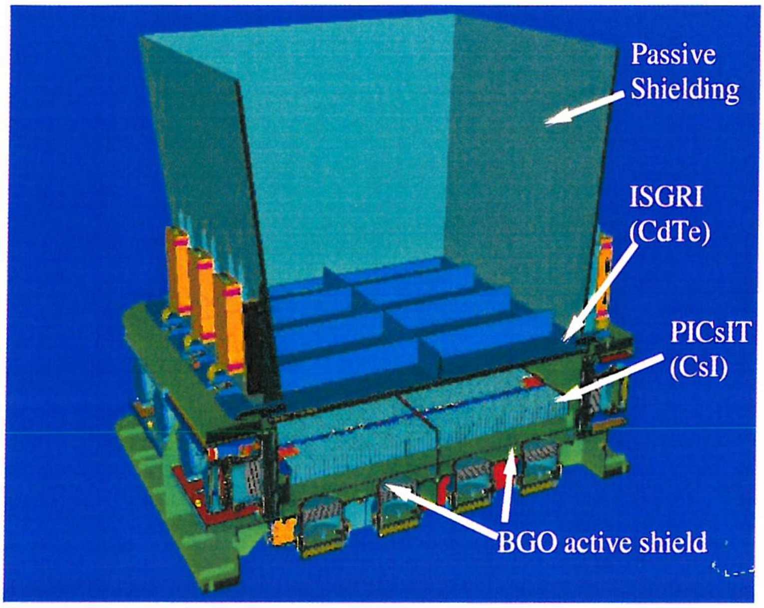

Figure 2.3: *Cut away view of the Imager on board INTEGRAL (IBIS). Picture taken from ESA web pages.*

2.2.3 Joint European X-Ray Monitor (JEM-X)

JEM-X supplements the main INTEGRAL instruments and plays a crucial role in the detection and identification of the γ-ray sources, and in the analysis and scientific interpretation of INTEGRAL γ-ray data. JEM-X will make observations simultaneously with the main γ-ray instruments providing images with arcminute angular resolution in the 3 - 35 keV energy band (providing coverage below the $\sim$6 keV Fe line complex). The baseline photon detection system consists of two identical high pressure imaging microstrip gas chambers. Each detector unit views the sky through its coded aperture mask located at a distance of approximately 3.2 m above the detection plane. A schematic view of JEM-X is shown in figure 2.4. The coded mask is a 22501 element Hexagonal Uniformly Redundant Array (HURA) written in a 0.5 mm thick tungsten plate. This thickness gives opacities of 99.9% at 35 keV and 95% at 60 keV. The number of open cells is 5844 (25%) and the mask-detector distance and mask element size gives the instrument an angular resolution of 3.35′ (Lund et al. 1998). Each gas chamber has a sensitive area of 500 cm^2 and contains a mixture of xenon (90%) and methane (10%) at 1.5 bar pressure. The chamber window is made of 250 μm thick Be foil, which gives good transmission of low energy X-rays and is impermeable to the gas. The JEM-X characteristics are summarised in table 2.1.

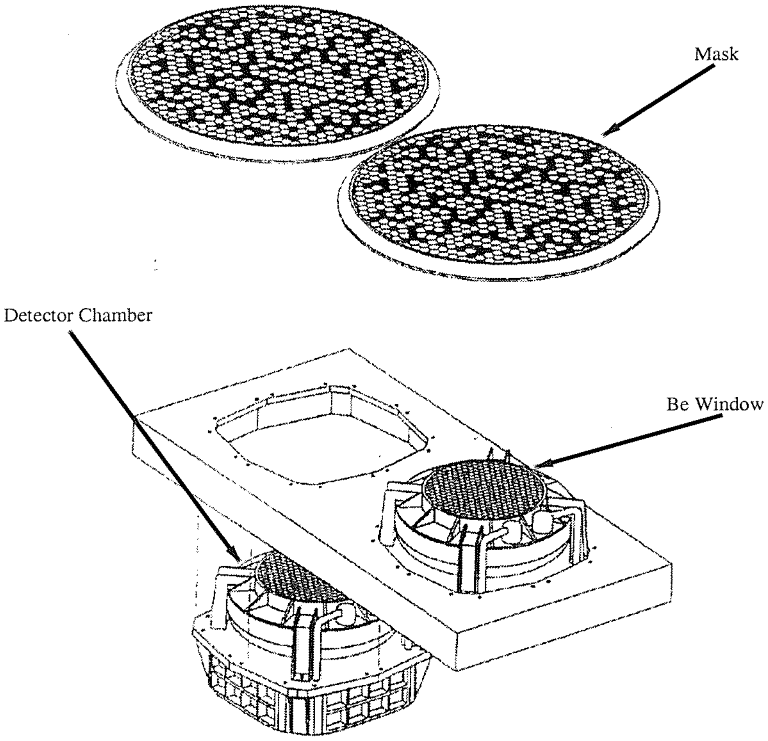

Figure 2.4: *Schematic view of the X-ray Monitor on board INTEGRAL (JEM-X). Picture taken from ESA web pages.*

2.2.4 Optical Monitoring Camera (OMC)

The Optical Monitoring Camera consists of a passively cooled CCD (2048×1024 pixels, imaging area: 1024×1024 pixels) working in a frame transfer mode. The CCD is located in the focal plane of a 50 mm (diameter) lens including a Johnson V-Filter to cover the 500 - 850 nm wavelength range. The OMC will be mounted close to the top of the payload module structure. A schematic view of the OMC is shown in figure 2.5. The serendipitous nature of GRBs means that the OMC will be able to look for optical afterglows from GRBs. The OMC can achieve a sensitivity down to 19.2 magnitudes in 1000 seconds (Giménez et al. 1999). Table 2.1 presents the characteristics of the OMC.

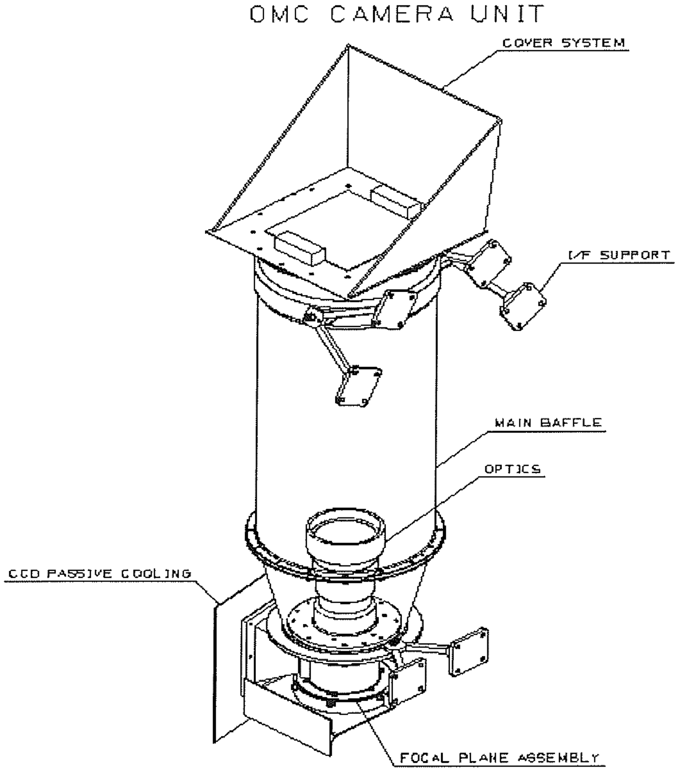

Figure 2.5: *Schematic view of the Optical Monitoring Camera on board INTEGRAL. Picture taken from ESA web pages.*

2.3 Scientific Objectives

Fine spectroscopy over the entire operational energy range will permit spectral features to be uniquely identified, and line profiles to be determined for physical studies of the source region.

Instrument	IBIS	SPI	JEMX	OMC
Bandpass	15 keV–10 MeV	20 keV–8 MeV	3–35 keV	500–850 nm
Detector Area (cm^2)	2600 (CdTe) 3100 (CsI)	500	1000	CCD (2048×1024 pixels)
Spec Res	6%@1MeV	0.2%@1MeV	15%@10keV	
FCFOV	9°	16°	4.8°	5°
Ang Res	$12'$	2°	$3'$	$17.6''$/pixel
PSLA (10σ)	$60''$	$< 30'$	$< 30''$	$\sim 8''$
Cont. Sens.	2×10^{-7}	7×10^{-8}	1×10^{-5}	19.2 m_v (10^3s)
Line Sens.	1×10^{-5}	5×10^{-6}	2×10^{-5}	
Timing Accuracy (3σ)	67 μs - 1000 s	100 μs	128 μs	> 1 s
Mass (kg)	628	1309	65	17
Power (W)	275	373	55	18
Data Rate (kbps)	57 (ave)	20 (ave)	7	2

Table 2.1: *Summary of the INTEGRAL instruments characteristics. Where FCFOV stands for Fully Coded Field Of View (degrees), Ang Res stands for Angular Resolution (FWHM), Spec Res stands for Spectral Resolution ($\Delta E/E$) and PSLA stands for Point Source Location Accuracy. The Continuum Sensitivities (Cont. Sens.) of IBIS and SPI are quoted at 1 MeV in units of photons* s^{-1} cm^{-2} keV^{-1}*, and that for JEM-X is in the same units but at 6 keV. The Line Sensitivity (Line Sens.) of SPI is at 1 MeV and in units of photons* s^{-1} cm^{-2}*, that for JEM-X is in the same units but at 6 keV, and that for IBIS is also in the same units but at 100 keV. The Continuum and Line sensitivities are given for* 3σ *detections in* 10^6 *seconds. Values taken from Winkler (1999b).*

The fine imaging capability of INTEGRAL within a large field of view will permit the accurate location, and hence identification, of γ-ray emitting objects with counterparts at other wavelengths, enable extended regions to be distinguished from point sources and provide considerable serendipitous science.

In the 15 keV - 10 MeV region, line-forming processes such as nuclear excitation, radioactivity, positron annihilation, cyclotron emission and absorption become important. Unique astrophysical information is contained in the spectral shift, line width, and line profiles. Detailed studies of these processes require the resolving power ($E/\Delta E = 500$) of a germanium spectrometer such as that employed on INTEGRAL. Lower resolution spectrometers (e.g. SIGMA, OSSE, COMPTEL) do not have sufficient energy resolution to permit a meaningful study of the diagnostic parameters of these lines. The last high-resolution space instrument, that on HEAO-3 in 1979-80, was 100 times less sensitive than INTEGRAL. Solid observational and theoretical grounds already exist for predicting detectable emission from such varied celestial objects as the Galactic Centre region, the interstellar medium, compact objects, novae and supernovae and a variety of AGN. The main areas INTEGRAL will cover are:

- Galactic Plane and Centre
- Nucleosynthesis (Hydrostatic, Supernovae, Novae)
- Galactic variables and transients
- Extragalactic sources
- Cosmic Diffuse Background (CDB)
- Gamma Ray Bursts (GRBs)
- Serendipitous Sources

2.3.1 Galactic Plane and Centre

A major part of the INTEGRAL core programme will be the Galactic Plane Survey (GPS). The two main objectives of the GPS are: to provide frequent monitoring of the plane in order to detect transient sources; and, to build up time resolved maps of the Galactic Plane in continuum and diffuse line emission (such as ^{26}Al and 511 keV) with modest exposure (Winkler et al. 1999a). In the first year the GPS will be allocated 2.3×10^6s, and it is planned to keep this constant for the second year (Winkler et al. 1999a). During the weekly scans INTEGRAL will oscillate around the Galactic equator, following a sawtooth pattern as shown in figure 2.6. An extension of this survey will be deep observations of the central Galactic region (Galactic Central Radian Deep Exposure, GCDE). The GCDE will be allocated 4.8×10^6s during the first year, which will remain constant up to year 5. The GCDE has three objectives: mapping line emission from radioisotopes (e.g. ^{26}Al, ^{44}Ti, 511 keV); mapping continuum emission from the Galactic ridge; and, performing deep imaging and spectroscopic studies of the central region of the Galaxy (Winkler et al. 1999a)

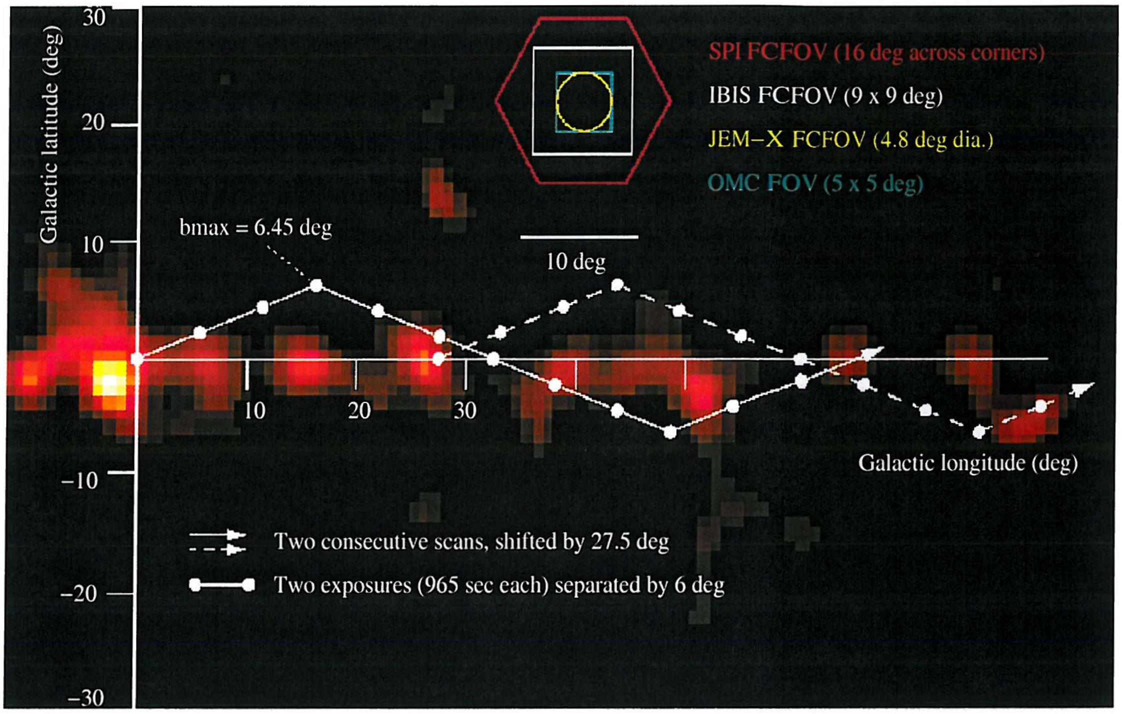

Figure 2.6: *A weekly scan consists of a "slew, stop, stare" profile along a saw-tooth track inclined at 21 degrees to the Galactic equator. Picture taken from ESA web pages.*

INTEGRAL will provide the tools for using γ-rays as a sensitive probe of the astrophysical processes going on within a few hundred parsec of the nucleus of our galaxy. The fine angular resolution of INTEGRAL will allow the identification of sources in crowded regions of the Galaxy. INTEGRAL's spectroscopic resolution will allow it to look for line emission, for example 511 keV emission, from the accretion regions of black hole candidates.

The suspected radio counterpart of the black hole at the center of our galaxy Sgr A*, has been studied by Goldwurm et al. (1998) with SIGMA between 1990-1997. ASCA, ART-P and ROSAT results have shown that at low energies lots of point sources, and also diffuse emission, are present in the area and can make identifications difficult. Even at energies greater than 50 keV, however, imaging will be crucial since SIGMA showed the presence of several high-energy sources located within 2^o of the Galactic Nucleus.

Lines from Annihilation

SPI will be able to measure the spatial distribution of the 511 keV line inside, and outside, the Galactic central radian, search for the possible anti-matter fountain, and measure the line width in the different disc components giving information about the physical state of the interstellar gas in which the positrons annihilate. Balloon-borne instruments have not had the sensitivity to measure the line profile and determine clearly the physical conditions of the annihilation sites. The broad fields of view of these instruments ($\sim 18^o$) allow them to observe only the average properties. INTEGRAL will be 30 times more sensitive and have much better angular resolution. Also, the contribution from other positron emitting point sources to the 511 keV emission of the interstellar medium will be addressed by SPI (Schönfelder 1998). INTEGRAL will be able to map the diffuse emission, resolve the point sources and measure the spectrum of each component.

Lines from cosmic ray - interstellar matter interaction

After the revision of the COMPTEL results on nuclear interaction line emission from Orion, the intensity level at which nuclear interaction lines can be expected from the interstellar medium is entirely open again (Schönfelder 1998). The narrow line components from excited $^{12}C^*$ and $^{16}O^*$ nuclei at 4.44 MeV and 6.13 MeV are typically 100 keV broad. The SPI sensitivities for such lines from a point-like source region will be about 1.5×10^{-5} photons cm^{-2} sec^{-1} and the sensitivity limit for the detection of these lines from the interstellar medium within the central radian of the Galaxy will be typically 1×10^{-4} photons cm^{-2} sec^{-1} rad^{-1}, which is comparable to the COMPTEL sensitivity limit (Schönfelder 1998).

It may be possible to observe the ^{12}C* and ^{16}O* lines associated with Wolf-Rayet and OB star associations. The ^{12}C* profile may depend on the composition of energetic particles in the stellar wind. SPI has the resolution to determine the profile and thus set constraints on the energetic particle composition. It is also expected that INTEGRAL will be able to measure the ^{12}C*/^{16}O* line ratio from Orion and the Galaxy. This ratio is also sensitive to the wind particle composition. With the increased sensitivity it is expected that INTEGRAL may be able to detect γ-rays from other nuclear species: ^{7}Li, ^{7}Be, ^{10}B, ^{11}B, ^{14}N, ^{20}Ne and ^{22}Ne. If the lines are broad then the sensitivity of SPI drops, and in this case IBIS may be better.

Continuum from cosmic ray - interstellar medium interactions

The improved angular resolution of INTEGRAL should make it possible to get a much better estimate of the total contribution to the Galactic γ-ray emission from unresolved sources. This remains one of the major uncertainties in previous work and has normally been neglected. The question of whether cosmic rays are enhanced in clouds (as might be expected if cosmic ray sources are embedded in them) can be addressed.

In the MeV range, the γ-ray continuum may be used to study the low-energy cosmic-ray electrons. These emit via a combination of bremsstrahlung emission when they interact with the ISM and inverse Compton radiation when they up-scatter 2.7K background photons. As discussed in chapter 1, CGRO has observed γ-ray continuum spectra from the Galaxy. The OSSE results (Kinzer et al. 1999) are consistent with a $\sim 6^{\circ}$ wide (in latitude) ridge in the soft γ-ray region. It has been suggested (Kinzer et al. 1999) that this may indicate a different cosmic ray electron distribution to the cosmic ray nucleon one. INTEGRAL's complementary combination of high spectral and angular resolution will be able to explore this more fully.

Transient sources in the Galactic Plane

Of particular interest to INTEGRAL is that SIGMA discovered highly variable 511 keV line emission from Nova Muscae, suggesting that these objects are significant contributors to positron production in the Galaxy. Based on the mass function obtained from optical spectroscopy of A0620-00, and additional optical spectroscopy and mass functions measured for V404 Cygni and Nova Muscae, which show they are certainly black holes, and on the association of hard X-ray spectral components with black hole candidates (e.g. Cyg X-1), it appears likely that the soft transients are black holes in binary systems. Observations of outbursts from such systems will meet one of the primary objectives of INTEGRAL - the study of black holes - and high resolution spectral line observations will be essential to understanding positron annihilation emission in the Galaxy.

Since INTEGRAL has a field of view of several tens of square degrees and almost all transient sources are within ± 10° of the Galactic plane, the observational strategy is to devote about 15% of the total observation time to scanning repeatedly (every few days) as much of the section of the Galactic plane as is possible within Sun constraints. The individual pointings will last for 300 sec and be spearated by 6°. In this mode transient sources along the plane will be detected near the maximum of the outburst and further detailed observations will be scheduled. It is expected that at least ten transient sources will be observed per year. The repeated scanning of the Galactic plane will also allow the monitoring of all sources in the plane for continuum and line variability.

2.3.2 Galactic variables and transients

The high sensitivity combined with excellent spectral, spatial and temporal resolution should enable INTEGRAL to offer new insights into the emission mechanisms of compact objects. Virtually all types of compact objects are significant sources of high-energy emission. INTEGRAL will image these objects in unprecedented detail at high energies, and the spectroscopic capabilities of the mission will provide the first detailed physical diagnostics of these systems at γ-ray energies

Cataclysmic Variables (CVs)

INTEGRAL could study many such systems ($>$ 100 CVs are known within 500 pc), and systematically study the high-energy properties of magnetic CVs of differing field strengths, as well as search for hard X-ray tails in the more abundant dwarf novae systems.

Neutron star systems

Repeated observations with SPI will provide the sensitivity and resolution necessary to look for lines within pulsar spectra. Higher sensitivity and resolution studies of the known sample of cyclotron line pulsars are required in order to study the line strength and shape as a function of pulse phase, and to search these systems for higher harmonics, which may allow more details of the magnetic field to be determined.

Higher sensitivity observations of LMXBs are needed to measure the cut-off energy and spectral indices to improve current models of LMXB hard X-ray emission. The hard X-ray component of LMXB spectra may be present only when the source is in a relatively low accretion rate state.

Black Hole Candidates

INTEGRAL, with its broad energy coverage (3 keV - 10 MeV), will provide an unparalleled opportunity to observe simultaneously the X-/γ-rays from black hole systems. Grove et al. (1998) used OSSE data to search for broad and narrow lines at 170, $\sim$ 480 and 511 keV. They set 5σ daily flux upper limits of 5 - 15 $\times$ 10^{-4} photons cm^{-2} s^{-1}. As can be seen from table 2.1 this is well above the SPI line sensitivity and so INTEGRAL offers the prospect of detecting these lines.

Black hole binary systems are characterized by distinctive X-/γ-ray signatures: the simultaneous presence of an ultra-soft X-ray spectral component with a dominant hard X-ray tail, or a power-law-like spectral component which extends out to $\geq$ 100 keV and contains the bulk of the systems luminosity. SIGMA data suggest that the black hole candidates have spectra significantly flatter than the neutron star systems, with photon spectral indices typically $\leq$ 2, rather than $\geq$ 2 as for the neutron star systems. Thus the bulk of the luminosity at high-energies appears in the hard X-ray and soft γ-ray bands for black hole candidates. It is important to confirm these results with higher signal-to-noise observations extending out to higher energies, where the turnover in the spectrum can be measured and the total luminosity thus constrained for neutron star and black hole systems.

The much greater sensitivity of INTEGRAL will allow 511 keV lines to be measured at the much lower fluxes needed to establish duty cycles for these presumed positron injection events. Compton reflection or scattering lines may also be measured as well.

2.3.3 Nucleosynthesis

INTEGRAL will allow the γ-ray lines from nucleosynthesis to be resolved as never before. The shapes of γ-ray line profiles from supernovae will provide information about the expansion velocity and density distribution inside the envelope, whilst the relative intensities of the lines provide direct insight into the physical environment at the time of the production.

Supernovae

Lehoucq et al. (1989) predict for supernova 1987A that ^{44}Ti, with a mean-life of 78 years and estimated yield of $10^{-4} M_\odot$, will have a γ-ray flux during INTEGRAL's life time in the 68 and 78 keV lines easily detectable with SPI. The profile of these lines could be used to probe the symmetry of the expansion. It should determine if the asymmetric, redshifted 847 keV ^{56}Co line, observed 613 days after the explosion (Tueller et al. 1990), was due to an asymmetric explosion or preferential visibility of expanding material on the far side of the ejecta. However, if the 68 and 78 keV lines are broad then ISGRI might provide better sensitivity, therefore it is important that IBIS and SPI co-aligned.

Gómez-Gomar et al. (1998) have studied the prospects for Type Ia supernova studies with INTEGRAL. They convolved detailed SN Ia models with the IBIS and SPI response matrices to investigate whether INTEGRAL would be able to discriminate between 4 models (detonation, delayed detonation, deflagration and sub-Chandrasekhar mass progenitor). They find the broad lines emitted by SN Ia reduce the sensitivity of SPI, however the strongest spectral feature (the 847 keV line) can still be detected at 3σ up to 11 - 16 Mpc. The broad band continuum was detected at up to 4 Mpc. Combining this information, plus the line widths measured by SPI, it is possible to discriminate between any pair of models (except delayed detonation and sub-Chandrasekhar mass progenitor) at up to 4 - 6 Mpc and to detect SN Ia at up to 11 - 16 Mpc.

The likelihood of detecting γ-ray line emission from a nearby type II supernova is much smaller because of the lower ^{56}Ni yield and the long obscuration time of type II supernovae to γ-rays (Schönfelder 1998).

Novae

Gamma-ray lines from classical novae have not yet been detected so far. Most promising are the lines from the $^{7}\mathrm{Be} \rightarrow {}^{7}\mathrm{Li}$ decay at 478 keV and from the $^{22}\mathrm{Na} \rightarrow {}^{22}\mathrm{Ne}$ decay at 1.275 MeV. For typical expansion velocities of a nova of 2000 km/s the line broadening will be 1.5% FWHM, i.e. 7.5 keV FWHM for the 478 keV line, and 20 keV FWHM for the 1.275 MeV line. The sensitivity limit of SPI for such line widths is about 1×10^{-5} photons cm^{-2} sec^{-1} (Schönfelder 1998). It is likely that novae must be closer than 1 - 2 kpc (Hernanz et al. 1996) to become visible in these lines. The evolution of the line width with time will allow detailed studies of the dynamics of novae. Detection of ^{7}Be may go some way to explaining the unusually high abundance of ^{7}Li in the universe.

Supernova Remnants

So far, γ-ray lines have been detected from two supernova remnants, namely Cas-A and the recently discovered COMPTEL-ROSAT remnant RX J0852.0-4622 (Schönfelder 1998). From both these remnants COMPTEL has detected the 1.157 MeV ^{44}Ti line with fluxes between 3 and 4×10^{-5} photons cm^{-2} sec^{-1}. At these flux levels, SPI will be able to measure the line profiles from both objects in a deep exposure observation. The simultaneously emitted hard X-ray lines at 68 keV and 78 keV should be detectable by IBIS. The knowledge of the line shape will be of fundamental importance for the study of the physical conditions in the remnant. If the distance of the COMPTEL-ROSAT supernova remnant is confirmed to be as close as 200 pc, this remnant should also cause part of the 1.809 MeV ^{26}Al emission detected by COMPTEL from the Vela region.

Since the central radian of the Galaxy will be deeply exposed during the INTEGRAL core program, the prospects are good for finding further, so far unknown supernova remnants with SPI during these observations. INTEGRAL will almost certainly discover previously unknown Galactic supernovae less than $\sim$500 years old via the γ-rays from ^{44}Ti. A 100 year old supernova at a distance of 10 kpc would produce a flux of a few times 10^{-5}photons cm^{-2} s^{-1} at 1.156 MeV which is quite detectable by SPI (Vedrenne et al. 1998).

^{26}Al and ^{60}Fe

In the case of the ^{26}Al Galactic distribution, the detection of the ^{60}Fe chain ($^{60}\mathrm{Fe} \rightarrow {}^{60}\mathrm{Co} \rightarrow {}^{60}\mathrm{Ni}$) γ-ray lines at 1.173 MeV and 1.332 MeV would be very helpful to clarify what is (are) the source(s) of this radioactive element. If its origin is type II supernovae, for instance, then as ^{26}Al and ^{60}Fe are co-produced in the same regions they will have the same spatial distribution. On the other hand Wolf-Rayet stars would show ^{26}Al emission but not γ-rays from the ^{60}Fe chain (Schönfelder 1998). The increased sensitivity of SPI makes it possible to search for the change in the 1.809 MeV to microwave ratio between the inner and outer galaxy that has been predicted by Knödlseder (1999).

Observations obtained with the Gamma Ray Imaging Spectrometer (GRIS) balloon experiment reported a ^{26}Al line profile that was surprisingly broad ($\Delta E = 5.4 \pm 1.4$ keV) after removing the instrumental line width (Naya 1996). With better sensitivity and imaging capabilities SPI will be able to measure the broadening of the line for different regions, which GRIS, having quite a broad field of view (~ 100°), couldn't do. In addition, SPI is expected to be able to separate foreground sources and to locate them in the galactic disk through the measurement of the centroid of the line at the level of a few times 0.1 keV, which can be achieved depending on the flux in the line, and gives access to Δv measurements of some 10s of km/s. Such a discrimination of foreground sources might have a significant impact on the total ^{26}Al mass which has to be produced in our galaxy to explain the ^{26}Al diffuse emission.

2.3.4 Active Galactic Nuclei (AGN)

The study of active galaxies in both fine and broadband spectroscopy will yield unprecedented knowledge of the particle interactions which take place in the region where the central engine's energy meets the galaxy's matter. Concurrent monitoring by JEM-X and the OMC on-board INTEGRAL provide important simultaneous data in the X-ray and optical range, respectively. Because of the greatly improved sensitivity of INTEGRAL, arc-minute resolution imaging is absolutely essential to avoid source confusion from the large population of AGN, and to associate γ-ray sources unambiguously with their optical, infrared and radio counterparts.

INTEGRAL will allow detailed studies of typically 100 or more AGN to be performed using the classical tools of broad and narrow band spectroscopy, but with improved sensitivity, energy resolution and imaging capability. A very important feature of INTEGRAL observations will be the simultaneous wide spectral coverage (from 3 keV - 10 MeV) which permits variations of the emission in the X-ray band to be directly related to γ-ray plasma processes.

The imaging capabilities of INTEGRAL are not only required for the definitive identification of the γ-ray emitting AGN, but provide the opportunity for the serendipitous discovery of many new γ-ray emitting AGN in the same way that many unexpected sources were found by the imaging instruments on board the EINSTEIN and EXOSAT satellites. The angular resolution of the IBIS and JEM-X coded masks will enable a source of hard X-/γ-ray emission to be located to within an error cirlce of 1 - 5$'$ in diameter, depending on the strength of the source, which is sufficient to ensure the identification of any newly discovered γ-ray AGN. SIGMA has demonstrated that the level of angular resolution designed into IBIS and JEM-X clearly is a necessity, even in the context of the extragalactic sky. SIGMA images of the sky region around 3C273 not only show emission from the quasar but also from a location 15′ away from it. This new source GRS 1227+025 is variable in the SIGMA domain and when it is in its high state its intensity is comparable to that of 3C273 in the 40 - 80 keV range, although its spectrum is softer. Thanks to its imaging power, SIGMA is able to separate the two sources and obtain reliable results on them individually. however an instrument with lower resolving power, such as OSSE, would erroneously attribute all of the spectral and intensity variations to 3C273. Inspection of the sky near most other AGN invariably reveals the existence of other X-ray sources. The 3C273/GRS 1227+025 situation also illustrates the capability of the coded aperture γ-ray systems to study more than one object simultaneously and thus increase the scientific returns of the mission. The number of serendipitous extragalactic sources detectable by INTEGRAL is difficult to estimate precisely due to the current uncertainties in the spectral shape and intensity, as well as the precise location of energy breaks in the emission spectra, all of which may be variable in time. IBIS with its unprecedented sensitivity spanning the 10 keV - 10 MeV range will certainly be able to detect a considerable number of AGN, determine the associated spectral breaks, and generate meaningful log N - log S distributions for the various AGN types. It is expected that ~100 AGN will be detected by INTEGRAL in the hundreds of keV energy range.

High resolution spectroscopy offers a unique chance to study the electron-positron annihilation line predicted by models under a wide range of parameters. Detailed measurements of centroid energy, width and shape will provide stringent constraints on the physical parameters deep inside these distant sources. Although the characteristics of the central regions of AGN are still highly uncertain and no lines have been detected so far, theories suggest that AGN can emit γ-ray lines which would be detectable with a sensitivity improvement of ~10. Models of the positron annihilation radiation from the galactic nuclei suggest that fluxes of $> 10^{-5}$ photons cm^{-2} s^{-1} in 511 keV emission could be expected from Cen A, NGC 4151 and other active galaxies, and should easily be detected by INTEGRAL. The INTEGRAL energy resolution will allow measurement of any redshift of the electron-positron line for AGN's with $z \geq 0.001$, i.e. for the majority of X-ray emitting Seyferts, BL Lac's and quasars. Comparison of γ-ray redshifts with those determined optically could provide intriguing insights into, for example, the depth of the gravitational well from which the high-energy emission emanates or any relativistic bulk motions of the high-energy plasma. Observations of redshifted annihilation lines could be particularly significant in the case of BL Lac objects for which optically determined redshifts are sometimes contradictory. Such redshifted lines could also provide a clear signature of the possible extragalactic nature of serendipitous sources.

The study of broad band spectral features also provides a powerful diagnostic for AGN studies. Material along the line of sight to an observer will change the spectral profile of the emergent X-/γ-ray spectrum by photon scattering and absorption. The amount of material can be evaluated by the low energy turnover in the emission profile. The search for, and study of, spectral features near 200 keV associated with Compton backscattering may lead to further deductions relating to the size and geometry of local cold matter behind a compact and luminous central γ-ray source. The strength and spectral profile of this emission is critically dependent on the relative location of nearby scattering material, such as the inclination angle of an accretion disc with respect to the direction between the prime γ-ray emitting source and the observer. Broad-band γ-ray spectral measurements may thus shed new light on unification theories based on geometrical aspect, size of accretion tori, etc.

The sensitivity of IBIS will allow detection of bright AGN in minutes, and this should allow IBIS to look at time variability on this sort of scale. IBIS will also study the polarization of γ-rays over the energy range (0.2 - 3 MeV) where Compton scattering dominates the interaction processes. Due to the fact that the γ-ray photons will be scattered from the nearby accretion disc, the emergent high energy radiation is likely to be strongly polarized. For the specific examples of 3C273 and Cen A based on the intensities seen by SIGMA/CGRO, IBIS will be able to observe in detail their polarization at 500 keV within a period of less than one hour if they are 100% polarized and detect the existence of polarization at the 10% level.

Recently, Dermer et al. (1997) used OSSE to observe Ultra luminous IR galaxies. They hoped to detect γ-rays from these sources to lend support to the idea that these are buried AGN. However, the upper limits they set tend to support the theory that the IR is from starbursts. INTEGRAL observations of these objects can measure the γ-ray emission and thus discriminate further between models.

2.3.5 Galaxies and galaxy clusters

The wide field of view of the INTEGRAL instruments is ideal for imaging whole galaxies and the resolution of IBIS will allow individual sources to be identified within each galaxy. It will also be possible to observe the collective emission of electron cosmic rays, supernovae in starbursts and jets for example.

INTEGRAL will be able to resolve galaxy cluster emission and thus discriminate between point sources (e.g. AGN) and diffuse sources (e.g. scattering of background photons in the intracluster medium) for those clusters currently detected. For many other clusters INTEGRAL will provide the first detection of γ-rays.

2.3.6 Cosmic Diffuse Background (CDB)

X-ray and EGRET measurements of the contribution to the background by AGN are clearly different. There is therefore expected to be a break, which is right in the INTEGRAL wave band. INTEGRAL should therefore help to reconcile these data sets and allow us to understand the contribution to the background by AGN more fully. High sensitivity, a wide field of view and high resolution will allow INTEGRAL to identify many more AGN, thus improving the current number statistics, and to measure their properties better thus improving the quality of data.

Below 100 keV the CDB is thought to come from a super-position of Seyfert galaxies, whereas above 3 MeV it is thought to be due to Blazars. In the range 100 keV - 3 MeV it has been suggested (Watanabe et al. 1999) that the CDB is due to supernovae, mainly SN Ia. INTEGRAL's high sensitivity will allow better constraints to be placed onto these models. Perhaps most importantly, INTEGRAL may be able to test for the presence of steps in the CDB due to the ^{56}Ni decay chain. A detection of these would be a massive step forward in understanding the CDB in this energy range.

2.3.7 Gamma Ray Bursts (GRBs)

Both SPI and IBIS are powerful instruments for studying γ-ray bursts: SPI because of its excellent energy resolution and IBIS with its localization capability, large area and wide energy range. The energy range over which bursts are studied will be extended with the inclusion of JEM-X and the OMC. No current mission has the combination of detection volume, energy resolution, energy range and localization capability of INTEGRAL. The expected number of GRBs per year detected within the fully coded field of view has been estimated to be 13 (SPI), 6 to 24 (IBIS) - where the lower and upper limits are given by the BATSE detection rate and extrapolation of the BATSE log N/log S distribution - and 2 to 6 (JEM-X) (Winkler 1998). GRBs in the IBIS field of view will be located with a precision $\leq 1'$. IBIS will measure the polarization of the emission from GRB sources both within and outside its fully and partially coded fields of view.

The ability to localise GRBs to arc-minute levels, when combined with the continuous telemetry link, allows positions of GRBs to be obtained in near real time (Mereghetti 1998). It is currently planned to alert the scientific community to GRBs detected by INTEGRAL via the Integral Burst Alert System (IBAS). The search for GRBs will be performed on ground by means of a near real time analysis done by the IBAS at the INTEGRAL Science Data Centre (ISDC). Under normal circumstances telemetry frames are expected at the ISDC within 30 s. Triggering and validation of a GRB may require between 2 and 20 seconds, therefore it is hoped to issue alerts to the general scientific community within a few tens of seconds of the GRB occurence (Mereghetti 1998). The positional accuracy of a burst detected during slew should be about $10'$, whereas at the start of an observation this could be lowered to $5'$ and during an observation may be further lowered to $\leq 30''$ (Mereghetti 1998)

GRB energy spectra may contain line features at energies around 30 - 50 keV (Briggs et al. 1999). The study of these features - the line shapes, energies and intensities as a function of time - will be a prime objective of INTEGRAL. However, INTEGRAL will perform interesting GRB science in many other areas too. It will define the continuum spectrum over a wide energy band (4 keV - 10 MeV) and resolve much of the controversy surrounding the various spectral components present in bursts. Since the GRBs will occur during routine pointings lasting typically 1 to 10 days, IBIS and SPI will observe the locations of GRB sources long before and long after the burst, making it possible to search for quiescent emission from burst sources at levels around 10^{-5} of the burst emission.

The OMC will search a 1000 square degree field of view with an angular precision of better than $1'$ for transient optical emission accompanying bursts to a level of sensitivity of 12^m for a one second transient and 13.4^m for a ten second transient. About 20 GRBs per year will occur within the field of view of the OMC. The OMC will also detect flare stars within its field of view at a rate of a few per hour.

The study of GRBs with INTEGRAL is a particularly attractive secondary objective, in view of the fact that no special pointings are required. This will be among the most interesting and significant "serendipitous" science to come out of the mission, due to the unprecedented combination of high energy and spatial resolution, and the large detector volume.

2.3.8 Serendipitous Sources

The coded aperture imaging technique allows one to observe several sources in the field of view simultaneously (multiplexing). When combined with the large fields of view and high sensitivities of IBIS and SPI this means that observations will not only contain the source requested but also some background sources. In this way many new sources will be observed by chance.

2.4 Orbit

INTEGRAL, with a total launch mass of about 4 tonnes, will be launched in 2002 into a highly eccentric orbit with a high perigee. This provides long periods of uninterrupted observation with nearly constant background and minimises the effects of the electron and proton radiation belts.

INTEGRAL will be launched using a Russian PROTON launcher. The initial orbit is a 72-hour orbit with an inclination of 51.6°, a height at perigee of 10,000 km and a height at apogee of 153,000 km. Though spacecraft design assumes compatibility for an ARIANE 5 48-hour orbit, with inclination 65°, height at perigee of 7000 km and height at apogee of 114,000 km.

Owing to radiation effects in the high-energy detectors, scientific observations will be carried out while the satellite is above a nominal altitude of 40,000 km. This means, that ~90% of the time spent in the orbit provided by PROTON can be used for scientific observations. An on-board particle radiation monitor allows assessment of the radiation environment local to the spacecraft. In case of low background environment, observations below 40,000 km altitude should be possible.

2.5 Summary

INTEGRAL is an ESA lead mission dedicated to fine spectroscopy and fine imaging of celestial γ-ray sources with concurrent X-ray and optical monitoring. INTEGRAL will be launched into a highly eccentric 72-hour orbit and is designed to last for 2 years. INTEGRAL will carry out a unique Galactic Plane Survey and its combination of high sensitivity, good spectral and good spatial resolution should allow it to identify and classify many γ-ray sources.

INTEGRAL consists of four co-aligned instruments: Spectrometer (SPI), Imager (IBIS), X-ray monitor (JEM-X) and Optical Monitor (OMC). SPI is composed of 19 germanium detectors and designed to give high spectral resolution ($E/\Delta E = 500$). IBIS uses two detector planes, one CdTe and one CsI, and is optimsed for high spatial resolution ($12'$ FWHM). JEM-X consists of two xenon filled gas chambers and primarily provides X-ray imaging to complement IBIS and SPI. The OMC uses a CCD with a Johnson V-Filter to cover the 500 - 850 nm wavelength range and provide simultaneous optical images. The whole spacecraft is 3-axis stabilised and has to maintain sun orthogonality to provide power for the payload.

Although INTEGRAL's orbit is optimised so that it avoids charged particle belts as much as possible, there is still an overwhelmingly large particle and radiation background in space. This is composed of cosmic rays, diffuse cosmic γ-rays and radioactivity induced within the satellite due to particle bombardment. Therefore, even with good spectral and imaging qualities, the particle and radiation background of space introduces important systematic background effects. The latest technique employed to minimise the effects of background noise is mass modelling, which is currently being developed at Southampton. The application of this technique to the INTEGRAL mission forms the bulk of this thesis and is discussed in the following chapters.

Chapter 3

The INTEGRAL Mass Model (TIMM)

3.1 What is mass modelling?

In the early days of satellite missions "mass models" contained complete descriptions of the payload components and were used to determine accurately the final mass of the satellite. With the recent dramatic increases in computer power "mass modelling" has evolved to mean the production of a computer (or analytical) model that replicates the dimensions, chemical composition and distribution of mass of the system. This provides a complete model of payloads and spacecraft, which can be used to evaluate the background noise and instrument performance characteristics.

With any space-based project detailed modelling of the payload needs to be carried out prior to launch to assess the instrument performance. The modelling procedure requires a good model of the radiation environment as well as a good description of the payload and spacecraft. Simpler models will already have been used during the design phase. Monte Carlo modelling is then used to predict the instrument's response to the background radiation environment as well as to the sources (Green et al. 1996).

Modelling of the effects of the radiation environment on the payload and spacecraft is vital for γ-ray astronomy. The instruments are required to work at very low signal-to-noise ratios and so a good quality background model is needed to optimise the scientific return from the payload.

The model can have various degrees of accuracy depending on the results it is required to produce. For instance, if a background noise spectrum and counting rate are to be calculated within an on-board astronomical γ-ray telescope, then the distribution of mass and composition of the material is important but very fine detail is not required. When investigating more complicated effects such as shadowing on the detector plane then more detail, especially in front of the detector plane, is necessary.

Mass modelling can be used to estimate:

- Continuum and line sensitivities
- Background spectra
- Background counting rates
- Trigger rates (used to estimate dead time)
- Detection efficiency
- Effects of spacecraft on payload
- Shadowing of detector planes
- Telemetry rates

Since the output of the Monte Carlo simulation is effectively positions, energies and times of interactions, the on-board processing algorithms can also be tested. This can be achieved in software by creating algorithms that model the electronics of the system. The software can then be used to replicate the modes of operation of the detector. This would usually involve applying lower and upper energy thresholds and then selecting events by their multiplicity (i.e. single-site or multiple-site events). Events below the low-energy threshold are normally ignored, whereas those above the high-energy threshold can be ignored or can raise an over-flow flag. This makes it possible to test the algorithms to be used in-flight. Vetoing strategies can also be applied and tested. By varying the algorithms (or models) one can see the difference between active and passive vetoes. The effects of dead time and pile-up can be investigated for an active veto strategy. By placing energy thresholds on the veto crystals a more realistic estimate of their efficiency can be obtained. By using the same output file format as the real telescope the analysis software can be tested. More complex algorithms to generate images from coded masks or Compton telescopes can be developed and refined. The mass model provides a place where the effects of any changes to the instruments can be determined. This is found to be useful during the design phase when instrument components may need to be moved, or if a post-launch fault develops and the instrument characteristics have to be re-evaluated.

The coded aperture technique relies on the ability of the mask to cast a shadow on the detector plane. Due to the penetrating nature of γ-rays, some of the support structure is semi-transparent and so a bright off-axis source may cast a shadow of the support structure, or other instruments, across the detection plane. This shadow will be super-imposed on the recorded shadow of the mask and, if not removed, will ultimately reduce the sensitivity of the telescope. An assessment of the severity of this problem can be made with a complete mass model and, if necessary, algorithms to account for the problems or remove the shadows can be developed.

Models can also be used to create background data sets for use in data analysis.

3.2 How is mass modelling done?

To simulate the response of a γ-ray telescope to the particle and radiation background of space, the package must have the following qualities:

(1) Be able to model all relevant particle types over the entire energy range necessary, i.e. photons, electrons, neutrons, protons, alphas, etc.

(2) Contain the cross-sectional data for all possible interactions.

(3) Follow the transport of the incident particles and their secondaries, through the material of the whole space vehicle.

(4) Be able to calculate the induced radioactivity in all parts of the payload and the spacecraft.

(5) Be able to simulate the induced radioactive decays, taking into account all the possible isotopic types, together with their lifetimes and decay products, and to follow the transport of these secondaries through the payload.

Although there are many Monte Carlo packages on the market no single one can perform all the tasks outlined above. Lei et al. (1996) presented the following summary of available Monte Carlo packages:

- EGS4: Developed at SLAC, it models photons and electrons (>1 keV).
- GEANT: Developed at CERN, it deals with photons and electron (>10 keV).
- FLUKA: Developed at CERN, it models energetic hadrons.
- HETC: Developed at Oak Ridge. It deals with energetic hadrons.
- MCNP: Developed at Los Alamos. It is capable of simulating photons, electrons and low energy neutrons (thermal to 20 MeV).
- MICAP: Low energy neutrons interactions. Developed at Oak Ridge.
- MORSE: Low energy neutrons interactions. Developed at Oak Ridge.
- ORIHET: Calculates induced radioactivitity. Developed at Oak Ridge, RAL and Southampton.

It is therefore necessary to adopt an approach that combines the power of a number of different packages into an integrated suite of programmes. To this end the Southampton group are developing the GGOD suite of software (Lei et al. 1996). This combines GEANT/GCALOR, with ORIHET and a Southampton developed code called DECAY. The development and testing of the DECAY code is the subject of chapter 4.

3.2.1 The GGOD Monte Carlo simulation suite

The GGOD suite of software, currently being developed at Southampton, is based around the GEANT package developed by CERN which models the interaction of particles and photons (E_γ >10 keV). GGOD combines the GEANT/GCALOR code and the ORIHET package with a locally developed code to process activated isotopes (the DECAY code). One of the main features of GGOD will be the ability to model decays of activated nuclei, which is important when modelling space-based instruments where the induced radioactivity is one of the major contributions to the detectors background noise. The basic data flow within GGOD is shown below (figure 3.1). There are three inputs to the GGOD suite: the detailed geometry of the γ-ray telescope, including the spacecraft, in GEANT format; the radiation environment in which the telescope is operating; and the radiation history, which is necesary to calculate the induced radioactivity over a period of time.

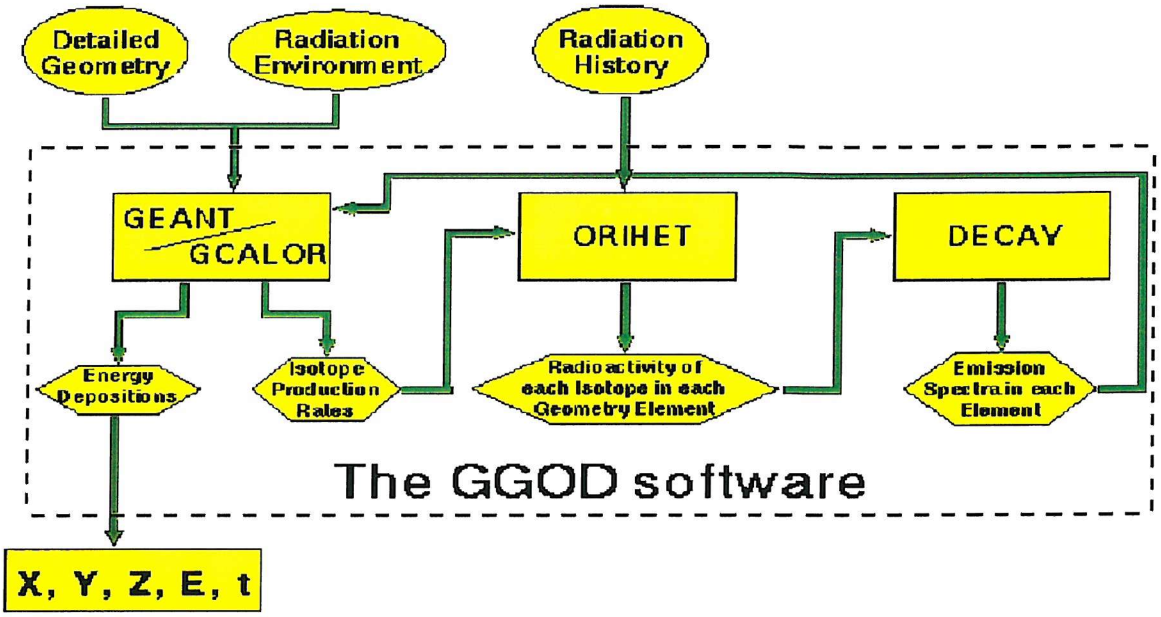

Figure 3.1: *The data flow within the Southampton developed GGOD software suite, taken from Lei et al. (1996). The GEANT/GCALOR packages are used to track photons and particles, storing both interactions and isotopic production rates. From the production rates determined, ORIHET calculates the decay rates at any given epoch. DECAY uses each isotope's decay scheme to generate the photons and particles necessary to model their decay, and these are passed to GEANT/GCALOR for tracking.*

The capabilities of GEANT have been extended, by combination with other packages, to allow modelling of interactions of many types of particle over a wide energy range. The whole GGOD suite tracks photons (E_γ >10 keV), electrons, energetic hadrons and low energy neutrons (10^{-5} eV - 20 MeV) using GEANT/GCALOR. GGOD also logs isotope production rates in the model materials, which will then enable the simulation of radioactive decays (using the DECAY code). The complete GGOD software therefore, enables the tracking of both prompt and delayed background components.

The first step in modelling any satellite is to construct the geometry of the satellite within GGOD. This is done using detailed technical drawings, chemical descriptions of the materials used and the masses of the component parts. The satellite geometries are made up of several volumes, each of which is a simple polygonal shape such as a cube, cone, etc. In general the larger scale structures are modelled first, and then the smaller volumes are placed within them to model the finer details. This gives the overall mass model geometries a tree-like logical structure. The exploded view of the geometry of the nuclear γ-ray spectrometer SPI, on board the INTEGRAL spacecraft, as shown in figure 3.2 gives an idea of the level of detail a "simple" mass model can achieve.

Having constructed the model, the next step is to simulate the photon and particle environment to which the instrument is subjected. The required input spectra for the various background sources (cosmic rays, cosmic diffuse γ-rays, atmospheric γ-rays and neutrons) are taken from the literature detailing previous measurements. The radiation history is put into ORIHET to allow calculation of the isotopic decay rates. Practically, as shown in figure 3.1, the geometry and environment are put into GEANT/GCALOR which tracks the prompt components (calculating X, Y, Z, E, t) and logs isotope production rates. ORIHET converts the production rates, using the radiation history, into decay rates for each isotope. The isotopes, and their decay rates, will be used by DECAY to model the appropriate induced radioactivity within GEANT (therefore calculating X, Y, Z, E, t). The prompt and delayed components can then be added together to determine the total background.

3.3 What sources of background are there in space?

One of the major problems with γ-ray astronomy is the very low signal-to-noise ratio. As a consequence of the optimisation of the instrument design to the detection of γ-ray photons, the detectors are also optimised to detect particle and photonic background. The spectrometer detectors in particular are optimised for the detection of γ-ray lines from radioactive decays in astrophysical sources,

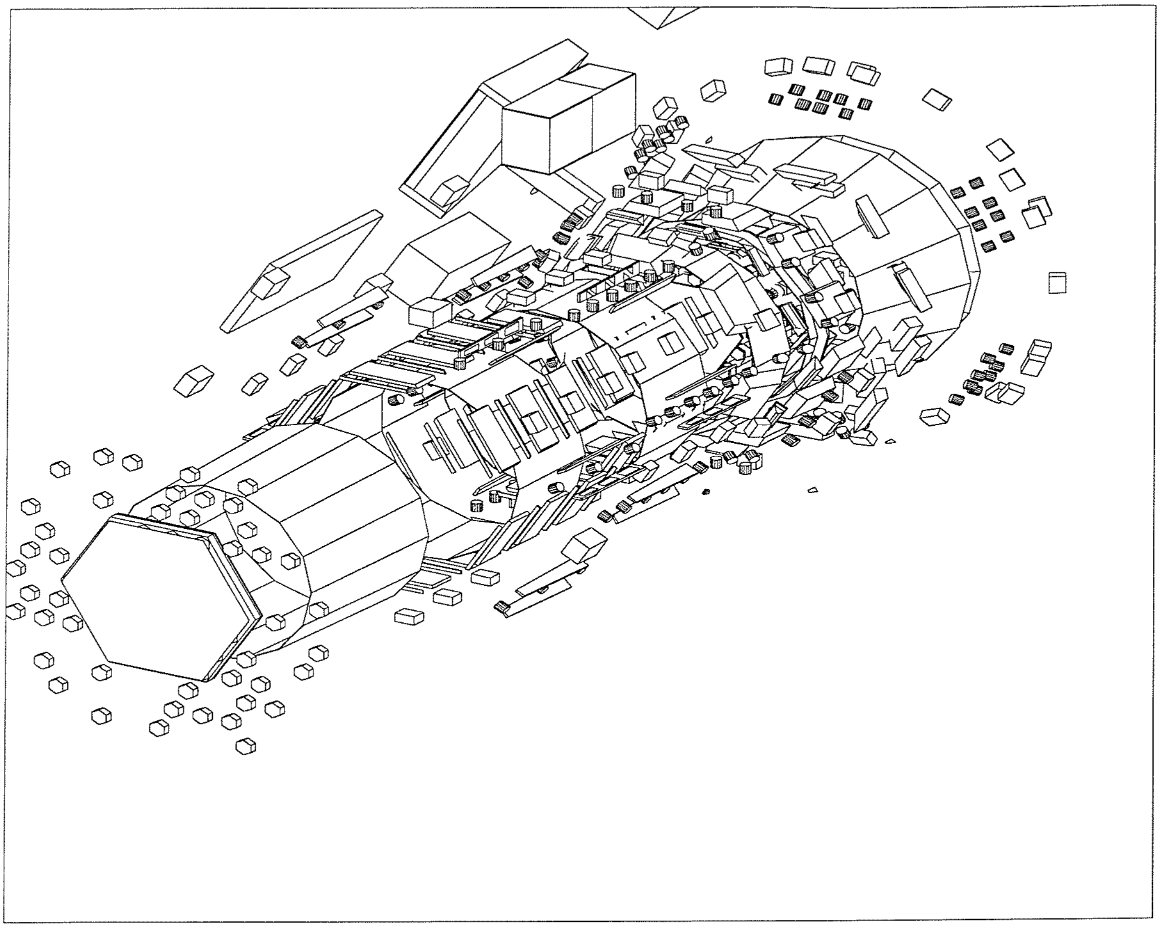

Figure 3.2: *An exploded view of the γ-ray spectrometer SPI, showing the complexity of a mass model.*

however, as a consequence of this they are also very good at detecting the decay of isotopes within the spacecraft and payload. Therefore the sources of background in the space environment can be thought of in terms of three groups: those from space (cosmic diffuse γ-rays and cosmic rays); those from the Earth (atmospheric γ-rays and neutrons) and those from the satellite (induced radioactivity).

3.3.1 Cosmic diffuse γ-rays

Cosmic diffuse gamma radiation, although of astrophysical importance in its own right, forms a background against which observations must be made. It can reach the detector, and gives a count rate which competes directly with that derived from the astronomical source of interest, by either entering the aperture or penetrating the shields. However, because of its isotropic nature, constant spectral shape and lack of rigidity dependence, it is the simplest of all the sources of background noise to evaluate in a quantitative manner. In the deep space environment this source will be truly diffuse. For near-Earth orbit the shielding effect of the Earth must be taken into account. At balloon altitudes, because of the attenuation and occultation by the Earth, and more important, due to the fact that the atmosphere itself is a bright source of γ-rays, the cosmic diffuse γ-ray contibution becomes less important compared to that from the atmosphere (Dean, Lei and Knight 1991).

Dean, Lei and Knight (1991) summarised the many attempts to measure the cosmic diffuse γ-ray background (figure 3.3).

The spectrum in figure 3.3 can be adequately fit by the expression:

$$\mathrm{d}N(E_\gamma) = 87.4 E_\gamma^{-2.3} \mathrm{d}E \quad \mathrm{photons\,cm^{-2}s^{-1}keV^{-1}sr^{-1}} \tag{3.1}$$

While this doesn't account for the apparent "MeV bump", this will not be a significant source of error. However, the difficulty of measurement of the cosmic diffuse γ-ray background means that there is debate over its spectral character. Above 15 keV Lei et al. (1996) give:

$$F \sim 167 E^{-2.38} \quad \mathrm{photons\,cm^{-2}s^{-1}keV^{-1}sr^{-1}} \tag{3.2}$$

While The INTEGRAL Mass Model (Lei private communication) uses:

$$F_{18keV-10MeV} = 112 E^{-2.3} \quad \mathrm{photons\,cm^{-2}s^{-1}keV^{-1}sr^{-1}} \tag{3.3}$$

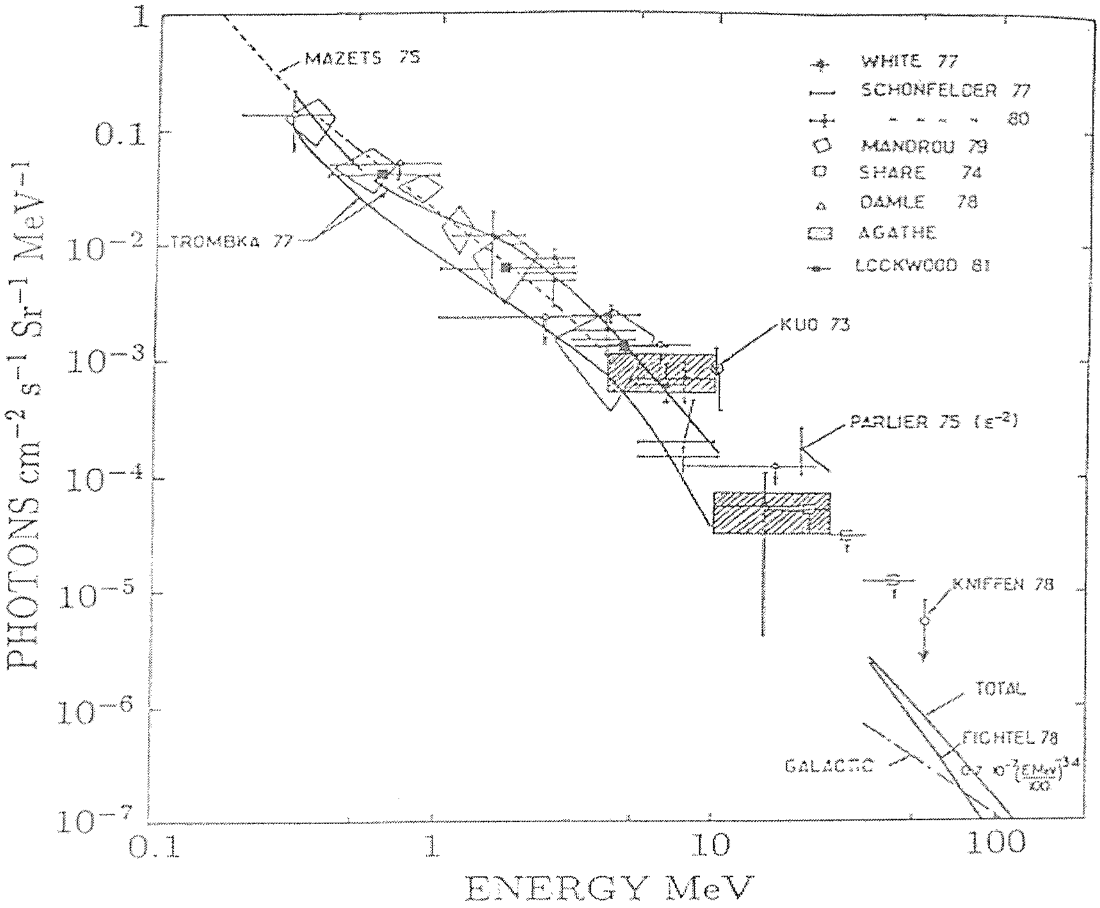

Figure 3.3: *The cosmic diffuse gamma radiation spectrum (taken from Dean, Lei and Knight 1991).*

Recently Kinzer et al. (1997) used HEAO1-A4 data to derive a new spectral shape (figure 3.4):

$$\mathrm{d}N(E_\gamma) = 828.5E^{-2.75}\mathrm{d}E \quad \mathrm{photons\,cm^{-2}s^{-1}keV^{-1}sr^{-1}} \tag{3.4}$$

From figure 3.4 it can be seen that current COMPTEL results indicate no "MeV bump" and provide a reasonable agreement with the HEAO results. The difference between equations 3.1, 3.2 and 3.3 is less than a factor of 2 in flux over the energy range 10 keV - 10 MeV, and this will not have a huge effect on the background calculated. The spectral shape derived from the HEAO1-A4 results gives a similar flux, the steeper spectrum biasing this toward low energies. Since high-energy γ-rays are rare the change of slope will probably not have too much effect in most cases.

3.3.2 Cosmic rays

Cosmic rays are very high-energy particles (mainly protons and alpha particles) of unknown origin that bombard the Earth's upper atmosphere. The cosmic ray flux at a given position in space is modulated by the solar activity. The Earth's magnetic field affects their penetration to the vicinity of the Earth, an effect known as the rigidity cut-off. Away from the Earth the isotropic cosmic ray flux is of the order of 4 protons $\mathrm{cm^{-2}\ s^{-1}}$ at solar minimum and about 2 protons $\mathrm{cm^{-2}\ s^{-1}}$ at solar maximum (Lei et al. 1996). In addition to protons, around 12% of cosmic rays are alpha particles. Figure 3.5 taken from Dean, Lei and Knight (1991) shows the form of the cosmic ray spectrum. The proton curve is fitted by a spectrum (calculated between 10 and 100 GeV) of:

$$F = 3.23 \times 10^9 E^{-2.7}\ \mathrm{protons\,m^{-2}s^{-1}sr^{-1}MeV^{-1}} \tag{3.5}$$

Cosmic rays are the dominant source of background noise in a γ-ray telescope. Direct cosmic ray passage through the detector does not normally contribute to the background noise since almost all of the energy deposited in the detector can be rejected by active veto systems. Its real contribution to the background noise comes from local radiation and induced radioactivity. Local radiation is the secondary particles generated by the cosmic ray in the materials of spacecraft and detector. Among them γ-rays and neutrons are the most important ones to the detector background noise, as the effects of charged particles would also be rejected by active veto systems.

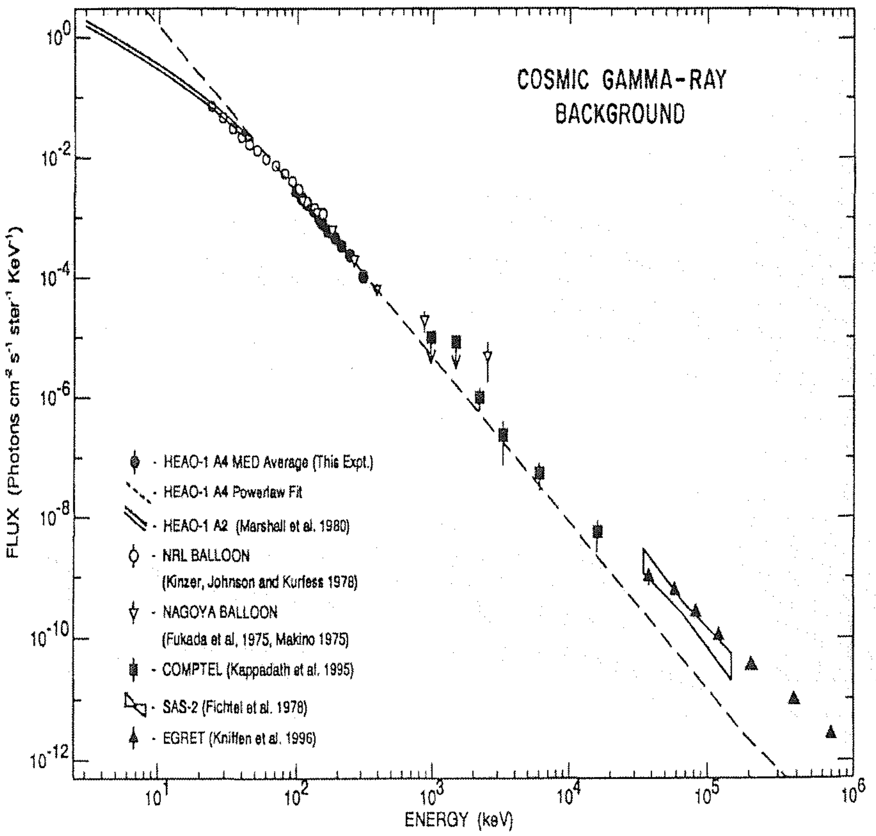

Figure 3.4: *Selected measurements of the diffuse cosmic γ-ray spectrum between 3 keV and 1 GeV as presented by Kinzer et al. (1997).*

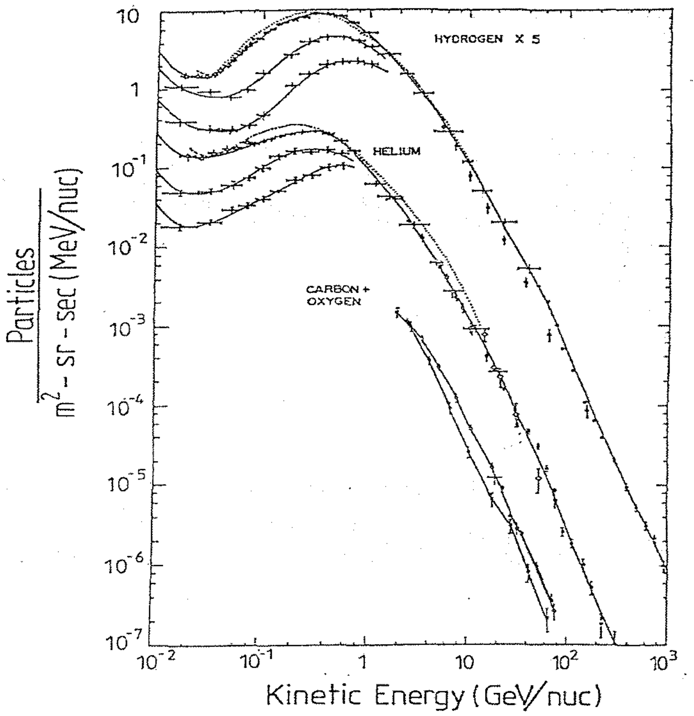

Figure 3.5: *Differential kinetic energy/nucleon spectra at three levels of solar modulation for cosmic ray protons and helium nuclei (taken from Dean, Lei and Knight 1991).*

3.3.3 Neutrons

Neutrons are generated by cosmic ray interactions in the atmosphere and throughout the bulk of the spacecraft (or balloon) and telescope. The intensity of albedo neutrons from the atmosphere is a function of rigidity cut-off, and falls with distance from the Earth squared. For a high Earth orbit aldebo neutrons are not important.

Generally speaking, active veto systems cannot discriminate against the background caused by neutron interactions inside the primary detector. The main reason for this is that neutrons can pass through material without depositing energy and so a veto signal is not produced. A further complication is that neutrons produce delayed background (via induced radioactivity) which may not be coincident in time with the veto deposit. Neutrons may interact with the detector by the following processes:

- Neutron Absorption (n,γ): A neutron may be captured by the nucleus to form an excited level equal to the binding energy of the composite nucleus. Multiple γ-ray lines are normally emitted resulting from the prompt de-excitation of the excited level to the ground state. Many of these γ-ray photons can be vetoed due to the escape of one, or several, of the simultaneously produced photons from the detector which lose their energy in the shield.

- Inelastic Scattering (n,n'γ): A fast neutron may collide inelastically with a nucleus and excite it to a higher level energy state ϵ. The critical energy required for such excitation is:

  $$E_c = (m_n + M)\epsilon/M$$

  where m_n is the neutron mass and M is the mass of the target nucleus. The inelastic scattering of neutrons will result in the production of many discrete lines superimposed upon the continuum produced by the absorption. In practice, excitation of these nuclei lead to a small background contribution (Dean, Lei and Knight 1991).

- Elastic scattering (n,n'): A neutron collides elastically with the target nucleus and is scattered isotropically in the centre-of-mass frame. The average amount of kinetic energy lost from the collision is equal to $2A/(A+1)^2$, where A is the mass of the target nucleus. For intermediate and heavy nuclei such as Na, I, and Cs, the amount of energy transferred is small and the intrinsic energy state of the recoil nucleus remains unchanged. This component is unimportant above

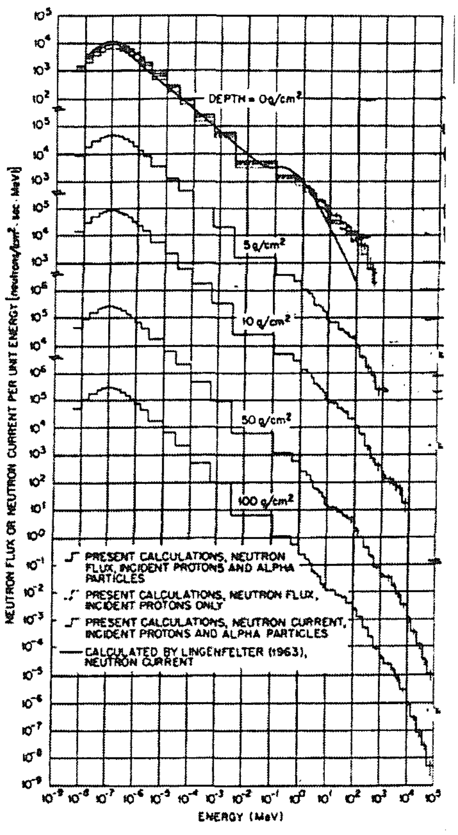

Figure 3.6: *Neutron spectra at various depths from the top of the atmosphere (calculated at 42° N and solar minimum). Figure taken from Armstrong et al. 1973.*

100 keV, but for high resolution germanium spectrometers its existence must be taken into account (Dean, Lei and Knight 1991).

Other interactions such as (n,2n), (n,p), (n,α), etc, do produce radioactivity but their contributions to the background are negligible (Dean, Lei and Knight 1991). Armstrong et al. (1973) calculated the neutron spectrum at various depths in the atmosphere (at 42° N) resulting from cosmic proton and alpha particle bombardment (figure 3.6).

3.3.4 Atmospheric γ-rays

At balloon altitudes, and for low Earth orbits, the atmospheric γ-rays cause more problems than the cosmic diffuse γ-rays, whose spectrum is much steeper, particularly at energies above about 1 MeV. However, inside the atmosphere, the cosmic diffuse γ-rays are difficult to separate from the atmospheric fluxes. Published experimental data normally include the total γ-ray fluxes as measured in the atmosphere. For the case in which telescopes operate at balloon altitudes, therefore, it is the practice not to distinguish the background noise caused by the different gamma radiations.

The intensity in orbit of the albedo γ-rays falls with distance from the Earth squared, and these are not important in high Earth orbits. Imhof et al. (1976) used a lithium-drifted germanium detector, placed on a low altitude satellite, to obtain a spectrum for the atmospheric γ-rays (figure 3.7). This can be fitted near the equator by:

$$N(E_\gamma) \propto E^{-1.39} \quad \mathrm{photons\,cm^{-2}s^{-1}keV^{-1}sr^{-1}} \tag{3.6}$$

and near the pole by

$$N(E_\gamma) \propto E^{-1.34} \quad \mathrm{photons\,cm^{-2}s^{-1}keV^{-1}sr^{-1}} \tag{3.7}$$

3.3.5 Activated or induced radioactive background

Activation of isotopes occurs due to the intense particle bombardment in space. This can happen via proton, alpha or neutron capture, or via spallation reactions. These isotopes tend to be unstable and so eventually decay. Over a period of time therefore, the spacecraft and detectors become radioactive. This creates a further source of photon and particle background that has to be modelled.

Practically, modelling this component involves working out the production rates of the different activated isotopes, then the activation of the volume as a whole, and then simulating all the decays that occur within each volume in the required time period.

3.4 The need for modelling of radioactive decays

Bloemen et al. (1994) reported the detection of γ-ray emission from Orion in the 3 - 7 MeV range with COMPTEL. They identified this with 4.44 MeV and 6.13 MeV lines from $^{12}\mathrm{C}^*$ and $^{16}\mathrm{O}^*$ respectively, due to charged particles interacting with matter in Orion. The observed flux they

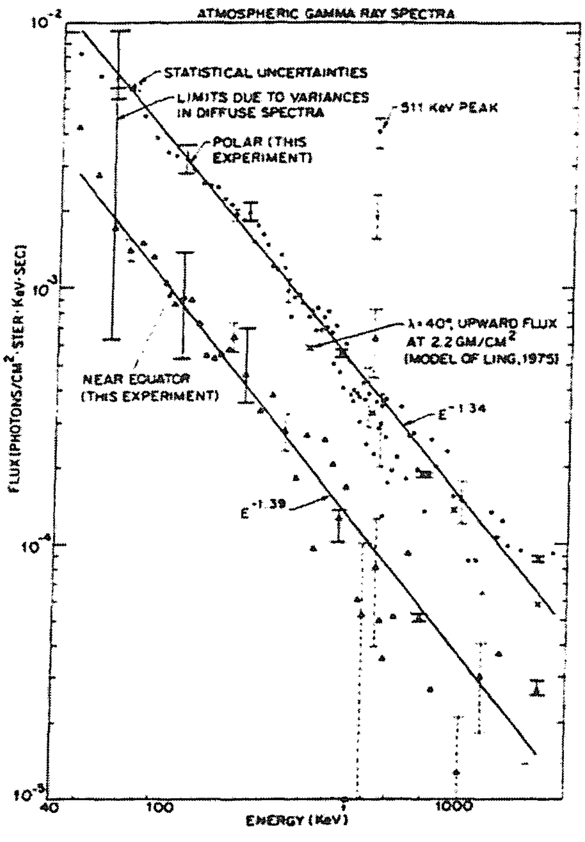

Figure 3.7: *Spectrum of the Atmospheric γ-rays as measured by Imhof et al. (1976) at both the poles and near the equator.*

found was 1×10^{-4} photons cm^{-2} s^{-1} (3 - 7 MeV), and was much larger than expected, suggesting a strong enhancement of Carbon and Oxygen in Orion.

Bloemen et al. (1997) presented new observations, which seemed to confirm the previous report of 3 - 7 MeV emission with a flux of 1.28×10^{-4} photons cm^{-2} s^{-1}. In addition they suggested that the emission is due to multiple sources (covering Orion A, B and the Mon R2 clouds). The emission appeared to be from broad 4.44 MeV and 6.13 MeV lines, and there may even be features due to line splitting.

Unfortunately, Bloemen et al. (1998) announced a retraction of these results. Having used time-of-flight analysis techniques to separate genuine source photons from background, they found that the previous results were distorted by ^{24}Na decays. This isotope happened to give two site events of ~5 MeV which were previously mistaken for source photons.

This example illustrates the complex nature of the induced component of the background and the clear need for modelling of this component. Within the GGOD suite this will be accomplished using the DECAY code (see chapter 4).

3.5 The INTEGRAL Mass Model (TIMM)

Most of the modelling work presented in this thesis has been carried out within the framework of the INTEGRAL mission and its particular modelling project, The INTEGRAL Mass Model (TIMM). Within the INTEGRAL project, in addition to the individual instrument teams models, there is an independent mass model (TIMM) that aims to provide unified and independent modelling of the entire payload and spacecraft. This mass model is constructed using information supplied by instrument teams about the mass distribution and chemical composition of material in their instrument. This information is collated, together with information about the spacecraft structure, to form a Monte Carlo model of the whole payload, which can be used to provide the following benefits to the INTEGRAL project:

- Assessment of the relative performance of each instrument.
- Assessment of the effect the payload has on a particular instrument.
- Transferability of calibration results between instruments.

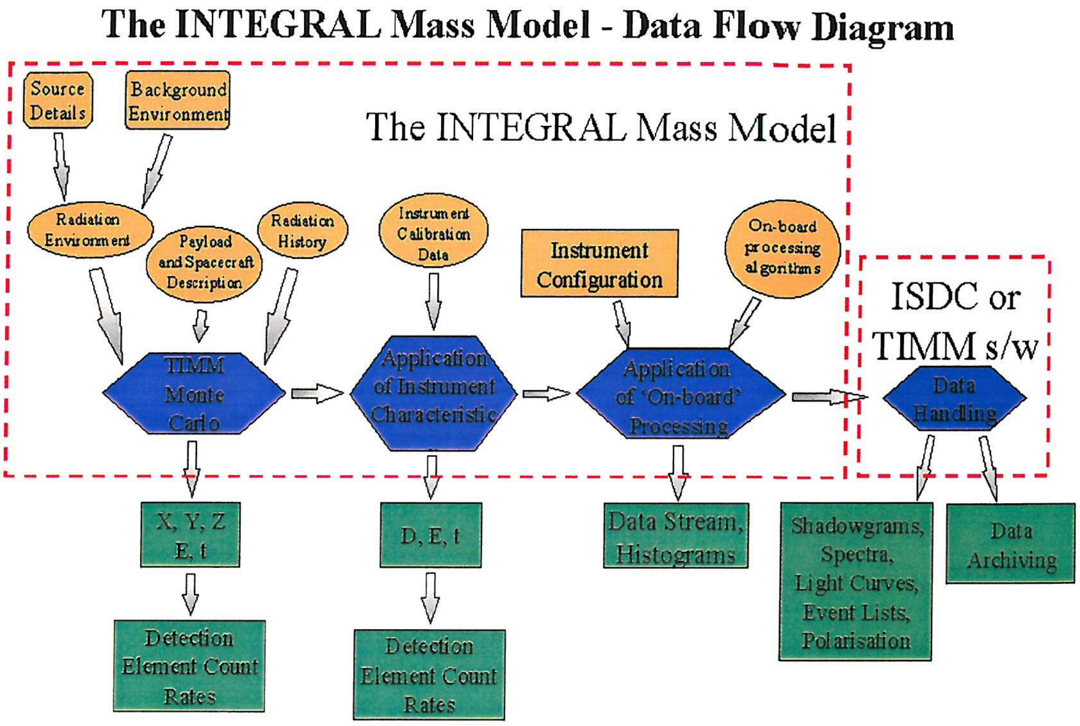

Figure 3.8: *The data flow within TIMM.*

- Uniform evaluation of event rates in detection elements.
- Assessment of on-board software algorithms and telemetry requirements.
- Assessment of off-axis shadows.
- Assessment of degradation of the instrument response due to particle bombardment in space.
- Assistance in post-launch trouble shooting.

Figure 3.8 shows the data flow diagram for TIMM. The model has at least eight inputs, and can provide detailed output data at a number of stages. The three most important inputs are the payload and spacecraft description, the radiation environment and the radiation history. These three inputs are combined in the detailed Monte Carlo package GGOD which is being developed at Southampton.

Given these three inputs, the TIMM Monte Carlo produces details of every energy deposit that occurs in the spacecraft and payload. In practice the information stored is limited to energy deposits in active components. However, if required, counting rates and spectra for the energy deposited in the non-active components could be produced. This could be useful in dose determination for components. For every energy deposit the volume and energy are stored. This data can then be binned to produce component counting rates, spectra, etc. To make these products comparable with real data the instrument logic and response needs to be accounted for. For TIMM this involves thresholding events and then selecting events dependent on multiplicity to generate a simple background spectrum. In future the spectral response could be added in to create a more realistic background spectrum. To generate sensitivity curves the spectral response is already used, but post-calibration, a more accurate knowledge of the response will improve these curves. The final step for TIMM would be to create code that converts the simulation results to the format of the raw spacecraft telemetry. The simulation results could then be analysed using the same software as the real spacecraft data.

The INTEGRAL instruments will be thoroughly tested and calibrated prior to launch. However after launch, the instrument characteristics may change, or components may fail, and these type of changes to the instrument performance will undoubtedly result in a slightly different analysis procedure. Unlike previous missions there will be no INTEGRAL flight spare, so if problems do arise there will be no physical test bed. Instead, there will only be computer based simulation tools and the results of ground and in-orbit calibrations. It is an aim of TIMM to be as detailed as possible by launch, to enable testing of new algorithms and trouble-shooting if problems do occur (Green et al. 1996).

Undoubtedly, some of the best science will be achieved by combining the data from all the instruments to attain good spectral, spatial and timing resolution over nearly four decades of energy (~3 keV to ~10 MeV). There is little communication between the instrument teams and so it is important that the complementarity and interaction between the instruments is independently assessed. This task is overseen by the INTEGRAL Science Working Team (ISWT), and they have agreed that an independent mass model and simulation programme is essential for the evaluation of the combined instrument characteristics.

3.5.1 How does TIMM fit in to the project?

TIMM is independent of the instrument teams and so ESA can call upon the mass model team to provide an independent estimate of instrument performance if required. The uniform nature of the modelling of all the instruments also means that sensible inter-instrument comparisons can be carried out. In its eventual form, TIMM will provide the best model of the instrument background and can also form the basis of a detailed source simulation tool. In the longer term, the background data generated by TIMM could be used to improve the sensitivity of the Galactic Plane Survey.

3.5.2 Relationship with the instrument teams

The relationship between TIMM and the instrument teams exists on two levels:

- The mass model relies on the instrument teams for the data input, in terms of geometry and chemical composition of materials, and processing and histogramming algorithms.
- The instrument teams should be aware of, and interested in the results of, the mass model and the teams should work together to explain any discrepancies in results of simulations.

3.5.3 Model detail

Depending on the purpose of the mass model different levels of detail will be required. For instance, if a background spectrum and counting rate is to be calculated then the distribution of mass and composition of the material is important but very fine detail is not required. However, if shadowing of a detector plane by a strong off-axis source is to be investigated then very fine structure is required, especially for IBIS where the detector pixels are ~4 mm in size. A strong consideration is the time needed, first in constructing the model, and then in running it. A very fine detail model will have large time overheads and if, as in the background case, a fine model is not required then that time is wasted. It is therefore planned to have three different levels of model:

- Major structures - detailed modelling of active components. Crude support structure and auxiliary devices for non-active components.
- Minor structures - more detailed structural information for non-active components.

- Fine Detail - Very detailed geometrical modelling of structural components which are in front of the detection planes.

Though the cruder models should have the correct mass of components, the precise geometrical modelling may not be accurate. Although the major model will be a subset of the minor model and fine detail models, it will be possible to use only the major model throughout the project for a speedy result. When calculating background rates the major model will be sufficient, but to investigate shadowing then only the fine detail model will be appropriate.

3.5.4 Structure of TIMM

The V1.0a Major component model

This was the first major component mass model and is based on data inputs received after the ISVR (1996) and before the Instrument Baseline Design Review (IBDR, 1997). The model is not very complex containing only 160 volumes (see figure 3.9).

The IBIS model (figure 3.10) consists of the mask, hopper and tube structures. The active volumes modelled are the ISGRI, PICsIT, BGO veto and the BGO calibration source tagging crystal. The mask contains several epoxy resin and adhesive layers as well as the actual tungsten mask elements (1.12 × 1.12 × 1.4 cm). The most important volumes are the active ones - ISGRI, PICsIT, and the BGO crystals - and these are modelled in the most detail. The ISGRI detector plane is modelled as a plane of CdTe cells (0.46 × 0.46 × 0.2 cm) with aluminium slats filling the gaps. The 16384 cells are placed into 8 modules. PICsIT is modelled in the same fashion, with 4096 CsI cells (0.92 × 0.92 × 3 cm) placed into 8 modules. The side and bottom vetoes are modelled using 16 BGO crystals (bottom 16 × 32.5 × 2 cm, side trapezia $\sim$ 40 × 36 × 2 cm) plus aluminum housing structures. The calibration source is modelled as a box containing a cylindrical BGO tagging crystal which has a pyramid shaped cut-out. The open end of the cut-out allows the source to view the detector plane of IBIS.

The major component model for JEM-X (figure 3.11) was built by Dr Andy Green using data taken from the JEM-X EID-B v2.2. The JEM-X model consists of 3 main components, the mask, the collimator and the detector. The mask consists of a central tungsten ring and support structures. The outer ring is an L-shaped ring made of Cu/Be. The mask pattern is made up of individual hexagonal tungsten mask elements placed into a vacuum. The JEM-X collimator consists of a

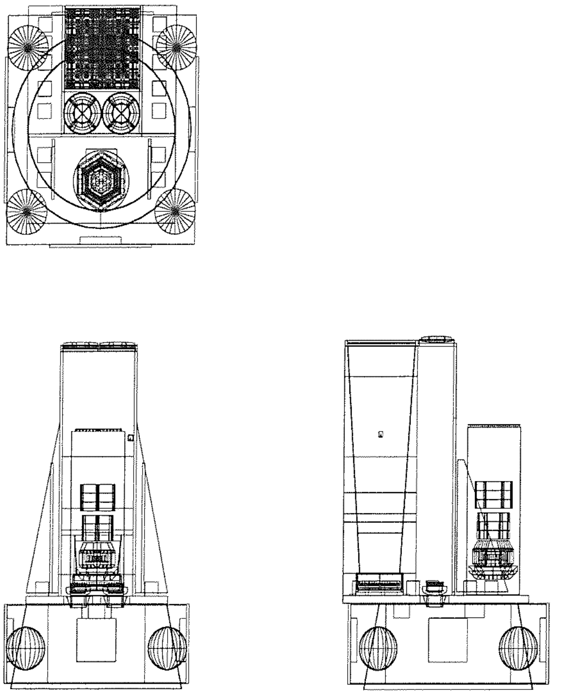

Figure 3.9: *The INTEGRAL Mass Model version 1.0a.*

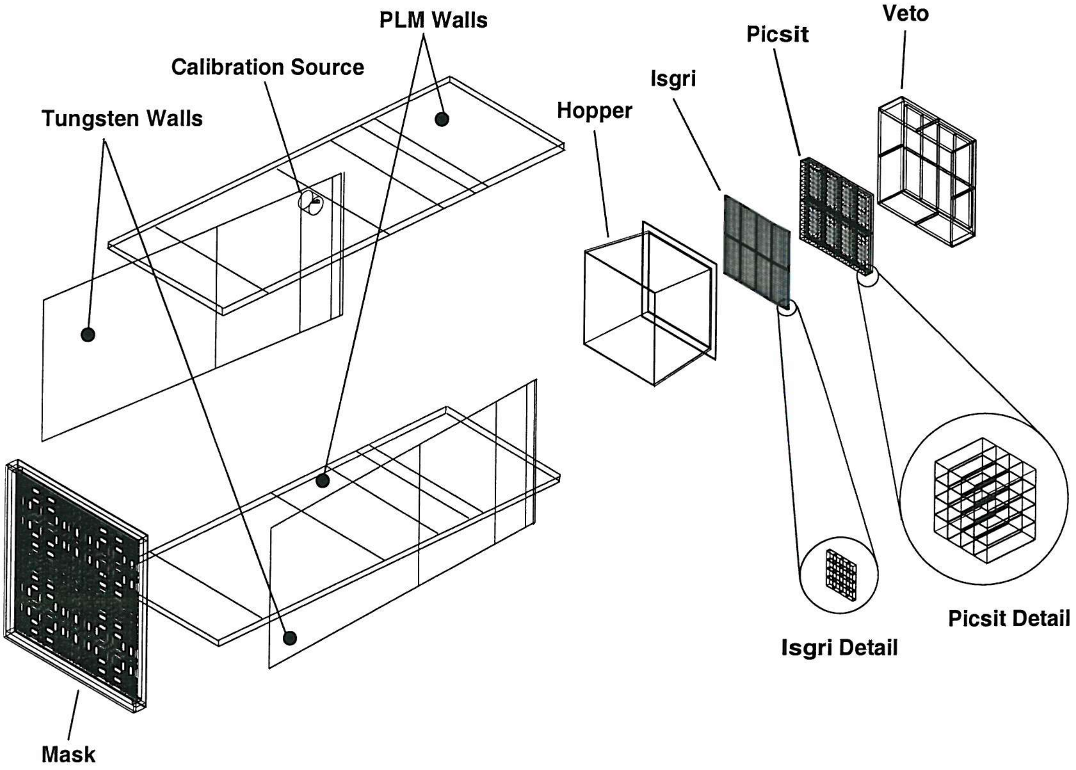

Figure 3.10: *An exploded view of the IBIS model taken from TIMM v1.0a.*

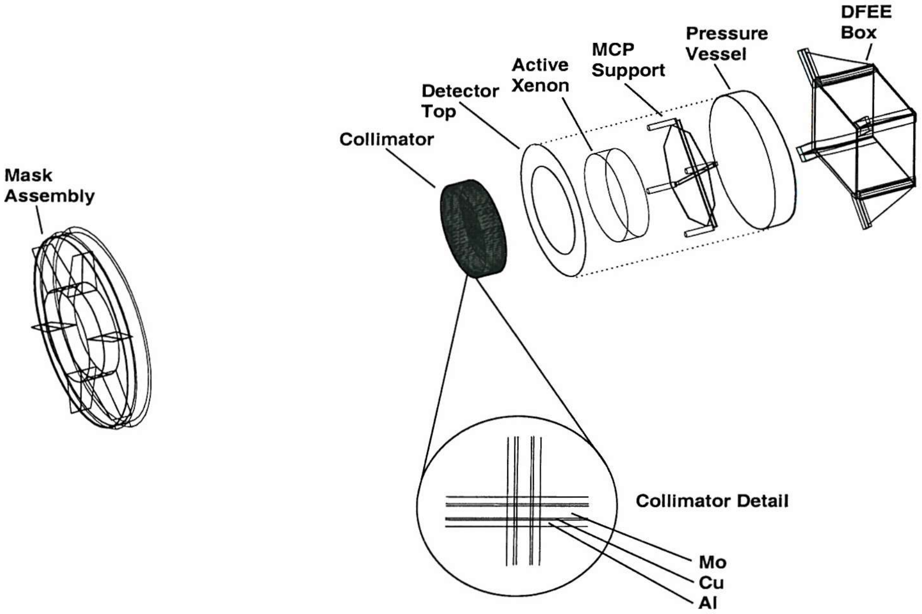

Figure 3.11: *An exploded view of the JEMX model taken from TIMM v1.0a.*

set of slats made of 3 materials, Molybdenum, Copper and Aluminium, arranged as a sandwich (Al/Cu/Mo/Cu/Al). The detector box is modelled as a complicated poly-cone which provides the gas container. There is a beryllium entrance window, stainless steel field guiding plates and the xenon detector gas. Within the model the xenon gas is split into two volumes, a sensitive volume between the field guiding plates and a non-sensitive volume occupying the remaining space. The material xenon is actually a 90% xenon - 10% methane mixture. The final part of the JEM-X model is the Detector Front End Electronics (DFEE) and its mounting brackets which are modelled using aluminium boxes and trapezia.

The spacecraft model (fig 3.12) consists of two main parts, the payload module (PLM) and the service module (SVM). The payload bench is the part of the spacecraft that the instruments will be mounted on and is modelled as a flat aluminium honeycomb box with 2 holes cut in it for the JEM-X DFEE. There are two boxes attached to the payload bench, the Remote Terminal Unit (RTU) and the Power Distribution Unit (PDU). The SVM is modelled as 6 Aluminium honeycomb boxes, to form the sides of a rectangular volume, with the thrust cone mounted inside. There is also simple modelling of the electronics boxes which are mounted on the side walls of the SVM and of the spherical fuel tanks (titanium filled with 10% hydrogen) positioned at the SVM corners. The

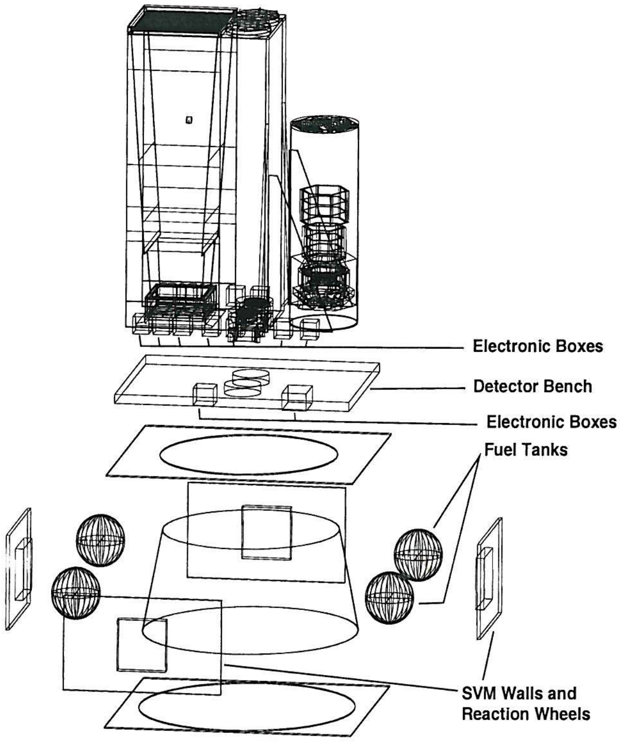

Figure 3.12: *An exploded view of TIMM v1.0a with the spacecraft structures labelled.*

walls of the PLM and the electronics mounted on the PLM are all modelled in a simple way.

As with IBIS the most important parts of the SPI model (figure 3.13) are the active components, the germanium detectors, the plastic veto and the BGO veto. The plastic veto is 0.5 cm thick and sits on top of the mask, which is modelled as 63 (3 cm thick, 3 cm radius) tungsten blocks. There are 19 germanium detector pixels, each of which is 7 cm thick and 3 cm in radius, though the actual germanium radius is 2.82 cm and the remaining 0.18 cm is a beryllium sheath. The crystals are mounted inside the cryostat (a hexagonal Be box). The BGO veto shielding consists of an upper veto ring, a middle veto ring (both containing BGO crystals plus carbon fibre holding structures) and a lower veto ring containing the rear and side shields. The outside of the SPI instrument is modelled using aluminium tubes.

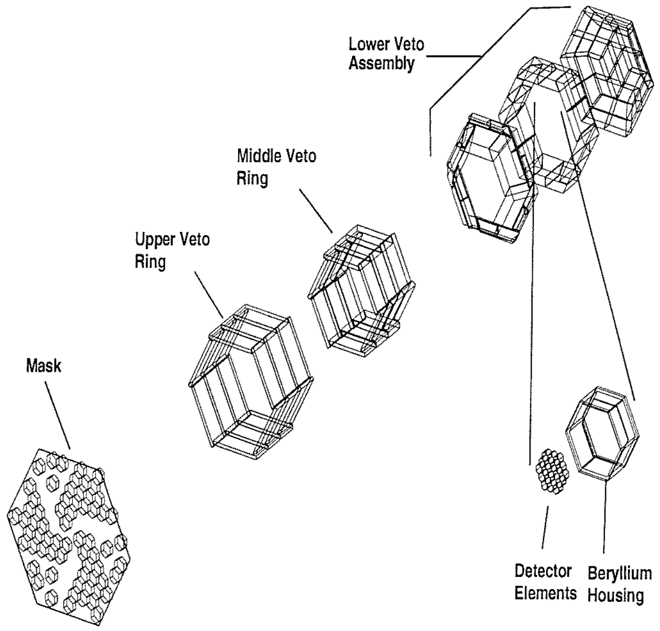

Figure 3.13: *An exploded view of SPI taken from TIMM v1.0a. Only the mask veto crystals, detector pixels and cryostat are shown.*

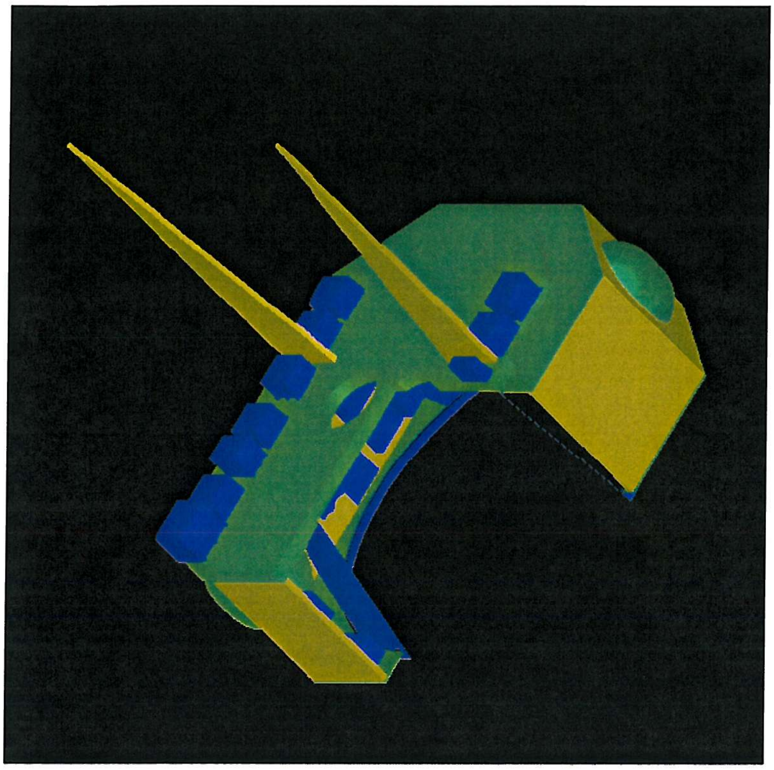

Figure 3.14: *Ray traced, cut-away, view of the v2.0 spacecraft model. Note the redesigned payload bench and the general increase in detail.*

TIMM v2.0 - post IBDR model

In this phase the model was updated to the IBDR specification and, for the first time, the DECAY code was implemented within GGOD. The main changes required to reach the IBDR specification were to the spacecraft (fig 3.14) and SPI (fig 3.15) models. The payload bench was changed to reflect the fact that it is actually a complicated shape. The electronics mounted onto the payload bench were modelled in much greater detail. The corners of the SVM were cut away, forming a more realistic octagonal shape. The electronics mounted onto the SVM walls were modelled as individual components, rather than lumps of aluminium, and the new shape of the fuel tanks was implemented.

The amount of detail within the SPI model was increased dramatically. Within the mask, the veto was moved to under the mask and a new support structure was placed on top of the mask. A more detailed model of the detector crystals and cryostat, taken from Goddard Space Flight Centre

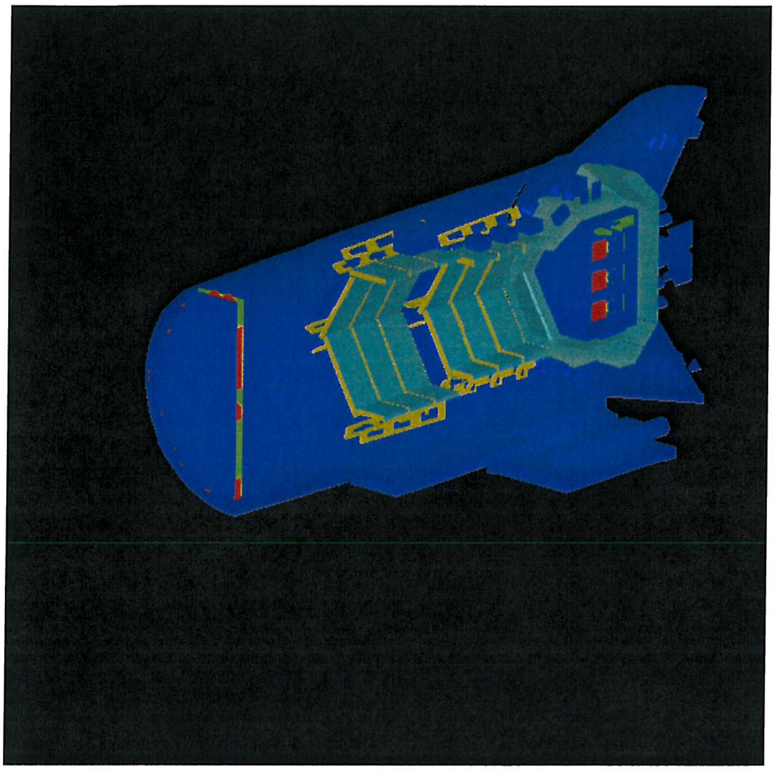

Figure 3.15: *Ray traced, cut-away, view of the v2.0 SPI model. Note the change of external shape and the increase in detail around the collimator rings.*

code, was also implemented. Though the veto and supports of the upper and middle collimator rings weren't changed, further support structures, electronics and PMTs were added. The outside wall of SPI, formerly a single Al tube, was rebuilt using several tubes and cones to form a more detailed approximation of SPI. A further major change was the addition of the active Stirling Cycle Coolers and the passive radiator to the outside of the SPI structure.

As well as the geometrical changes to TIMM, the event modes produced by the output from the model were also changed to match those of the instrument teams.

TIMM v2.1 and v2.2

The main changes between the v2.0, v2.1 and v2.2 models involved the JEM-X instrument. In the earlier models JEM-X was physically present, the data structures were unused, and to some extent unusable. Whilst some geometrical changes were made to the mask, these were very minor. The major changes to TIMM in these models were the extension of GEANT to lower energies and the re-writing of the JEM-X data structures. The energy range of JEM-X, 3 - 35 keV, falls below the low-energy cut-off of the default GEANT tracking (10 keV). This meant that some investigation was required to set-up GEANT to track photons, within the JEM-X materials, down to an energy of 1 keV. Once this was done, and the output data structures were re-written, the model was re-run to produce usable JEM-X background data.

TIMM v3.0 - post Instrument Hardware Design Review (IHDR)

Toward the end of 1998, the first post-IHDR model, version 3.0 of TIMM was completed. Between v2.2 and v3.0 there were very minor changes to JEM-X and the spacecraft. The main differences between v2.2 and v3.0 are the addition of the Optical Monitoring Camera (OMC) and star trackers to the model.

The main change to the JEM-X model is the addition of an active veto. This is a tube of xenon/CH_4 which surrounds the active xenon/CH_4 in the detector. Within the spacecraft minor adjustments of the JEM-X DFEE and the PLM wall positions have been made. For the first time the Optical Monitoring Camera (OMC) is placed into TIMM. The OMC is modelled as a tube, with a baffle on the top, and an optics system at the bottom. It is mounted on the PLM walls at the side of JEM-X. Chemically the OMC is composed mostly of aluminium. The star trackers are attached to the PLM walls on the opposite side to the OMC. The star trackers have a very simple structure: a baffle with optics and an electronics box underneath.

TIMM v3.1, v3.2 and v3.3

These are transitional versions, testing out the possibility of using Euclid files to contain the geometries and materials (making TIMM more portable) and of converting from Sun Solaris to RedHat Linux operating systems. In v3.3 the calibration source was completely remodelled, and is now composed of a thin titanium sheet plus a thin BGO sheet (the tagging crystal) and two PMTs.

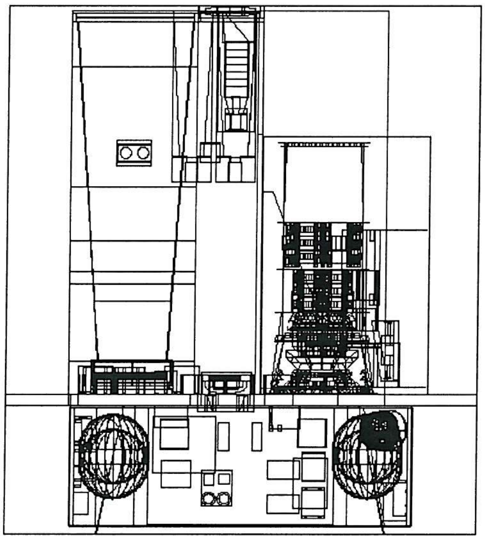

Figure 3.16: *Geant++ drawing of version 3.4 of TIMM.*

TIMM v3.4 - pre-Instrument Critical Design Review (ICDR)

This is the latest, pre-ICDR, version of TIMM (fig 3.16). The main changes are to SPI and to the event modes output from the model. The SPI cryostat has been rebuilt based on designs from Saclay. The SPI mask has been altered to a more detailed design, consisting of support structure, mask elements, plastic veto and PMTs. The output from TIMM has been re-written to fix some small bugs in the event modes, and generally tidy up the output code and event modes.

A further small change to the model is the addition to the star tracker of a small (1 cm^2 and 50 μm thick) square of sensitive silicon to simulate the active part of the silicon CCD chip. This is to allow estimation of the likely prompt flux within the star tracker during both normal operations, and in particular, during solar flares.

3.6 Summary

Gamma ray astronomy is made difficult because of the low signal-to-noise ratio. It is therefore important to understand the background in great detail to maximise the scientific return of a mission. The latest technique to do this involves building a computer model (a "mass model") of the spacecraft and payload, and putting the radiation environment and history into a Monte Carlo simulation code. This allows one to estimate the background noise within the detectors. This technique is known as mass modelling.

To allow a full and proper simulation of the INTEGRAL mission, the Southampton group are involved in creating a software suite (GGOD) that will allow simulation of both prompt and delayed components. The GGOD package makes use of developed codes such as GEANT/GCALOR and ORIHET, but locally this has been extended by developing the DECAY code. This code allows one to process the induced (or delayed) component of the background and is described in the following chapter.

Chapter 4

The DECAY Code

4.1 Introduction

As mentioned in the previous chapter, The INTEGRAL Mass Model (TIMM) will utilise the Southampton developed GGOD software suite. In preliminary versions of GGOD a very approximate code was used to model the induced decays, which for detailed investigations is inadequate, and so a more accurate code was required. This improved code, called DECAY, is described in this chapter.

The combination of the GEANT and GCALOR codes can only track particles via prompt processes, such as ionisation and scattering. These codes can't process the products of activation, the decay of which may be delayed from the original interaction by seconds to years. To achieve this a code is required to process the production rates of activated isotopes and, using the half-lives of those isotopes, calculate the decay rates at any given epoch. Within GGOD this is carried out using the ORIHET code. Once this has been done then one can simulate the delayed component of the background via the DECAY code. DECAY is required to allow simulation of the radioactive decay of any given isotope. To meet this requirement it is necessary to have decay schemes available for all (or many) of the known isotopes. The necessary isotopic data was taken from the Evaluated Nuclear Structure Data Files (the files used were ordered by parent nuclide i.e. the PENSDF2 data files) database held at Brookhaven National Laboratory (BNL) by the National Nuclear Decay Centre (NNDC) and the BNL. All types of decay, except spontaneous fission and delayed particle decays, have been included in the DECAY code.

In the following sections the physics modelled by the DECAY code is summarised, then the code itself is discussed (sec. 4.3), followed by the preliminary tests (sec. 4.4). After preliminary testing of DECAY three more complete tests were used to validate GGOD as a whole. These tests are presented in sections 4.5 - 4.7.

4.2 Physics behind the simulator

There are many different types of particle and photon emission that have to be simulated in order to fully model α decay, β decay and isomeric transitions (IT). The primary emissions such as α, β^+ and β^- particles are necessary to produce even a crude model. For more accuracy the secondary emissions (γ-rays and conversion electrons) would be included, and for the most accurate modelling the tertiary emission (X-rays and Auger electrons) would also be required. The processes that give rise to these particles and photons are described in this section.

4.2.1 Alpha decay

In heavier nuclei the binding energy per nucleon is low enough to allow for the emission of α particles by Coulomb repulsion (Eq 4.1).

$$^{A}_{Z}X_N \rightarrow ^{A-4}_{Z-2} X^*_{N-2} + \alpha \tag{4.1}$$

In the one-body model the alpha is imagined to be pre-formed within the nucleus and it moves backwards and forwards within a potential well that describes the nucleus (fig 4.1). The potential energy outside the nucleus is described by Coulomb repulsion. Every time the α particle presents itself to the barrier it has a very small chance of passing through. Over a period of time the alpha particle is presented to the barrier many times and eventually penetrates it by quantum mechanical tunneling. This model accounts for the fact that unstable nuclei don't decay immediately. After emission of the α particle the daughter nucleus may be left in an excited state, this will result in a release of one or more γ-rays as the nucleus de-excites.

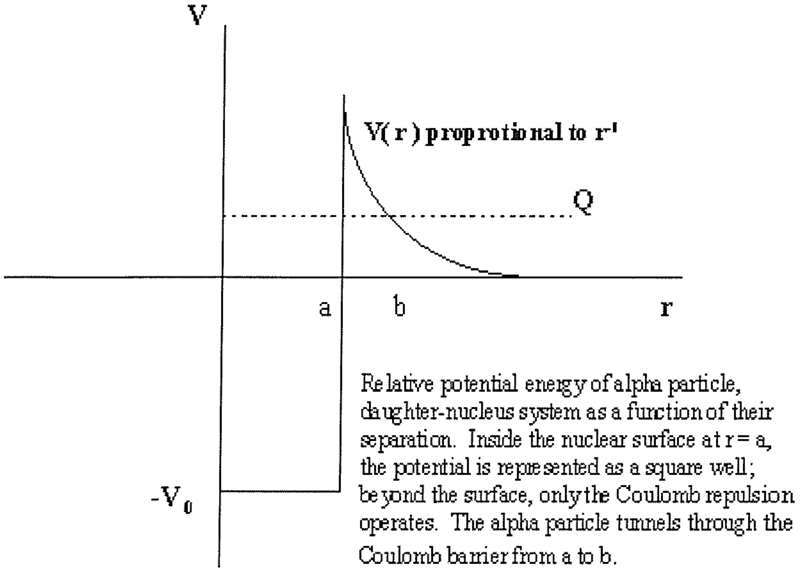

Relative potential energy of alpha particle, daughter-nucleus system as a function of their separation. Inside the nuclear surface at r = a, the potential is represented as a square well; beyond the surface, only the Coulomb repulsion operates. The alpha particle tunnels through the Coulomb barrier from a to b.

Figure 4.1: *Simple one body potential for α decay, where Q is the total available energy (sometimes called the disintegration energy) and V is the potential energy at distance r from the nucleus centre.*

4.2.2 Beta$^+$ decay

Beta$^+$ decay actually accounts for two phenomena, β^+ decay and electron capture (EC). In β^+ decay a proton in the nucleus is converted to a neutron with the release of a positron and a neutrino (Eq 4.2). The positron and the neutrino share out the energy and this leads to a continuum of emitted positron (e$^+$) energies rather than a single prominent peak.

$$ {}^{A}_{Z}X_N \rightarrow {}^{A}_{Z-1} X^*_{N+1} + e^+ + \nu \tag{4.2} $$

In EC an electron is captured from an atomic shell (Eq 4.3). The shell from which the electron is captured can vary, and is not limited to the inner ones (i.e. the K and L shells).

$$^{A}_{Z}X_N + e^- \rightarrow ^{A}_{Z-1} X^*_{N+1} + \nu \tag{4.3}$$

Both β^+ and EC can leave the nucleus in an excited state from which emission of γ-rays can occur.

4.2.3 Beta$^-$ decay

In the nucleus a neutron is converted to a proton and an electron, with emission of the electron, (then known as a β^- particle) and an anti-neutrino (Eq 4.4). Similar to β^+ decay these two particles share the energy of the interaction giving a spectrum which is a continuum rather than a set of finite peaks. Gamma-ray emission may occur if the end state is an excited one.

$$^{A}_{Z}X_N \rightarrow ^{A}_{Z+1} X^*_{N-1} + e^- + \bar{\nu} \tag{4.4}$$

4.2.4 Gamma-rays

Gamma-rays are secondary products of α and β decay processes. After the initial particle is emitted the nucleus can be left in an excited state. This is an unstable situation and de-excitation occurs, where the nucleus emits γ-rays to reduce its energy state and become stable again. Most γ-rays have energies over 100 keV, though it is possible to get many below this energy. The numbers and energies of γ-rays emitted are well defined by the possible energy levels of the nucleus as shown in the decay scheme in figure 4.2.

4.2.5 Conversion electrons

Instead of emitting a γ-ray, the energy of an excited nucleus can be used to eject an orbital electron, which is then known as a conversion electron and can range in energy from ~keV to ~MeV. Simplistically, one can think of the γ-ray emitted from the nucleus as interacting with one of the atomic shell electrons, and ejecting it from the atom. The number of electrons emitted can be calculated from the conversion coefficient. When the electron is emitted it leaves an unfilled electron shell and this leaves the atom unstable. After conversion electron emission, one of the outer electrons will fall inwards to fill the hole and thus make the nucleus more stable. This process will release either a

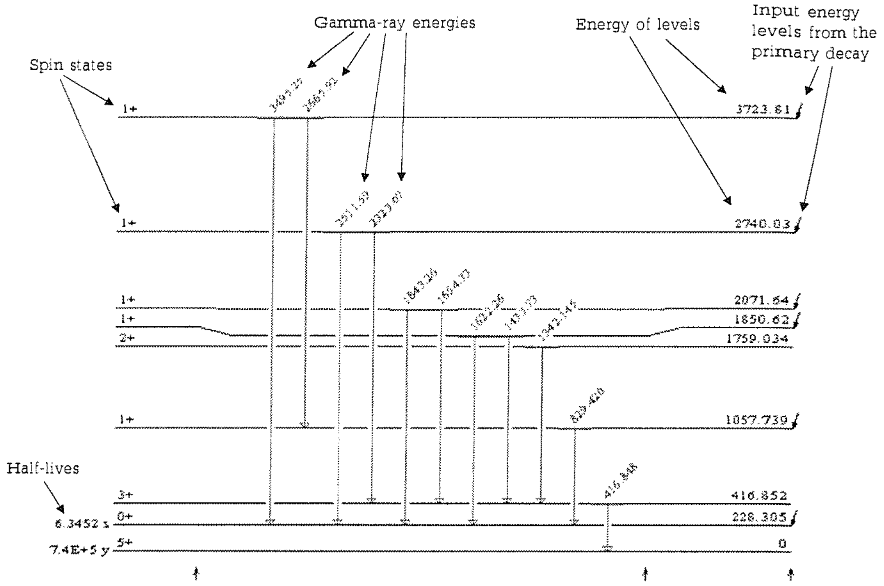

Figure 4.2: *A typical decay scheme generated from the PENSDF2 database. Transition is* ^{26}Si *decaying to* ^{26}Al.

characteristic X-ray or an Auger electron, and will happen numerous times, until the atomic shells have adjusted and are stable again. In any process where γ-ray emission occurs, conversion electron emission is also possible.

4.2.6 X-rays and Auger electrons

Characteristic or fluorescence X-rays are the products of electron shell transitions as shown in figure 4.3. The X-rays have an energy equal to the binding energy of the final shell minus the binding energy of the initial shell, which is usually below 100 keV. K shell X-rays, which involve transitions between the other shells and the K shell, are the highest energy X-rays with L shell X-rays and then M shell X-rays and so on at progressively lower energies.

The other products of electron shell transitions are Auger electrons. The emission of X-rays and Auger electrons are competing processes and are therefore mutually exclusive. As shown in fig 4.3,

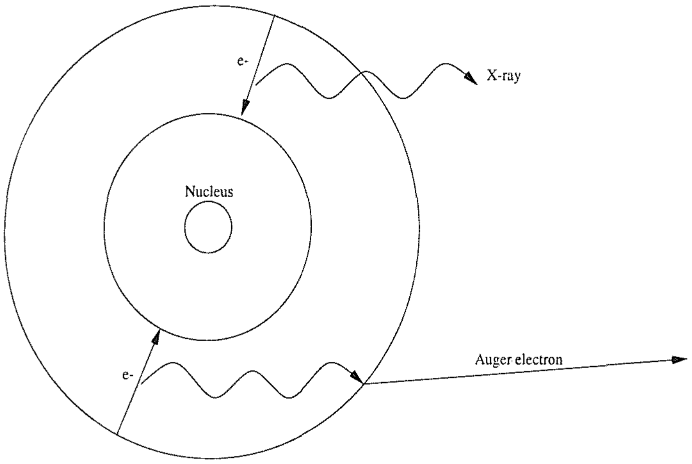

Figure 4.3: *Origin of X-rays and Auger electrons.*

Shell	X-ray energy (keV)	Auger electron energy (keV)
K	40 to 100	20 to 80
L	~10	~5
M	~3	~1
N	~1	~1

Table 4.1: *Typical X-ray and Auger electron energies.*

Auger electron emission occurs when a shell electron absorbs an X-ray and is thus emitted. Auger electron energies are equal to the binding energy of the final shell minus twice the binding energy of the initial shell. As expected from their origin, Auger electrons are lower energy phenomena than X-rays (table 4.1). The relative numbers of X-rays compared with Auger electrons can be determined from the fluorescence yield (Eq 4.5), and varies depending upon the transition concerned.

$$\frac{N_k}{(1-N_k)} = (-6.4 + 3.4Z - 0.00010Z^3)^4 \times 10^{-8} \tag{4.5}$$

In equation 4.5, Z is the proton number and N_k is the number of K shell X-rays (Marmier and Sheldon 1970).

4.2.7 Isomeric transitions (IT)

Unlike α and β decays isomeric transitions do not emit a primary particle. This type of decay occurs when a nucleus is in a semi-stable excited state, a metastable state, which may last for seconds and is therefore temporally separate from the decay that created it. This semi-stable configuration decays, effectively via nuclear de-excitation, with emission of γ-rays. As with all γ-ray emission there is a chance of conversion electrons, X-rays and Auger electrons also being emitted.

4.3 The DECAY code

Before the code is described there is a brief summary of the pre-processing steps that were taken to create the databases used by DECAY.

4.3.1 Pre-processing

The PENSDF2 files contained more data than was required and therefore it was decided to pre-process the data files. The flow chart (fig 4.4) shows the steps the pre-processing program went through. The PENSDF2 file was opened and then searched through to find the relevant information. Having located a useful block the Data Set Identification (DSID), which contains the name of the parent isotope, the daughter isotope and the decay type, was read in. The next piece of information read was the parent record, which contains the initial energy of the parent isotope, in case it is a metastable state, and the Q value of the decay. The records from then on, except comment and some continuation records, were read in and dealt with as appropriate.

Alpha records

The α records contain the energy, intensity and the nuclear energy level decayed to. If necessary the intensities of the α decay were normalised to create percentage probabilities.

Beta$^+$/EC records

The β^+/EC records contain the total intensity, the β^+ intensity, the electron capture intensity and the nuclear energy level each β^+/EC decays to. If necessary the β^+/EC intensities were normalised to create the final β^+/EC probabilities. Continuation records containing the probabilities for electron capture from the various electron shells were also read in.

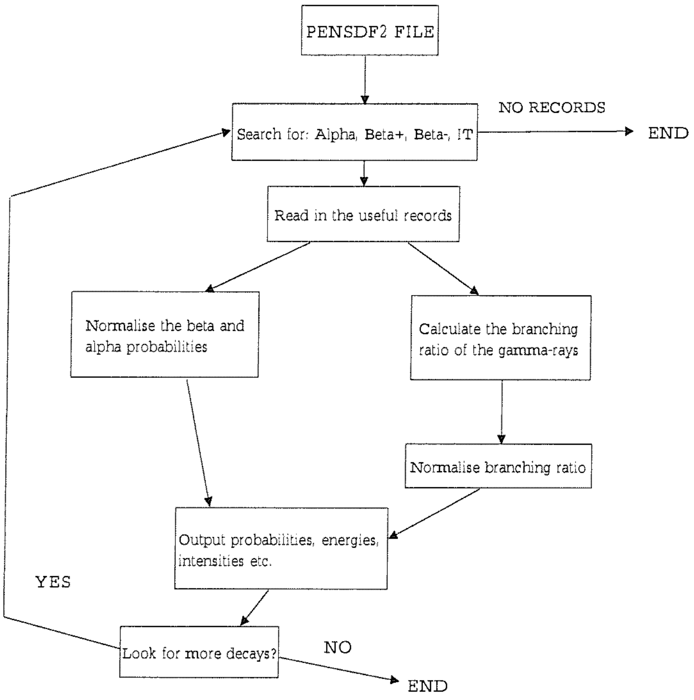

Figure 4.4: *The pre-processing program flow chart.*

Beta$^-$ records

The β^- records gave the intensity, the endpoint energy of the β and the nuclear energy level decayed to. As usual, intensities were normalised if necessary.

Level records

The level records contain the energy of each of the levels within the decay scheme.

Gamma records

The γ records contain the energy, relative intensity and the nuclear energy level from which the γ-ray originates. The intensity was used to calculate normalised branching ratios for the γ-rays. The continuation records, containing the conversion electron coefficients, were also read in.

Output phase

Once all of the PENSDF2 information for an isotope had been read in, and processed, the new database files were written. The first records output were the α, β^-, β^+/EC or IT records. The α records contain 4 columns: an identifier (1, 2, ...), the α energy, the α intensity and the coincident energy level. The β^- records contain four columns: an identifier (1, 2, ...), the intensity, the endpoint energy and the coincident level. The β^+/EC record contains 8 columns: an identifier (1, 2, ...), the β^+/EC intensity, the coincident level, the β^+ probability, the probability of EC from the K, L and M+ shells respectively, and finally the endpoint energy (for β^+). There was no output for the isomeric transitions, just a key that identifies the decay type.

For β^- decays the endpoint energy of the β particle was either read in from the PENSDF2 file or calculated using equation 4.6. For β^+ decays the endpoint energy was always calculated using equation 4.6, where the endpoint energy (E_β) was calculated from the Q-value, the energy level that the β decayed to (E_{endlevel}) and the initial energy level of the parent isotope (E_{parent}) for meta-stable states.

$$E_\beta = Q - E_{endlevel} + E_{parent} \tag{4.6}$$

Equation 4.6 assumes that the (anti-)neutrino is massless and gives results which are approximately correct.

The second records output were the energy levels, which took the form of two columns, containing the level number and the energy.

Following this the γ records were output in 9 columns: the γ number, its energy, the normalised branching ratio, the coincident level and the probability of a γ-ray or a K, L, M, or N+ shell conversion electron. The conversion electron probabilities were calculated from the conversion electron coefficients. The coefficients give the ratio of electrons ejected from a particular shell to γ-rays emitted for the transition. From this the probability of γ-ray emission can be derived in terms of the conversion coefficients (Eq 4.7).

$$P_\gamma = \frac{1}{(\alpha_K + \alpha_L + \alpha_M + \alpha_N + 1)} \tag{4.7}$$

In equation 4.7 P_γ is the γ-ray probability and α_k etc. are the relevant conversion coefficients. From this equation further derivation proves that the probability of K, L, M and N+ conversion electron ejection is equal to the probability of γ-ray emission multiplied by the conversion coefficient.

The fourth record output was the information record, this contains the parent isotope, the daughter and the decay type. Below this, the probability of this type of decay occurring and the Q value for the decay, are output.

If the isotope concerned has another possible decay path then the above processing procedure is repeated. A data file therefore contains all the possible decay paths for an isotope one after another. For each isotope there may be more than one data file if the isotope has a metastable state, these are treated in GGOD like separate isotopes because their half-lives and decay products are different from the ground state isotopes.

4.3.2 Simulation

The first step in the simulation procedure is to read in and store the data. Once this is done the simulation can begin. Naturally, the first thing simulated is the initial α, β or EC event. After this the nuclear de-excitation is simulated, and then if appropriate, atomic de-excitation is modelled (fig 4.5). Isomeric transitions are slightly different in that there is no initial particle, and they are therefore treated in the same way as nuclear de-excitation.

After the primary decay has been simulated the results are output. The output consists of the decay type, the intensity of the particle and the level to which the initial particle decayed. Also output are the energies (endpoint energies for β decays) of the particles. If EC has occurred then atomic de-excitation is simulated.

The secondary decay is then simulated if there are any γ-rays coincident with the current nuclear energy level. If there are coincident γ-rays, their energies and branching ratios are output, and then their emission is simulated. Firstly the energy to be emitted was determined, then whether this is a γ-ray or a conversion electron is determined depending on the conversion coefficients. If a conversion electron is produced then the simulator models the release of X-rays/Auger electrons that usually occur after such a process. If a γ-ray is emitted then its energy is output along with the new level decayed to. If this level is the ground state (energy = 0 keV), then output of the parent isotope and the decay type occurs. If this is not the ground state, then the process of determining the coincident γ-rays and simulating emission occurs again. If no coincident γ-rays are found then the energy level represents a metastable state and the decay simulation ends. Another decay of this isotope can then be simulated, but since the information is stored the read in phase can be ignored. If a new isotope is required then the simulator has to read in the new decay information.

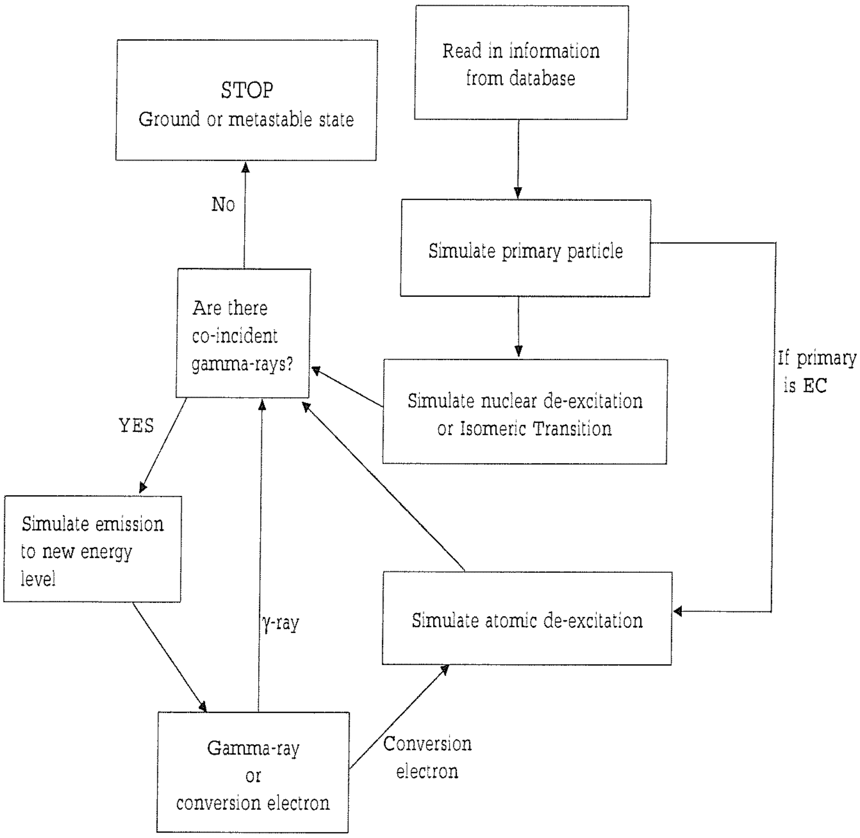

Figure 4.5: *The simulation program flow chart.*

4.3.3 Consideration of limitations

To understand the results it is important to be aware of the limitations of the simulator. The main limitation occurs in the generation of the Auger electrons and X-rays, where there is appreciable uncertainty in the intensity of those originating from the higher shells. For the K and L shell X-rays and Auger electrons the energy levels involved and the fluorescence yields used were calculated with reasonable precision and the results for these are therefore quite acceptable. For the M, N and N+ shells the fluorescence yields were arbitrarily set, so that equal numbers of Auger electrons and X-rays were produced for these levels, and this could prove wrong. In future a better approximation of the fluorescence yields will fix this problem and improve the results.

A further limitation is that the decay schemes used are uncertain in some cases, leading to unavailable or unuseable data files. This is a problem of the database and can only be fixed when newer versions of PENSDF2 are created.

4.4 Preliminary tests

The accuracy of the results from the DECAY code is heavily dependant upon the inputs to the code (i.e. the production rates calculated within GEANT/GCALOR, the decay rates calculated by ORIHET and the decay schemes from the database). Any errors, systematic or statistical, that occur in the production rates, will of course be magnified within ORIHET and then again within DECAY. Within GEANT/GCALOR the volume in which activation occurs is stored, but not the actual position of activation, and so surface effects etc. can not be investigated. It is beyond the scope of this thesis to validate GEANT/GCALOR, however this will effectively be done in sections 4.5-4.7, when GGOD is tested. In this section there is a brief examination of the ORIHET code, followed by an in depth look at the DECAY code.

4.4.1 Validation of decay rates calculated by ORIHET

The calculation of the decay rates involves taking the production rates (in atoms/s) and converting them to produce the decay rate expected after a certain time has elapsed. This is complicated by the calculation of the decay rates of the daughter products (and their daughters etc) as well.

For this test a very simple activation rate file containing only ^{235}U was created. The production rate was set to 100 atoms/s for an irradiation time of 1 year (3.1536×10^7 s). Table 4.2 shows the resultant decay rates, along with calculated decay rates for comparison. The calculated rates were produced using the decay constant (λ), and assuming that all of the ^{235}U atoms were produced at the beginning of the year. The number of atoms that would have decayed during the year was calculated, and this was then divided by the initial number of atoms to produce the decay rate at the end of the year. This is very crude, though it should give answers within a factor of ten of the correct answer, which is confirmed by the ratio of ORIHET to calculated values shown in column 4. The ORIHET and calculated values for the first three isotopes in the chain (^{235}U, ^{231}Pa and ^{231}Th) are within a factor of two. For the later isotopes in the chain the difference ranges between a factor of four and six. Allowing for uncertainties within ORIHET and the crudeness of the calculation this is not too bad.

Isotope	ORIHET value	Calculated value	Ratio	Generation
^{207}Tl	1.12×10^{-14}	6.52×10^{-14}	0.17	11
^{211}Pb	1.12×10^{-14}	6.52×10^{-14}	0.17	9
^{211}Bi	1.12×10^{-14}	6.52×10^{-14}	0.17	10
^{211}Po	3.36×10^{-17}	1.63×10^{-16}	0.21	11
^{215}Po	1.12×10^{-14}	6.52×10^{-14}	0.17	8
^{219}Rn	1.12×10^{-14}	6.52×10^{-14}	0.17	7
^{223}Fr	1.57×10^{-16}	6.52×10^{-16}	0.24	5
^{223}Ra	1.12×10^{-14}	6.52×10^{-14}	0.17	6
^{227}Ac	1.12×10^{-14}	6.52×10^{-14}	0.17	4
^{227}Th	1.11×10^{-14}	6.45×10^{-14}	0.17	5
^{231}Th	1.01×10^{-7}	9.85×10^{-8}	1.025	2
^{231}Pa	1.07×10^{-12}	2.08×10^{-12}	0.51	3
^{235}U	1.01×10^{-7}	9.85×10^{-8}	1.025	1

Table 4.2: *Comparison of decay rates produced by ORIHET with those calculated for a* ^{235}U *source produced at the rate of 100 atoms/s for one year. Column 4 contains the ratio ORIHET to calculated rate.*

The decay rates are not just affected by the half-lives of the individual isotopes but also by the

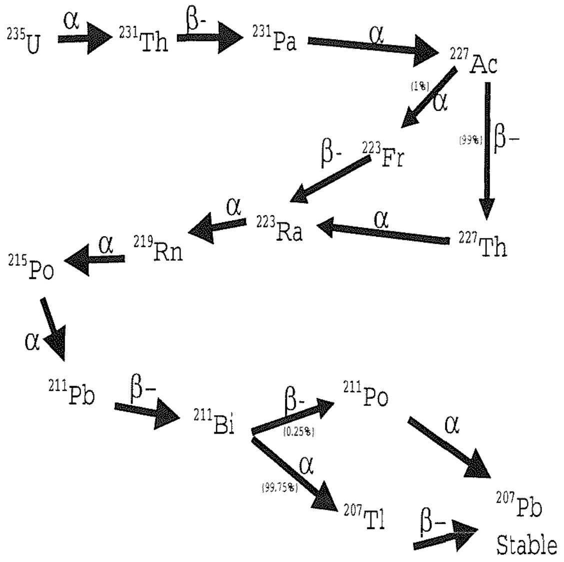

Figure 4.6: *The* ^{235}U *decay chain. The type of decay, and where appropriate, the percentage of decays leading to a product, are given.*

decay rates of the isotopes preceeding them in the decay chain (fig 4.6).

In table 4.2 there is good agreement between the ORIHET result and the calculated value for ^{235}U. The half-life of the second isotope in the chain (^{231}Th) is so short that over a year it is expected to fully decay away. The decay rate for ^{231}Th would be 1 (i.e. all the produced atoms decay), however when the production rate from ^{235}U is accounted for, the decay rate of ^{231}Th is the same as that of ^{235}U. The third isotope produced is ^{231}Pa, and from its half-life the decay rate should be $\sim 2.12 \times 10^{-5}$, however again the production rate must be taken into account (9.85×10^{-8} atoms/s) and therefore the true decay rate will be $\sim 2 \times 10^{-12}$. Following this process through, the decay rates for all of the other isotopes in the chain were calculated. If these are compared with the ORIHET values, then it can be seen that there is reasonable agreement, especially when taking into account the crudeness of the calculation.

Having briefly shown that ORIHET works acceptably well the DECAY code is now considered. The decays of four different isotopes are simulated, and the spectra produced are compared with their decay schemes. These tests have been carried out using a 1cm^3 CsI(Tl) detector, placed inside a NaI well detector, with a Ge detector covering the aperture (fig 4.15). This is a more complex setup than is necessary because later a comparison between simulated and real data from just such a setup will be presented.

4.4.2 ^{24}Ne

The first test carried out was to model the β^- decay of ^{24}Ne to ^{24}Na. Since this was a falsely created test case, and ORIHET was not used, decays of the daughter do not need to be considered. The Q value for this decay is ~2470 keV and 100% of decays lead to a 472 keV γ-ray with 8% of those being accompanied by a 874 keV γ-ray. To obtain a spectrum with good statistics 1 million events were simulated. When a decay occurs it is expected that the β particle will deposit some (or all) of its energy within the CsI(Tl) crystal (the range of a 2.5 MeV electron is about 2.5 mm in CsI(Tl)). A few of the β particles may escape the CsI(Tl) crystal and deposit energy in the germanium or sodium iodide detectors. Only about 12.5% of the β particles will start within 2.5 mm of the edge of the CsI(Tl) crystal, and of these one could roughly assume one half will be travelling in the correct direction to leave the crystal. The transmission of CsI(Tl) at the γ-ray energies considered is so high that most of the γ-ray energy will escapse from the CsI(Tl) crystal. The CsI(Tl) spectrum will therefore be largely dominated by the β continuum. The spectra of the other two detectors will be dominated by the γ-ray lines. The 472 keV line should be the largest line, but it is unclear whether the 874 keV line or the sum peak (at 1346 keV) will be the second most dominant line. This is dependant on the detector geometry.

The simulated CsI(Tl) spectrum (fig 4.7) is dominated by the β continuum as expected. The simulated spectra obtained with the germanium (fig 4.8) and sodium iodide (fig 4.9) detectors are dominated by the γ-ray lines from the decay and are completely different to that from the CsI(Tl) (fig 4.7) detector.

The spectrum measured within the germanium detector shows peaks at ~30 keV, ~160 keV, ~310 keV, 472 keV, 874 keV and 1346 keV. The peak at 30 keV is probably related to K shell X-rays from the CsI(Tl) crystal. The geometrical setup simulated makes it quite likely that photons produced within the CsI(Tl) crystal could be scattered between both the Ge and NaI detectors. This would create backscatter peaks and Compton edges within the detector spectra. A large backscatter peak in one detector should be accompanied by a large Compton edge in the other detector. The

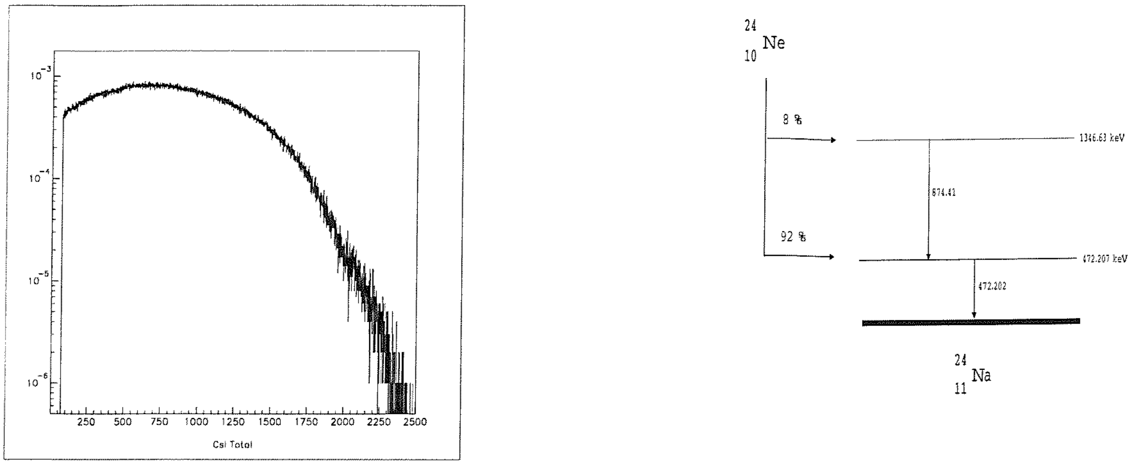

Figure 4.7: *Modelled spectrum produced by* ^{24}*Ne decay within a 1cm*^{3} *CsI(Tl) crystal (no energy resolution has been applied). The right hand figure shows the* ^{24}*Ne decay scheme.*

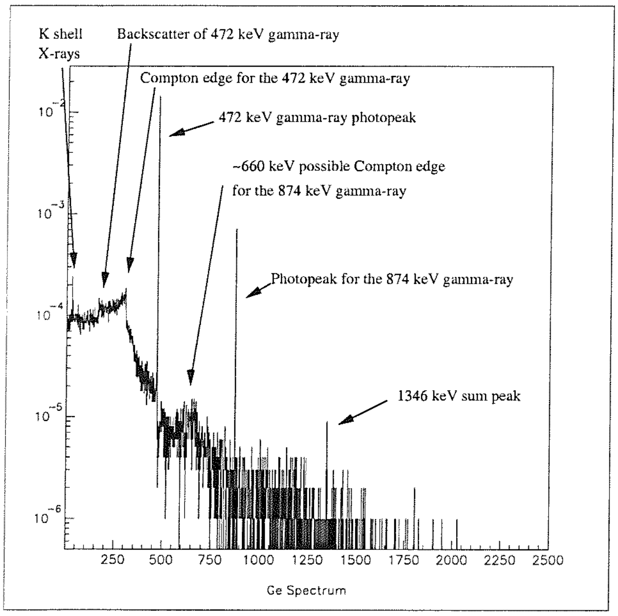

Figure 4.8: *Modelled spectrum produced by* ^{24}*Ne decay within a 1cm*^{3} *CsI(Tl) crystal, as measured with an adjacent Ge detector (no energy resolution has been applied).*

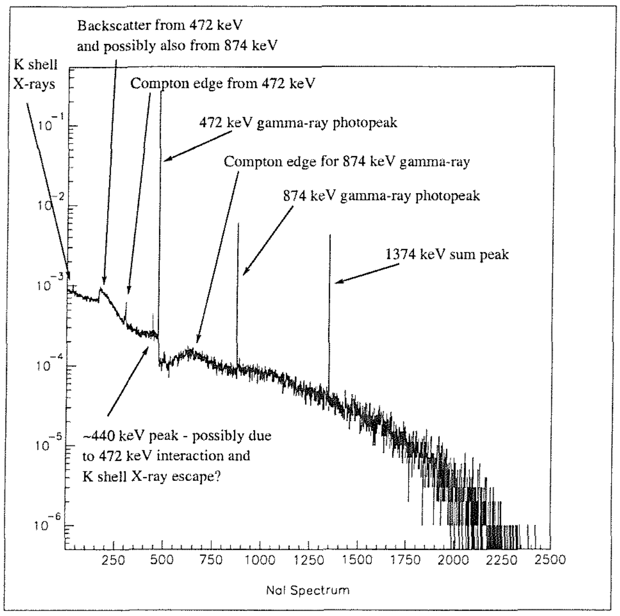

Figure 4.9: *Modelled spectrum produced by* ^{24}*Ne decay within a 1cm*^{3} *CsI(Tl) crystal, as measured with an adjacent NaI detector (no energy resolution has been applied).*

backscatter peak for a 472 keV γ-ray would be at 165.76 keV and the Compton edge would be at 306 keV. There is evidence in the modelled spectrum for both of these features. For an 874 keV γ-ray the backscatter peak would be at 197.7 keV and the Compton edge would be at 676.3 keV. Looking at figure 4.8 there is evidence of an increase in counts around ~660 keV, but the count rate is already boosted around 190 keV and it is therefore hard to clearly see the backscatter peak. The sum peak at 1346 keV is clearly observable. The fact that there are two γ-rays emitted at the same time gives the opportunity for many other combinations such as double backscatter peaks etc. These are very rare, as one would expect, though the increase in counts around 500 keV and 820 keV could be due to combination of backscatter and Compton edge photons.

The NaI spectrum contains less noise than the germanium spectrum because of the greater active volume and higher stopping power. The number of counts observed within the NaI is clearly very much larger than in the Ge. Again there are peaks at ~30 keV, ~170 keV, ~300 keV, 440 keV, 472 keV, ~500 keV, 874 keV and 1346 keV. These have the same explanations as in the Ge case. In this spectrum there a clearer case for a feature at ~195 keV (i.e. the backscatter from the 874 keV γ-ray). In comparison with all the other lines, the 170 keV line looks to be broadened and this could be the superposition of the two backscatter peaks, the 170 keV being more important because there are many more 472 keV γ-rays. Within both the Ge and NaI spectra, there appears to be evidence of the backscatter peaks and Compton edges associated with both the 472 keV and the 874 keV γ-rays. These are probably due to scatter of γ-rays between these two detectors.

4.4.3 ^{137}La

Having looked at β^- decay, the second test case considered the β^+/EC decay of ^{137}La to ^{137}Ba. Figure 4.10 shows the spectrum detected in the CsI(Tl) crystal. The main peak is at 37 keV, and this is almost certainly due to K_β (M and above shells to the K shell) X-rays. The peak at 31 keV is probably due to K_α (L to K shell) X-rays. The remaining peak at 4 keV is probably due to X-rays from the L shell. Auger electrons are not very common for this isotope and may not be present at all in the spectrum. The lack of any continuum suggests that these decays are mainly electron capture and not β^+, which is as expected from the decay database. The modelled spectrum is fairly consistent with the decay scheme (also shown in fig 4.10).

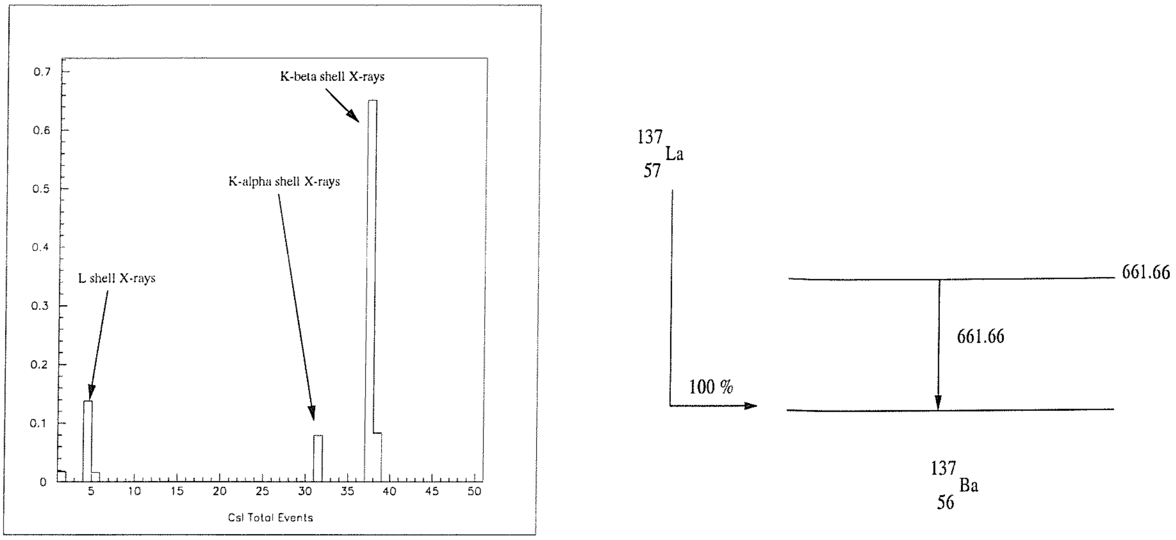

Figure 4.10: *Spectrum detected in the CsI(Tl) crystal for the decay of a* ^{137}*La source (no energy resolution has been applied). On the right, the decay scheme is shown.*

4.4.4 ^{137}Cs

The third decay modelled was the β^- decay of ^{137}Cs to ^{137}Ba. At first glance the spectrum modelled in the CsI(Tl) detector is rather unusual (fig 4.11).

The shape however can be explained in terms of the simultaneous emission of the β^- particle and a γ-ray. The total spectrum is clearly not just a β spectrum. The multiple site spectrum, though not perfect, is recognisable as a β spectrum. The single site spectrum resembles the total one. The single site spectrum is calculated from all those events whose energy was deposited solely within the CsI(Tl) detector. The multiple site spectrum is the spectrum observed in the CsI(Tl) detector from those events that interact in at least one other detector. The multiple site spectrum is composed of events where the β^- particle is largely contained within the CsI(Tl), but the γ-ray (or most of its energy) escapes. For the single site spectrum both the β^- particle and γ-ray (or a large fraction of the γ-ray energy) are contained within the CsI(Tl). Above 662 keV there are great number of events that are β^- plus γ-ray within the single site spectrum, and these distort the shape of the total spectrum.

In the NaI spectrum (fig 4.12) there are clear peaks at ~30 keV, ~180 keV, ~480 keV, ~632 keV,

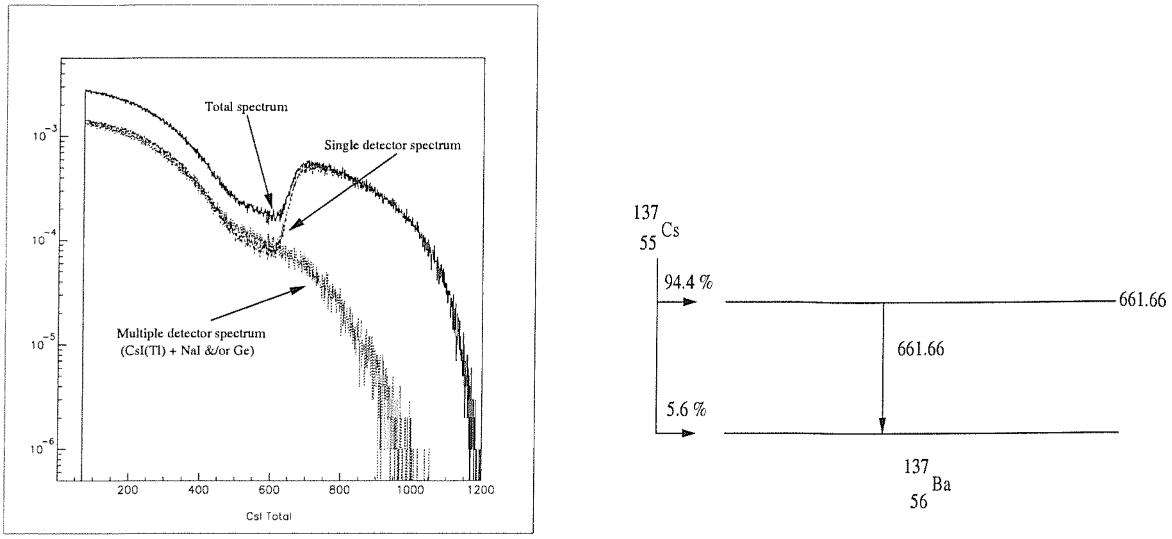

Figure 4.11: *Spectrum detected in the CsI(Tl) crystal for the decay of a* ^{137}*Cs source (no energy resolution has been applied). The decay scheme for* ^{137}*Cs is shown on the right.*

662 keV and ~692 keV. The 30 keV line is undoubtedly due to K shell X-rays. The backscatter peak of the 662 keV γ-rays would be at 184 keV, and this is clearly visible, as is the end of the Compton continuum at 477 keV. The dominant feature of the whole spectrum, as expected, is the 662 keV photopeak, however there is a possible feature at 632 keV. This could be due to a 662 keV γ-ray minus the K shell X-ray. This would be unlikely to occur in high numbers, but is nevertheless a possibility. There is also some evidence of the β continuum above 662 keV. The germanium spectrum (fig 4.13) is similar to the NaI spectrum. The K shell X-rays are visible, as are the backscatter and Compton continuum features. Between the end of the Compton continuum and the photopeak there are some events and these are most likely to be multiple scatters. The photopeak is, as expected, very dominant, however there is not much in the way of a continuum after it, which is probably explained by the reduced stopping power and smaller active area of the Ge detector.

4.4.5 ^{201}Fr

The last decay considered was the α decay of ^{201}Fr to ^{197}At. Figure 4.14 shows the spectrum as modelled in the CsI(Tl) detector from the decay of ^{201}Fr. There is only one peak and that is at

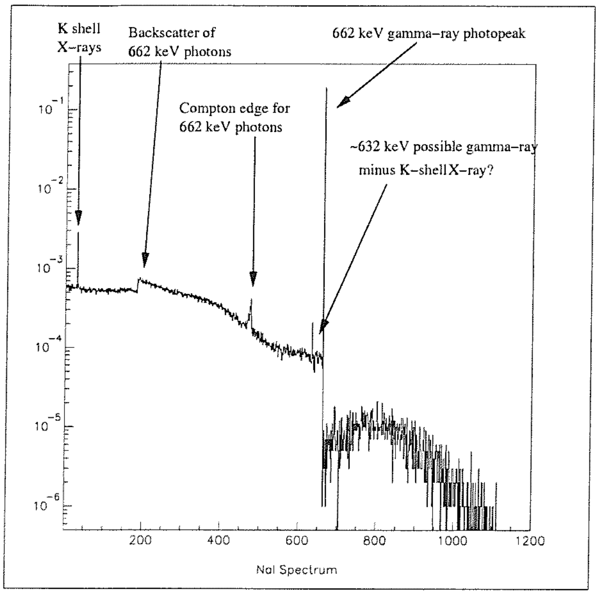

Figure 4.12: *Spectrum detected in the NaI crystal for the decay of a* ^{137}*Cs source (no energy resolution has been applied).*

7388 keV. From Firestone et al. (1996) it is predicted that the α particle should have an energy of 7388 keV, which is in exact agreement with the simulations. All of the α particle energy is deposited within the CsI(Tl) crystal because the range of an α particle is very much smaller than the crystal size (range of an 8 MeV α in silicon is <20 μm (Knoll 1989)).

4.4.6 Conclusions of preliminary tests

Four isotopes have been used to test the ability of the DECAY code. The spectra produced by the radio-isotopes within the three detectors have been compared with expectations, and have been found to agree reasonably well. It has been shown that the ORIHET and DECAY codes can generate, to reasonable accuracy, the correct isotopes, with their proper decay rates, and can then simulate these isotopes accurately. For GGOD to be validated it would also be necessary to test GEANT and GCALOR. This is outside the scope of this thesis, though the next three sections present tests of the whole GGOD package, which will effectively provide some validation of GEANT and GCALOR.

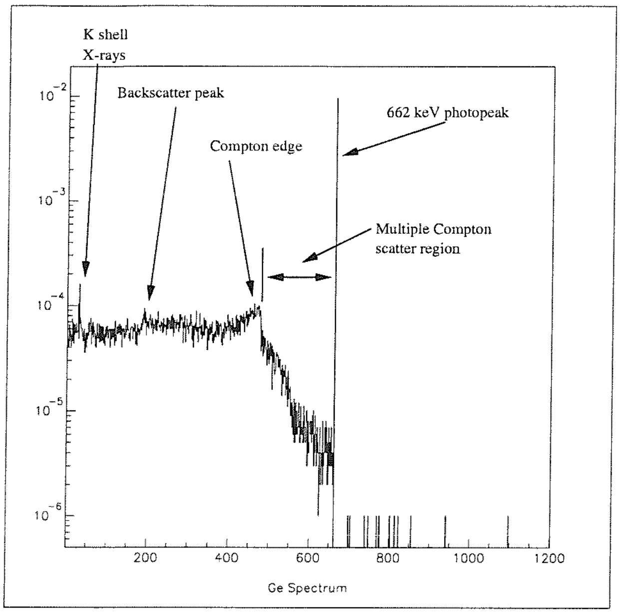

Figure 4.13: *Spectrum detected in the Ge crystal for the decay of a* ^{137}Cs *source (no resolution has been applied).*

4.5 Simulations of beam test data

4.5.1 Introduction

The first comparison of GGOD to real data involved modelling the delayed effects of proton bombardment on a CsI(Tl) crystal. Lei et al. (1993) used a proton beam based at the SATURNE National Laboratory in Saclay to bombard 1 cm^3 CsI(Tl) crystals with 0.2 and 1 GeV protons. After proton bombardment the crystal was placed into the well of a NaI cylindrical veto detector. Onto the aperture of the NaI crystal a Ge veto detector was placed (fig 4.15). This setup allowed the measurement of the internal radiation of the crystal, plus the coincident external events. By removing the external coincident events one is left with a spectrum of events that happen completely within the CsI(Tl) crystal. This spectrum was measured at various intervals after the end of irradiation of the crystal and thus decay rates and spectral evolution could be investigated. This experiment was originally carried out to assess the internal background of CsI(Tl) crystals, with particular reference to the INTEGRAL mission. Therefore, it is of increased relevance to the INTEGRAL mission to be able

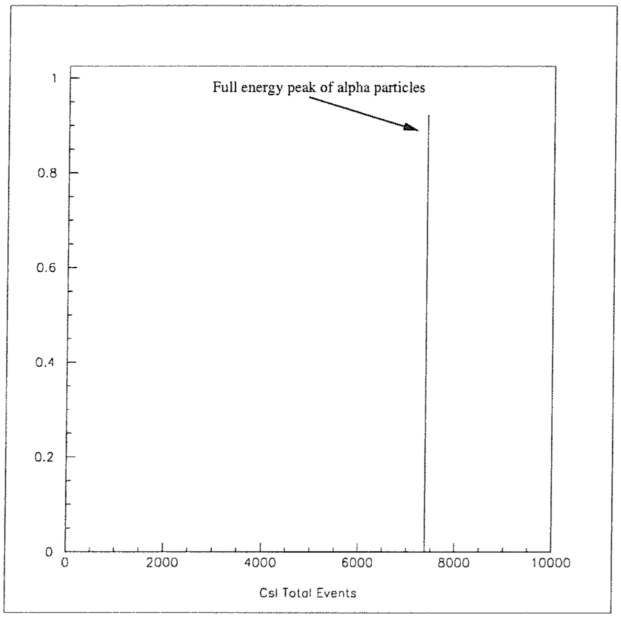

Figure 4.14: *Spectrum detected in the Ge crystal for the decay of a* ^{201}*Fr source (no energy resolution has been applied).*

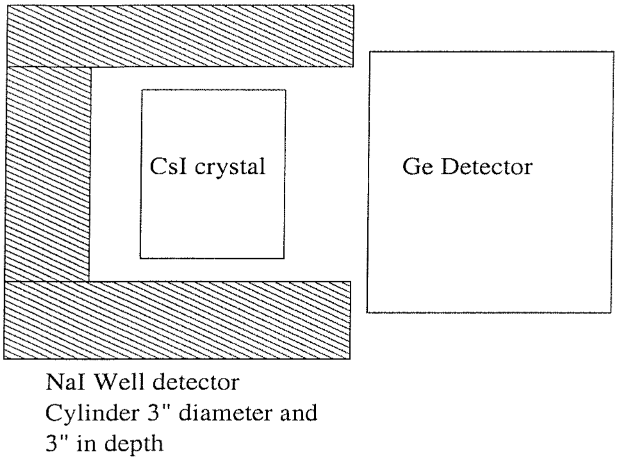

Figure 4.15: *Set up of the SATURNE apparatus.*

to model these results in order to achieve a better understanding of the future background. This experiment was primarily concerned with measuring the relative strengths of γ-ray lines to allow isotope identification. No effort was made to optimise the detectors or electronics to record the events in absolute terms. It should therefore be noted that some discrepancies between the real and modelled data may arise due to this lack of optimisation.

The first step in modelling this situation was to run a simulation of the proton bombardment to calculate the isotopes produced, and their rates of production, using GEANT/GCALOR. From this the decay rates at a period of time after the end of irradiation were calculated using ORIHET. These decay rates were then put into a second simulation to create the final spectrum. To produce a more realistic spectrum, for the purpose of comparison, both energy resolution and low energy thresholds were applied to the simulated data. The energy resolution of the CsI(Tl) crystal used is given in equation 4.8 (Bird, private communication). Lei et al. (1993) gave the low-energy thresholds of all three detector crystals as 70 keV.

$$FWHM(\%) = 2891 \times \text{Energy(keV)}^{-0.9031} \tag{4.8}$$

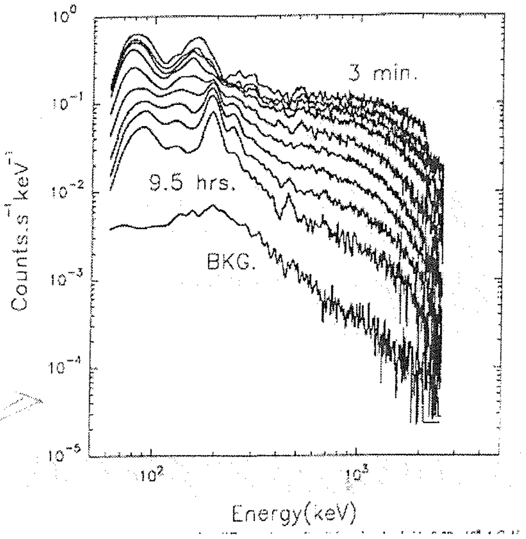

Figure 4.16: *The CsI(Tl) detector spectra as measured at different times after it has been bombarded by 2.02×*10^8 *1 GeV protons. Also shown in the figure is the background spectrum measured with the crystal before the bombardment (Lei et al. 1993).*

4.5.2 Results

Figure 4.16 shows the measured spectral evolution with time after irradiation. The spectral evolution given by the simulations (fig 4.17) shows broad agreement. Below 100 keV the real data are probably slightly unreliable, as the results are strongly influenced by the electronics of the CsI(Tl) detector, and so this part of the spectrum is largely ignored from now on. In the real data, the first feature at $\sim$ 170 keV, probably corresponds to the modelled peak at $\sim$ 130 keV. A further point of reasonable agreement is the peak at $\sim$ 300 keV. There is also a suggestion of further peaks (i.e. at $\sim$ 500 keV) as well, which agree nicely with the early spectra. Moving to later times, both the fall in activity of the source and the steepening of the spectra from $\sim$ 200 – 500 keV, are reproduced by the simulations. There does however appear to be a slight overabundance of $\sim$ 120 keV photons in the simulation results, though the $\sim$ 200 keV peak appears prominently in both the simulated and real results. There is evidence in both the real and simulated data of a faint peak at $\sim$ 220 – 250 in the very late time spectra. An area of slight disappointment is the apparent factor of 2 - 5 difference in the overall normalisation of the real and simulated spectra. Dead time effects in the real experiment, which are not included within the simulations, could explain this discrepancy.

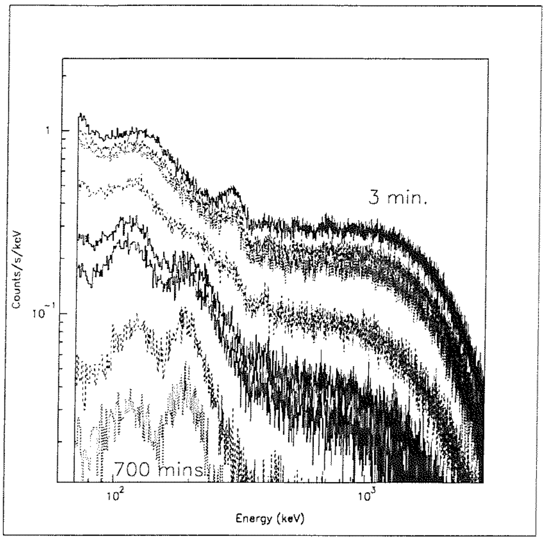

Figure 4.17: *The CsI(Tl) detector spectra, at different times after 1 GeV proton bombardment, as modelled by GGOD.*

A plot of the count rate (in the energy range 400 keV to 2.5 MeV) against the time after irradiation (fig 4.18) shows a clearly exponential shape. These points could be fit with a few simple exponential curves, but this isn't really valid as there are many isotopes with different half-lives producing this result. In comparison with the results of Lei et al. (1993) there are some differences (fig 4.19). To the real data two lines have been fit with half-lives of 17 minutes and 1.3 hours, whereas the simulations have been fit by two lines with 8 minutes and 3.5 hour half-lives. Since these curves are due to many isotopes a difference is not unexpected. Lei et al. (1993) would have obtained spectra over a period of $\sim$ 100 seconds, whereas the model results have the equivalent of 1000 seconds worth of flux under them. This gives the simulations about a factor of 3 less statistical variance, and possibly this could make the resultant comparison less agreeable. Since there is no scientific basis for the lines fit to these curves, this discrepancy is not dwelt upon too much.

A further quantity that was calculated, and compared, was the single to multiple site event ratio. For this Lei et al. (1993) fired a beam of 0.2 GeV protons at a 1 cm^3 CsI(Tl) crystal. Spectra were then measured between 370 and 4600 seconds after the end of irradiation. From these the ratio of single to multiple site events was calculated, and then all the individual spectra were summed to give the final spectra shown in figure 4.20.

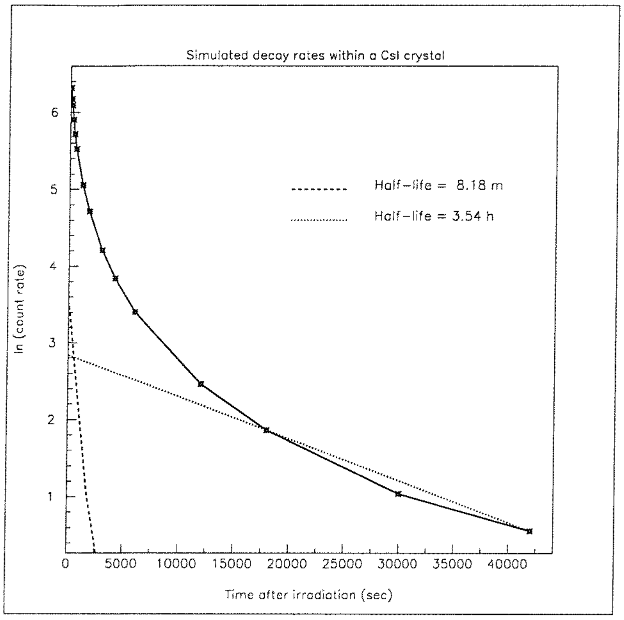

Figure 4.18: *Plot of the modelled count rates (between 400 keV and 2.5 MeV) against the time after irradiation.*

The modelled results (fig 4.21) were generated by bombarding a crystal with 0.2 GeV protons, then measuring the spectrum at various intervals after the end of irradiation (between 300 and 5000 seconds), and then adding up the individual spectra. The real data (fig 4.20) and the simulated data (fig 4.21) show reasonable agreement. The multiple site spectrum in the model seems to be higher than that suggested by the real data, but other than this the general shape and features are reasonably well reproduced, except for the break at $\sim$ 2 MeV. In all simulations this feature has proved unreproducable and may be an instrumental effect. It is possible that jitter in the electronics of the real experiment has altered the numbers of multiple and single site events recorded.

Table 4.3 shows the real and the modelled single to multiple ratio. Clearly the absolute values of the single to multiple ratios are different, and this is a cause for concern, however the abscence of any trend with time after irradiation is repeated in the modelled results. It is this fact that allowed summation of the individual spectra to form figs 4.20 and 4.21.

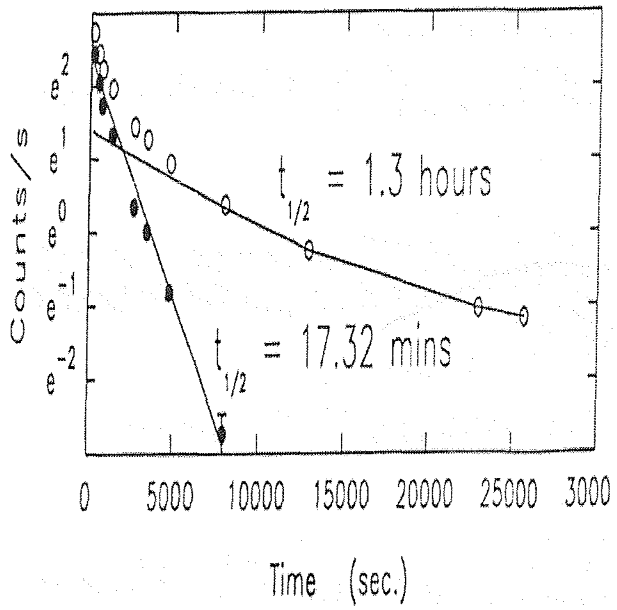

Figure 4.19: *The count rates (o) between 400 keV and 2.5 MeV of the CsI(Tl) crystal measured after proton irradiation. Its decay can be reasonably fitted by two exponential components with half-lives of 17.32 minutes and 1.3 hours (Lei et al. 1993).*

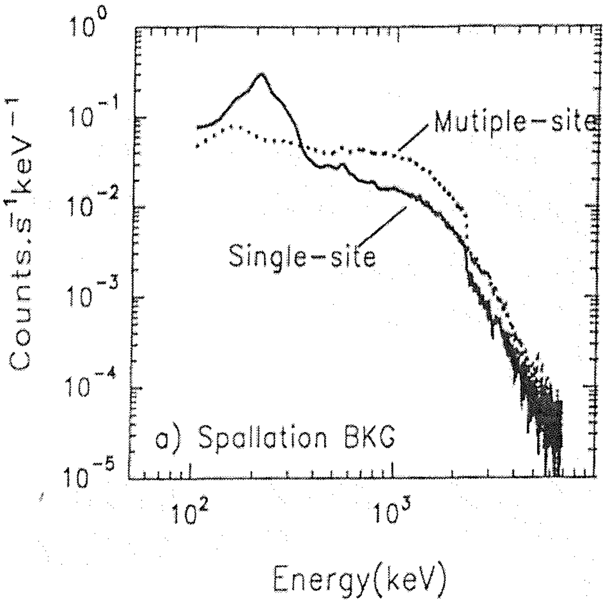

Figure 4.20: *The single site and multiple site event spectra in the CsI(Tl) crystal. This spectrum is for crystal 11, which was exposed to 0.2 GeV protons for 27 minutes and 19 seconds.*

Modelled		Real	
Time (secs)	S/M ratio	Time (secs)	S/M ratio
300	0.203	370	0.46
500	0.201	450	0.48
700	0.203	660	0.44
1000	0.206	950	0.5
1500	0.198	1290	0.47
2000	0.198	1620	0.45
3000	0.192	1960	0.37
4000	0.195	3500	0.38
5000	0.184	4200	0.45
		4600	0.52

Table 4.3: *Comparison of the modelled single to multiple ratio (S/M) and the real S/M ratio determined by Lei et al. (1993). Both results calculated for the case of a CsI crystal bombarded with 0.2 GeV protons.*

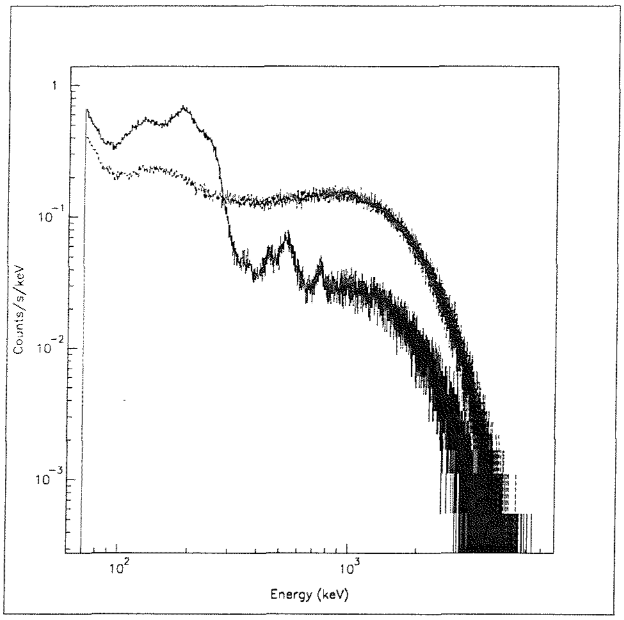

Figure 4.21: *Comparison of modelled multiple and single site events for a CsI(Tl) crystal bombarded with 0.2 GeV protons (single site - solid line; multiple site - dashed line).*

4.5.3 Conclusions

In this sub-section real data and simulations have been compared to validate the GGOD approach. The spectral evolution, with time after irradiation, has been modelled with reasonable accuracy. The features present within the real data have been reproduced by the simulations, and the evolutionary trends are also visible and comparable to the real data. The normalisation between the real and modelled results (a factor 2 - 5) is disappointing but not too bad a result. It appears that the simulated detector is more efficient than the real one, which is to be expected. Throughout the real spectra presented there is a break at ~2 - 3 MeV, which has not been reproduced in any of the simulated data. This is probably an instrumental effect, perhaps caused by the dynamic range of the electronics. There are differences in the decay rate curve, with the two different sets of curves fitted making this clear, and in the absolute value of the single to multiple site ratio. The general exponential shape of the decay rate curve is reproduced, as is the lack of trend in the single to multiple site ratio with time. The single and multiple site spectra have been modelled accurately as well. The single to multiple ratio could be affected by the gate time on the veto crystals in the real data. When an event is detected within the CsI(Tl) crystal, the electronics have to wait until a threshold is passed before it can trigger the readout of the veto crystals. Any potential drift between reaching the threshold in the CsI(Tl) crystal and reading out the veto crystal could cause events to be missed. Small problems here could affect greatly the number of multiple site events recorded. It should further be noted however, that the continuum of the multiple site events looks higher than the real data, and perhaps there could also be some over simulation of these events.

Despite small differences, many of the trends and features of the real data have been reproduced quite well, and the GGOD suite seems to model the SATURNE beam tests reasonably accurately. When conducting the real experiment it was not envisaged that a comparison of this type would ever take place, and so no effort was made to facilitate such a comparison. This limits the possible agreement that one could ever have expected to obtain between the simulations and the real data. When judging the success or failure of the simulations one has to bear in mind the following sources of error:

- Inaccuracies in the knowledge of the real proton flux
- Effects of Dead time in the experiment

- Lack of optimisation of experiment to record events in absolute terms (electronic jitter)
- Incorrect or imperfect cross-sections within GCALOR

Considering these limitations, and bearing in mind that many of the differences between the real and simulated results can, at least partly, be explained by the lack of optimisation of the experiment, it is likely that the current agreement is as close as could reasonably be expected.

4.6 Modelling the background within the HEAO-1 A4 instrument

The second test of GGOD involved applying it to the space environment in an attempt to reproduce the background seen in the HEAO-1 observatory.

4.6.1 Introduction

The High Energy Astrophysical Observatories (HEAO) were a series of 3 spacecraft launched at the end of the 1970's, and into the early 1980's, to investigate the X/γ-ray sky. The first of the series HEAO-1 carried four instruments on board. The fourth instrument, The Hard X-ray and Low Energy Gamma-Ray Experiment (A4), built by UCSD and MIT, consisted of one High Energy Detector (HED), four Medium Energy Detectors (MED) and two Low Energy Detectors (LED). These gave the total instrument an energy range of 10 keV to 10 MeV. The detectors were phoswich-type detectors made of NaI(Tl) and CsI(Na), and there were also large veto shields made of CsI(Na). These simulations are focused on one part of the A4 instrument - the High Energy Detector.

HEAO-1 was launched into a near circular low Earth orbit (apogee $\sim$ 450 km), with inclination 22.75°. The spacecraft was about 9 m long and about 3.6 m in diameter (Matteson et al. 1978).

4.6.2 Method

The model of HEAO-1 was constructed crudely inside the GGOD simulation code. The construction was based on Matteson et al. (1978) and it follows closely figure 4.22. The HEAO-1 spacecraft was modelled as a hexagonal annulus, 20 cm thick, made of Al and with a length of 9 m and diameter 3.6 m. The outer and inner veto shields are approximated as a single hexagonal prism of CsI(Na), with thickness and radius of ~35 cm. The aperture shield is approximated with a plastic sheet, hexagonal in shape, about 1 cm thick and 35 cm in radius. The main volume of interest, the High Energy Detector, was simulated with two cylinders, one of CsI(Na) (6.2 cm radius and 10 cm thick) corresponding to the veto and the other of NaI(Tl) (6.2 cm radius and 7.5 cm thick) representing the HED crystal. The other detectors, Low and Medium energy, were also represented in a similar way. As can be seen, this is a very crude model, and this will obviously effect the results.

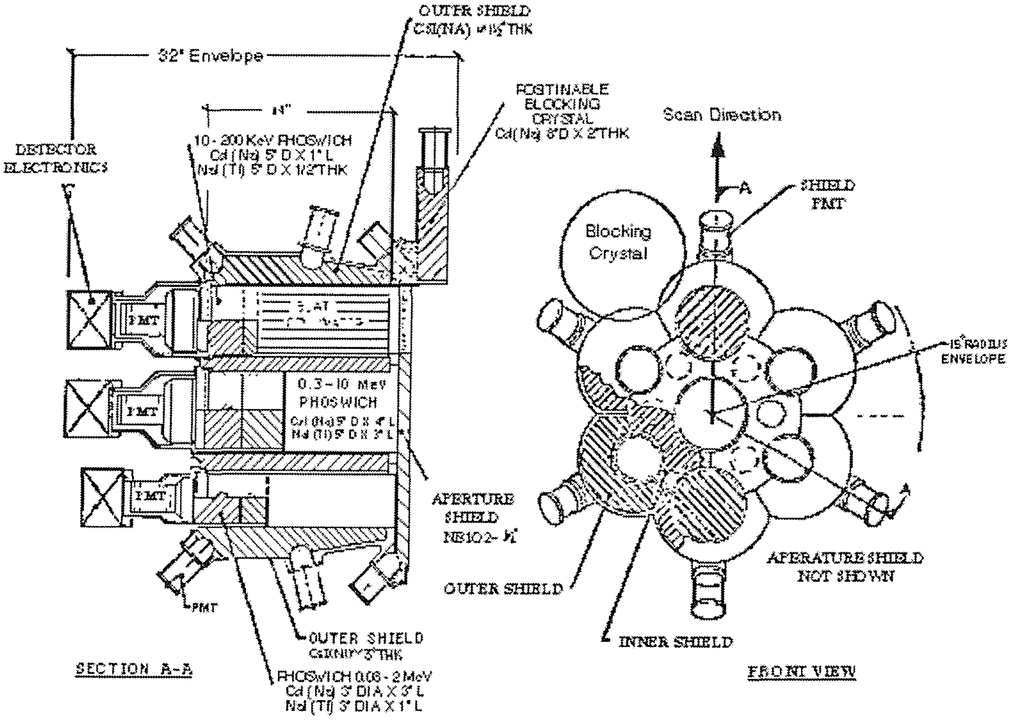

Figure 4.22: *The Hard X-ray and Low Energy Gamma-Ray Experiment (Matteson et al. 1978).*

The background was simulated using five distinct components: cosmic diffuse γ-rays, atmospheric γ-rays, neutrons, cosmic rays and the decay of any induced radioactive isotopes produced by particle bombardment.

Once the spectra for all the various components had been generated they were summed to give the total veto-on and veto-off spectra. These were compared with the anti-coincidence curve given in figure 8 of Matteson et al. (1978) and the sum of both anti-coincidence and coincidence curves respectively.

Cosmic Diffuse Gamma-rays (CDG)

Though the Earth occults some of the CDG flux, they were simulated as 4π in extent, due to the rotation of HEAO-1. The overall flux modelled was half that expected, for 4π illumination, due to the presence of the Earth. The spectral form of the diffuse γ-rays was taken from Dean, Lei and Knight (1991) and is given by equation 4.9.

$$N(E_\gamma) = 87.4E^{-2.3} \quad \text{photon cm}^{-2}\text{s}^{-1}\text{keV}^{-1}\text{sr}^{-1} \tag{4.9}$$

This was integrated over the energy range 100 keV to 20 MeV, giving an omni-directional photon flux of ~0.25 photons $\text{cm}^{-2}\text{s}^{-1}$.

Atmospheric Gamma-rays

The atmospheric γ-ray spectrum was determined from figure 5 of Imhof et al. (1976). The equator line was used to determine the flux and this was then normalised to account for the reduced rigidity of the HEAO-1 orbit. The spectral form is given in equation 4.10.

$$N(E_\gamma) = 0.6E^{-1.39} \quad \text{photon cm}^{-2}\text{s}^{-1}\text{keV}^{-1}\text{sr}^{-1} \tag{4.10}$$

After integration of the energy range 300 keV to 50 MeV, and normalisation, this gave a flux of 0.32 photons $\text{cm}^{-2}\text{s}^{-1}$. The normalisation factor used to account for the rigidity was 1.4, and was determined by dividing the approximate values of F given in figure 3 of Dean, Lei and Knight (1991) at the rigidities of 10 GV and 15 GV. This was effectively omni-directional flux because HEAO-1 spins on its axis.

Neutrons

Though neutrons come mainly from the atmosphere, they can however be regarded as all-sky because HEAO-1 spins on its axis. The spectrum of the neutrons was worked out from figure 1 of Armstrong et al. (1973) with an assumed depth of 0 g cm^{-2}. Two power laws were used to approximate the curve, an up slope one (Eq 4.11) and a down slope one (Eq 4.12). The spectra were calculated, integrated over the appropriate energy and then the flux was normalised to account for the higher rigidity.

$$N(E_{nus}) = 7.95 \times 10^8 E_n^{0.7} \quad \text{neutron cm}^{-2}\text{s}^{-1}\text{MeV}^{-1} \tag{4.11}$$

$$N(E_{nds}) = 0.0357 \times E_n^{-0.7778} \quad \text{neutron cm}^{-2}\text{s}^{-1}\text{MeV}^{-1} \tag{4.12}$$

The up slope neutrons were integrated over the energy range 10^{-8} to 10^{-7} MeV and the down slope neutrons were integrated over the energy range 10^{-7} to 10^{3} MeV. This gave fluxes, assuming a latitude of 42°, which then needed to be modified to give the flux at the latitude of HEAO-1 which was 22°. The lower latitude has a higher rigidity and this resulted in an effective decrease in the neutron flux, due to the reduced bombardment of the atmosphere by cosmic rays.

Cosmic Rays

The cosmic ray flux was worked out from figure 1 in Dean, Lei and Knight (1991). The spectrum was calculated using the hydrogen line, since the other components are of much less significance. The derived spectrum is given in equation 4.13.

$$N(E_p) = 3.23 \times 10^9 E^{-2.7} \quad \text{proton m}^{-2}\text{s}^{-1}\text{sr}^{-1}\text{MeV}^{-1} \tag{4.13}$$

This was integrated over the energy range of 11 GeV to 10^3 GeV. This component takes the longest computer time to simulate, and to simulate the South Atlantic Anomaly (SAA) passages would have required a substantial amount of computer time, therefore the spectra were simulated for ~10 hours after SAA passage.

Decay of induced radioactive isotopes

The radioactive isotopes created by the particle bombardment of HEAO-1 were treated as usual with GGOD.

4.6.3 Results

Figure 4.23 shows the total veto off and veto on spectra, with their components, and the appropriate Matteson et al. (1978) curves. In the veto off case the cosmic rays dominate above 600 keV, whereas in the veto on case induced radioactivity is the dominant component.

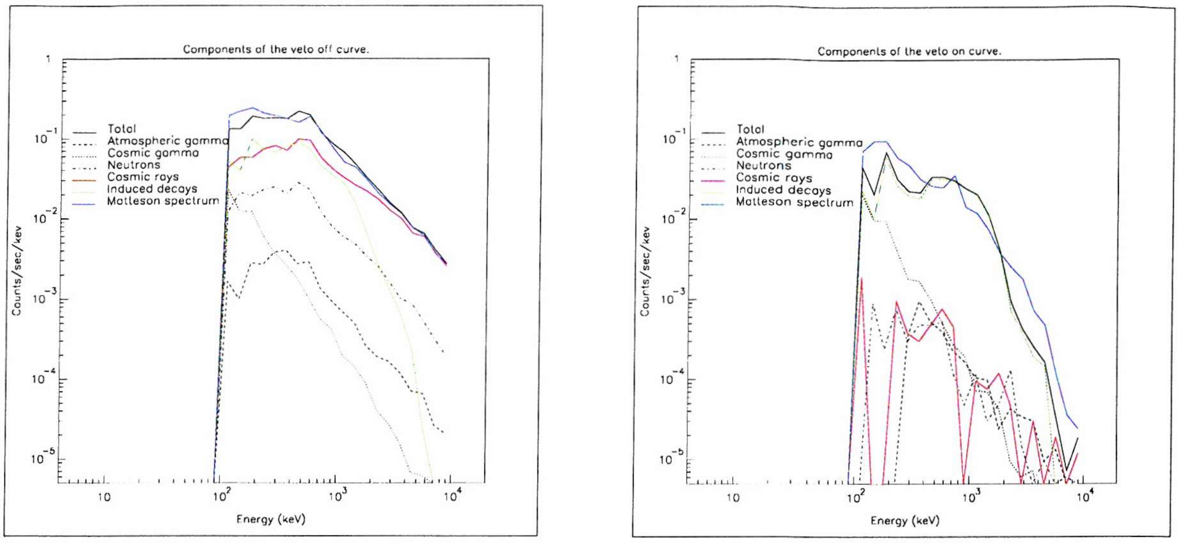

Figure 4.23: *Veto off spectrum (left) and the veto on spectrum (right).*

The simulated and real veto off spectra are similar above about 400 keV, though below this there is some difference. In the case of the veto on curves, there is much more difference, which could be due to the South Atlantic Anomaly passages or the crudeness of the modelled veto set-up. The veto is modelled as a simple block, but in reality is made up of inner and outer blocks, which may have some effect. Though effects in the model could cause discrepancies, it is important to bear in mind that the real instrument may not be perfect. Effects such as drift of the low-energy threshold on the veto, blinding of the veto, or even drift in the the co-incidence timing of the veto electronics, could all effect the veto on curves and produce the observed discrepancies. Adding in the low energy (100 - 300 keV) components of the atmospheric γ-rays would better simulate the veto off spectrum.

4.6.4 Conclusion

Considering the very approximate nature of the model, the simulations provide a reasonable agreement to the measured data. With improvements in the model of HEAO-1 used, and in the knowledge of HEAO-1's performance in space, it should be possible to improve the final result and match the predicted curves of Matteson et al. (1978) more closely. Taking into account the limitations of this simple set-up the results show that GGOD works to a reasonable degree of accuracy.

4.7 Modelling the background in the GRIS balloon spectrometer

The third, and final, test of GGOD applied the technique to modelling the background within a balloon-borne spectrometer.

4.7.1 Introduction

Background reduction techniques, and hence sensitivity improvement, are continually being investigated for γ-ray spectrometers. One of the suggested techniques to reduce the background generated in germanium detectors is to reduce the number of isotopes present in the actual germanium crystals. The balloon spectrometer GRIS (Gamma Ray Imaging Spectrometer) consists of a series of high-purity germanium detectors surrounded by thick NaI(Tl) veto shields (15 cm minimum path length). GRIS was built by the Goddard Space Flight Centre (GSFC) and flown several times with the aim of obtaining spectra of astronomical sources. In this sub-section modelling of the October 1996 flight from Alice Springs is presented. In this particular flight six of the seven germanium detectors were made from standard germanium (20.5% ^{70}Ge, 27.4% ^{72}Ge, 7.8% ^{73}Ge, 36.5% ^{74}Ge, and 7.8% ^{76}Ge), and one (Detector 6) was made from enriched germanium ($>$ 97% ^{70}Ge, $\sim$ 3% ^{72}Ge). Though GRIS can operate in both open and closed modes only the open mode has been modelled here. In the closed mode a NaI crystal, the blocking crystal, is placed across the aperture to close it, and in the open mode this crystal is swung out of the way making the aperture fully open. The open configuration was designed for astronomical measurements, while the closed configuration was designed for measuring the instrumental background radiation. In principle if one could accurately determine the internal background radiation, then this could be subtracted from the observations, improving the astronomical results of the spectrometer.

Modelling the background accurately within the GRIS detectors, and evaluating the difference between normal and enriched germanium crystals, is important for future spectrometers. The very high resolution of germanium detectors makes them excellent spectrometers, and for future missions the sensitivity possible could be increased greatly by detailed knowledge of the background

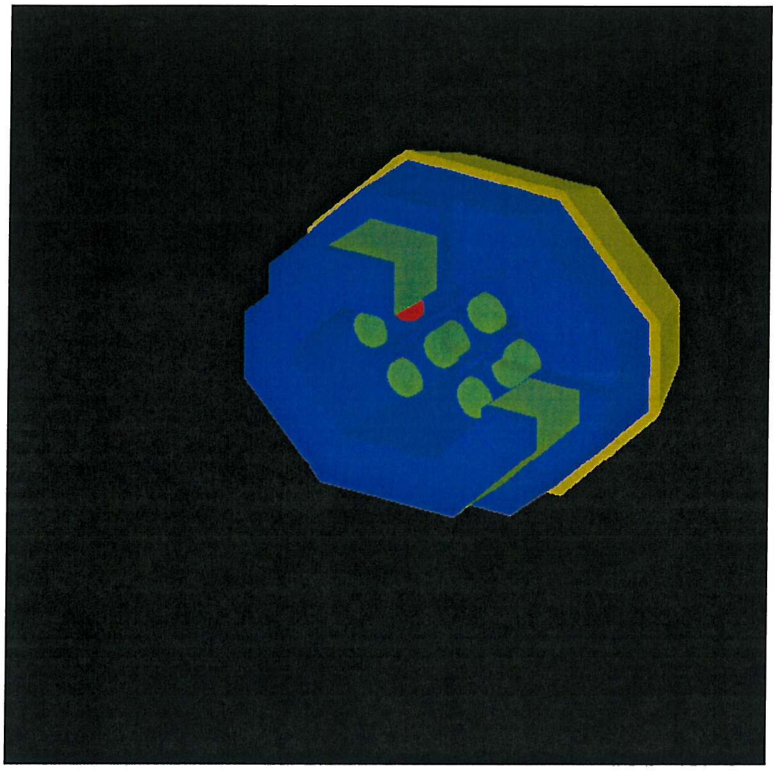

Figure 4.24: *A cut away view of the GRIS payload. The green, blue and yellow hexagonal rings around the sides and back are the NaI veto shields. In the centre are the detectors themselves, the green ones are natural Ge and the pink one is the enriched Ge.*

within these detectors. Modelling GRIS offers an opportunity to enhance understanding of the background in germanium detectors, and to compare the backgrounds obtained with natural and enriched germanium crystals. Modelling the background in germanium is of considerable importance to INTEGRAL, and the SPI instrument in particular.

4.7.2 Method

The mass model of the GRIS balloon used in this work was kindly supplied by Juan Naya of NASA GSFC. Locally this was incorporated into the GGOD software suite. The situation simulated was the open mode, at the latitude of Alice Springs and a depth of 5 $\mathrm{g\,cm^{-2}}$.

In modelling GRIS six components were taken into account to generate the background. These are briefly listed below and then described in more detail.

- Cosmic rays
- Atmospheric neutrons
- Atmospheric γ-rays
- Shield leakage
- Atmospheric protons
- Induced radioactive decays

Cosmic rays

As mentioned in chapter 3 these are highly energetic particles, mainly protons, which bombard the atmosphere. In the atmosphere cosmic rays only travel downwards, and so practically in the simulations, these only hit GRIS from the top and sides. The spectral form used for the cosmic rays is given in equations 4.14 and 4.15.

$$f_{10^4-3\times10^4\ MeV} = 1.3 \times 10^3 E^{-2} \quad \mathrm{pr\,cm^{-2}\,s^{-1}\,MeV^{-1}} \tag{4.14}$$

$$f_{>3\times10^4\ MeV} = 1.8 \times 10^6 E^{-2.7} \quad \mathrm{pr\,cm^{-2}\,s^{-1}\,MeV^{-1}} \tag{4.15}$$

After integration over the appropriate energy ranges, equations 4.14 and 4.15 give the following fluxes.

$$f_{10^4-3\times10^4\ MeV} = 0.15431 \quad \mathrm{pr\,cm^{-2}\,s^{-1}} \tag{4.16}$$

$$f_{>3\times10^4\ MeV} = 0.0226204 \quad \mathrm{pr\,cm^{-2}\,s^{-1}} \tag{4.17}$$

Neutrons

Using Armstrong et al. (1973) the neutron flux at 5 $\mathrm{g\,cm^{-2}}$ was calculated (eq 4.18 & 4.19). This was then normalised from Palestine to Alice Springs (Dean, Lei and Knight 1991) to account for the difference in rigidity.

$$f_{10^{-8}-10^{-7}\,MeV} = 6.55 \times 10^{7} E^{0.477} \quad \mathrm{n\,cm^{-2}\,s^{-1}\,MeV^{-1}} \tag{4.18}$$

$$f_{10^{-7}-10^{3}\,MeV} = 0.0112\,E^{-0.92} \quad \mathrm{n\,cm^{-2}\,s^{-1}\,MeV^{-1}} \tag{4.19}$$

Integration of equations 4.18 and 4.19 gives the following fluxes.

$$f_{10^{-8}-10^{-7}\,MeV} = 1.96 \times 10^{-3} \quad \mathrm{n\,cm^{-2}\,s^{-1}} \tag{4.20}$$

$$f_{10^{-7}-10^{3}\,MeV} = 0.205 \quad \mathrm{n\,cm^{-2}\,s^{-1}} \tag{4.21}$$

The rigidity corrected fluxes are given in equations 4.22 and 4.23.

$$f_{10^{-8}-10^{-7}\,MeV} = 1.568 \times 10^{-3} \quad \mathrm{n\,cm^{-2}\,s^{-1}} \tag{4.22}$$

$$f_{10^{-7}-10^{3}\,MeV} = 0.164 \quad \mathrm{n\,cm^{-2}\,s^{-1}} \tag{4.23}$$

Gamma-rays

Since GRIS is inside the atmosphere the γ-ray component is composed of both atmospheric and cosmic diffuse γ-rays that travel vertically downward. In effect this component contains both aperture photons and shield leakage photons that arrive at the upper surface of GRIS (eq 4.24 and 4.25).

$$f_{2\times10^{-2}-4\times10^{-2}\,\mathrm{MeV}} = 1.2 \times 10^{3} E^{1.28} \quad \mathrm{ph\,cm^{-2}\,sr^{-1}\,s^{-1}\,MeV^{-1}} \tag{4.24}$$

$$f_{4\times10^{-2}-8\,\mathrm{MeV}} = 5.88 \times 10^{-2} E^{-1.75} \quad \mathrm{ph\,cm^{-2}\,sr^{-1}\,s^{-1}\,MeV^{-1}} \tag{4.25}$$

After integration the fluxes are:

$$f_{2\times10^{-2}-4\times10^{-2}\ \mathrm{MeV}} = 0.272 \quad \mathrm{ph\,cm^{-2}\,sr^{-1}\,s^{-1}} \tag{4.26}$$

$$f_{4\times10^{-2}-8\ \mathrm{MeV}} = 0.86 \quad \mathrm{ph\,cm^{-2}\,sr^{-1}\,s^{-1}} \tag{4.27}$$

If one assumes that the cosmic γ-ray component is not significant, then a correction for rigidity must be applied. This accounts for the fact that atmospheric γ-rays are produced by cosmic rays. The corrected fluxes are given in equations 4.28 and 4.29.

$$f_{2\times10^{-2}-4\times10^{-2}\ \mathrm{MeV}} = 0.2176 \quad \mathrm{ph\,cm^{-2}\,sr^{-1}\,s^{-1}} \tag{4.28}$$

$$f_{4\times10^{-2}-8\ \mathrm{MeV}} = 0.688 \quad \mathrm{ph\,cm^{-2}\,sr^{-1}\,s^{-1}} \tag{4.29}$$

Shield leakage

Having already dealt with the γ-rays from above, the shield leakage component is now defined to be those γ-rays that hit GRIS from the sides and bottom. A small number of these γ-rays will penetrate the shielding without raising a veto signal, and will thus be detected as background. Following the work of Gehrels (1985) equations 4.30 to 4.32 were used to model the shield leakage.

$$f_{65^\circ-95^\circ} = 0.094\,E^{-1.61} \tag{4.30}$$

$$f_{95^\circ-130^\circ} = 0.150\,E^{-1.47} \tag{4.31}$$

$$f_{130^\circ-180^\circ} = 0.047\,E^{-1.45} \tag{4.32}$$

The average equation for the shield leakage is $0.097\,E^{-1.51}$ $\mathrm{ph\,cm^{-2}\,sr^{-1}\,s^{-1}\,MeV^{-1}}$ (10 keV to 10 MeV). This was used in the modelling for convenience, and the flux given by integration is 1.9328 $\mathrm{ph\,cm^{-2}\,sr^{-1}\,s^{-1}}$. This was modelled over the side and bottom of the input cylinder only. The γ-rays are locally produced by particle interactions and therefore a correction for rigidity is needed. This gives a flux of 1.54624 $\mathrm{ph\,cm^{-2}\,sr^{-1}\,s^{-1}}$. When this was carried out it was found that the spectra were statistically very poor at high energies (> 1 MeV). Variance reduction was therefore used to try to counter this problem. Simply, the spectrum was split into two parts, 10 keV - 1 MeV and 1 MeV - 10 MeV, and these were simulated separately. The low-energy part was run for an equivalent of 100 seconds, and the high-energy part was run for an equivalent of 1000 seconds. These two runs were then analysed to produce spectra in Counts $\mathrm{s^{-1}\,keV^{-1}}$, which were then added to form the final shield leakage spectrum. In this way 17 million photons were used in the simulation, as opposed to the 107 million that would have been needed, thus cutting down dramatically the overall simulation time.

Atmospheric protons

From Gehrels (1985) and McDonald & Webber (1959), taking initial spectra for 41° and depth 35 $\mathrm{g\,cm^{-2}}$, I have extrapolated to 34° and 5 $\mathrm{g\,cm^{-2}}$. The resultant spectra are given in equations 4.33 to 4.36.

$$f_{5-16\ \mathrm{MeV}} = 1.475 \times 10^{6} E^{2} \quad \mathrm{pr\,cm^{-2}\,s^{-1}\,MeV^{-1}} \tag{4.33}$$

$$f_{16-100\ \mathrm{MeV}} = 3.78 \times 10^{-4} \quad \mathrm{pr\,cm^{-2}\,s^{-1}\,MeV^{-1}} \tag{4.34}$$

$$f_{100-300\ \mathrm{MeV}} = 6.43 \times 10^{-3} E^{-0.61} \quad \mathrm{pr\,cm^{-2}\,s^{-1}\,MeV^{-1}} \tag{4.35}$$

$$f_{300-6600\ \mathrm{MeV}} = 1.78 E^{-1.6} \quad \mathrm{pr\,cm^{-2}\,s^{-1}\,MeV^{-1}} \tag{4.36}$$

When integrated the fluxes obtained are:

$$f_{5-16\ \mathrm{MeV}} = 0.001954 \quad \mathrm{pr\,cm^{-2}\,s^{-1}} \tag{4.37}$$

$$f_{16-100\ \mathrm{MeV}} = 0.031752 \quad \mathrm{pr\,cm^{-2}\,s^{-1}} \tag{4.38}$$

$$f_{100-300\ \mathrm{MeV}} = 0.0532 \quad \mathrm{pr\,cm^{-2}\,s^{-1}} \tag{4.39}$$

$$f_{300-6600\ \mathrm{MeV}} = 0.081687 \quad \mathrm{pr\,cm^{-2}\,s^{-1}} \tag{4.40}$$

These bombard GRIS from all of the sky and so are simulated over all 4π steradians.

Induced radioactive decay

As expected this will be handled by the GGOD code. The default irradiation time used was 16 hours, though because of the complex nature of this quantity 2, 8, 24, and 32 hour irradiation times were also modelled. This gave a range of spectra as might be recorded at various times throughout the flight.

4.7.3 Results

After simulation of the components, the results were analysed and the spectra generated were added to form the final background spectrum. The shield threshold was set to 80 keV, while the detector thresholds were 20 keV (Naya, private communication). Only single site events (i.e. those that interacted in one, and only one, detector) were accepted as genuine background events.

Figure 4.25 shows the spectrum generated assuming the irradiation time was 16 hours. The background spectrum is heavily dominated by the γ-ray component, and no significant lines are present. Figure 4.26 shows the components of the background. The continuum generated by the γ-rays swamps the radioactively produced lines, though above ~500 keV the spectrum is distorted by the increase in the induced and shield leakage components. Above a few MeV the shield leakage component dominates. The prompt particle components (neutrons and hadrons) are insignificant in the spectrum. The γ-rays are the dominant components (gammas and shield leakage), though the induced decays are important between ~600 keV and ~1.5 MeV. In the model used GRIS has an aperture of $100^\circ \times 75^\circ$, resulting in the background being almost completely due to the γ-ray component, which arrives at the detector plane through the aperture.

The real data recorded by the GRIS balloon payload (fig 4.27) shows much more prominent line features than the simulated spectra. The continuum also seems to sit a factor of 2 to 5 lower than that in the simulated spectra. The background spectrum (fig 4.27) was actually measured during several 1992 flights of GRIS, during which a slightly different observing configuration was used. The aperture of this configuration was only $\sim 17^\circ$, rather than the model aperture of $100^\circ \times 75^\circ$. If the γ-ray component is normalised by the correct factor, then the simulations can still be compared to the real data, though the results will not be very accurate. Figure 4.28 shows the background

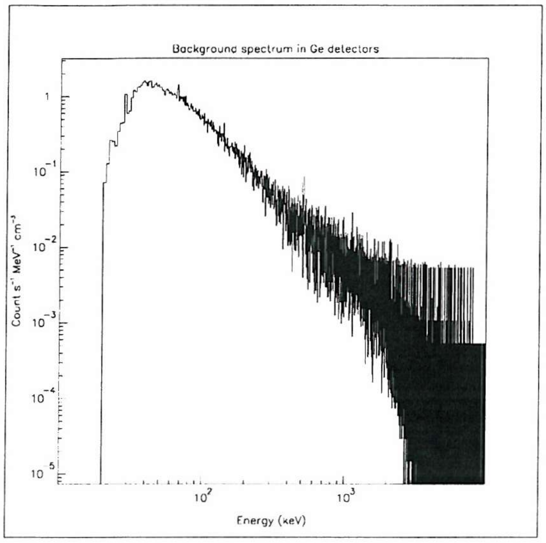

Figure 4.25: *The total background spectrum in the Ge detectors. This has been modelled assuming that the irradiation time was 16 hours. Note that no energy resolution has been applied.*

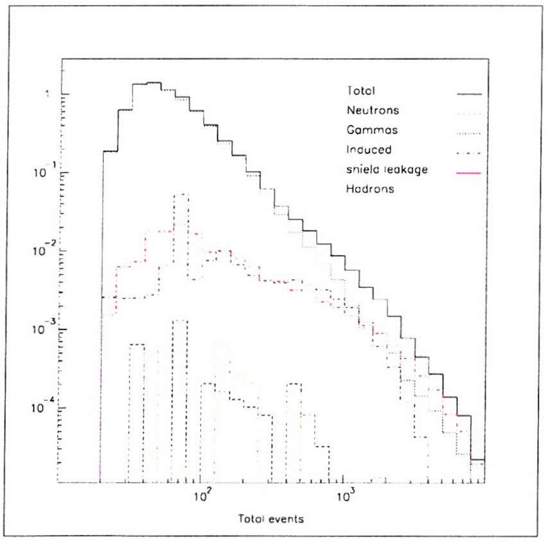

Figure 4.26: *The total background spectrum, and its components, as would be measured in the Ge detectors. This has been modelled assuming that the irradiation time was 16 hours.*

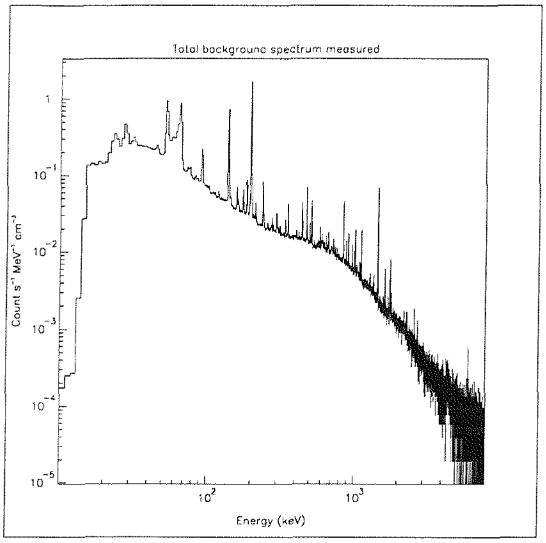

Figure 4.27: *The real background spectrum measured by the Ge detectors in GRIS.*

spectrum generated using the normalised γ-ray component. The area of the aperture in the model is 731.2 cm^2, and the distance between the detectors and this plane is 15.6 cm, therefore the aperture solid angle of the model is 3 steradians. For an aperture of 17°, assuming it to be circular, the solid angle is 0.2936 steradian. To compare the model results and the real data, the γ-ray component has to be divided by 10.2. The normalised spectrum resembles the real data more closely. The normalised simulated spectrum shows many lines, three of which (at ~70, ~100 and ~120 - 130 keV) are seen in the real data. The overall shapes of the two spectra, particularly the bump at ~800 keV, are similar. Above 1 MeV the statisitics in the simulted spectra aren't good enough to allow too much detailed comparison to be made. Though scaling of the γ-ray component was crude, it has brought quite a reasonable agreement between the two spectra. The continuum levels are very similar, and many of the lines are reproduced, though there are some lines missing.

To investigate the difference the irradiation time makes, four more spectra were created with assumed irradiation times of 2, 8, 24 and 32 hours respectively. The γ-ray component in these spectra has been normalised, and the results are plotted in figures 4.29 and 4.30. There are no great differences between the four spectra, though quite a few of the lines change in intensity over time, as would be expected. There is no effect on the continuum level of the spectra, as would be expected since they are composed of many components.

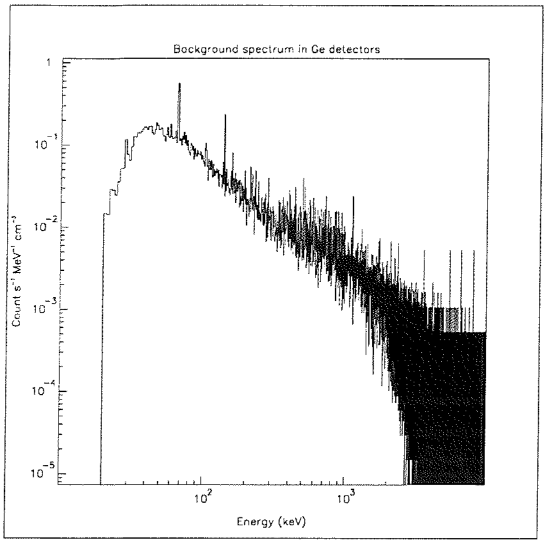

Figure 4.28: *The total background spectrum produced by simulation, with the Gamma component normalised to a* $\sim 17^{\circ}$ *aperture, and assuming a 16 hour irradiation time.*

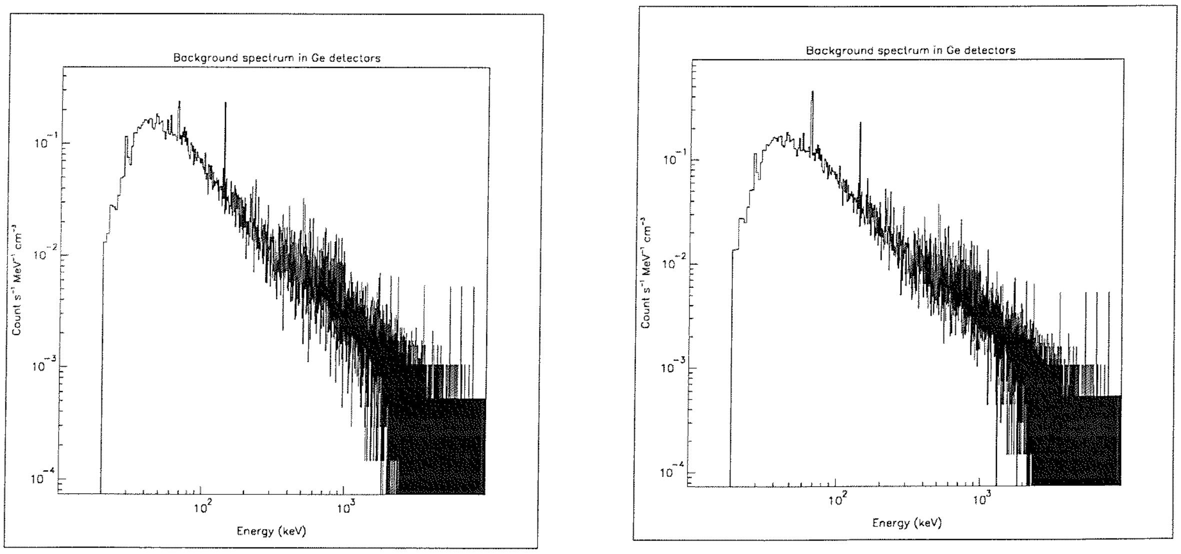

Figure 4.29: *The total background spectrum as modelled in the Ge detectors assuming a 2 hour (left) and an 8 hour (right) irradiation time.*

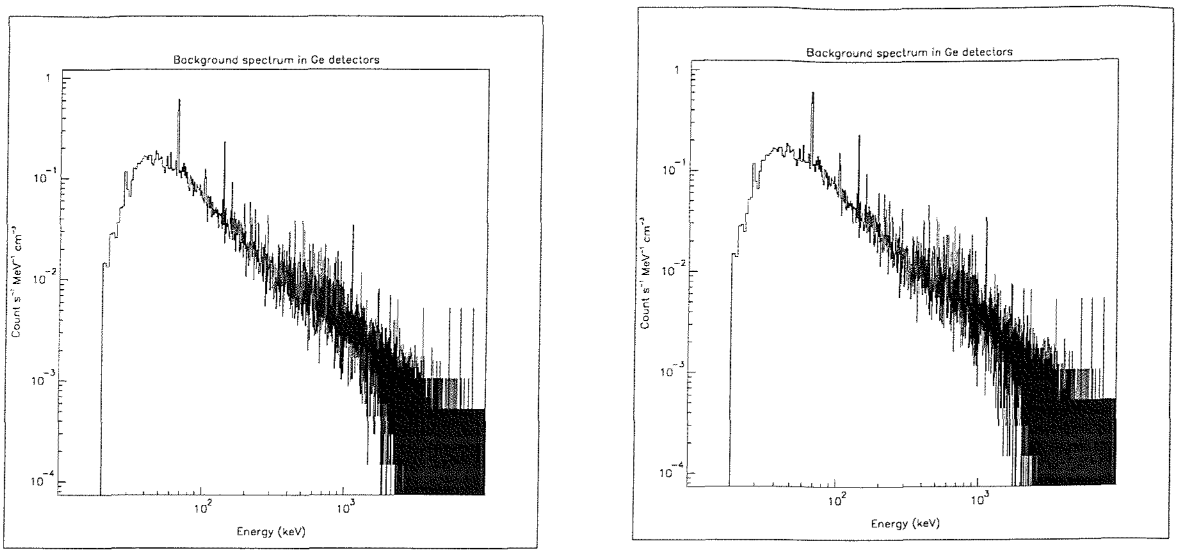

Figure 4.30: *The total background spectrum as modelled in the Ge detectors assuming a 24 hour (left) and a 32 hour (right) irradiation time.*

Having compared the modelled and real spectra, the difference between the natural and enriched detectors was then considered.

Figure 4.31 shows the background measured by Barthelmy et al. (1994) in one of the natural Ge detectors and the enriched Ge detector. The simulated spectra (figs 4.32 and 4.33) show the induced component of the background within a natural and an enriched Ge detector. Many of the lines are reproduced in the modelled results, and these are shown in table 4.4. The basic improvement in line background from natural Ge to enriched Ge is clearly reflected by the simulations, though the intensities of the individual lines are not well modelled.

4.7.4 Conclusions

An attempt has been made to simulate the background within the GRIS instrument, though this is particularly difficult because of the effects of the atmosphere. There have been some discrepancies between the simulations and the real results, though the generalities are largely the same. After normalisation of the γ-ray component, to account for the difference between real and modelled apertures, the spectra are quite similar. Both spectra show similar continuum levels and shapes,

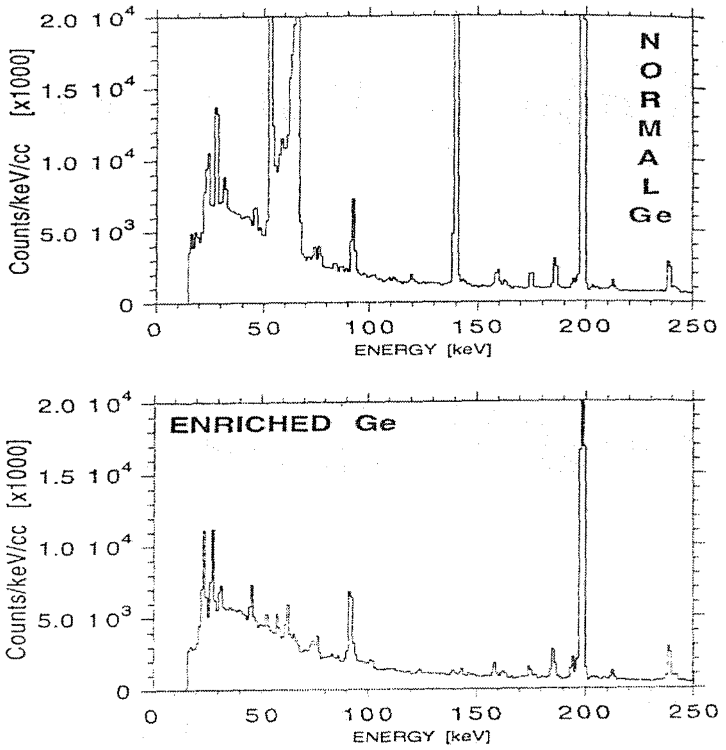

Figure 4.31: *Background spectra for the normal and enriched germanium detectors, in the low-energy range, flown on GRIS (Barthelmy et al. 1994).*

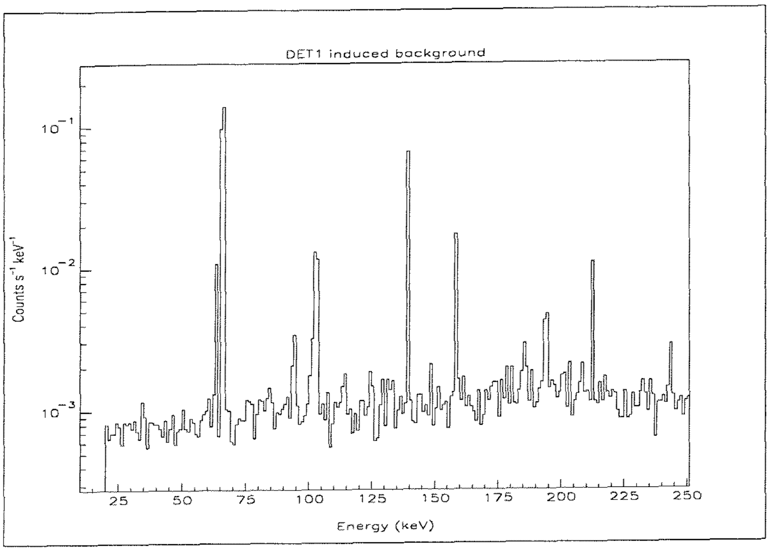

Figure 4.32: *The induced background as modelled in a natural germanium detector (DET 1).*

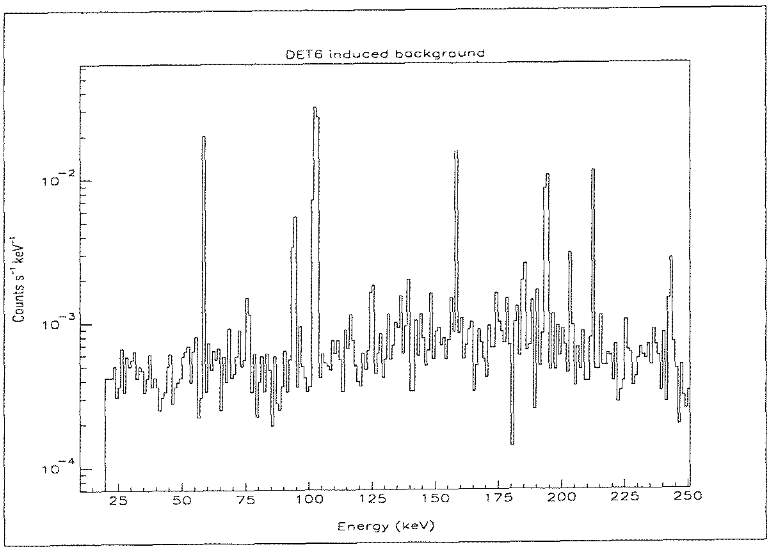

Figure 4.33: *The induced background as modelled in the enriched germanium detector (DET 6).*

Natural Ge		Enriched Ge	
Line energy (keV)	Presence	Line energy (keV)	Presence
20 - 30	No	20 - 30	No
53.4	No	~45	No
66.7	Yes	57 -60	Yes
~93	Yes	~75	Yes
140	Yes	~93	Yes
160	Yes	~100	Yes
175	No	~125	Yes
~187	Possibly	~140	Possibly
198.4	No	160	Yes
~210	Possibly	175	No
~240	Possibly	~185	Possibly
		192 - 200	Possibly
		~212	Yes
		~240	Yes

Table 4.4: *Summary of the lines present in the real data for the natural and enriched Ge detectors on board GRIS. The columns headed presence indicate whether or not those lines are reproduced in the modelled results.*

and both have many lines present. In the modelled spectrum it is surprising that the 53.4 keV line is not reproduced. A comparison between the spectra detected in the natural and enriched detectors, shows that many of the real lines are reproduced by the simulations. Again however, the surprising absence of the 53.4 keV line is noted. Both the 53.4 and 66.7 keV lines are due to the decay of ^{73}Ge. This isotope undergoes isomeric transitions from a nuclear energy level of 66.7 keV, via the emission of two γ-rays. These γ-rays have energies of 53.4 and 13.3 keV. In reality there is an intermediate energy level, at 13.3 keV, between the 66.7 keV level and the ground state of ^{73}Ge which has a half-life of 2.95 μs. In the real data it is likely that for some events the delay between the 53.4 and 13.3 keV γ-rays is greater than the gate time of the detectors. This would result in two events being recorded, one of 53.4 keV and one of 13.3 keV, instead of the full 66.7 keV. Currently, in the simulations this can not be modelled as no time delay between the two γ-rays is considered. Therefore the modelled results contain only 66.7 keV events, due to the absorption of both γ-rays. The intensities of the lines, in the natural and enriched spectra, are not always well matched. Considering the differences between the flown and modelled setups of GRIS, and the inherent uncertainties of GGOD, this is still a very good result. Whilst there is some work left to do to match the models to the real data, it seems that the GGOD suite gives reasonable results at the moment.

4.8 Summary

To enable accurate modelling of the background in astronomical missions, such as INTEGRAL, it is necessary to model the induced radioactive decay component. At Southampton an integrated suite of software (GGOD) is being created to do this, an important part of which, the DECAY code, has been presented in this chapter.

DECAY has been developed to model α decay, β^+/EC decay, β^- decay and isomeric transitions using the decay schemes collated by the NNDC. Modelling the various decay types involves not only modelling the primary particle, but also the nuclear and atomic de-excitation processes. This allows DECAY to simulate the γ-ray, conversion electron, X-ray and Auger electron emission that occurs during the decay of an isotope. Though DECAY has been tested, reasonably successfully, on its own, most of the testing has concentrated on the full GGOD suite.

Wihin GGOD the prompt background components, and the isotopic production rates, are modelled in GEANT/GCALOR. From this ORIHET calculates the decay rates at the required epoch, and DECAY uses this information to simulate this background component. This whole procedure has been tested using 3, quite different, examples.

The first test, modelling the beam test data, shows good agreement with the real spectral features and their evolution with time after irradiation. Most of the differences between the real and simulated results could be explained by deficiencies in the real experiment.

The second test considered, involving a space based application, was modelling of the background in HEAO-1. A very crude model of the spacecraft and payload was used in the simulations. The veto off spectrum produced models the real data quite well, and with the addition of the atmospheric γ-rays over the energy range 100 - 300 keV, could do even better. The veto on spectrum models the continuum level reasonably well at higher energies, but poorly at lower energies. This may be due to the crudeness of the veto setup in the model or to leakage through the veto on HEAO-1.

The final test involved modelling of the GRIS balloon spectrometer. Once an appropriate normalisation to account for differences between real and modelled setups was applied, the simulations were found to approximate the real data quite well. Several of the real line features have been reproduced, as has the continuum shape and overall continuum level. Comparison of modelled data for natural and enriched Ge detectors, with real data, shows many of the lines observed are produced in the model. The intensities are not necessarily correct, but this a very good first step towards modelling Ge detectors accurately.

When considering the limitations of the models used in the three examples, and those of GGOD (i.e. in the production rates, decay rates and decay schemes), the results presented are a strong validation of the current ability of GGOD to model the background reasonably accurately.

The GGOD suite is still in the development stages and there are obviously areas in need of improvement, for example the ability to model semi-stable energy levels within the nuclear deexcitation process. This is outside the scope of this thesis. As stated previously, development of GGOD has been driven by the need to model the background for the INTEGRAL mission. Chapter 3 introduced the model (TIMM), and having now presented the software used to carry out the modelling process, the results of this process are presented now in chapter 5.

Chapter 5

TIMM: Results, discussion and analysis

5.1 Introduction

The many versions of The INTEGRAL Mass Model (TIMM) have all been used to generate four core results: Background spectra and count rates, detection efficiencies, line and continuum sensitivities and trigger rates and spectra. In section 5.2 the core results, and others, are presented and discussed for the latest TIMM model (version 3.4). Section 5.3 discusses the evolution of the core mass model results between versions 1.0a and 3.4, and finally in section 5.4 a critical appraisal of TIMM, and mass modelling in general, is undertaken.

5.2 TIMM v3.4 results

TIMM v3.4, run during November 1999, produced the most up to date results of the TIMM project. Version 3.4 of TIMM was constructed on the INTEGRAL group Linux PC cluster at Southampton. Many of the results have been produced for both solar maximum and solar minimum cases. The simulations have been split into 3 different parts, cosmic diffuse γ-rays, (prompt) cosmic rays and induced radioactivity (or delayed cosmic rays). For each case 100 seconds worth of flux has been simulated using the GGOD software.

5.2.1 IBIS background spectra and count rates

The background count rates measured with the IBIS instrument are given in table 5.1. The operational modes shown are: ISGRI single pixel events (ISGRI Single), ISGRI-PICsIT Compton events (Compton), PICsIT single pixel events (PICsIT Single) and PICsIT 2 or 3 pixel events (PICsIT Multiple). The energy thresholds applied were: ISGRI 20 - 600 keV, PICsIT 100 keV - 5 MeV and BGO > 100 keV.

Mode	Total	Solar CDG	Maximum Cosmic Rays	Induced Radioactivity
ISGRI Single	422.8	335.3	48.1	39.37
Compton	53.3	12.79	18.73	21.78
PICsIT Single	1048	237.3	196.9	614.2
PICsIT Multiple	468.8	61.57	116.1	291.1

Mode	Total	Solar CDG	Minimum Cosmic Rays	Induced Radioactivity
ISGRI Single	483.3	335.3	83.74	64.23
Compton	77.37	12.79	30.59	33.99
PICsIT Single	1488	237.3	313.4	937.8
PICsIT Multiple	697	61.57	198.5	436.9

Table 5.1: *The background count rates (count/s) measured in IBIS at both solar maximum (top) and solar minimum (bottom).*

Figure 5.1 shows the background spectra, at both solar maximum and minimum, for single pixel events recorded in ISGRI. At solar maximum the spectrum is dominated by diffuse γ-rays up to ~300 keV. In the solar minimum spectrum the cosmic diffuse γ-rays are only dominant up to 100 - 200 keV. The single pixel background in ISGRI is largely dominated by the aperture flux, which is mostly cosmic diffuse γ-rays.

Figure 5.2 shows the Compton background at solar maximum and minimum. Compton events interact in a single pixel in ISGRI and 1 or 2 pixels in PICsIT. There is no dominant component, but above ~500 keV the cosmic diffuse γ-rays become less important than the cosmic rays and induced radioactivity.

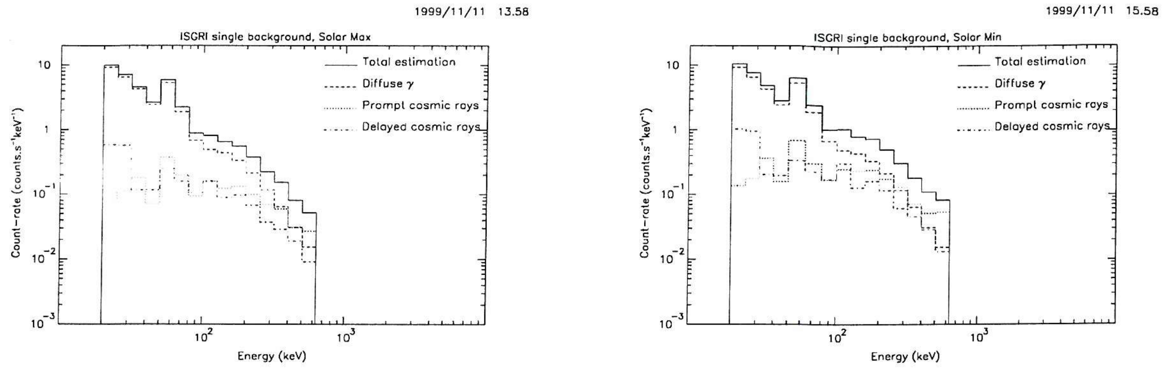

Figure 5.1: *Single pixel ISGRI background spectra at solar max (left) and solar min (right).*

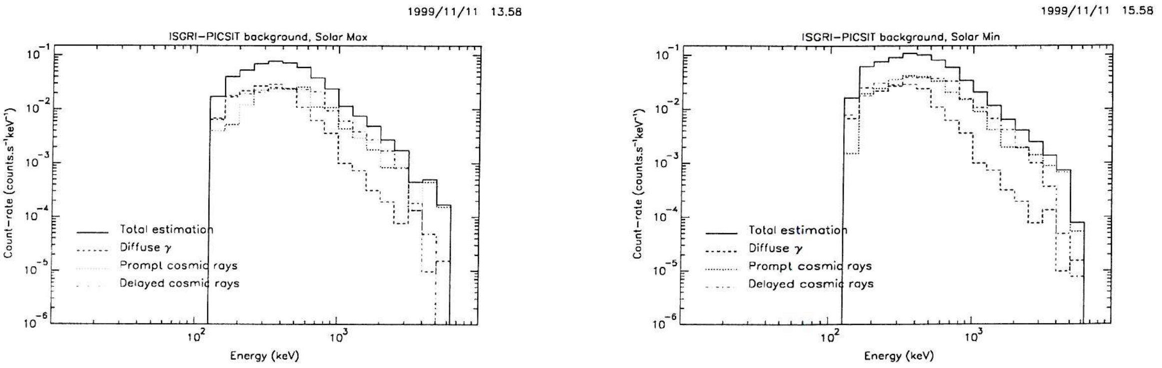

Figure 5.2: *Compton background at solar max (left) and solar min (right).*

The PICsIT single pixel background (fig 5.3) is quite complex. The largest component over the range 100 keV - 2 MeV is the induced radioactivity. In the solar max simulations, between 100 - 300 keV, the cosmic diffuse γ-rays are about a factor of two to four below the induced component. The cosmic diffuse γ-ray spectrum flattens completely below ~250 keV and this is probably due to the presence of the ISGRI detector plane. At solar min the increased induced radioactivity, due to increased cosmic ray flux, means that the cosmic diffuse γ-rays at 100 - 300 keV are a factor of four to five lower than the induced radioactivity. Above 2 MeV the cosmic rays are the dominant background component in both solar max and min spectra. Overall the presence of ISGRI causes the cosmic diffuse γ-ray spectrum to be flat at 100 - 300 keV. This leads the PICsIT single pixel background to be largely composed of induced radiation over a broad energy range (100 keV - $\sim$2 MeV).

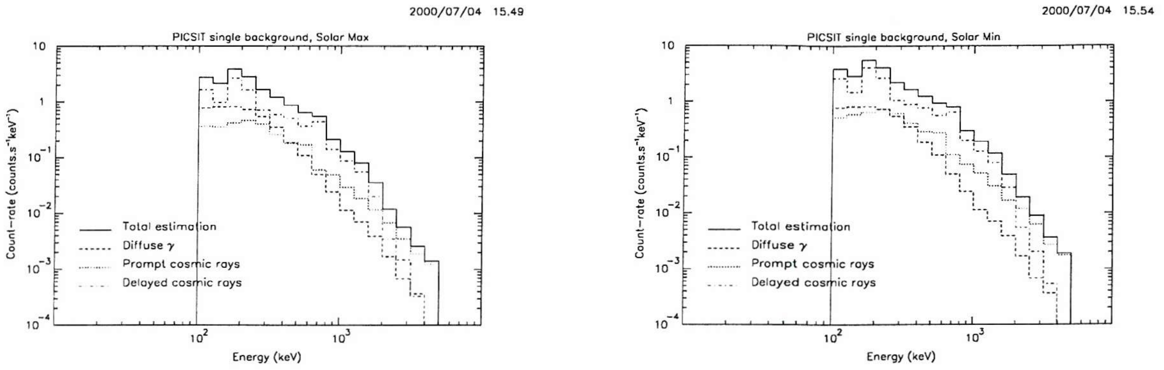

Figure 5.3: *PICsIT single pixel background spectra at solar max (left) and solar min (right).*

Figure 5.4 shows the PICsIT multi-pixel background at solar max and min. The biggest component up to 3 MeV is the induced background, but at about 3 MeV the prompt cosmic rays become the most important component.

The PICsIT total events spectra (fig 5.5) are composed of both single and multiple site PICsIT events. The single site spectrum is dominant. The background is mainly induced radiation up to 2 - 3 MeV where the prompt cosmic rays become more important.

5.2.2 IBIS detection efficiencies

Figures 5.6 and 5.7 show the detection efficiencies for the ISGRI single pixel mode, the Compton mode, the PICsIT single pixel mode and the PICsIT multiple pixel mode. No mask or imaging effects have been taken into account in determining these quantities. Three different efficiencies are shown in each of the figures: firstly, the total efficiency, which is the probability of detecting an event regardless of the energy actually measured in the detector; secondly, the full energy efficiency, which

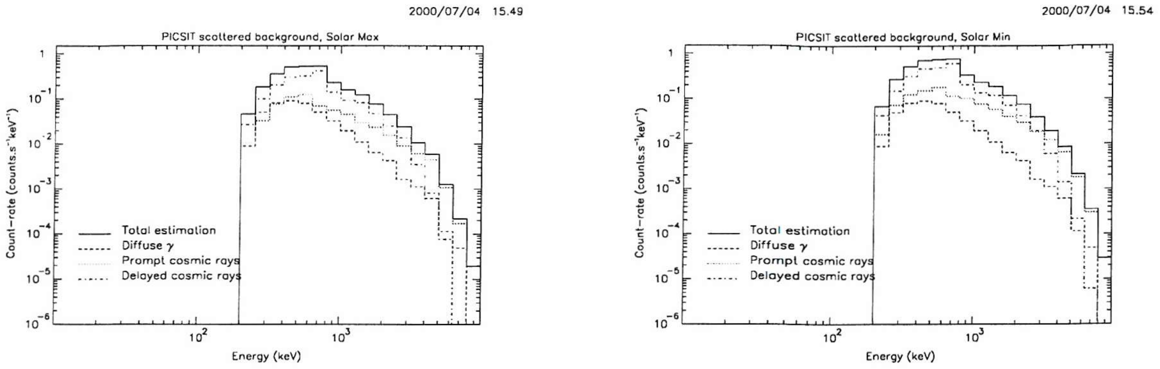

Figure 5.4: *PICsIT multi-pixel background spectra at solar max (left) and at solar min (right).*

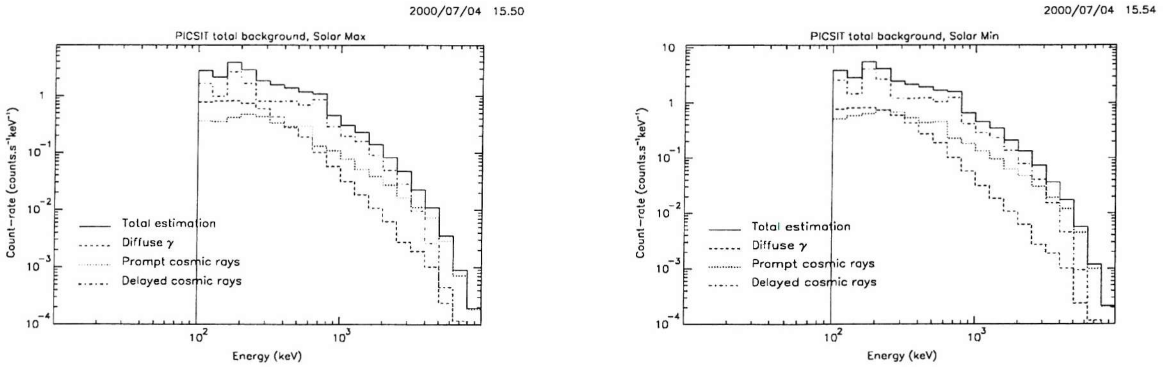

Figure 5.5: *Total PICsIT background spectra at solar max (left) and at solar min (right).*

gives the probability that an event will be detected at its full energy, within the energy resolution of the detector; and thirdly, the ΔE efficiency, which represents the probability that an event will be detected at the full energy to within E/2. In all cases the energy resolution used in the full energy efficiency calculations has been taken from the IBIS ICDR.

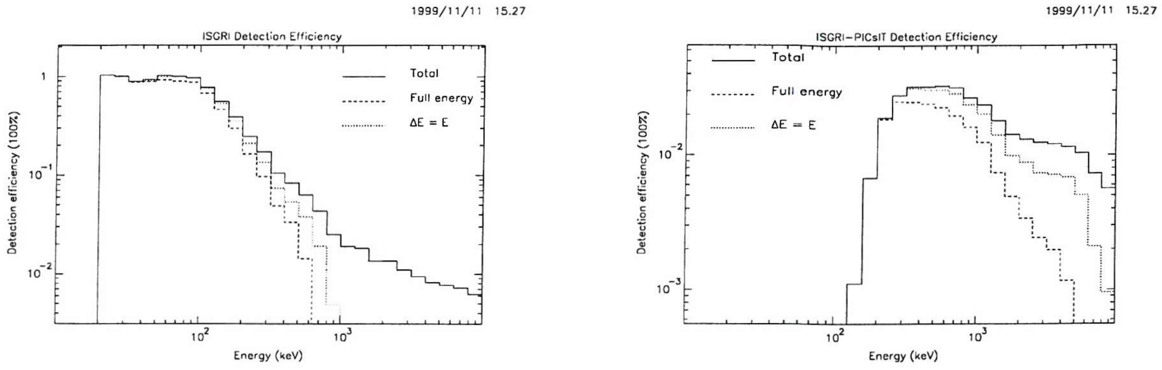

Figure 5.6: *The detection efficiency for ISGRI single pixel events (left) and for Compton events (right).*

The ISGRI single pixel efficiency is close to 1 (100%) from 20 - 100 keV. In some cases it may even be slightly greater than one, due to scatter off of passive material between and around the ISGRI pixels. Above 100 keV the efficiency starts to drop off dramatically. The total efficiency is ~10% at 400 keV and ~1% at 3 MeV. This drop off is to be expected since ISGRI is quite thin, has a low stopping power, and is therefore relatively transparent to high-energy photons. Physical effects within the CdTe crystals, such as charge trapping, are not included in the efficiency calculations.

The detection efficiency for Compton events reaches a maximum of ~4% between 300 and 800 keV (fig 5.6). The PICsIT detection efficiency peaks at between 200 and 300 keV at ~80% then falls off steadily. It might be expected that the efficiency of PICsIT should be ~100% between 100 - 300 keV, given both the transmission of CsI and the 3 cm thickness of the PICsIT pixels, but clearly in figure 5.7 this is not the case. This is due to the ISGRI detector plane interfering with the detection of photons in PICsIT, by either absorbing photons or scattering them. Scattered photons, subsequently fully absorbed by PICsIT, would be recorded at far less than their full energy. Probably all of the low-energy (~100 - 300 keV) events which pass through ISGRI unhindered are absorbed in PICsIT. Above 200 keV the ISGRI efficiency (for single site events) is down to ~25% and so there are more events arriving at the PICsIT detector plane unhindered. The full energy efficiency is much lower than the total efficiency, even at 200 keV, which is probably due to scatter in ISGRI reducing the total energy deposited in PICsIT below the full energy threshold. The ΔE efficiency band is much wider and so many of these events can still be counted within this category.

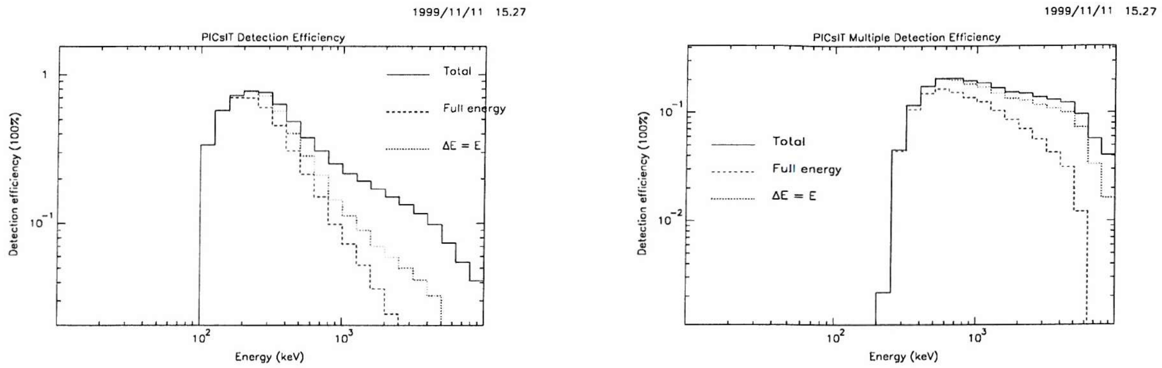

Figure 5.7: *The detection efficiency for PICsIT single pixel events (left) and for PICsIT multiple pixel events (right).*

Figure 5.7 shows the PICsIT multiple pixel detection efficiency. The total efficiency reaches a maximum of 20% at 500 - 800 keV, and drops slowly to 10% at ~7 - 8 MeV. The full energy efficiency drops much more rapidly from ~15% at ~600 keV to ~1% at ~6 MeV. The multiple pixel events are composed of Compton scatters (within PICsIT) and pair production events. At 2 - 3 MeV the single and multiple pixel modes have similar efficiencies (~15%), but above this the multiple pixel mode is more efficient. The full energy efficiency of the multiple pixel mode is higher than the single pixel mode from about 800 keV upwards. So while events are detected at similar numbers within both modes, the nature of the γ-ray interaction mechanism, means that large amounts of initial γ-ray energy is lost in the single pixel mode, probably due to scatter (of photons and electrons) out of the single pixel and into the surrounding materials.

5.2.3 IBIS sensitivity

Figure 5.8 and 5.9 show the continuum and line sensitivities calculated for IBIS. The sensitivities are calculated at solar maximum and account for the incident pixel reconstruction (IPR) efficiency as well as the increasing transparency of the mask elements at higher energies. The loss of sensitivity in the coding and deconvolution process of the coded mask imaging is not included within the calculations. ISGRI dominates the sensitivity at low energies, whereas the PICsIT single and multiple modes dominate above 200 keV. The Compton mode hardly increases the sensitivity at all. In fig 5.9 the continuum sensitivity of IBIS is compared with that of the OSSE and SIGMA instruments, and with the spectrum of the source 3C273. IBIS is about a factor 10 more sensitive than SIGMA and about a factor of 3 or so more sensitive than OSSE. Up to ~400 keV the IBIS line sensitivity is better than that of OSSE (fig 5.9). Between 400 keV and 2 MeV the two are comparable, but above 2 MeV OSSE is more sensitive. IBIS is more sensitive than HEAO-3 over virtually its whole energy range.

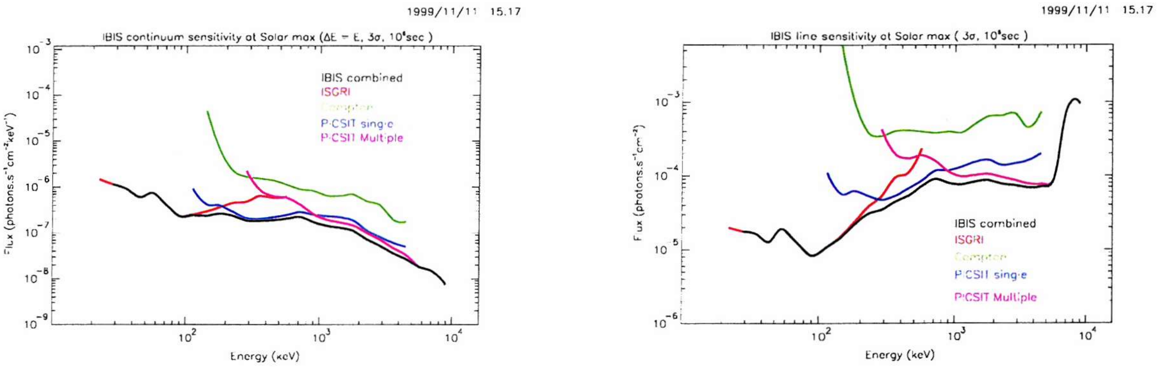

Figure 5.8: *The IBIS continuum sensitivity (left) and line sensitivity (right) at solar max.*

5.2.4 IBIS Event rates and spectra

Table 5.2 shows the event rates measured in IBIS for both the solar minimum and maximum cases. The event rate spectra (figs 5.10 and 5.11) are shown for the solar maximum case only. The diffuse cosmic γ-rays are the largest component at low energies (20 - 80 keV) in the ISGRI spectrum (fig 5.10). Note the prominent fluorescence line at 50 - 60 keV. From 80 keV upwards the dominant component is prompt cosmic rays. Note the peak around 2 MeV, this is probably due to minimum

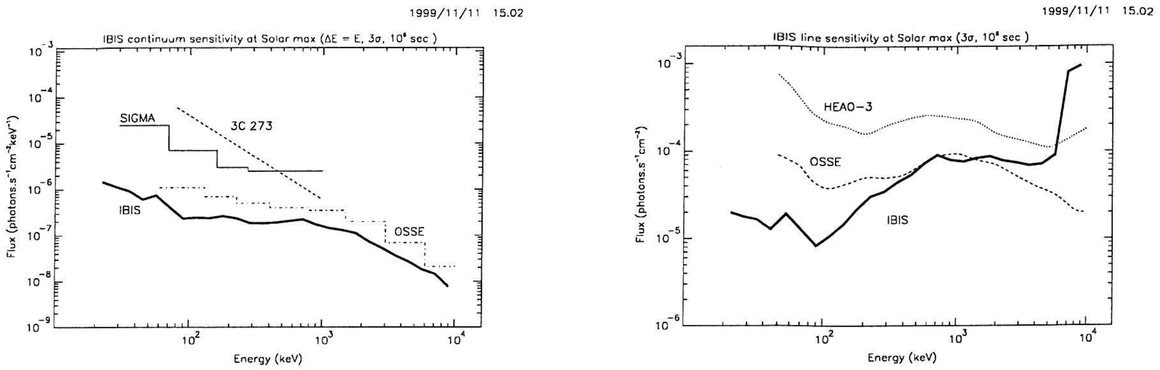

Figure 5.9: *The IBIS continuum (left) and line (right) sensitivity at solar max.*

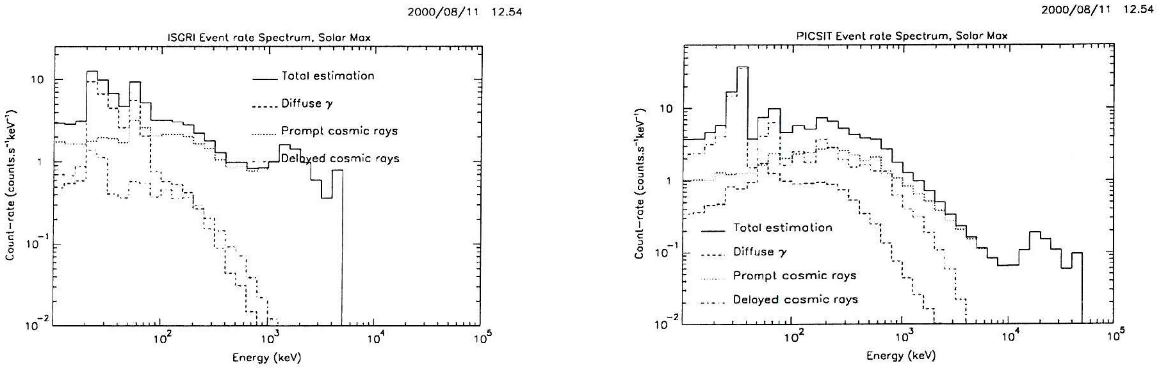

Figure 5.10: *Event rate spectra at solar max for ISGRI (left) and PICsIT (right). Note these spectra extend well below the low energy thresholds.*

		Solar	Maximum	
	Total	Cosmic Diffuse γ-rays	Prompt Cosmic Rays	Induced Radioactivity
ISGRI	5074	376.1	4534	164
PICsIT	9832	382.5	7676	1773
BGO	28350	4463	15090	8800
CTag	1406	350.4	817.7	237.6
		Solar	Minimum	
	Total	Cosmic Diffuse γ-rays	Prompt Cosmic Rays	Induced Radioactivity
ISGRI	8585	376.1	7951	258.4
PICsIT	16130	382.5	13020	2726
BGO	45770	4463	26870	14440
CTag	2227	350.4	1475	401.4

Table 5.2: *Event rates (count/s) in the IBIS detectors at both solar maximum and solar minimum. CTag refers to the Calibration Tagging Crystal.*

ionizing particles. These deposit ~1 - 2 MeV/g, which with CdTe's density of ~6.06 g/cm^3 and the thickness of ISGRI of ~0.2 cm, gives ~1.2 - 2.4 MeV. The spectrum falls away after this peak, though there is a peak at 5 MeV, but this is the overflow bin and is therefore not a spectral feature as such. The PICsIT event spectrum is dominated up to 80 keV by induced radiation. Above 1 MeV the prompt cosmic rays dominate the spectrum. Note the minimum ionizing particle peak at 13 - 27 MeV and the overflow bin at 50 MeV. Fig 5.11 shows the IBIS BGO veto spectrum, which is dominated at low energies by cosmic diffuse γ-rays. At high energies the cosmic rays and the induced radiation are more important. The huge peak at ~6 MeV is due to the α decays of ^{210}Bi, ^{211}Bi, ^{212}Bi, ^{213}Bi and ^{214}Bi. Also note the min ionizing peak at 20 - 30 MeV and the overflow bin at 50 MeV.

5.2.5 SPI background spectra and counting rates

Table 5.3 shows the background count rates as calculated within SPI during both solar minimum and maximum. The germanium detectors have low-energy thresholds of 20 keV and high-energy

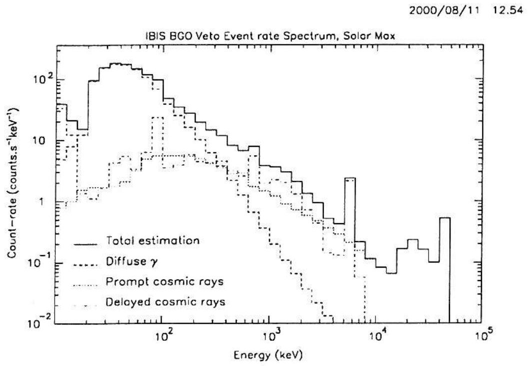

Figure 5.11: *The IBIS veto event spectrum at solar max. Note this spectrum extends well below the threshold.*

thresholds of 8 MeV. Both the plastic and BGO vetoes have low-energy thresholds of 100 keV. Fig 5.12 shows the germanium single detector background. Below 70 keV this is dominated by diffuse cosmic γ-rays, however above 100 keV the most important component is the induced radioactivity. This is because the externally generated background in SPI is excellently suppressed by the massive BGO shielding, leaving the internally generated background to dominate. Table 5.3 shows that the internal background (induced radioactivity) is $\sim$3 times the external background for the single detector events at solar maximum.

		Solar	Maximum	
Mode	Total	CDG	Prompt Cosmic Rays	Induced Radioactivity
Single	244	59.4	7.85	176.7
Multi no 511	72.02	2.54	4.84	64.64
Multi with 511	8.23	0.05	0.06	8.12
		Solar	Minimum	
Mode	Total	CDG	Prompt Cosmic Rays	Induced Radioactivity
Single	318.9	59.4	15.29	244.2
Multi no 511	102.5	2.54	9.3	90.64
Multi with 511	12.67	0.05	0.23	12.39

Table 5.3: *The background count rates (count/s) in the SPI detectors at both solar maximum and solar minimum.*

The multiple detector without 511 keV photons mode (fig 5.12) background spectrum is dominated over its entire energy range by induced radioactivity, again because of excellent external background suppression. The multiple detector with 511 keV photons mode (fig 5.13) background is almost totally due to the induced radioactivity. In these two modes photons are classed as 511 keV if they have energies equal to 511 ± 0.5 keV.

Figure 5.13 also shows the background for all types of SPI events with a resolution of 1 keV. Overall the background of SPI is dominated by the induced radioactivity above about 100 keV. In fig 5.13 the line-dominated nature of the SPI background (due to radioactive decay) can clearly be seen.

5.2.6 SPI efficiency

Figures 5.14 and 5.15 show the detection efficiency for the various modes of SPI. As with IBIS, no mask or imaging effects have been taken into account. The single detector efficiency is highest at ~200 keV being above 90%. The efficiency at near 20 keV is very low, approximately 50%, and this may be due to the beryllium cryostat. The multiple detector without 511 keV photons mode has a low efficiency (max 20%). The full energy efficiency is much lower than the total and this is probably due to scattering in the beryllium cryostat, or even in the BGO shielding. The low-energy threshold

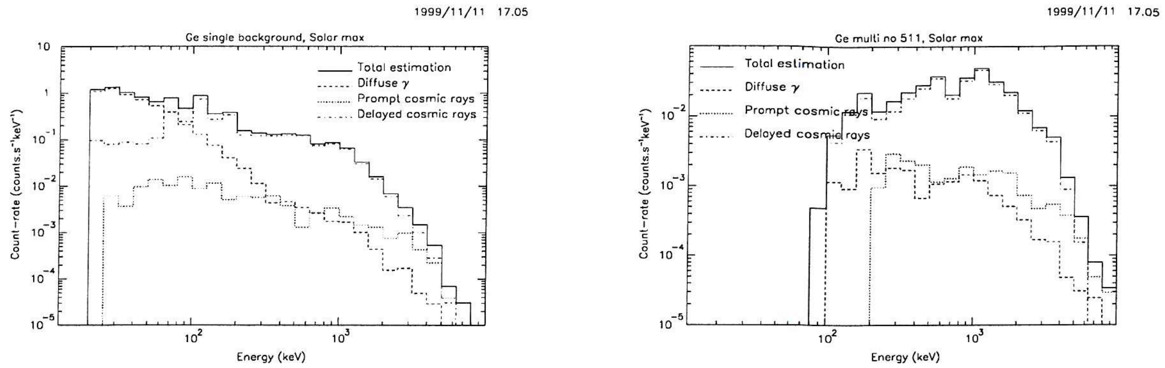

Figure 5.12: *Background spectra for the single detector events (left) and for the multiple detector events without 511 keV photons (right) as generated for solar max.*

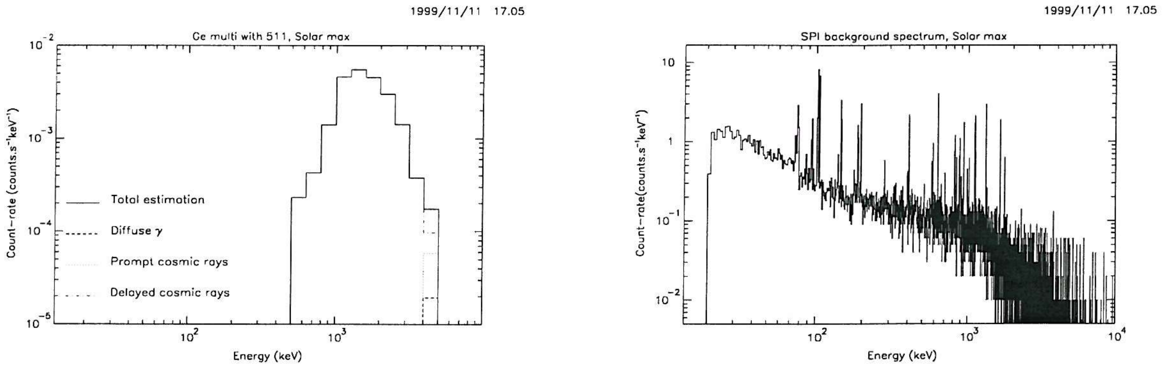

Figure 5.13: *The multiple detector with 511 keV photons background spectrum (left) and the total SPI background spectrum with 1 keV resolution (right).*

of the BGO is 100 keV, and it is quite possible that scattering into or out of this could reduce the full energy efficiency of the Ge detectors, without triggering the veto. The multiple detector with 511 keV photons mode (fig 5.15) has a very low efficiency (max ~2%). These events are mainly pair production events, and hence there are none below 1022 keV.

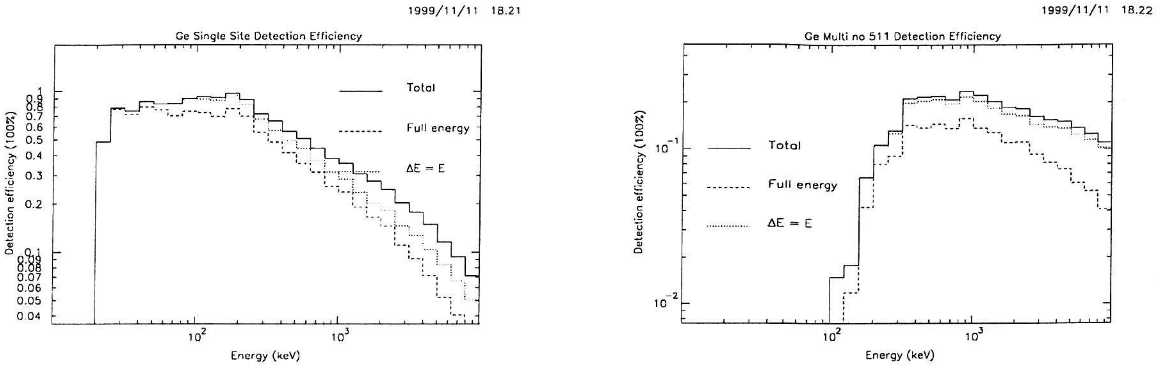

Figure 5.14: *The detection efficiency for both the single detector mode (left) and for the multiple detector without 511 keV photons mode (right).*

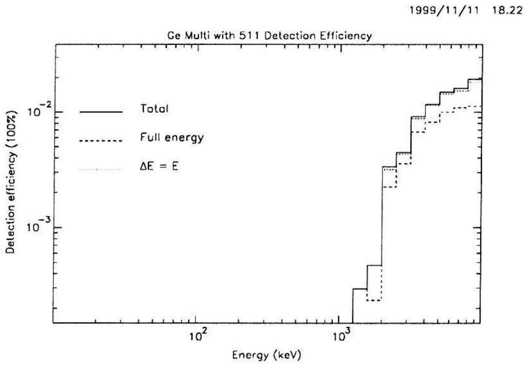

Figure 5.15: *The detection efficiency of the multiple detector with 511 keV photons mode.*

5.2.7 SPI sensitivity

The sensitivity of SPI's various modes is shown in figures 5.16 and 5.17. The two most important modes, with respect to the line sensitivity, are the single detector mode and multiple detector without 511 keV photons mode. The scarcity of events with 511 keV photons makes the multiple detector with 511 keV photons mode the least important. IPR, mask transparency, coding and deconvolution effects have not been included in the estimation of the sensitivities. The single detector mode and multiple detector without 511 keV photons mode are also the most important modes for the continuum sensitivity. Figure 5.17 compares the line and continuum sensitivities of SPI with those of HEAO-3, OSSE and SIGMA. The line sensitivity of SPI is significantly better than that of OSSE, whereas the continuum sensitivity is similar.

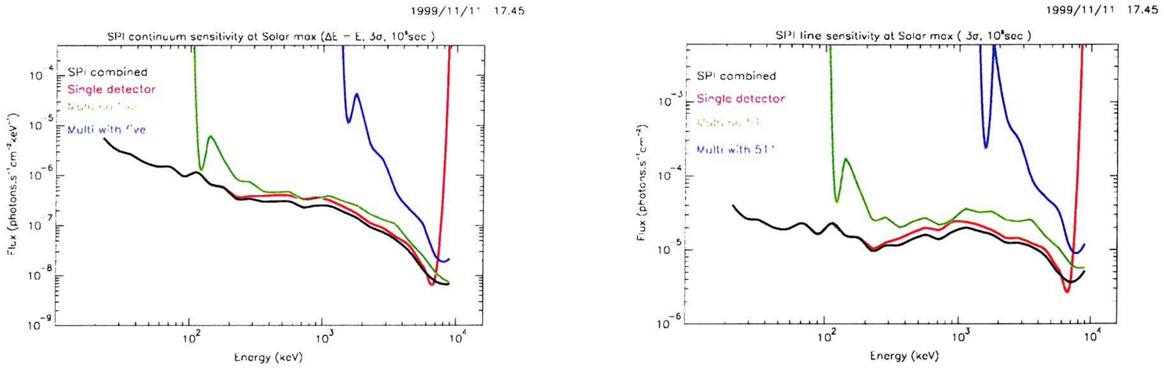

Figure 5.16: *The SPI continuum (left) and line (right) sensitivity as calculated at solar max.*

5.2.8 SPI event rates and spectra

Table 5.4 shows the SPI event rates as calculated at both solar max and solar min. Figures 5.18 and 5.19 show the spectra for the germanium, BGO and plastic detectors. The germanium spectra are largely composed of the induced radioactivity and the prompt cosmic rays. The feature at 50 MeV is the high-energy overflow bin. The BGO spectrum is dominated at low energies by the cosmic diffuse γ-rays, at medium energies by induced radioactivity and at high energies by the cosmic rays. There is a clear peak at $\sim$6 MeV due to the radioactive decay of bismuth. There is very little evidence for a minimum ionizing peak wihtin the BGO spectrum. This could be because there is so

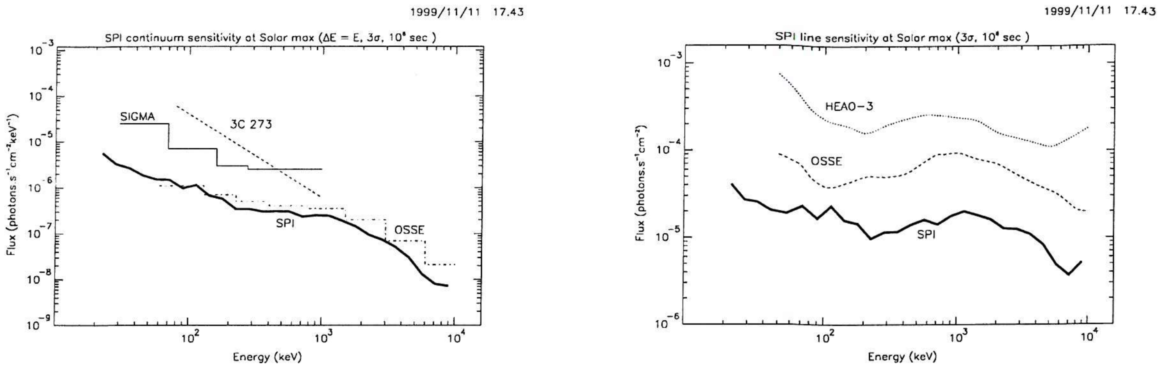

Figure 5.17: *The SPI continuum (left) and line (right) sensitivity compared with OSSE, SIGMA and HEAO-3.*

much BGO that it is impossible for particles to skim through a single piece. This is further backed up by the relatively large number of events in the overflow bin, as compared with IBIS. The strangest event spectrum is that of the plastic scintillator. The peak at ~1 MeV is probably due to minimum ionizing particles in the prompt cosmic rays ($\rho_{plastic}$ ~1 g/cm^3 & thickness ~5 mm giving a min ionizing energy of ~1 MeV).

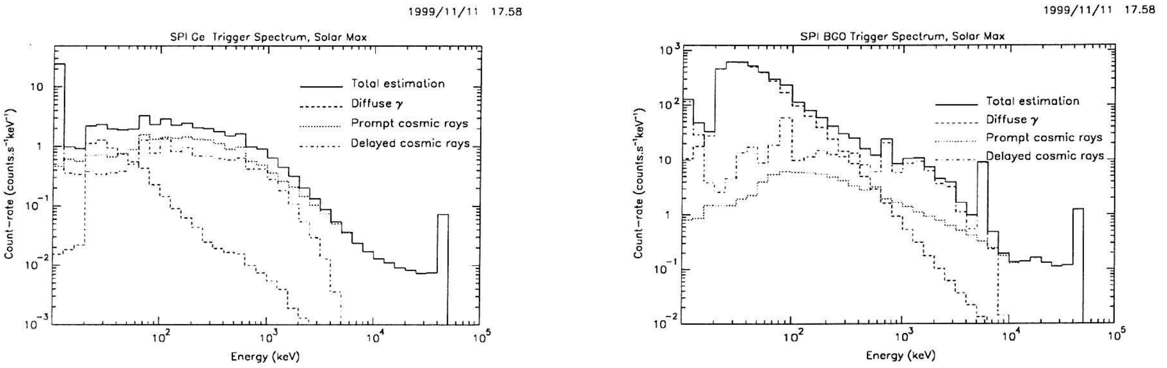

Figure 5.18: *Event rate spectra in the germanium (left) and in the BGO (right) estimated at solar max.*

		Solar	Maximum	
	Total	CDG	Prompt Cosmic Rays	Induced Radioactivity
Ge	3426	76.12	2528	821.8
BGO	69510	10970	23420	35120
Plastic	6362	83.1	6258	21.47
		Solar	Minimum	
	Total	CDG	Prompt Cosmic Rays	Induced Radioactivity
Ge	5302	76.12	4045	1180
BGO	106500	10970	42910	52630
Plastic	11640	83.1	11510	38.27

Table 5.4: *Event rates (count/s) for the SPI detectors at both solar maximum and minimum.*

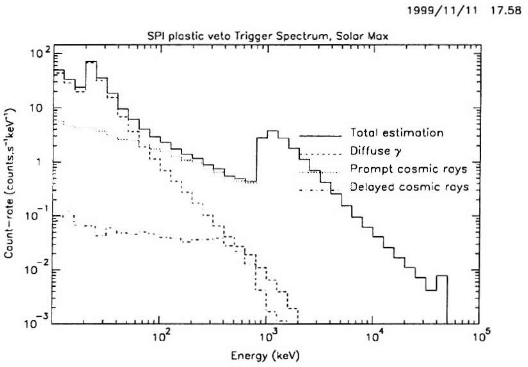
1999/11/11 17.58

Figure 5.19: *The event rate spectrum as measured in the plastic veto.*

5.2.9 Spatial distribution of the background

ISGRI

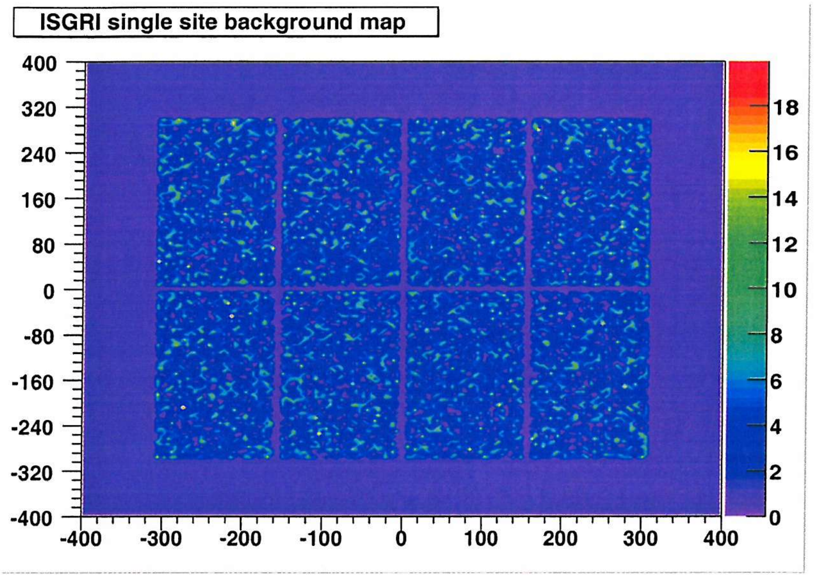

Figure 5.20: *Spatial distribution of the ISGRI single pixel events. SPI and JEM-X are at negative* x.

Figure 5.20 shows the distribution across the ISGRI detector plane of the single pixel events. From the scale on the right it seems that the number of counts recorded varies by almost a factor of 10 between the highest and lowest pixels, though there is no evidence of any overall non-uniformity within the detector plane map. The background appears to be randomly scattered across the detector plane as would be expected for uniform background sources. Figure 5.21 shows the projection of the x and y axes from the background map, and here, much more clearly, non-uniformities can be seen. The average background level is about 340 counts, however there are many peaks above this, quite a few of which are located at the edges of the detector modules. Between the ISGRI detector modules there are passive support structures, and the increase in background around these is most likely due to scatter into, and out of, these supports. An event Compton scattering within a pixel that is completely surrounded by other pixels, will be rejected from the ISGRI data as a multiple pixel event. If instead, the event were to scatter into passive material and be completely absorbed, then it would register as a valid single pixel event (at less than the full photon energy). The converse is also true, that events scattering out of passive materials into the pixels may be recorded as single pixel events.

At the very edges of the detector plane, the pixels are very "hot" compared with the average (480 counts cf. 340 counts). In ISGRI this could be due to scatters off of the hopper, other passive parts of IBIS above the BGO veto crystals, or even sub-threshold scatters from the veto itself. The increase in effective pixel area, due to having the top plus some of the side of the crystal exposed, will also have some effect on the number of counts. The y axis projection shows many of the same features, the increase in counts around the edges of the modules and the dramatic increase at the edge of the detector plane, for example.

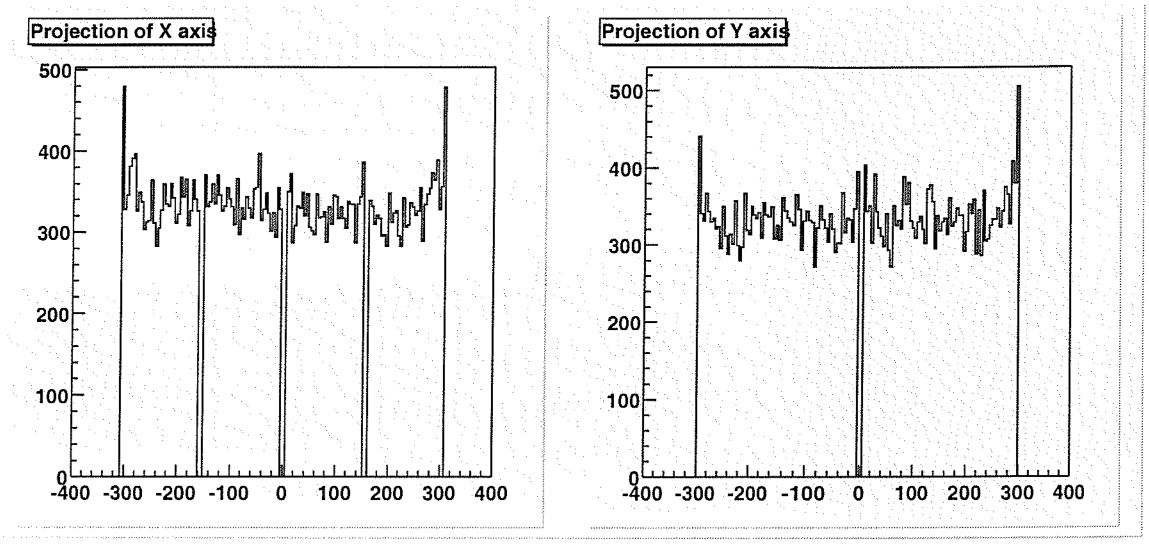

Figure 5.21: *Projection of the x and y axes of the ISGRI single pixel background events. SPI and JEM-X are at negative x.*

PICsIT

Figure 5.22 shows the detector plane map for the PICsIT single pixel events. This is much more uniform, in terms of numbers of counts per pixel across the detector plane, than that of the ISGRI single pixel events. There are quite a few "hot" pixels evident within the plane, though as noted with ISGRI their distribution looks fairly random.

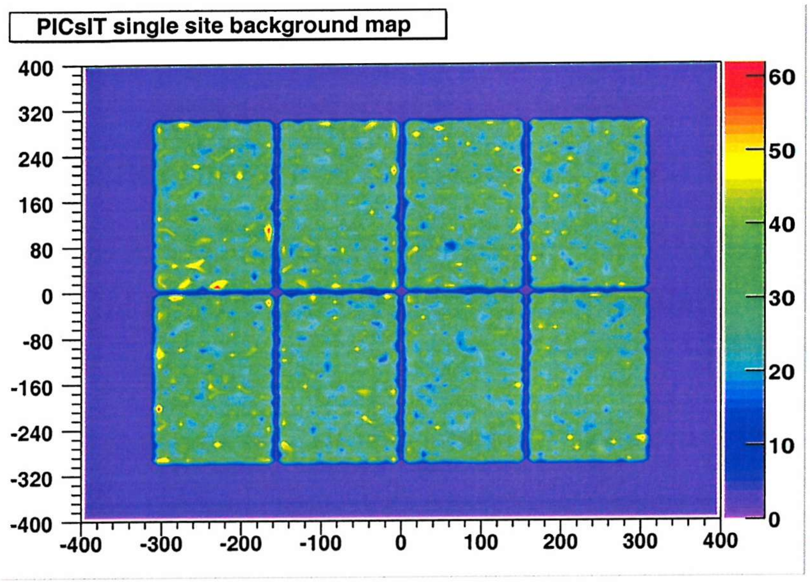

Figure 5.22: *Background map of the PICsIT single pixel events. SPI and JEM-X are at negative x.*

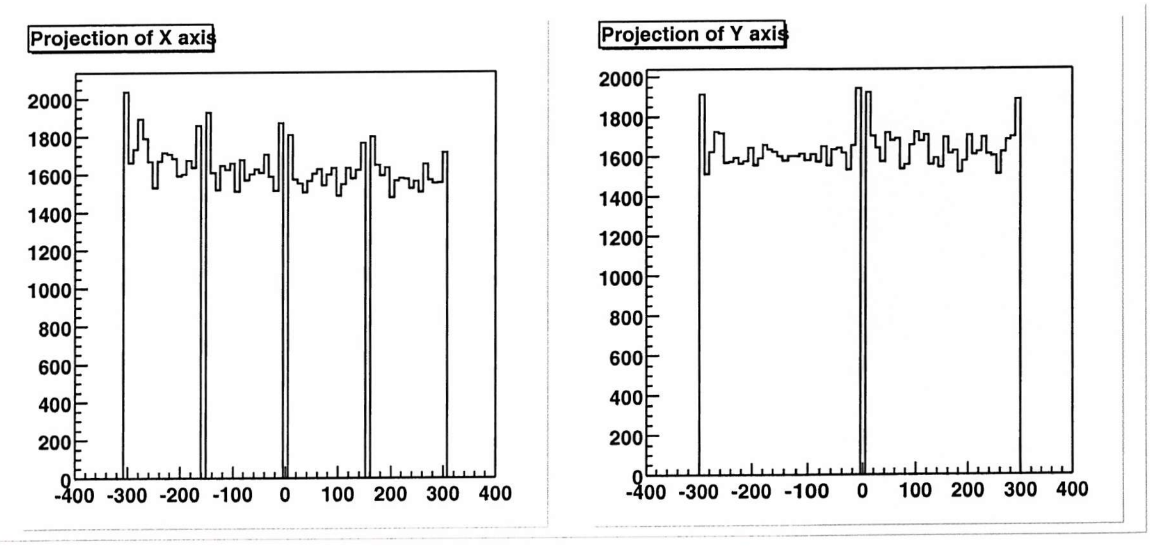

Figure 5.23: *Projection of the x and y axes of the PICsIT single pixel background events. SPI and JEM-X are at negative x.*

The projections of the x and y axes for the PICsIT single pixel background events tell a similar story to those of the ISGRI events. The projection of the x axis shows the same peaks around the passive material as in ISGRI. However, there are some differences between PICsIT and ISGRI, most notably there is some evidence of an increase in the PICsIT counts towards SPI/JEM-X. This is most likely due to an increase in scattered events from the -x direction, causing non-uniformity in the illumination of PICsIT. This is not seen in ISGRI because events that scatter from SPI/JEM-X into IBIS would have to be of high energy to penetrate the passive material and be detected in IBIS. At the energies required ISGRI is almost transparent. In the x axis projection there is much less of an increase at the edges of the detector plane than would be expected from the ISGRI plots. A probable explanation is the increase in shielding of the PICsIT plane. Scattering of events off of the hopper and passive materials above ISGRI into the side of PICsIT is not very likely, as ISGRI is in the way. The PICsIT plane is also surrounded by the active BGO veto system, and there is very little passive material between the veto and PICsIT from which events would be able to scatter into or out of. In effect PICsIT sits within an actively shielded box, and so scatters from external materials into the pixels forming the detector plane edges, or from those pixels into passive materials, are less likely than for ISGRI. The y axis projection shows peaks at the detector plane boundary and at the gap in the centre between the detector modules. The background across the plane has an average value near 1600 counts, though there are quite a few variations around this level.

Figure 5.24 shows the detector plane map for the PICsIT multiple pixel events. From fig 5.24 it seems the number of counts between adjacent pixels may vary by up to a factor of 6, but over the detector plane there is a random distribution of counts. From the background map there looks to be faint evidence of an increase in the number of counts towards SPI/JEM-X and this is roughly borne out in the projection of the x axis (fig 5.25). In the x axis projection it is clear that there is not the same increase in number of counts towards the detector module boundaries. At the edge of the detector plane the number of counts actually decreases dramatically. This is due to events scattering into passive materials and thus not being recorded as multiple pixel events. In the x and y projections (fig 5.25) there are some hints of features (peaks and troughs), which if seen in future datasets would merit further investigation. The small number of events detected within the Compton mode has meant that spatial variations for this mode have not been investigated thus far, though clearly in future this may also be undertaken.

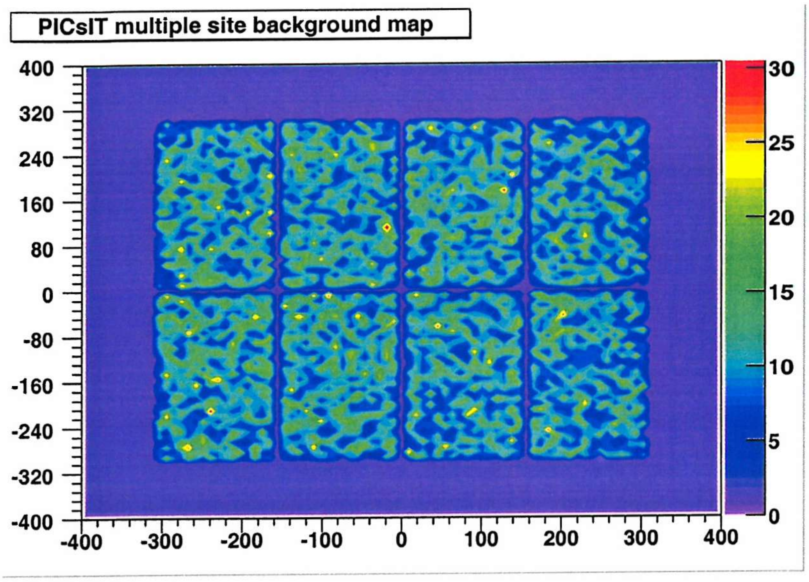

Figure 5.24: *Background map of the PICsIT multiple pixel events. SPI and JEM-X are at negative x.*

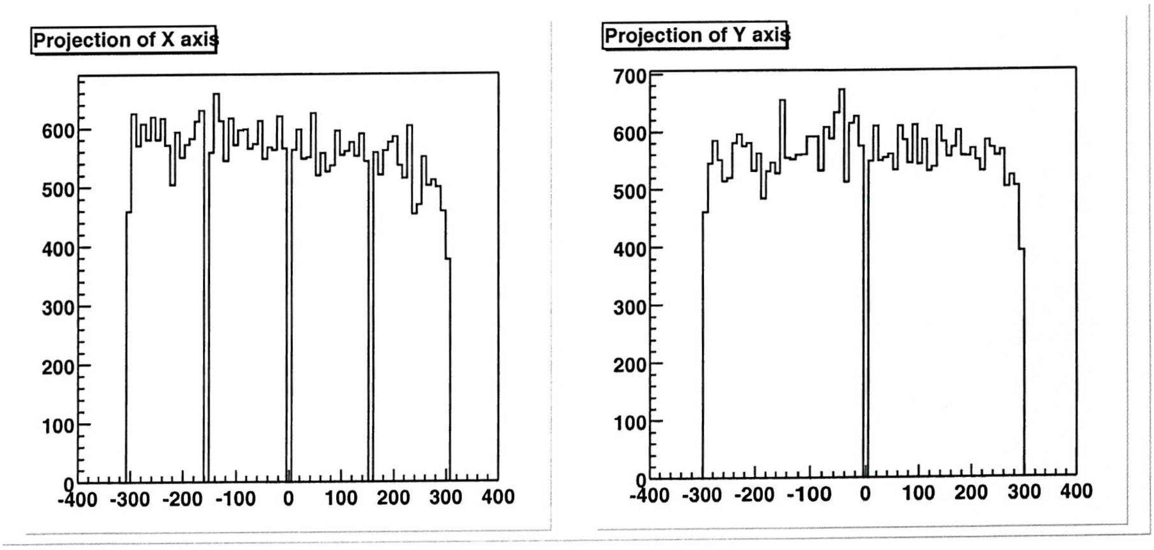

Figure 5.25: *Projection of the x and y axes of the PICsIT multiple pixel background events. SPI and JEM-X are at negative x.*

SPI

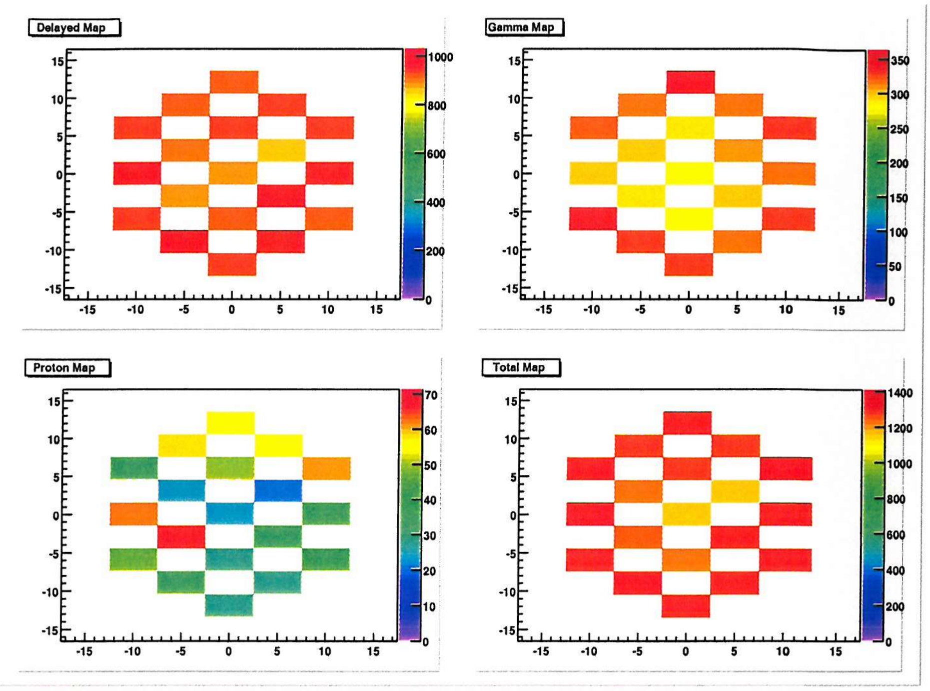

Figure 5.26: *Map of the background recorded using the SPI single detector mode at solar maximum.*

Figure 5.26 shows the background recorded in the SPI instrument using the single detector mode at solar maximum. The dominant background component is the delayed (induced radioactivity), and this is also fairly uniform. The second largest component, the diffuse cosmic γ-rays (Gamma Map), look to have some non-uniformity. It is hard to see, but the edge detectors seem to have a higher number of counts in them than the central detectors. This is probably caused by scatters from passive materials (i.e. the cryostat), or from sub-threshold scatters off of the veto, into the Ge detectors. The smallest component, the prompt cosmic rays (Proton Map), has no obvious pattern. The total background map is fairly uniform, though there is reason to believe that an enhancement is seen in the edge detectors.

The multiple detectors without 511 keV photons mode is, as mentioned earlier, dominated by the delayed events. In figure 5.27 the delayed component of the background is shown to have a clear structure across the detector plane. The edge detectors have much less counts recorded in them

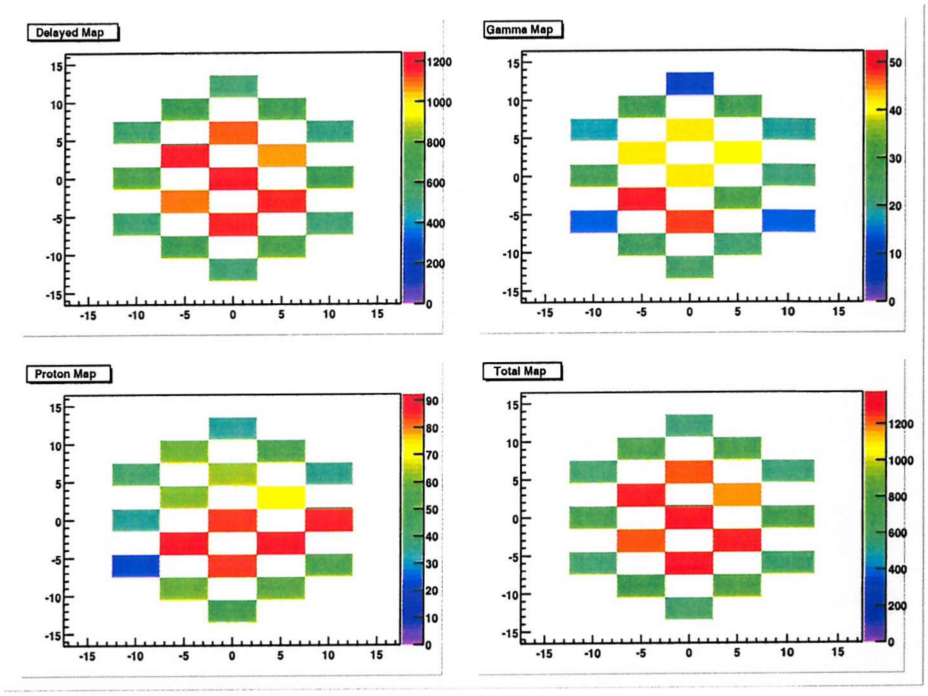

Figure 5.27: *Map of the background recorded using the SPI multiple detector without 511 keV photons mode at solar maximum.*

than the central detectors. This is to be expected, since if events are to be recorded in two detectors then this will be much more likely for those starting in the central detector than those starting in any of the edge detectors. The other two components of the background also show the same basic pattern as is expected. The total background for this mode shows the same centrally concentrated pattern, due to the Compton events which compose this mode.

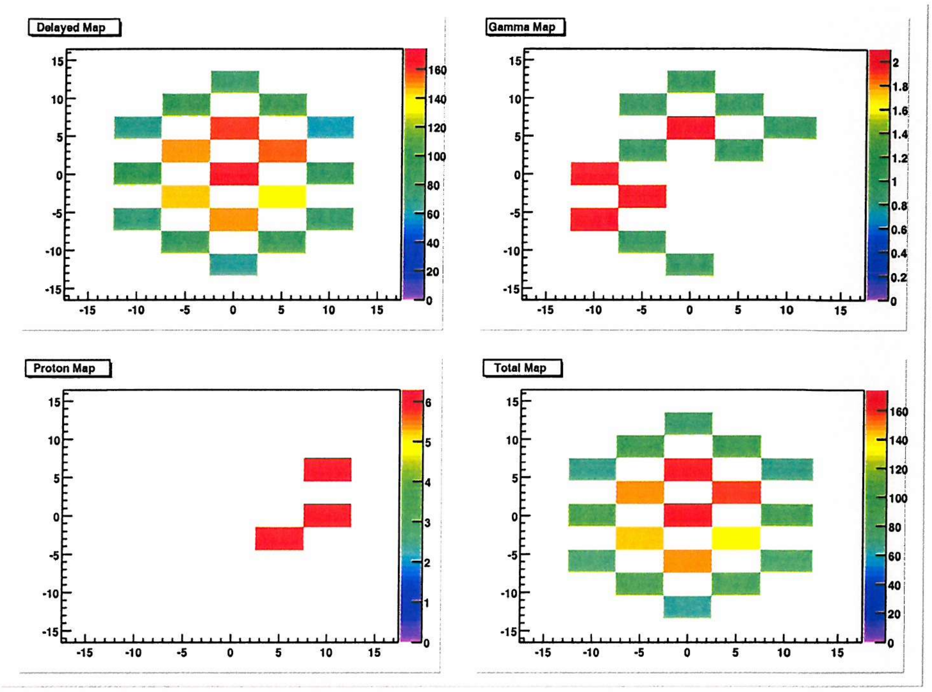

Figure 5.28: *Map of the background recorded using the SPI multiple detector with 511 keV photons mode at solar maximum.*

The SPI multiple detectors with 511 keV photons mode contains many less events than the other two modes, but similar to them, is dominated by the delayed events (fig 5.28). The nature of this mode means that it will be dominated by pair-production events, which necessarily means that the spatial distribution across the detector plane will be centrally peaked. This is borne out in figure 5.28, where the delayed background (and therefore the total) is clearly centrally concentrated.

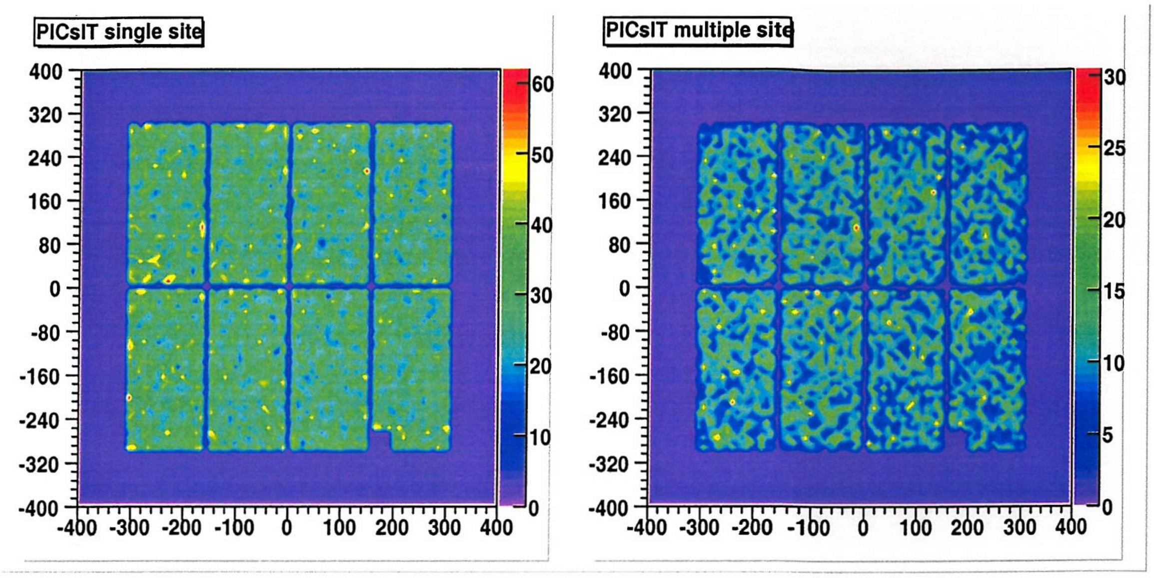

Figure 5.29: *Background map of the PICsIT single and multiple pixel events. Within the map are five random dead pixels as well as one dead asic (16 pixels).*

The effects of dead pixels on the background spatial distribution

In flight it is possible that some pixels may fail, or may experience problems requiring their output to be effectively ignored, and thus the pixels will be "dead". When this happens it is likely that the background properties within the adjacent pixels will be affected. For example the dead pixel will now function as a passive scatterer, and events that were previously multiple pixel could now be classed as single pixel. Thus it is expected that the multiple pixel background in the adjacent pixels will decrease while the single pixel background increases. The background maps (fig 5.29) show the spatial distribution of the background in PICsIT with some dead pixels added in. The five single dead pixels (spread randomly over the 8 modules) have no noticeable effect when the plane is looked at overall. In the bottom right hand module a whole polycell, containing 16 pixels, has been made dead, and this is clearly seen in the maps. When comparing figs 5.29 with figs 5.23 and 5.21 the general background looks the same. In detail though, around the dead polycell there is an increase in the single pixel background and a decrease in the multiple pixel background. In the projections (fig 5.30) there are differences around the dead polycell (x ~200 cm), where the number of counts

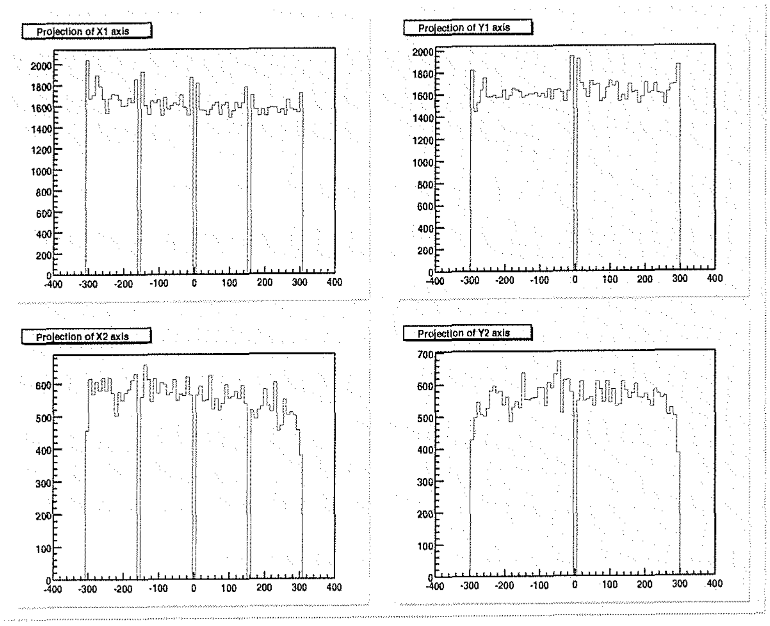

Figure 5.30: *Projection of the x and y axes of the PICsIT single and multiple pixel events. The top two figures refer to the single site events (X1 & Y1) and the bottom two refer to the multiple site events (X2 & Y2).*

recorded has decreased (cf. fig 5.23). In the y axis projection the number of counts recorded in the edge pixels (at -300 cm) is less and there is a trough followed by a peak (cf. fig 5.23). The trough is due to the missing pixels reducing the overall number of counts, but the peak is probably due to the increase in single site events around the dead polycell. Looking at the bottom two histograms in fig 5.30, which are the multiple site projections, there is the same drop in the number of counts due to the missing pixels but no evidence of peaks due to increased numbers of events. In both sets of projections it is hard to see the effects of individual dead pixels. The main expectations, lower multiple site events and increased single site events in the pixels adjacent to the dead pixels, are shown by the dead polycell, however the effect of an isolated dead pixel may be too small to see when one looks at the broad detector plane picture.

In SPI the effects of dead pixels would naturally be much more dramatic than in IBIS. If one whole detector failed then clearly the number of events recorded in the single detector mode would drop, and the numbers recorded in the multiple detectors, with and without 511 keV photons, modes would also drop. In the worst case if the central detector failed, the detector plane would only contain "edge" detectors and the numbers of events in the multiple detector modes would be decreased dramatically.

5.2.10 Source effects

The pattern seen on the detector plane when illuminated by a source will obviously be determined by the distribution of mass in front of the detector plane. The basic premise of the coded mask imaging technique is that any source shone through the mask will imprint the shadow of the mask onto the detector plane count rate map. Figures 5.31, 5.32 and 5.33 show the number of counts measured across the detector plane when the source is at 0,0 (theta, phi), 30,180 and 56,180.

In fig 5.31, the on axis source, one can clearly see the IBIS mask pattern in both the ISGRI single pixel and the PICsIT single pixel modes. In the scattered event modes (Compton and PICsIT multiple modes) the mask pattern is impossible to see. Deconvolution of the detector map to produce an image is beyond the scope of this thesis and is not discussed. The main points, as far as this thesis is concerned, are the ability to detect the mask pattern clearly with the single pixel modes and the uniformity of detection across the detector plane. It is clear to see that at low energies the mask pixels are very opaque and thus the pattern is very clear (ISGRI single), whereas at higher

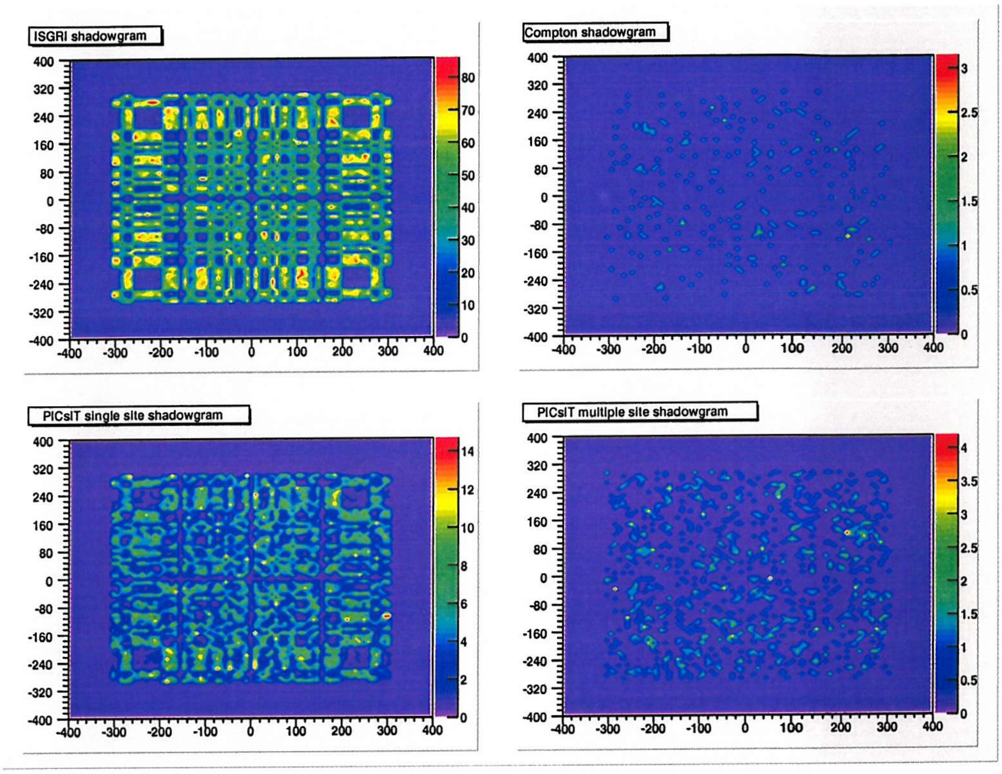

Figure 5.31: *Map of the IBIS detector plane, all four different modes, when illuminated by a source at 0,0 (i.e. on axis).*

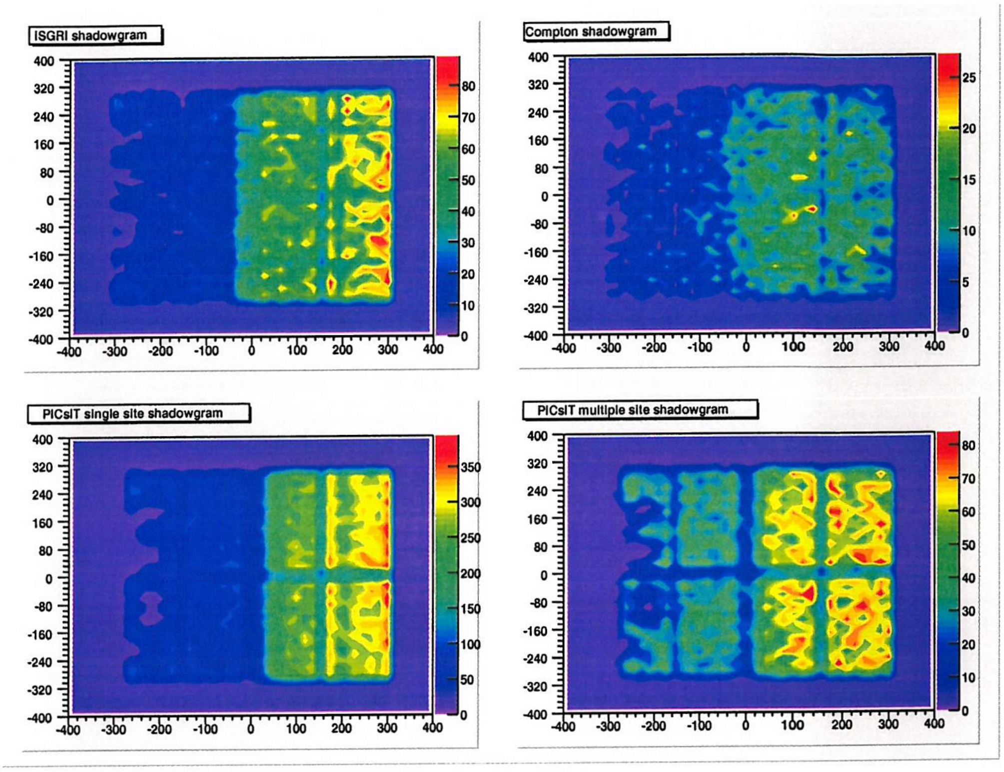

Figure 5.32: *Map of the IBIS detector plane, all four modes, when illuminated by a source at 30,180 (i.e. 30 degrees off axis on a line intersecting the centres of IBIS, JEM-X and SPI). This source intersects the IBIS hopper.*

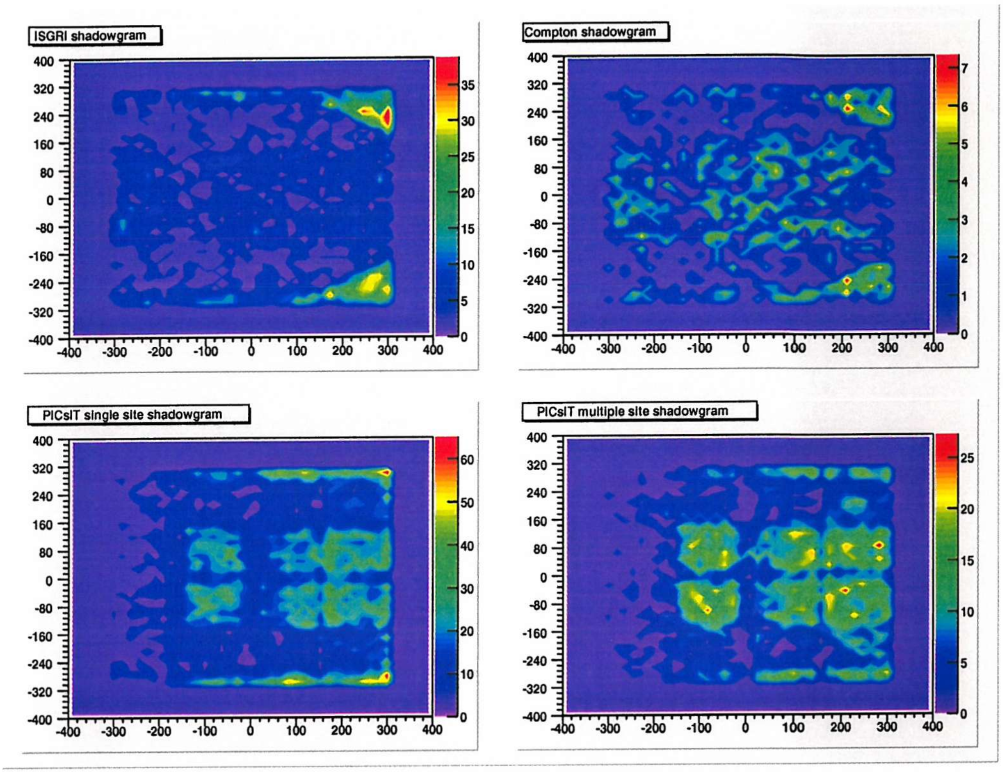

Figure 5.33: *Map of the IBIS detector plane, all four modes, when illuminated by a source at 56,180 (i.e. a source shining through the SPI UCR onto the IBIS plane).*

energies the mask pixels are less opaque and the pattern detected is less clear (PICsIT single). As sources move off axis other passive materials above the detector plane will become important and will distort the detected mask pattern (figs 5.32 & 5.33). With the source at 30,180 the IBIS mask pattern is not seen, and now the hopper dominates the spatial distribution of the detected events. In all four of the IBIS modes there is a clear trend in the number of counts recorded increasing towards positive x. The left hand four modules are in the shadow of the hopper and so very few events are seen in these modules. In the ISGRI and PICsIT single pixel modes, the number of counts seen increases as the module moves out of the shadow of the hopper (toward +x), the farthest right two modules having clearly the largest number of events within them. It is very interesting to note that the left hand edge of the farthest two right modules appears to have an increased number of events (the ridge of events at x $\sim$ 180 cm). This is due to an increase in the effective area of the detector pixels as the source sees not only the top of the pixel but also some of the side of the pixel. Towards x = 300 cm the number of counts reaches its peak, due to the decrease in passive materials between source and detector plane. In the scattered modes the picture is similar. In the Compton mode there is a definite increase in the number of events but there is not the same continual increase from left to right. The same is true of the PICsIT multiple pixel mode, though this also shows possible evidence of the SPI mask. In the two left most modules it is possible that the features present are caused by the thick tungsten blocks that compose the SPI mask. The difference in count rates between the modes is due to the spectrum of the source used (α = -2.2) and the transparency of the passive material. Those events which had a high enough energy to get through the passive material were more likely to be recorded in PICsIT and so the PICsIT modes have higher numbers of counts than ISGRI and Compton modes. At first it is surprising that the increase in number of counts recorded should begin earlier in ISGRI than in PICsIT. This is most likely due to the presence of the BGO veto, which surrounds PICsIT and thus provides not only extra active shielding, but to an extent extra passive shielding as well.

Figure 5.33 shows the detector plane map for a source shining through the SPI upper collimator ring (UCR) onto the IBIS detector plane. The collimator ring severly attenuates the input flux.

The effect of on axis illumination on the SPI detector plane is shown in figure 5.34. The 3 cm thick tungsten mask pixels are clearly very opaque and thus there is a great difference in the single detector mode between the counts detected through open and closed pixels. The multiple detector modes, which contain far less events, are less clear than the single detector mode. It is hard to see

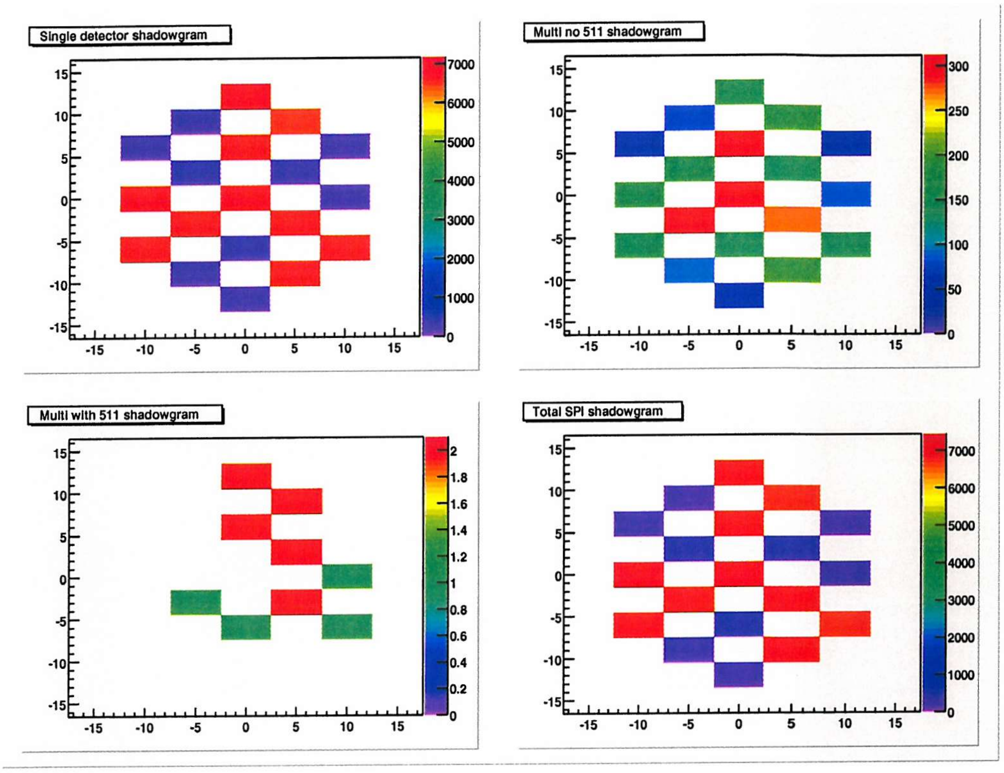

Figure 5.34: *Map of the SPI detector plane generated by illumination from an on axis source.*

any evidence of the mask pattern in the multiple detector background maps. The total detector plane map is dominated by the single detector mode and therefore clearly shows the mask pattern.

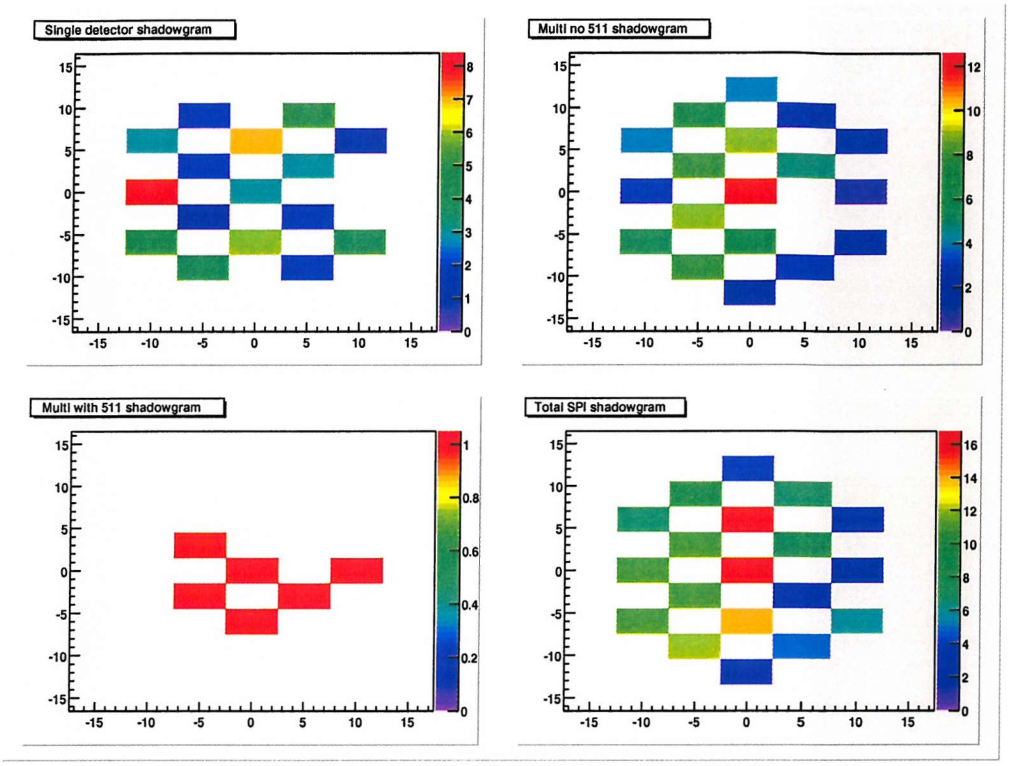

Figure 5.35: *Map of the SPI detector plane generated by illumination from an off axis source at 30,0 degrees.*

Figure 5.35 shows the effects of illumination by a source at 30,0 (30 degrees off axis in the direction of IBIS). The spatial map obtained from this observation is not very recognisable as anything. The source illuminates SPI through the IBIS mask and through the collimator rings of the SPI veto, thus the number of events recorded is very small (compared with the on axis source). The statistical quality of the data is poor, and there is no overall pattern. The multiple detector without 511 keV photons mode, shows the usual central concentration, but no other patterns are visible. The coarse nature of the SPI detector plane would naturally mean that to resolve the IBIS mask pattern would be impossible, though the massive BGO shielding around SPI makes this even more difficult.

5.2.11 Spatial variation of detector efficiency

As has been shown earlier the background varies across the detector plane due to passive materials between the modules and around the modules. Figure 5.36 shows the projections of the x and y axes across the detector plane of the detection efficiency for the PICsIT single pixel mode. This has been created by firing a parallel beam of photons straight down on to the detector plane. This was actually done below the mask so that effects caused by the varying shielding provided by the mask pixels are not included. At the detector plane the pixels recieve a uniform illumination, which can then be used to calculate the efficiency. As with the background there is a clear increase in the number of events recorded at the edges of the detector modules, which translates into an increase in the detection efficiency. Again, as with background, this is due to scatter into, and out of, passive material causing events that would otherwise be multiple pixel events to be recorded as only single pixel events.

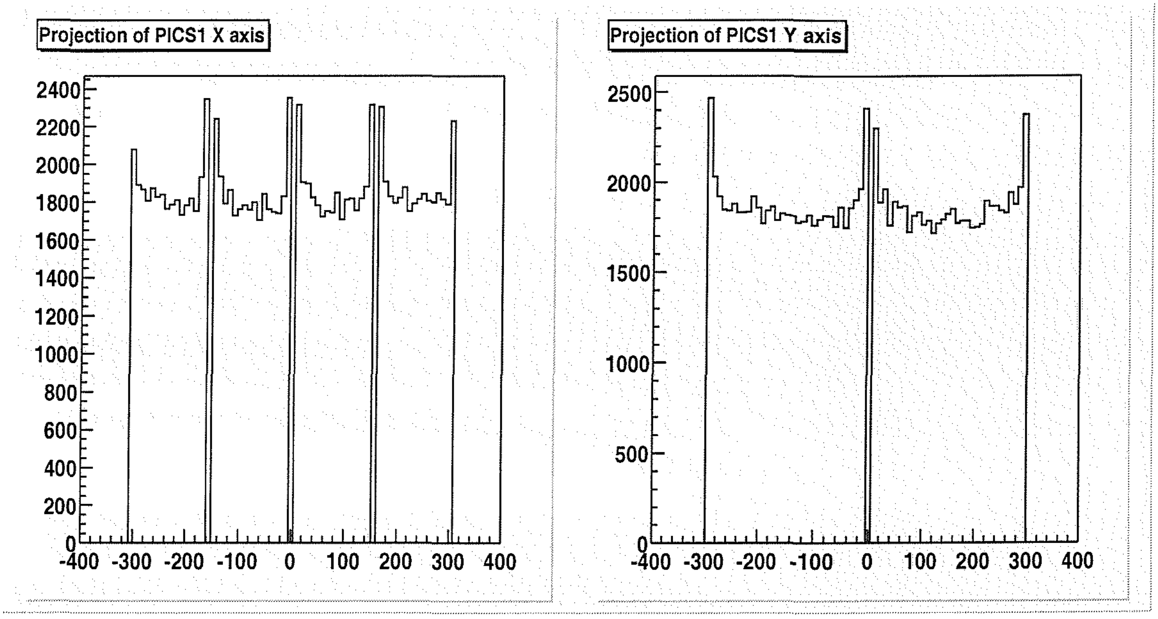

Figure 5.36: *Projection of the x and y axes of the IBIS detector plane showing, for the PICsIT single pixel event mode, the number of events recorded when a parallel beam of photons (20 keV - 10 MeV, power-law with* $\alpha = 10^{-5}$*) is input.*

To calculate the detection efficiency of the SPI instrument a flat spectrum of photons was fired

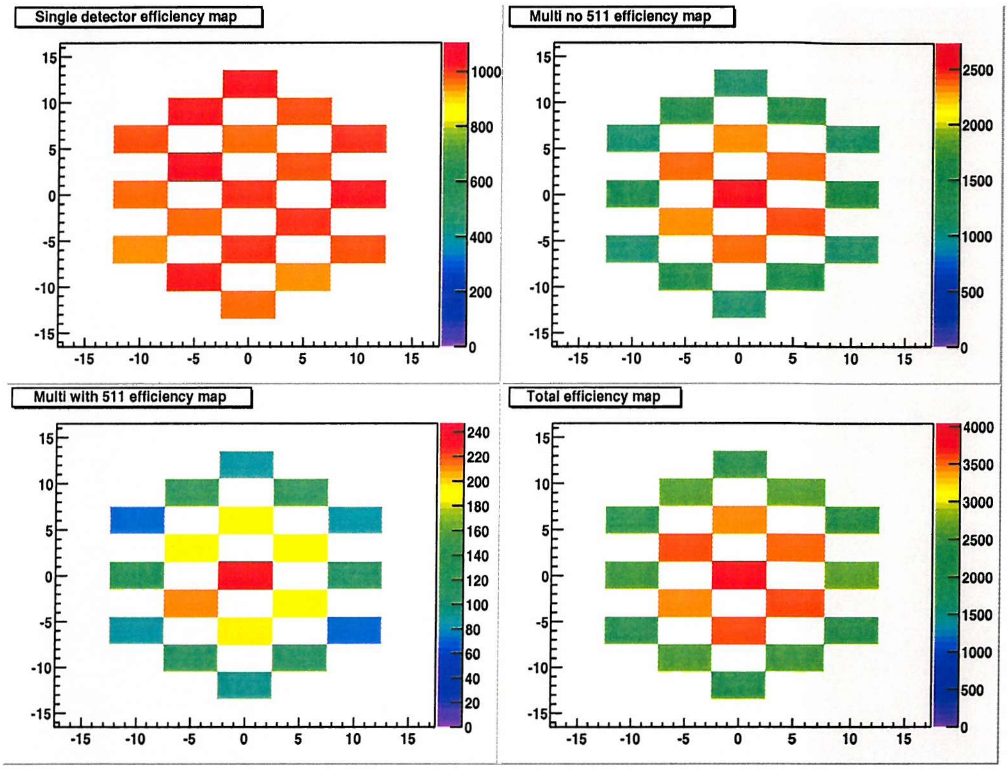

Figure 5.37: *Detector plane map of SPI. This has been created by firing into SPI a parallel beam of photons (20 keV - 10 MeV; power-law with* $\alpha = 10^{-5}$*).*

onto the detector plane from below the mask. Figure 5.37 shows that the single detector events lie uniformly over the detector plane. The nature of the multiple detector without 511 keV photons mode means that the detection efficiency is highest in the middle 7 detectors, where more events are recorded. This pattern, again due to the nature of the observing mode, is also repeated within the multiple detector with 511 keV photons mode. The total efficiency is therefore centrally dominated, due to the flat input spectrum, which creates more events within the energy range of Compton scatter and pair production mechanisms.

5.3 Evolution of TIMM results

Most of the results of TIMM have not changed much during the successive evolutions of the model. Most changes are of order <10%, and not factors of 10, which indicates that detailed modelling of the detector planes is crucially important. As long as the area immediately around the detector plane is modelled accurately the results probably will not change by more than 50% throughout successive model versions.

Between v1.0a and v3.4 of TIMM the background spectra and count rates, detection efficiencies, line and continuum sensitivities, and event spectra and count rates, of both IBIS and SPI, are all very similar. Variations are at most 50% in the spectra, and under 10% in the count rates, which in the context of mass modelling is very small.

This consistency in the products indicates that accuracy close to the detector plane is critical, but that the extra detail away from the detector plane is not so necessary. This may mean that during the life time of the mission it will be possible to generate background spectra and count rates with a very rough model. However, for effects like shadowing etc. a much more detailed model may still be necessary.

5.4 Critical appraisal of Mass Modelling and TIMM

When TIMM was proposed it was planned to allow optimisation of the instruments on INTEGRAL, to generate an understanding of the background pre-flight, to aid calibration, and generate in-flight background data-sets. The generated background could then be subtracted from the observations to improve the quality of data produced by INTEGRAL. At the time of proposal this was a very ambitious project. With the knowledge and experience gained at Southampton on other projects, such as modelling of the BATSE background, this is now a reasonable aim. These recent developments have lead to a more complete definition of Mass Modelling within the context of a major mission such as INTEGRAL. In this section the future role that Mass Modelling should have within a mission is defined using the knowledge and experiences of the TIMM project. This section forms both a critical appraisal of TIMM and Mass Modelling, and a guide for future missions. The aims of Mass Modelling, the phases a modelling project should go through and the work to be done in those phases are discussed, all with reference to TIMM.

5.4.1 The overall aim of Mass Modelling

The Southampton group are currently involved in a project to produce an all-sky survey, using a Mass Model to generate the background data, for the BATSE instrument. From the Southampton experience with the BATSE and TIMM projects it is now clear that two distinct types of Mass Model can exist: a Static Mass Model and a Dynamic Mass Model. TIMM is an example of a Static Mass Model, and the current BATSE Mass Model held at Southampton, is an example of a Dynamic Mass Model.

A Static Mass Model is one that is designed to allow calculation of non-varying quantities, such as the average value of the background count rate. This is useful in the pre-flight phase, for optimisation of the payload and spacecraft design and characteristics, and in the ground calibration phase.

A Dynamic Mass Model is one that is designed to allow an evaluation of dynamically changing quantities, such as the background count rate and spectra that would be measured during a complete orbit of the Earth in a low Earth orbit satellite. In this case the background will change with magnetic latitude, longitude and space craft attitude, and is therefore a more dynamic quantity.

Static and Dynamic Mass Models can use the same geometrical and chemical model, however, for the dynamic model further software will need to be developed, over and above the Monte Carlo simulation code, to account for all of the dynamic effects. Both the Static and Dynamic models will be required to allow the achievement of the goals of Mass Modelling, and it is the development of both of these techniques that will allow this aim to be realised.

In future missions the aims of Mass Modelling should be: to assist the development and optimisation of the spacecraft and payload; to allow pre-flight prediction and understanding of the background *and operational characteristics of the instrument; to enhance and improve the ground based and in-flight calibration of the telescope; and finally, to generate dynamically varying background data sets that can be subtracted from the observations to improve the telescope sensitivity.*

The ultimate goal of Mass Modelling is therefore to improve obervations, and this particularly for surveys (BATSE, INTEGRAL, SWIFT) is of fundamental importance to the γ-ray astronomy community. Production and usage of a model within a mission can be divided into several distinct phases:

- Phase 1: Design and optimisation
- Phase 2: Prediction of static characteristics
- Phase 3: Ground based calibration
- Phase 4: In-flight calibration
- Phase 5: Creation of Dynamic model and generation of background data sets
- Phase 6: Use of data sets to improve observations

Though these phases are envisaged as separated there will naturally be some temporal overlap.

5.4.2 Phase 1: Design and optimisation

This is the opening phase of any mission. Experience with TIMM shows that when an initial payload design has been created, a rough model can be created in a short time frame ($\sim$ 1 month). This will contain the detector in some detail (i.e. accurate chemical and geometrical information is necessary), and an accurate estimate of the detector's position relative to the remainder of the instrument mass.

Before the Mass Model is built, the choice of Monte Carlo simulation code to be used has to be made. This is dependant on the type of simulations required, but for a space based mission such as INTEGRAL, GEANT3/GCALOR was found to allow simulation of all the necessary particles over the appropriate energy ranges. This was extended to form the GGOD software suite and this is clearly an ideal Monte Carlo suite. At CERN work is currently being done to develop Geant4, and this will include many add on functionalities, which will cover many of those contained within GGOD. Therefore in future missions either GGOD or Geant4 (plus add on software packages) would be good choices of Monte Carlo code.

Once the package is chosen, the model is constructed. For TIMM it was decided to construct models that contain a minimal amount of detail in the early stages. From experience, it seems that it is necessary to have the detector modelled to high precision, but many of the other parts of the payload can be crudely modelled. In general as long as the mass and chemical distributions within the spacecraft are approximately correct, to within 10 - 20%, then the accuracy of the results will be reasonable. For TIMM the first model built (version 1.0a) has produced results that are still comparable to the current ones, within a factor of 2. Considering the changes to the spacecraft, and the enhancement of model detail, this is remarkably good agreement. Originally in the TIMM project it was envisaged to have three different models, with varying levels of detail, however in practice this has not been realised because it has not proved practical. For the purposes of optimisation of the payload, one very small part of the model may require very high detail, however the effect of this on the whole model may be minimal. The effort required to build a very detailed model of the entire preliminary design of the spacecraft and payload, which could be several man months, to test out whether the background is increased by moving the instrument 5 cm to the left is not merited.

Throughout the lifetime of a mission, one of the biggest stumbling blocks to the successful implementation of a model will be the information flow between the model team and instrument/spacecraft teams. This has been borne out within the INTEGRAL project, where the data flow has at times halted the whole modelling effort, and at other times swamped the modelling team. This variable data flow has been further compounded by the type and quality of data offered by the instrument and spacecraft teams. For building an instrument one needs different information than is needed for modelling it. Having dispensed with the idea that a complete model, to a very high level of detail is necessary in the optimisation phase, it is easy to see that knowledge of every nut and bolt on the spacecraft is unnecessary. Thus there are two different problems with data flow: firstly, the variable availability of the data, and secondly, the variable quality of the data. During the TIMM project no data has been received for months and then a deluge of data containing the exact size and shape of every nut on the instrument, but excluding their positions, has arrived. In both of these cases one can do nothing constructive. From the experience of TIMM, it is clear that knowledge of the chemical composition of a 1 mm diameter nut is not important, but the dimensions and positions of the detector plane crystals is fundamental. To ensure the construction, throughout the entire project and especially in the beginning, of accurate and successful model one needs to ensure good communication between the teams designing and building the instruments and those modelling them. On top of this one needs to ensure that both teams know what data is needed, and what data is irrelevant.

A further question that has arisen during the TIMM project with data flow is, what format should the data exchange take place in (i.e. Technical drawings, CAD files etc.)? During the lifetime of TIMM the data flow has been largely via technical drawings, though there has been some limited usage of EUCLID files. Computer Aided Design (CAD) drawings have not been used because there is no easy way to put these into GGOD, however if one used Geant4 then this is now possible. The variability of CAD formats though makes this option of questionable desirability. Technical drawings provide their own particular problems, apart from how to transport them, it can also be difficult to read them and translate what is shown into GEANT geometries on the computer. Computer files seem the easiest way to exchange data, however this is only true if everybody involved uses the same co-ordinate system, computer software and naming and numbering conventions for geometries and materials etc. In the case of TIMM this has not always been true, and transfer of computer files has therefore been difficult and sometimes unhelpful. It has been found over the course of TIMM's lifetime so far that the best way to exchange information is via technical drawings. Recently with the establishment of the TIMM mass modelling conventions, and with increased collaboration with the instrument modelling teams, it is hoped that data flow will improve and that information exchange via computer files will be made easier.

In summary, in this phase the initial decision as to the Monte Carlo code to be used has to be made and then the initial model has to be built. It is then possible to improve the detail as needed to carry out the design and optimisation investigations required. After a while the design of the instruments will become reasonably frozen and at this point most of the modelling effort moves onto predicting the in-flight characteristics of the instrument.

5.4.3 Phase 2: Prediction of static characteristics

Once a fairly stable instrument design has been settled upon, then it is time to improve the detail in the model and generate the preliminary estimates of the instrument characteristics. This is the phase that TIMM has been in for that last few years, and generally this phase will last most of the pre-flight mission time. The process of updating the detail within the model has many of the same problems as building the initial model, in particular with respect to data flow and exchange issues.

Improving the model really requires updating those components nearest to the detector planes, and those components fundamental to the instrument operation. Obviously the material nearest the detector plane will have the most effect on the results and good detail here is of great importance. It is also true that in some types of instruments, coded aperture systems for example, there are other parts of the telescope where high levels of detail are necessary. In the case of TIMM, the masks of IBIS, JEM-X and SPI need to be modelled in high detail, as errors here will distort the quantities generated in simulations. A further important component to get correct is the shielding, again in TIMM the active shields are very important, but also in particular for IBIS, the passive hopper and tungsten walls are very important. Clearly then, one can devise several rules of thumb as to which parts of the model need to be modelled in high detail and which don't. The detector crystals, all material adjacent to those crystals and any material between them and any veto systems have to be detailed. Active veto shielding, plus adjacent passive material, has to be detailed. Passive shielding, such as hoppers and collimators, also require high detail. Finally, any other parts of the imaging system, such as coded masks etc, require detailed construction. All of the other parts of the instrument and spacecraft can be put in very roughly, though it is always wise to improve these to a reasonable standard. At all costs the essential parts of the instrument have to be detailed, but the other parts can be detailed as required depending on available man power, information, disk space, cpu time, etc. Clearly these external factors, though not directly a feature of the model, will be very important. The more detail required, the more information that will be needed, and the more man power that will be needed to collate and understand the information, as well as to build the model. The disk space and cpu time available are really very important in the context of modelling, but the advances in computer technology mean that this area is ever changing. In 1996 at the start of TIMM, the disk space available was limited to a few Gigabytes on Sun Sparc machines. To carry out a complete TIMM background simulation would use all the available disk space and take about 1 month of solid cpu time. In an astronomy group like Southampton's this is impractical, though in a dedicated institute this might have been acceptable. By 1997, the TIMM team had secured usage of the IBM SP2 machine at Southampton university. This offered 30 nodes (separate computers) and thus the time to run the model could be cut down to 10 days or so, though because this was a central university computer the queueing time meant that model runs still took at least 1 month to carry out. Towards 1998 - 1999 the fall in the price of PC's, and the increase in their specification, meant that the Southampton group set up a Linux PC cluster. This contains at least 12 PC's (400

MHz and above) and has a total disk space of over 150 Gigabytes. With this current set up complete mass model runs can be done in just over a week. In the near future the increases in PC clock speed and memory could cut this turn around time down further. Clearly though, the more detailed a model the longer the run time will be, and the more information that is stored from the simulations, the more disk space that will be required. Therefore a certain amount of optimisation is required to ensure a sensible turn around time and a sensible usage of disk space.

When one tries to produce an estimation of the background within telescopes as would be measured in space, one needs more than just the telescope geometry, one also needs the logic through which the events are processed. This includes things such as the energy thresholds, energy resolution, event modes and the order in which thresholds and active vetoing are applied. Ideally during this phase the logic of the system can be optimised or developed, with or without mass model help. If the modelling team uses the same logic and file format as the instrument teams, then model output can be used to test the development versions of the mission analysis code. Within INTEGRAL this has not been the case. In future missions better dissemination of results by the modelling team, and better feedback and communication between the instrument teams, analysis software development teams and the modelling teams would be better. It would be of more use to the whole project if the model results could be analysed by the analysis software, providing both checks on the model results and on the analysis software. Use of the actual analysis software would allow one to produce the same outputs as for the real data, in the exact same way as for the real data, and would thus quantify the Mass Model results. An ideal situation for future missions would be to locate the modelling and analysis software writing teams at one institute, thus ensuring better communication.

5.4.4 Phase 3: Ground based calibration

This is the current phase that the INTEGRAL mission and TIMM are entering. Some preliminary calibration simulations have been carried out, and further simulations will be run in the second half of 2000. Two possible ways to carry out this phase are: 1) to carry out the actual measurements recording positions, sources, etc. and then to attempt to simulate and understand the results; and, 2) to simulate sources at various positions in an attempt to understand the accuracy of the various parameters to be recorded and plan the tests accordingly, and then to carry out the calibration and then the simulations.

The second of these approaches has been decided on as the way forward for INTEGRAL. Up to this time, simulations of sources within a room of approximately the correct dimensions have been carried out to understand what may happen. In the near future the effort will move onto looking at the accuracy with which one needs to know the positions of the sources, relative to the room and the payload. When this has been done it should be clear what information needs to be recorded, and the accuracy to which it needs to be measured, during the calibration phase. Post-calibration, simulations will be run and effort will be made, by both the modelling team and the instrument calibration teams, to understand the results. If this can be successfully done, then both the model and the instruments will be calibrated.

5.4.5 Phase 4: In-flight calibration

After launch the change from a Static Mass Model to a Dynamic one should begin. The in-flight calibration phase will initially involve using the static model to understand what is going on. For INTEGRAL, which is in a high Earth orbit, this may work well. However, for a low Earth orbit mission, it is much more likely that a dynamic model will be necessary. The period of a high Earth orbit is long ($\sim$days) giving an individual observation of an hour or so a reasonably constant background, thus allowing the use of a static model, probably with some normalisation of the background level. However the period of a low Earth orbit is short ($\sim$90 mins) and so the background will vary over the length of an observation quite dramatically, thus a dynamic modelling approach may be necessary. For INTEGRAL observations of order 10^5 - 10^6 seconds in length are expected and so for these cases a dynamic approach is also necessary.

The simplest form of dynamic approach would obviously be to generate normalisation factors for the various background components that change with magnetic latitude, longitude and spacecraft attitude. The challenges of in-flight calibration of a Mass Model are as yet unknown, though should not be underestimated. Effects such as blinding within the veto shields, which may not show up during ground calibration with photon sources, may have a noticable effect in orbit. This phase is crucial to the successful achievement of the goals of Mass Modelling, but is by no means simple.

5.4.6 Phase 5: Creation of Dynamic model and generation of data sets

Once the satellite is in orbit, then the model required will be truly dynamic. This will probably use various quantities from the spacecraft telemetry, such as altitude, atitude, latitude, longitude, time etc., to calculate the background. This is a complicated procedure which the Southampton group has recently succeeded in proving with the BATSE instrument. Using this type of approach background data sets can be generated for any position within the orbit, at any time after launch.

5.4.7 Phase 6: Use data sets to improve observations

Subtraction of the background data from the observed data, will hopefully leave only source data. However, for an observation of a single source there may be contamination due to multiple sources in the field of view. For INTEGRAL this should not be a problem because coded aperture systems allow multiplexing. The main usage of the background data is not observations of a single source, but surveys, where a series of pointings collected over months or years are used to generate a map. For INTEGRAL, the TIMM generated data, will be used to improve the sensitivity of the Galactic Plane Survey. In the case of BATSE, the Southampton group, are on the way to producing the first sensitive all-sky map, in the energy range 20 - 120 keV, using data collected from the last 8 - 9 years. In the future it is hoped to improve on this map using the same techniques with the SWIFT satellite.

5.5 Summary

In this chapter the results of the latest run of TIMM have been presented. Not only have the basic quantities been presented, but also maps of their spatial variation across the detector plane. The evolution of the TIMM results has been briefly mentioned. The general strategy that future models should follow, using the lessons of TIMM, has also been discussed.

The results of TIMM have been consistent from the initial models (v1.0a) right through to the current model (v3.4). The sensitivity of IBIS is seen to be dominated at low energies by the ISGRI single pixel events, and then at higher energies by the PICsIT single pixel and then multiple pixel modes. The Compton mode does not appear to contribute significantly to the sensitivity of IBIS. In SPI it has been seen that the single detector mode will dominate the sensitivity of the detector. The background in IBIS appears to be largely dominated by continuum, and when the energy resolution is factored in, this will be even more correct. In SPI the opposite is the case, the background is line dominated due to induced radioactivity.

From the background maps it has been seen that there are many effects present which one must have some knowledge of, and whose importance is only just being realised. Though deconvolution has not been attempted here, as it is beyond the scope of this thesis, it is fair to say that the edge effects present in both IBIS and SPI will produce artefacts within the deconvolved images. How important these prove to be will only be discovered later on in the project. From the maps presented it is clear that not only does the background vary across the detector plane, but also the efficiency varies, and therefore so does the sensitivity. Investigation of this is also beyond the scope of this thesis, but clearly the ability to detect off axis sources is important for survey work and thus this may have to be investigated in the future.

The most important characteristic for any instrument is the sensitivity. This is determined by both the background and the dead time of the instrument. Within IBIS there is concern that the dead time is too high, and several strategies have been proposed to solve this problem, whilst maintaining the sensitivity. The investigation of these strategies using TIMM is discussed in the following chapter.

Chapter 6

Vetoing strategies for IBIS

6.1 Introduction

Once a mass model has been constructed it is then possible to use it to optimise the instrument design. This chapter presents an example of instrument optimisation using TIMM.

As mentioned in earlier chapters, most modern γ-ray telescopes employ active veto systems to reduce the background. Vetoing is done by searching for coincidence signals within the detector plane and the active shields surrounding it. If no coincidence signal is found then the count is accepted as genuine. As discussed previously, the INTEGRAL background comes in the form of charged particles, γ-rays and induced decays. Many of todays γ-ray telescopes employ a thin plastic scintillator over the aperture as a charged particle veto (see figure 6.1). In general a plastic scintillator (of $\rho \sim$ 1g/cm^3) with a thickness of 1 - 2 mm will be transparent to γ-rays, however a minimum ionising proton will deposit $\sim$2 MeV/g. Therefore, deposits within the plastic scintillator can be attributed to charged particles. Active shielding around the side and bottom of a detector plane is based on similar principles, however these tend to be thicker and of denser materials so as to detect γ-rays as well as particles (figure 6.1). The plastic scintillator vetoes out all charged particles coming through the aperture, whereas the side and bottom crystals veto charged particles and γ-rays from outside the aperture. Decay products from within the active veto crystals are vetoed in the same way as other particles and photons. However, because of the necessity for coincident signals any radioactive decay products which deposit their energy wholly within the detector plane cannot be

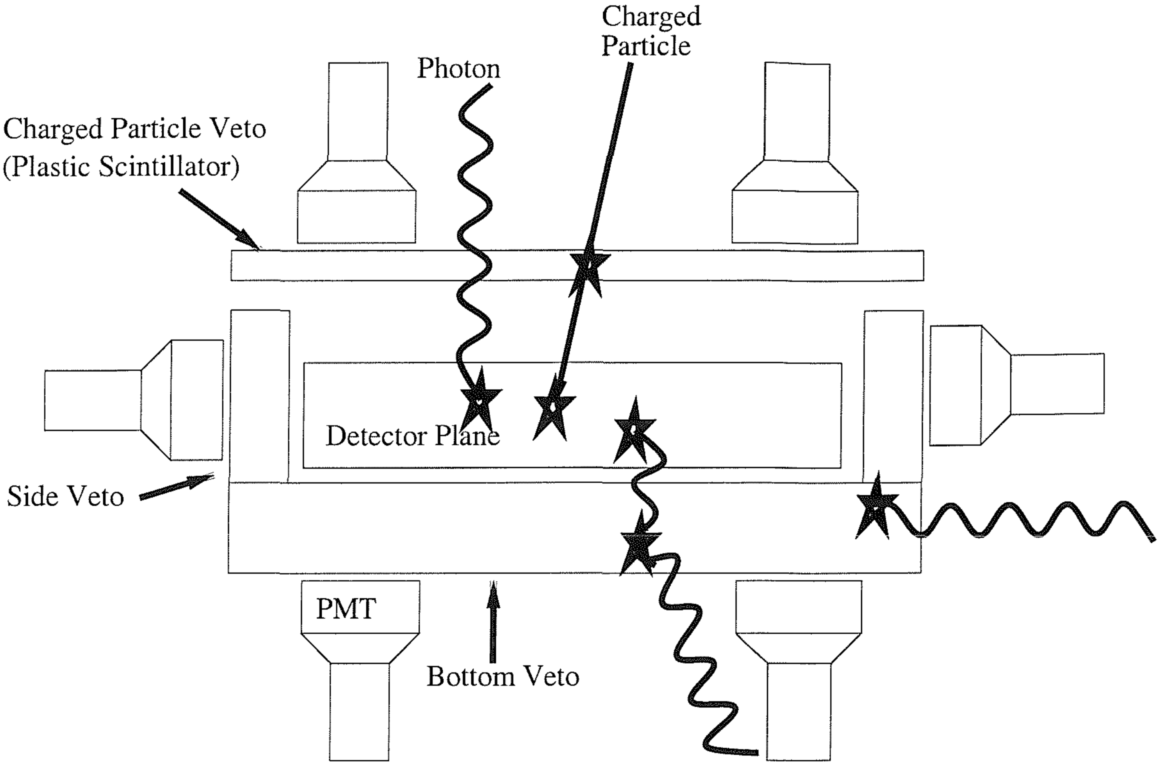

Figure 6.1: *Simplified model of an active veto shielded detector.*

vetoed.

6.2 The IBIS veto

Unusually, IBIS doesn't have a plastic scintillator (see figure 6.2). This is compensated for by ISGRI, since any particles which enter through the aperture can be vetoed by their large energy deposits within the ISGRI pixels. Around the side and bottom of the two detector planes is the BGO active shielding (figure 6.2). Between the detector plane and the mask there is passive shielding, in the form of tungsten (and tin), which stops lower energy γ-rays and thus limits the detector planes field of view. IBIS also has a calibration source attached (figure 6.2) that contains its own BGO veto unit (The Calibration Tagging Crystal).

IBIS, in common with almost all other γ-ray telescopes, normally operates with a full veto. This means that a coincident signal in any of the BGO crystals (or a charged particle flag in ISGRI), will cause all of the detector plane modules to be read out and any events therein to be discarded. While this minimises the background count rate, simulations indicate this causes a major problem: high dead time. When the detector plane records an event the detector plane modules are read-out, if a signal is recorded within the veto then the detector plane is shut down. This means that for a small period of time ($\sim 20\mu$s for a real event and 3 μs for a vetoed event) no other events can be recorded, this is called the dead time. The percentage dead time will depend upon the count rate in both the veto and the detector plane. Currently with a full veto the IBIS dead time is estimated to be $\sim$ 20%, which means that IBIS is effectively observing for only $\sim$ 80% of an observation. The real problem is therefore, how to reduce the dead time (and maximise the effective observing time) whilst maintaining a low background (and thus preserving sensitivity). Two possible solutions have been suggested:

- Zoning (or segmenting) the IBIS veto. Normally an event anywhere in the veto shields causes the whole of the detector plane to be shut down. In the case of a zoned veto only the parts of the detector plane nearest the veto module where the signal was recorded would be shut down.
- Raising the BGO low-energy thresholds. The veto crystals (like those of the detector plane) have low-energy thresholds below which events are not detected. Varying the energy this is set at will determine the number of events recorded. The higher this threshold is set, the higher the background count rates will be, but this will in some part be offset by the reduced number of veto signals and hence the reduced dead time.

6.3 Zoning the IBIS veto

A zoned veto would minimise the dead time, hence increasing the useful observing time, by only rejecting interactions in the detector plane module(s) adjacent to the triggered veto module. Instead of reading out the whole detector plane (all 8 modules), one might only read-out the 4 modules adjacent to the veto crystal within which the signal occurs. This would mean half the detector plane would still be able to detect incoming photons and so the dead time is effectively reduced. The veto system is composed of 8 BGO modules on the bottom and 8 on the side. The ISGRI and PICsIT

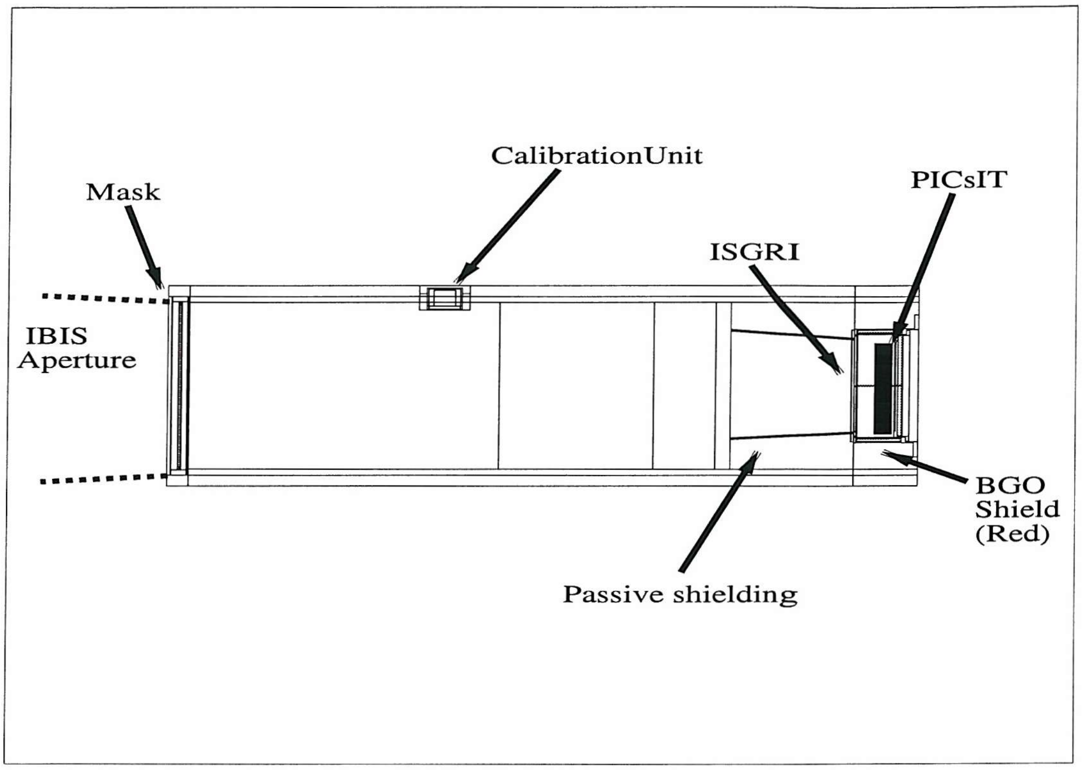

Figure 6.2: *Geant++ drawing of the IBIS istrument produced using the IBIS model from v3.3 of TIMM.*

detector planes are each split into 8 modules which sit above the 8 bottom modules of the veto, and are surrounded by the veto's side modules. The nature of the ISGRI and PICsIT detector planes lend themselves to zoned vetoing, which would be applied at the module level. While zoning reduces the effective dead time, there is a price to pay, and that is an increase in the background count rate within the detector plane. This would be caused by multiple scatter events, which previously could have been vetoed as one event, and now might only get partially vetoed. In some modules the event would be recognised as background and ignored, whereas in others it would be accepted as signal. Any event Compton scattering off of the side shield with a scatter angle ~90° could potentially travel across the detector plane far enough to be recorded as signal.

In this section a series of zoned veto set-ups are considered, from full veto to one detector plane module at a time, and evaluated using TIMM. Each of the set-ups are evaluated in terms of dead time and relative continuum sensitivity. In all cases the overwhelming factor which determines the success or failure of a set-up will be the relative continuum sensitivity. Whilst reducing dead time is an important aim, the sensitivity has to be maintained at the very least.

6.3.1 The Set-ups

Figure 6.3 presents a numbering scheme for the veto crystals and a lettering scheme for ISGRI and PICsIT detector planes. The veto systems are presented in table 6.1. The first column contains the veto modules numbered 1 to 16. Subsequent columns list the various zoned set-ups (zoned 1-5) and the ISGRI/PICsIT modules vetoed by the relevant veto module. Zoned 1 represent the most localised form of set-up, where just the adjacent modules are vetoed. Zoned 2-4 represent step wise increases in the number of modules vetoed. Set-ups 1-4 consider how many detector modules each veto crystal should cover. Set-up 5 considers things from the opposite perspective, by having 4 veto modules to each detector module.

6.3.2 Method

The dead time is calculated from the background count rate within the detector plane and the count rate in the veto crystals. These were calculated from simulations of the standard background components at solar maximum. The results were analysed for a full veto system and for the various zoned veto set-ups. For full veto mode all 8 ISGRI and PICsIT modules are vetoed when any BGO

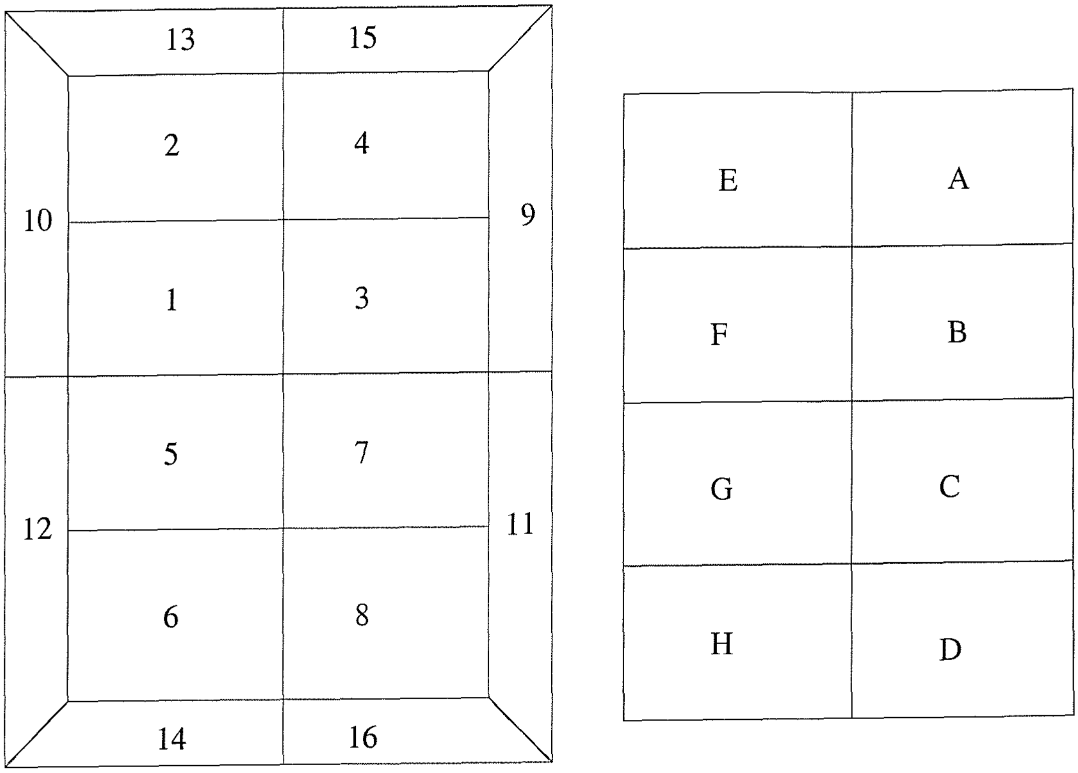

Figure 6.3: *Numbering scheme for the Veto modules and lettering scheme for the ISGRI and PICsIT modules. From this and table 6.1 each of the zoned veto patterns can be worked out.*

			Set-up		
Veto Module	Zoned 1	Zoned 2	Zoned 3	Zoned 4	Zoned 5
1	F	E,F,G,B	B,E,F,G,A	B,C,E,F,G,A	E,F,G
2	E	A,B,E,F	A,B,E,F,G	A,B,C,E,F,G	E,F
3	B	A,B,C,F	A,B,C,E,F	A,B,C,E,F,G	A,B,C
4	A	A,B,E,F	A,B,C,E,F	A,B,C,E,F,G	A,B
5	G	F,G,H,C	D,F,G,H,C	B,D,F,G,H,C	F,G,H
6	H	C,D,G,H	C,D,F,G,H	B,C,D,F,G,H	G,H
7	C	B,C,D,G	B,C,D,G,H	B,C,D,F,G,H	B,C,D
8	D	C,D,G,H	B,C,D,G,H	B,C,D,F,G,H	C,D
9	A,B	A,B,C,E	A,B,C,E,F	A,B,C,E,F,G	A,B
10	E,F	A,E,F,G	A,B,E,F,G	A,B,C,E,F,G	E,F
11	C,D	B,C,D,H	B,C,D,G,H	B,C,D,F,G,H	C,D
12	G,H	D,F,G,H	C,D,F,G,H	B,C,D,F,G,H	G,H
13	E	A,E,F,G	A,B,E,F,G	A,B,C,E,F,G	E
14	H	D,F,G,H	C,D,F,G,H	B,C,D,F,G,H	H
15	A	A,B,C,E	A,B,C,E,F	A,B,C,E,F,G	A
16	D	B,C,D,H	B,C,D,G,H	B,C,D,F,G,H	D

Table 6.1: *Table summarising the various zoned set-up patterns. Combining this with figure 6.3 one can see what each pattern means.*

	FULL VETO	ZONED 1	ZONED 2	ZONED 3	ZONED 4	ZONED 5
ISGRI	447.6	667.5	542.8	518.3	496.3	643.4
Compton	65.6	148.5	82.9	76.3	71.9	120.0
PICsIT	1827.7	3220.1	2215.3	2093.1	2014.8	2844.5
Total	2340.9	4036.1	2841.0	2687.7	2583.0	3607.9

Table 6.2: *Count rates (count/s) for IBIS veto set-ups. PICsIT contains both the single and multiple pixel modes.*

veto module is triggered.

In the analysis code the first step is to split the interactions up according to the detector in which they occur. At this point the lower energy thresholds are also applied. These are 15 keV for ISGRI, 100 keV for PICsIT (at detector pixel level) and 100 keV BGO veto (at module level) and there is an energy window of 350 keV to 2 MeV for the calibration source. The veto and then upper thresholds are applied. These are 600 keV for ISGRI and 5 MeV for PICsIT. All counts above 600 keV in ISGRI and 5 MeV for PICsIT are rejected. The events are then put into the four observing modes for IBIS: ISGRI single pixel, Compton, PICsIT single pixel and PICsIT multiple pixel.

Once the background and veto event rates are known, it is then a case of calculating the dead time. This was done assuming a gate time of 4 μs. The systems were then evaluated to find out which one has the lowest relative continuum sensitivity.

6.3.3 Results

The total background count rates of ISGRI, PICsIT and Compton events are shown in the table 6.2. The veto event rate measured in the full veto case is ~32,300 counts/s. This represents all the interactions with the BGO veto. When this is combined with the dead time due to the calibration source (~5.6%) this gives the total dead time of the system. When the zoned veto is used the dead time will be a fraction of that calculated for the full veto case. The total percentage dead times are presented in the table 6.3. These are worked out by taking the fraction of the veto that is used per PICsIT module (on average) and multiplying the veto event rate by it. Another, arbitrary, factor of 1.25 is used to account for the probable rise in the veto event rate. This takes into account the

	FULL VETO	ZONED 1	ZONED 2	ZONED 3	ZONED 4	ZONED 5
Module ratio	16	2.5	8	9.5	12	4
% Dead Time	18.55772	8.14928	13.7073	15.2233	17.7493	9.66528

Table 6.3: *Dead Times (%) for IBIS veto systems. The module ratio represents on average the number of BGO veto modules to each ISGRI or PICsIT module.*

	Continuum Sensitivity (F)	Relative Continuum Sensitivity
FULL VETO	53.6126	1
ZONED 1	66.2887	1.2364
ZONED 2	57.3784	1.0702
ZONED 3	56.3057	1.0502
ZONED 4	56.0393	1.04526
ZONED 5	63.1975	1.1788

Table 6.4: *Continuum and Relative Continuum Sensitivities for IBIS veto set-ups. The relative sensitivity is relative to the full veto sensitivity.*

fact that the veto crystals now act independently of each other (e.g. an event which interacted in 2 BGO crystals previously would be counted as 1 veto event but now is 2). While this is rough the results should not change too much when calculated in depth.

From these two variables the continuum sensitivity (F) was calculated using the following formula:

$$F \propto \sqrt{Background/Time}$$

The results obtained by doing this are given in table 6.4.

6.3.4 Conclusion

Having one veto module to veto an adjacent ISGRI/PICsIT module is unfeasible (zoned 1), however modifying this by vetoing half of ISGRI/PICsIT at a time works better (zoned 2). The more modules that are vetoed the better the relative continuum sensitivity gets (zoned 3 and 4).

As expected zoning the veto can be used to decrease the dead time, however the background count rate has been shown to increase in response. It has been found that these two factors combine to degrade the sensitivity when zoned vetoing is applied. Zoning of the BGO veto modules will not improve the continuum sensitivity of IBIS. At a higher veto rate the optimised systems sensitivity becomes closer to that of the full veto and if the projected background flux were to increase then possibly either zoned 3 or 4 may become feasible.

6.4 Raising the BGO low-energy threshold

The second suggested solution to the high dead time problem was to raise the low-energy thresholds of the IBIS BGO veto modules. This would lower the count rate within the veto crystals (and so reduce the dead time) but would result in an increased background count rate. Once again dead time has to be reduced whilst maintaining sensitivity. In this section the dead time and background count rates are compared for 5 different thresholds: 100, 150, 200, 250 and 300 keV. The full veto was applied as before and background count rates and veto event rates were obtained from which the dead time and sensitivity was calculated.

6.4.1 Results

Table 6.5 shows the measured background counting rates and the veto event rates. The background count rate is composed of all the events in ISGRI and PICsIT which are unvetoed. This includes single site plus Compton event categories. The BGO event rate includes the side and bottom BGO crystals and the BGO calibration tagging crystal. Having obtained the background count rates and the veto event rates (tab 6.5), the dead time and continuum sensitivity are calculated (table 6.6).

6.4.2 Conclusion

The IBIS sensitivity appears to get worse (a higher value) if the low-energy thresholds on the BGO veto modules are raised. The higher the low-energy threshold, the larger the background counting rate, and the worse the sensitivity. This is an impractical way to resolve the IBIS dead time problem whilst maintaining the sensitivity. However if some small loss in sensitivity is accepted then this may be a practical solution.

Threshold (keV)	Background (cts/s)	Veto Event Rate (cts/s)
100	1849.4	20505
150	1891.3	19395.8
200	1947.5	17471.4
250	2004.3	16589.3
300	2059.9	15838.2

Table 6.5: *Summary of the background count rate and the veto event rate for IBIS, when different BGO veto low energy thresholds are applied.*

Threshold	Dead time	Cont. Sens.	Rel. Sens.
100	0.13802	46.31982	1
150	0.1335832	46.7215	1.0087
200	0.1258856	47.20137	1.019
250	0.1223572	47.7884	1.0317
300	0.1193528	48.363986	1.0441

Table 6.6: *The threshold, dead time, continuum sensitivity and relative continuum sensitivity for various veto thresholds. The thresholds are given in keV, the dead time is a fraction and the relative sensitivity is given relative to the 100 keV threshold.*

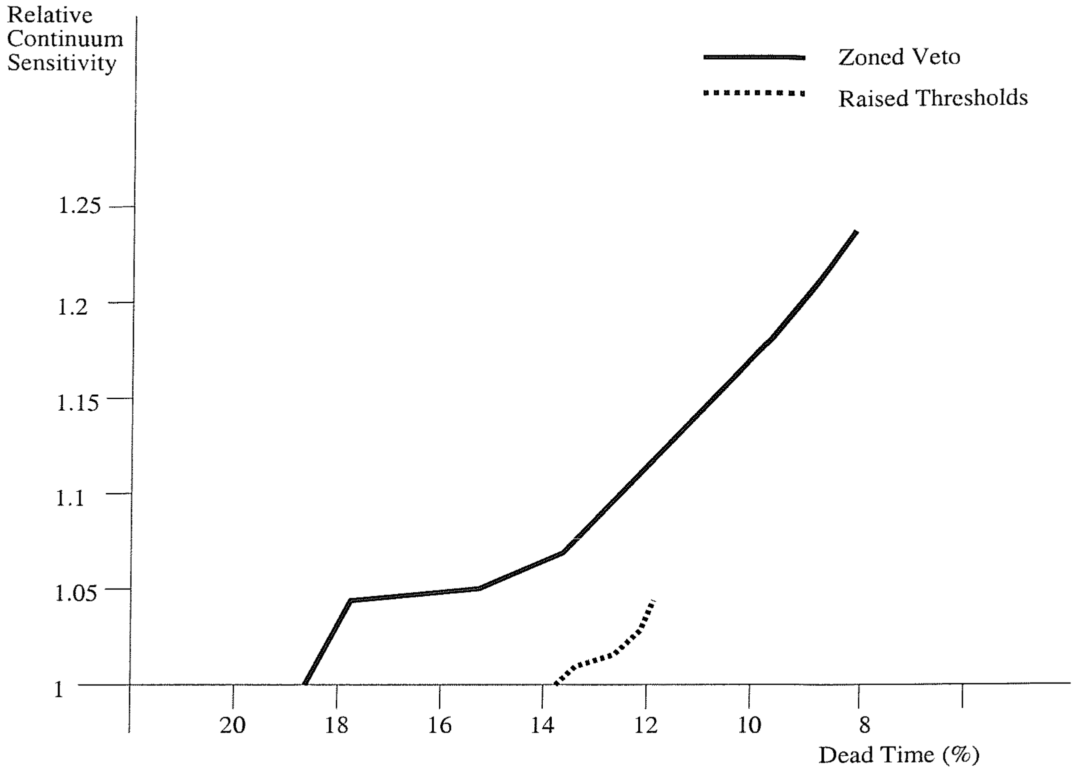

Figure 6.4: *Comparison of the change in relative continuum sensitivity against dead time for zoned veto systems and higher thresholds.*

6.5 Summary

Two alternatives for solving the high dead time problem within IBIS, whilst maintaining the sensitivity, have been investigated using TIMM to model the background and veto count rates. The investigations used different versions of TIMM, with different geometries and output event modes, and so the results are not directly comparable, however the relative trends are still valid. It has been shown that neither of the methods can solve the dead time problem whilst maintaining the sensitivity. However, figure 6.4 shows a comparison of these two methods in terms of relative continuum sensitivity and dead time. It is clear to see that if some loss of sensitivity could be tolerated then the most effective way to reduce the dead time would be to raise the IBIS veto low-energy thresholds.

The IBIS ICDR gives the veto schemes that the IBIS team are currently planning to use in-flight. For PICsIT there are two schemes, one of which has 5 veto modules per PICsIT module, and the second of which has 7.5 veto modules per PICsIT module. Both of these work out somewhere between the zoned 2 and zoned 5 set-ups, and therefore from the results presented here, it can be predicted that these set-ups will not reduce the dead time while maintaining the sensitivity.

Chapter 7

X-/γ-ray observations of 47 Tuc

This chapter presents X-/γ-ray observations, using both the Rossi X-ray Timing Explorer (RXTE) and BeppoSAX satellites, of the nearby globular cluster 47 Tuc. In the first two sections the rationale for observing this source is briefly presented, then the historical observations are reviewed, followed by the new observations. Section 7.6 discusses the new results and conclusions are drawn in section 7.7.

7.1 Introduction

The nearby globular cluster 47 Tuc has previously been surveyed by many X-/γ-ray satellites looking to detect high-energy emission from millisecond pulsars (MSPs; see section 7.3). Its stellar population and dense core have long made it one of the favourite places to look for MSP emission. MSPs, or recycled pulsars as they are sometimes called, are generally formed when an old pulsar is spun up to a short period via accretion in a binary system (see Bhattacharya & van den Heuvel 1991 for a complete review of MSPs). It is the requirement for the pulsar to have been in a binary that makes objects such as 47 Tuc the most promising places to look for MSPs.

In the conventional scenario, a neutron star either captures a main sequence or (sub)giant star via tidal interaction or forms a binary via an exchange encounter (Bhattacharya & van den Heuvel 1991). Either option results in a close binary system. MSPs are assumed to be the end products of low mass X-ray binary evolution, where the neutron star is spun up to a millisecond period during an accretion phase. Eventually, evaporation of the companion or ionisation of the binary can lead to the formation of an isolated MSP (Bhattacharya & van den Heuvel 1991).

Theoretically therefore, an association such as 47 Tuc should contain many binary and isolated MSPs. This expectation has been backed up by radio results that have shown 47 Tuc contains at least 20 MSPs (Camilo et al. 2000, Robinson et al. 1995, Manchester et al. 1991; table 7.1).

7.2 Why should X-/γ-ray MSP emission be visible from 47 Tuc?

In this section hard X-ray/γ-ray MSP emission theories are briefly presented, and using the published radio observations, the expected X-/γ-ray luminosity of 47 Tuc is calculated.

7.2.1 Binary MSP emission

Tavani (1993) estimated the X-/γ-ray luminosity of binary MSPs assuming the emission comes from a shocked region, where the material evaporated off of the companion star and the wind from the pulsar collide. Using this theory, and assuming a power-law index of -2, Ford et al. (1996) calculated the X-/γ-ray emission from a single binary MSP in 47 Tuc to be $\sim 1.3 \times 10^{33}$ erg/s. Taking the number of binary MSPs from the radio results of Camilo et al. (2000), and the X-/γ-ray luminosity for a single binary MSP of Ford et al. (1996), one can calculate the expected X-/γ-ray luminosity from the 47 Tuc binary MSPs to be $\sim 1.7 \times 10^{34}$ erg/s.

7.2.2 Isolated MSP emission

Chen (1991) estimated the emission in hard X-rays/γ-rays from an isolated millisecond pulsar, assuming that the fast spin periods would balance the weak magnetic fields, and that they were therefore similar to younger pulsars like the Crab and Vela (Eqs. 7.1 & 7.2).

$$l_\gamma = 7.8 \times 10^{32} p \qquad \text{for p} < 14.5 \text{ ms} \tag{7.1}$$

$$l_\gamma = 2.4 \times 10^{36} p \qquad \text{for p} > 14.5 \text{ ms} \tag{7.2}$$

Source	Period (ms)	Binary Status	Orbital Period (days)
47 Tuc C	5.756780	No	
47 Tuc D	5.357573	No	
47 Tuc E	3.536329	Yes	2.2568
47 Tuc F	2.623579	No	
47 Tuc G	4.040379	No	
47 Tuc H	3.2103	Yes	2.3578
47 Tuc I	3.484993	Yes	0.2298
47 Tuc J	2.100633	Yes	0.1207
47 Tuc L	4.3462	No	
47 Tuc M	3.676644	No	
47 Tuc N	3.053954	No	
47 Tuc O	2.643343	Yes	0.13597
47 Tuc P	3.643021	Yes	0.1472
47 Tuc Q	4.033181	Yes	1.1891
47 Tuc R	3.480463	Yes	0.0662
47 Tuc S	2.83	Yes	1 to several
47 Tuc T	7.589	Yes	1 to several
47 Tuc U	4.342827	Yes	0.4291
47 Tuc V	4.81	Yes	~0.2
47 Tuc W	2.352344	Yes	0.133

Table 7.1: *Summary of radio sources detected in 47 Tuc (Camilo et al. (2000); Robinson et al. 1995; Manchester et al. 1991).*

Source	Period (ms)	Luminosity (erg/s)
47 Tuc C	5.756780	4.49×10^{33}
47 Tuc D	5.357573	4.18×10^{33}
47 Tuc F	2.623579	2.04×10^{33}
47 Tuc G	4.040379	3.15×10^{33}
47 Tuc M	3.676644	2.87×10^{33}
47 Tuc N	3.053954	2.38×10^{33}

Table 7.2: *The Periods and Luminosities of the isolated millisecond pulsars in 47 Tuc, as calculated following Chen (1991).*

In eqs. 7.1 & 7.2 p is the spin period of the pulsar in milliseconds and l_γ is its hard X-/γ ray luminosity in erg s^{-1}. Chen (1991) used this, plus the known pulsar period distribution at that time, to estimate the average luminosity of an individual isolated MSP to be $\sim 3 \times 10^{33}$ erg s^{-1}. If one uses eqs. 7.1 & 7.2 along with the known periods of the 47 Tuc isolated MSPs one gets a luminosity of 1.9×10^{34} erg s^{-1} (table 7.2). This is approximately the same as if one had used the average determined by Chen (1991).

The total luminosity estimated for the MSPs, using the binary MSP luminosity of Ford et al. (1996) and the isolated MSP luminosity of Chen (1991), in 47 Tuc is therefore $\sim 3.6 \times 10^{34}$ erg s^{-1}.

7.2.3 A cautionary note

An alternative estimate of isolated MSP emission was given by Rudak & Dyks (1998). Contrary to Chen (1991) they have suggested that isolated MSPs will be weak γ–ray emitters. They proposed a simplified polar cap model where electrons are accelerated in the pulsar magnetic field inducing cascades of electrons/positrons and photons. The energy of the electrons in the plasma has to be above E_{min} and below the lower of E_{max} or E_{w}:

$$E_{\mathrm{w}} = 1.2 \times 10^7 B_{12} P^{-2} \quad \mathrm{MeV} \tag{7.3}$$

$$E_{\mathrm{max}} = 4.6 \times 10^7 B_{12}^{1/4} P^{-1/8} \quad \mathrm{MeV} \tag{7.4}$$

$$E_{\rm min} = 1.2 \times 10^7 B_{12}^{-1/3} P^{1/3} \quad {\rm MeV} \tag{7.5}$$

$E_{\rm min}$ represents the minimum energy that accelerated electrons require for pair creation. $E_{\rm max}$ is the maximum energy the electrons can be accelerated to, determined by curvature cooling in a purely dipolar magnetic field. $E_{\rm w}$ is the absolute maximum energy to which the electrons can be accelerated and is determined by the potential drop across the polar cap. A consequence of this model is that when $E_{\rm max} < E_{\rm min}$ there will be no emission i.e. the pulsar is "dead".

7.3 Previous X-/γ-ray surveys

7.3.1 Previous soft X-ray observations

Hertz & Grindlay (1983) observed 47 Tuc as part of a globular cluster survey using both the HRI and IPC instruments on Einstein. These resulted in detections of 47 Tuc with different luminosities. The HRI limit is 3.9×10^{34} erg/s and the IPC limit is 7.1×10^{33} erg/s, both in the 0.5 - 4.5 keV band. Aurière, Koch-Miramond & Ortolani (1989) used recalibrated Einstein IPC data to obtain an X-ray spectrum of 47 Tuc and to try to study its variability. Depending on the model fit the luminosity (0.2 - 4 keV) is 7-8.7 $\times 10^{33}$ erg/s. The core source X0021.8-7221 has pulsations at 120.2 seconds and at 4.58 seconds, which they suggest implies it is a cataclysmic variable.

Hasinger, Johnston & Verbunt (1994) observed 47 Tuc with the ROSAT HRI. They detected 4 sources in the core and 4 within 90 arcseconds, as well as finding some evidence for diffuse emission. The luminosities they estimate for the core sources are higher than those expected for cataclysmic variables and they suggest that the X-ray sources are neutron star binaries. This data has recently been re-analyzed and combined with new data by Verbunt & Hasinger (1998). Five sources are now detected in the core with a further four within two arcmins. They also produced light curves for the five core sources, two of which (X9 and X10) show a high degree of variability. They identify the source X9 (X0021.8-7221) with a blue variable star and suggest that it is a soft X-ray transient.

7.3.2 Previous hard X-ray observations

Barret et al. (1993) used SIGMA to observe 47 Tuc in the energy range 40 - 1200 keV. They found no significant emission above the 2σ confidence level in any of their nine observations. Similarly, in

Energy Range	Luminosity (erg/s)	Instrument
0.5 - 2.5 keV	3.5×10^{33}	ROSAT HRI (d)
0.5 - 4.5 keV	3.9×10^{34}	Einstein HRI (d)
0.5 - 4.5 keV	7.1×10^{33}	Einstein IPC (d)
40 - 100 keV	2×10^{35}	SIGMA (u)
$>$ 100 MeV	1.2×10^{35}	EGRET (u)
0.75 - 10 MeV	2.67×10^{35}	COMPTEL (u)
20 - 120 keV	5.8×10^{34}	BATSE (u)

Table 7.3: *Summary of previous X-ray observations (u - upper limits, d - detections).*

the sum of their observations, they detect no flux from 47 Tuc. From their observations a maximum 2σ upper limit, in the 40 - 100 keV band, for the luminosity of 47 Tuc is 2×10^{35} erg/s.

47 Tuc has been observed with three of the instruments on board the Compton Gamma Ray Observatory (CGRO): the Energetic Gamma Ray Experiment Telescope (EGRET) which uses spark chambers to provide coverage over the energy range 30 MeV to 30 GeV; the imaging Compton telescope (COMPTEL) which makes use of Compton scattering to image over the energy range 1 MeV to 30 MeV; and the all–sky monitor BATSE which is sensitive in the energy range 20 keV to 1 MeV. Michelson et al. (1994) used the EGRET all sky survey to search a number of globular clusters for emission at $>$ 100 MeV. They found no significant emission from 47 Tuc above the 2σ confidence level and placed an upper limit to the luminosity of 1.2×10^{35} erg/s. O'Flaherty et al. (1995) observed 47 Tuc with COMPTEL. They detected no emission and so set a 2σ upper limit to the luminosity in the 0.75 - 30 MeV band of 9.63×10^{35} erg/s. They also set an upper limit over the 0.75 - 1 MeV band of 2.67×10^{35} erg s^{-1} (see table 7.3). Ford et al. (1996) used BATSE to monitor 27 globular clusters in the band 20 - 120 keV for 1400 days. They detect no emission (outbursts or persistent) from 47 Tuc, and set a 2σ upper limit of 5.8×10^{34} erg s^{-1}. Using a photon spectrum of E^{-2} and models by Chen (1991) and Tavani (1993) they set upper limits on the number of isolated MSPs and the number of binary MSPs to be 19 and 46 respectively.

7.4 RXTE Observations

This section details observations carried out in December 1996 using both the Proportional Counter Array (PCA) and the High Energy X-ray Timing Experiment (HEXTE) on board RXTE. A detailed description of the RXTE mission is given by Bradt, Rothschild & Swank (1993). The total live time accumulated was ~65,000 seconds, which was split over a period of five days. The PCA is an array of five proportional counters, covering an energy range of 2 - 60 keV with timing resolution down to 1 μs. The HEXTE instrument consists of two clusters of phoswich detectors, which cover an energy range of 15 - 250 keV with timing resolution down to 8 μs.

7.4.1 Spectral analysis

PCA data reduction followed the standard method provided by the Guest Observer Facility (RXTE GOF 1998). Lightcurves and spectra were extracted using a Good Time Interval (GTI) to filter the data. The GTI identifies periods of good data e.g. when more than 30 minutes have passed since the satellite went through the South Atlantic Anomaly or the elevation is high enough to avoid Earth occultation. The PCA detectors have 3 layers of anodes, and extractions were carried out firstly over all 3 layers and then over the top-layer only. For low-energy X-rays, the top-layer only data are expected to have a higher signal-to-noise ratio. Background files were generated using the L7 background models. Both the raw and background files were corrected for dead time, and then the appropriate response matrices were generated.

HEXTE analysis involved separating the data into on-source and off-source files, extracting spectra and correcting for dead time. For each of the HEXTE clusters the spectra were combined to form a final spectrum. The response matrices were downloaded from the legacy site (legacy 1998). The response files used were *hexte_97mar20c_pwa.rmf* and *hexte_97mar20c_pwb013.rmf*.

7.4.2 Timing analysis

A search was undertaken for periodicities in the range 0.1 milliseconds to 40 kiloseconds. The upper limit of 40 kiloseconds was set by the length of the observation, which including dead time and before filtering, was ~86,000 seconds. It was therefore not practical to look for periods on a longer timescale. This period range was split into two parts which were analysed, for efficiency, in different ways. Firstly, the longer period range (320 - 40,000 s) was analysed using an epoch folding technique. Secondly, the short period range (0.0001 - 320 s) was analysed using a Fast Fourier Transform technique.

For the long period searches we used standard-2 format PCA data, extracted to form a lightcurve, using the same Good Time Interval as for the spectral analysis. Only top-layer detections in the range 2 - 10 keV were extracted to maximize the signal-to-noise ratio. The background files were the same ones used for the spectral analysis, and the extraction criteria were the same as the standard-2 PCA data. Both raw and background lightcurves were dead time corrected. The background lightcurve was then subtracted from the raw lightcurve, creating the source lightcurve. Barycentric correction was then applied to the source lightcurve.

For the short period searches, the recipe given by the Guest Observer Facility (RXTE GOF 1998) was followed using Goodxenon format PCA data. This was filtered to give continuous cleaned data over the energy range 2 - 10 keV. A Fast Fourier Transform was then used to search the data for periodicities.

7.4.3 Spectral analysis results

Fig. 7.1 shows the PCA (top-layer only) and HEXTE data plotted together. A model consisting of a 3 keV bremsstrahlung with an absorption column of 2.4×10^{20} N_H/cm^2 and a power-law (with the same absorption column) of index 1.76 has been fitted. The bremsstrahlung component dominates at lower energies (similar to previous X-ray results; Hasinger et al. 1994), whilst the power-law dominates at higher ones (as suggested by theory; Tavani 1993). However, the power-law seems to be a poor fit to the HEXTE data. The PCA (top-layer only) count rate over the energy range 2 to 10 keV is 0.826 cts s^{-1}.

To compare these results with the BATSE observations of Ford et al. (1996), the energy band 20 - 120 keV is considered. The HEXTE spectrum at these energies shows emission at $\sim 1.4\sigma$. This is not significant enough to be classed as a detection of 47 Tuc and so we set a 2σ upper limit of 5.4×10^{33} erg/s. The upper limit on luminosity derived from the model is a factor of 10 lower than the previous upper limit from the BATSE survey (Ford et al. 1996).

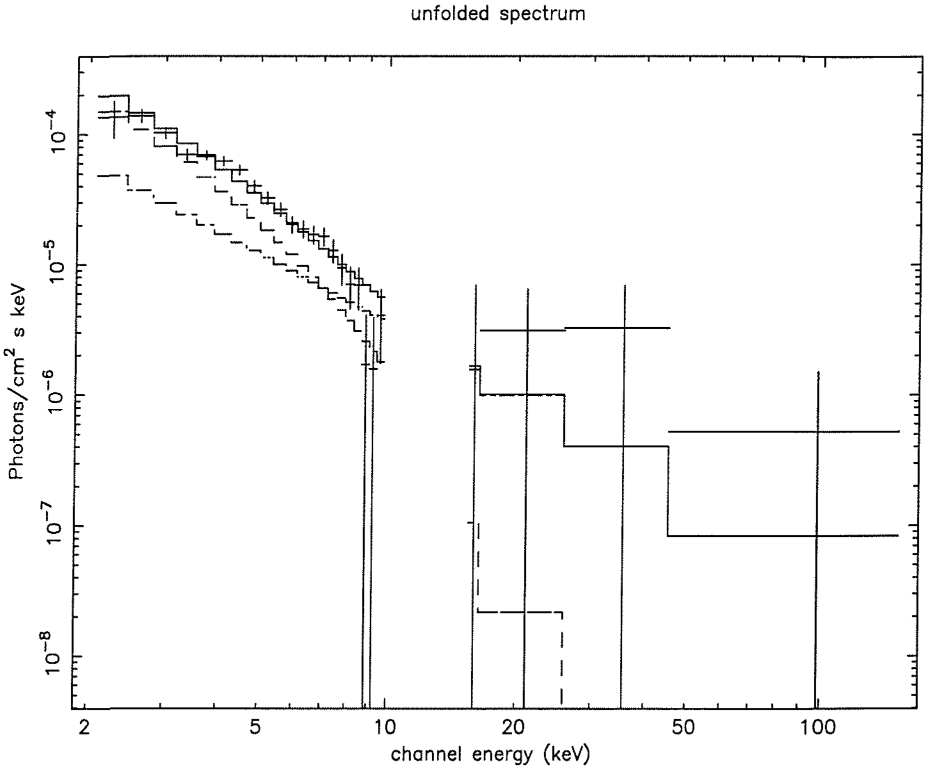

Figure 7.1: *Combined PCA and HEXTE spectrum of 47 Tuc.*

Frequency (Hz)	Period (s)	Amplitude (%)	Luminosity (erg/s)
2.5×10^{-5} - 1.02×10^{-3}	39940 - 980	4.68	2.5×10^{32}
1.01×10^{-3} - 2.56×10^{-3}	990 - 390	2.98	1.59×10^{32}
2.56×10^{-3} - 5.243	390.625 - 0.1907	2.2	1.18×10^{32}
5.12 - 5.24288×10^{3}	0.195 - 1.9×10^{-4}	6.0	3.21×10^{32}

Table 7.4: *Summary of the timing analysis upper limits over the 2 - 10 keV region. The upper limit in amplitude is given as a percentage of the 2 - 10 keV flux. The corresponding upper limit in Luminosity is also shown.*

7.4.4 Timing analysis results

In both the power spectrum and epoch folding searches, the analysis of Leahy et al. (1983) was followed. No peaks at 90% confidence were found in any of the power spectra or epoch folding searches. The upper limits on pulse amplitudes are summarized in table 7.4. Any periods present would have to have amplitudes less than about 6% of the 2 - 10 keV flux to have avoided detection.

7.5 BeppoSAX Observations

The X-ray satellite SAX, a major program of the Italian Space Agency and the Netherlands Agency for Aerospace Programs, was launched on April 30 1996 from Cape Canaveral. After launch it was named BeppoSAX in honour of Giuseppe (Beppo) Occhialini. The payload is characterized by very wide spectral coverage from 0.1 to 300 keV, with well balanced performance from both its low and high-energy instrumentation. The payload includes a set of four X-ray concentrators, with imaging gas scintillation proportional counter detectors located at their focal planes. One of these detectors, the Low Energy Concentrator Spectrometer (LECS), is sensitive to X-rays in the energy range 0.1 - 10 keV (Parmar et al. 1997). The other three, the Medium Energy Concentrator Spectrometers (MECS 1,2 & 3), cover a narrower energy range 1.3 - 10 keV (Boella et al. 1997). The third instrument on board BeppoSAX is the High Pressure Gas Scintillation Proportional Counter (HPGSPC). This is a xenon (90%) – helium (10%) gas scintillating proportional counter operated at a pressure of five atmospheres and sensitive in the energy range 4 - 120 keV (Manzo et al. 1997). The fourth instrument, the Phoswich Detection System (PDS), is composed of four actively shielded

NaI(Tl)/CsI(Na) phoswich scintillators and is sensitive over the energy range 15 - 300 keV (Frontera et al. 1997).

The observations presented here were carried out between December 20th–21st 1997. Data from all 4 of the BeppoSAX narrow field instruments was obtained. The exposure length for the LECS instrument was 12919 seconds, and for the MECS (detectors 2 & 3 only) the exposure was 23661 seconds. The exposures for the HPGSPC and PDS were 9993 seconds and 9251 seconds, respectively.

These data were analysed with the SAX analysis software (SAXDAS v2.0.1), using the standard procedure given in the cookbook by Fiore, Guainazzi & Grandi (1999). This consisted of generating cleaned and linearized event files and good time intervals. For LECS and MECS xselect was used to extract images and spectra. For spectral analysis, 2 extraction radii have been used, the default (8.′5 LECS and 4′ MECS) and a smaller radii (4′ LECS and 2′ MECS) to account for the faintness of 47 Tuc. Background spectra were generated using blank sky files from the Science Data Centre (SDC), extracted at the same detector plane coordinates and with the same radii. For both the source and background spectra 2 other regions, $\sim 20'$ away from any sources, were extracted. These were compared with each other to see if any normalization of the background was necessary. For these observations no normalization was needed. The default radii spectra were compared with the Supervised Standard Scientific Analysis (S3A) products to validate the data reduction process. For PDS the SAXDAS pipeline software was used to create the gain equalized event file and the good time intervals. The results presented used fixed rise time thresholds (to reduce background) and a count rate filter to minimise spikes in the data. Again, for the HPGSPC the event files and good time intervals were generated using the SAXDAS pipeline software. From these files a background subtracted spectrum was generated. The results presented are the combination of this analysis and the S3A analysis conducted by the SAX SDC.

7.5.1 Results

A negative count rate was found in the HPGSPC spectrum suggesting the background had been over-subtracted. This could possibly be due to strong ^{55}Fe and Uranium lines seen in the HPGSPC background spectrum. For this reason the HPGSPC results are not considered further.

Fig. 7.2 shows images obtained over selected energy ranges by the LECS and MECS(2,3) instruments taken from the S3A standard analysis. Clearly shown in the centre of the image is 47 Tuc, to

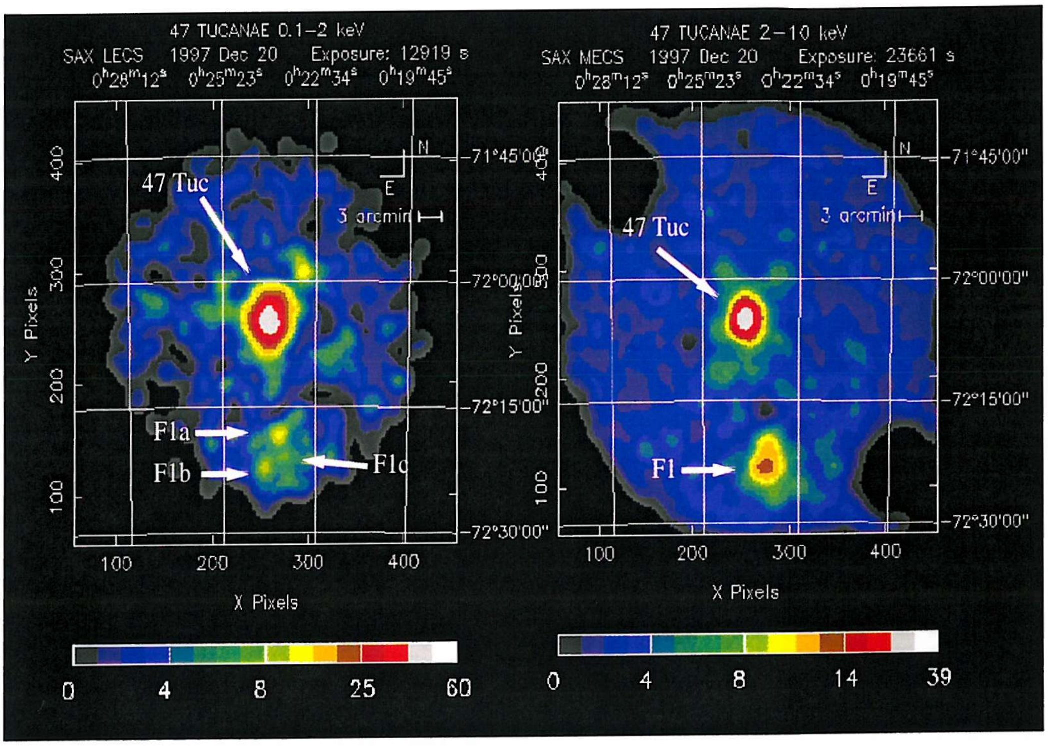

Figure 7.2: *LECS and MECS images of the 47 Tuc field generated by the S3A analysis.*

	Source	Count Rate (counts/s)	Error (counts/s)	RA α_{2000}	Dec δ_{2000}	σ
LECS	47 Tuc	1.78×10^{-2}	$\pm 1.5 \times 10^{-3}$	$00^h23^m57.^s5$	$-72°04'23.''3$	11.8
	F1	6.61×10^{-3}	$\pm 1.8 \times 10^{-3}$	$00^h23^m30.^s0$	$-72°18'47.''6$	3.77
MECS	47 Tuc	1.74×10^{-2}	$\pm 1.1 \times 10^{-3}$	$00^h24^m2.^s1$	$-72°04'50.''0$	16
	F1	2.03×10^{-2}	$\pm 2.2 \times 10^{-3}$	$00^h23^m24.^s0$	$-72°22'48.''8$	9.4

Table 7.5: *Sources detected above 3σ in the LECS and MECS images.*

the south there is also a prominent field source(s). The LECS image is over the energy range 0.1 - 2 keV and the MECS image covers 2 - 10 keV. 47 Tuc is detected at 11.8σ (1.8×10^{-2} counts/s) in the LECS image and 16σ (1.7×10^{-2} counts/s) in the MECS image (see table 7.5).

Guhathakurta et al. (1992) give the cluster centre as $00^h24^m5.^s83, -72°4'51.''4$. This is in good agreement with the LECS and MECS positions given in table 7.5.

Spectral Results

In Fig. 7.3 LECS and MECS spectra, extracted using the default radii (8.′5 LECS and 4′ MECS) are shown along with the PDS spectrum. Fitted to the data is a combination of power-law (α = -1.58) and bremsstrahlung models, with an absorption column (2.4×10^{20} n_H/cm^2), and constants to normalize between LECS, MECS and PDS instruments (Fiore et al. 1999). Various other models were fitted to the data, from which it appears that 2 component models provide the best description of 47 Tuc. In particular, the combination of power-law and bremsstrahlung, two bremsstrahlung or bremsstrahlung and black body provide the best-fit. The model I prefer, and that which was earlier fitted to the RXTE data (Ferguson et al. 1999), is the power-law plus bremsstrahlung model. This is preferred to a double bremsstrahlung, and bremsstrahlung plus black body on PDS to MECS ratio grounds. In the power-law plus bremsstrahlung model the LECS constant is 1.224 and the MECS constant is 1.432, giving a LECS/MECS ratio of ~ 0.85 which is within the accepted limits. The PDS/MECS ratio should be between 0.77–0.93 (Fiore et al. 1999). Unfortunately, it is much higher (~ 4). For a double bremsstrahlung model the ratio is ~9.7, and for bremsstrahlung plus black body it is about 200. The high PDS/MECS ratio suggests either an error in the data reduction or in the model fit and this is discussed in more detail later. Table 7.6 shows the fluxes and luminosities

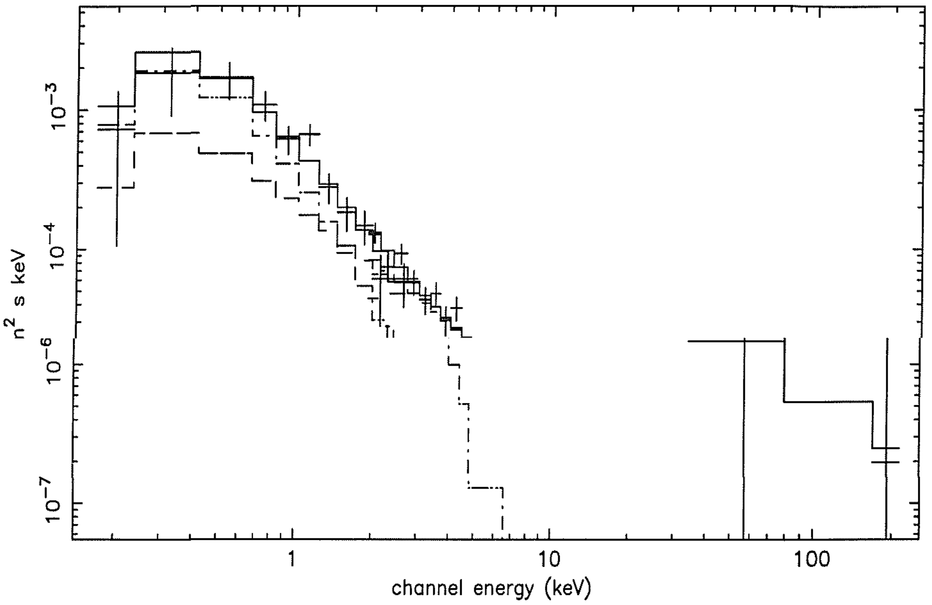

Figure 7.3: *The LECS and MECS spectra of 47 Tuc plus the PDS spectrum of the 47 Tuc field.*

Energy Band (keV)	Flux (erg/s/cm^2)	Luminosity (erg/s)
0.1–2	1.5×10^{-12}	3.85×10^{33}
0.5–2.5	1.3×10^{-12}	3.22×10^{33}
0.5–4.5	1.7×10^{-12}	4.18×10^{33}
2–10	1.3×10^{-12}	3.42×10^{33}
20–120	1.5×10^{-11}	3.84×10^{34}

Table 7.6: *Fluxes and luminosities calculated for 47 Tuc.*

determined from the model. Above 10 keV the total detection is 2.1σ. When the smaller extraction radii are used the luminosities are less by as much as 20%. The luminosity, in the energy band 20 - 120 keV, given in the table 7.6 is a factor of 7 higher than the 2σ upper limit set by Ferguson et al. (1999) using RXTE.

Timing analysis

Fig. 7.4 shows the lightcurves generated by the S3A standard analysis. There is no evidence for significant variability. A thorough period search has not been conducted because of the small number of counts detected.

7.5.2 Field Source

Fig. 7.5 shows the combined LECS and MECS spectrum of the field source, which has been fitted with a power-law. This is not a good fit. There is an excess at 1 keV and at 5 - 6 keV. In the LECS image (fig 7.2) the field source appears to be more than one object, for ease of reference I shall call the field source complex F1. In the LECS image there are three sources, one northerly, one south-south-westerly, and a third south-easterly. For ease of reference I will call them F1a, F1b and F1c respectively (fig. 7.2). From archival ROSAT PSPC data (Fig. 7.6) F1 can be associated with the two southerly sources. Krockenberger & Grindlay (1995) attributed these to a background galaxy cluster.

In the MECS band the location of the field source appears between F1b and F1c. There is also some extension of emission in the northerly direction, which is coincident with F1a, thus I

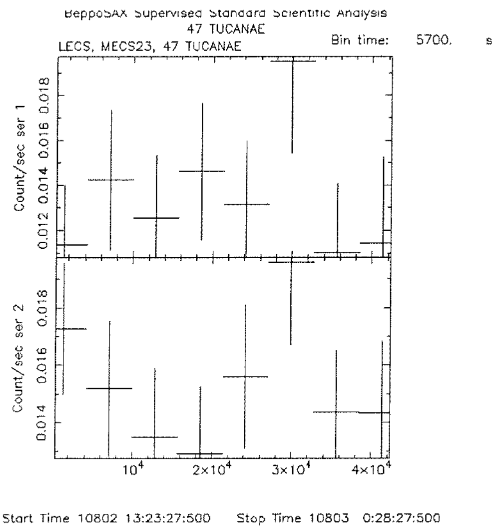

Figure 7.4: *Lightcurves generated by the S3A analysis for 47 Tuc.*

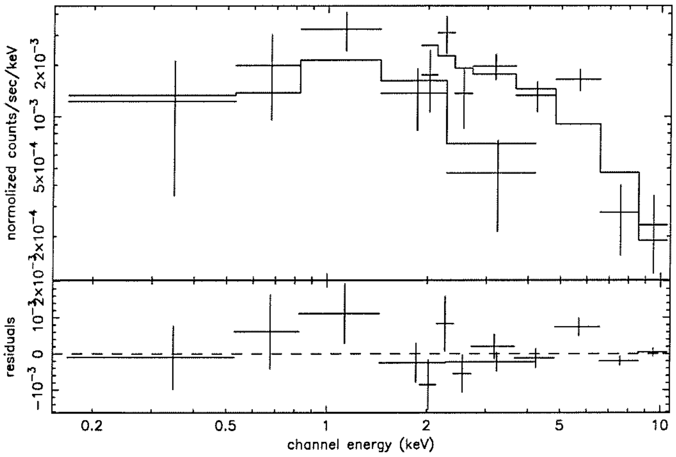

Figure 7.5: *LECS and MECS spectra of the field source complex.*

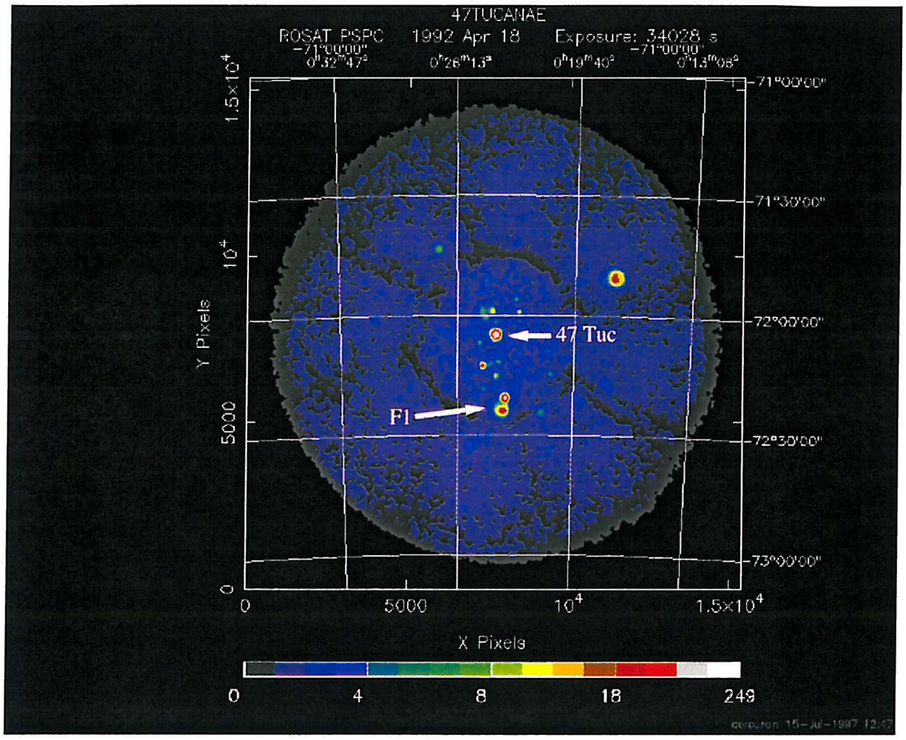

Figure 7.6: *Archival ROSAT PSPC image of the 47 Tuc field taken over the total energy band (0.1 - 2.4 keV).*

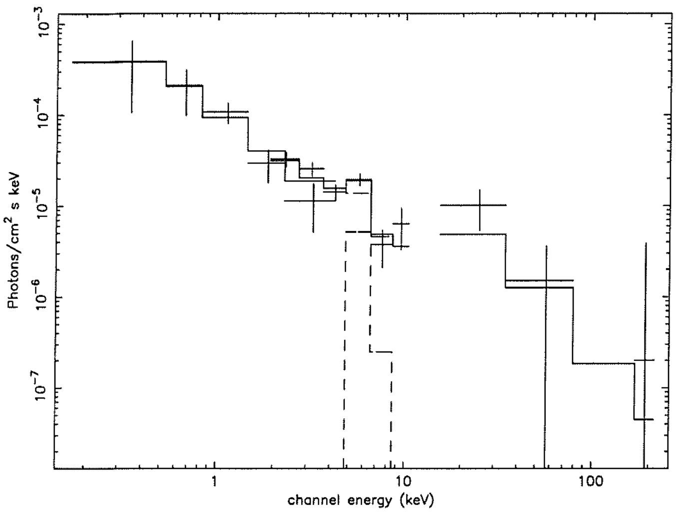

Figure 7.7: *Combination of LECS and MECS spectra for F1 and PDS spectra for the whole 47 Tuc field.*

associate the MECS source with F1. Geffert, Aurière & Koch-Miramond (1997) identify the X-ray source No. 3 of Hasinger et al. (1994) with an unamed faint galaxy at $\alpha_{2000} = 00^h23^m30.^s8$ and $\delta_{2000} = -72°20'44.''0$. I associate F1 with this galaxy. Fig. 7.7 shows a plot of the LECS and MECS spectra from F1, plus the 47 Tuc field spectra from the PDS. To this I fit a spectrum typical of Seyfert I's. Due to the limited quality of the data only one model was tried. The fit is not particularly good (reduced $\chi^2 = 1.095$ with 8 dof), but indicates that it is possible to describe the field source complex as a Seyfert I. The fitted model consisted of a constant term (to normalize between the instruments), an absorption edge, an absorption column, an emission line and an exponentially absorbed power-law plus Compton reflection component (Magdziarz & Zdziarski 1995). The energy of the edge was fixed at 7 keV. The energy and width of the emission line were fixed at 6.4 keV and 100 eV, respectively. The constants were arbitrarily set to 0.9,1 and 0.9 (LECS, MECS and PDS). The power-law index was frozen at 1.9, with redshift frozen at zero and elemental abundances fixed at solar. The remaining seven parameters were allowed to vary freely. The model fit has an energy cut-off around 3.2 MeV and an inclination less than 20°. The normalization of the reflection component is very high, too high to be due to a physical source, and this is probably due to the high PDS to MECS ratio. A Seyfert I spectrum may be possible if this hard X-ray excess could be accounted for.

There looks to be a further source in the LECS image at $\sim 00^h22^m56.^s5, -71°58'14''$. Taking into account the LECS PSLA this could be coincident with X1 from Verbunt & Hasinger (1998), whose coordinates are given as $00^h22^m45.^s38, -71°59'8.''8$.

7.6 Discussion

7.6.1 The low-energy band

The luminosity detected in the 2 - 10, 0.5 - 2.5 and 0.5 - 4.5 keV bands with SAX is lower than the RXTE value (Ferguson et al. 1999; Table 7.7). This is to be expected since RXTE had a 1° field of view and so includes many background sources (see fig 7.2 & 7.6). The BeppoSAX luminosity in 0.5 - 2.5 keV band, 3.2×10^{33} erg/s, is in good agreement with the luminosity given by Verbunt & Hasinger (1998; table 7.3).

7.6.2 The high-energy band

Earlier the total luminosity of the millisecond pulsars in the 20 - 120 keV band in 47 Tuc, was estimated at $\sim 3.6 \times 10^{34}$ erg s^{-1}. As can be seen from the table 7.7 the luminosity determined by RXTE is incompatible with this prediction. Surprisingly the luminosity observed with BeppoSAX is consistent with the prediction. The difference between these two observations is surprising, but may be explained by the difference in power-law index &/or the complex nature of the 47 Tuc field. The difference in power-law index probably accounts for a factor of 2 difference in the luminosities between the models over the band 20 - 120 keV. I now consider the impact of the field source on the BeppoSAX results.

7.6.3 Field Source Complex (F1)

The presence of F1 poses a question: Do the hard X-rays come solely from 47 Tuc, solely from F1 or from a combination of both? In the following discussion these three possibilities are addressed.

Fig. 7.3 shows the power-law plus bremsstrahlung, with absorption column and constants, fitted to the LECS, MECS and PDS data. As previously mentioned, the PDS to MECS ratio is much higher than expected. This could be due to 2 effects: 1) improper data reduction, or, 2) use of an inappropriate model. When the PDS was analysed, the standard procedure given by Fiore et

Energy Band (keV)	Luminosity (erg/s)	Instrument
0.5 - 2.5	5.4×10^{33}	RXTE PCA
0.5 - 2.5	3.2×10^{33}	BeppoSAX
0.5 - 4.5	7.7×10^{33}	RXTE PCA
0.5 - 4.5	4.2×10^{33}	BeppoSAX
2 - 10	5.4×10^{33}	RXTE PCA
2 - 10	3.4×10^{33}	BeppoSAX
20 - 120	5.4×10^{33}	RXTE HEXTE (upper limit)
20 - 120	3.8×10^{34}	BeppoSAX
20 - 120	1.2×10^{34}	BeppoSAX (fixed PDS/MECS ratio)

Table 7.7: *Summary of the RXTE and BeppoSAX results.*

al. (1999) was followed, and errors are expected to be minimal. Fig. 7.8 shows a plot of the SAX data (points in the boxes) and the RXTE data (adapted from Ferguson et al. 1999) for 47 Tuc. For the SAX spectra the default extraction radii were used. The HEXTE and PDS data agree relatively well. This suggests that the PDS to MECS ratio is too high because there is a very real hard X-ray excess. It is therefore unlikely that the hard X-rays come solely from 47 Tuc.

Fig. 7.7 shows a Seyfert I model fit to the F1 LECS and MECS spectra and the PDS spectrum. As noted earlier the relative reflection component is rather large and this is indicative of a high PDS to MECS ratio. It seems that a Seyfert I model may provide a rough description of the data, if there is a further hard X-ray excess. It is therefore unlikely that the hard X-rays come solely from F1.

Both 47 Tuc and F1 could be best fit if the hard X-rays seen in the PDS were split between them. A bremsstrahlung plus power-law (free parameter giving α = -1.42) model fit to the 47 Tuc data with the LECS to MECS and PDS to MECS ratios fixed at 0.85, gives a flux in the 20 - 120 keV band of 4.6×10^{-12} erg cm^{-2} s^{-1}. This flux gives a luminosity of 1.16×10^{34} erg s^{-1} which is twice the HEXTE luminosity (assuming the distance to 47 Tuc is assumed to be 4.6 kpc). When the relative normalization of the reflection component is set to a reasonable value (e.g. 1) the flux given for F1, in the 20 - 120 keV band, is 1.2×10^{-12} erg cm^{-2} s^{-1}. When summed this gives a flux for the 47 Tuc field of $\sim 5.8 \times 10^{-12}$ erg cm^{-2} s^{-1}. A power-law fit to the PDS data alone gives a flux of 9.92×10^{-12} erg cm^{-2} s^{-1}, only a factor of 1.7 higher than the sum of the 47 Tuc and F1 fluxes.

It is therefore possible that 47 Tuc and F1 dominate the high-energy flux in the 47 Tuc field.

The hard X-ray/γ-ray excess seen in the 47 Tuc field is very likely due to a combination of 47 Tuc, F1 and several other weaker sources. When this is taken into account, and a sensible PDS/MECS ratio is used in spectral fitting, the luminosity in the 20 - 120 keV band for 47 Tuc is $\sim 1.2 \times 10^{34}$ erg s^{-1}. This is a factor of 2 higher than the HEXTE results, but is compatible when one notes the differing photon indexes used. The power-law indexes have been determined as free parameters in a best fit process rather than being fixed, hence the difference between the two models.

7.7 Conclusions

Using RXTE a 2σ upper limit on the 20 - 120 keV emission from the 47 Tuc field of 5.4×10^{33} erg s^{-1} has been set. Emission, in the range 20 - 120 keV, from the 47 Tuc field has been detected with BeppoSAX at the level of 3.8×10^{34} erg s^{-1}, which would be compatible with expectations if due to the MSPs in 47 Tuc. The increase in high-energy luminosity between the RXTE and BeppoSAX observations suggests the presence of a variable source within the field.

When physically realistic models were fitted to the low and high-energy emission detected with BeppoSAX, the luminosity of 47 Tuc was calculated to be 1.16×10^{34} erg s^{-1}. Therefore a range of luminosity for 47 Tuc in the 20 - 120 keV band, dependant on power-law index, is $5.4 - 11.6 \times 10^{33}$ erg s^{-1}. This is a factor of 3 below that expected, and is not consistent with the emission theories of Chen (1991) and Tavani (1993) and the known MSP population.

From the BeppoSAX data, the HEXTE data and the model fits, it is probable that there are hard X-ray sources other than 47 Tuc in the field of view. The LECS and MECS images clearly show the presence of F1. This field source, which can be crudely fit at low-energies by an AGN spectrum, is coincident with a faint galaxy/galaxy cluster. Though the data is not great, it is possible that this source may contaminate the high-energy results.

The model of Chen (1991) appears to over-estimate the luminosity of the isolated millisecond pulsars in 47 Tuc. One reason could be a lower than expected efficiency for conversion of spin-down luminosity to X-/γ-rays (Zhang and Cheng 1998). An alternative theory for isolated MSP emission was suggested by Rudak & Dyks (1998). In tables 7.8, 7.9 and 7.10 the model of Rudak and Dyks (1998) is used to estimate E_{min} and E_{max} for the isolated millisecond pulsars in 47 Tuc. Only in the case of 47 Tuc F (with B = 10^9G) will E_{max} be greater than E_{min}. Therefore, for most

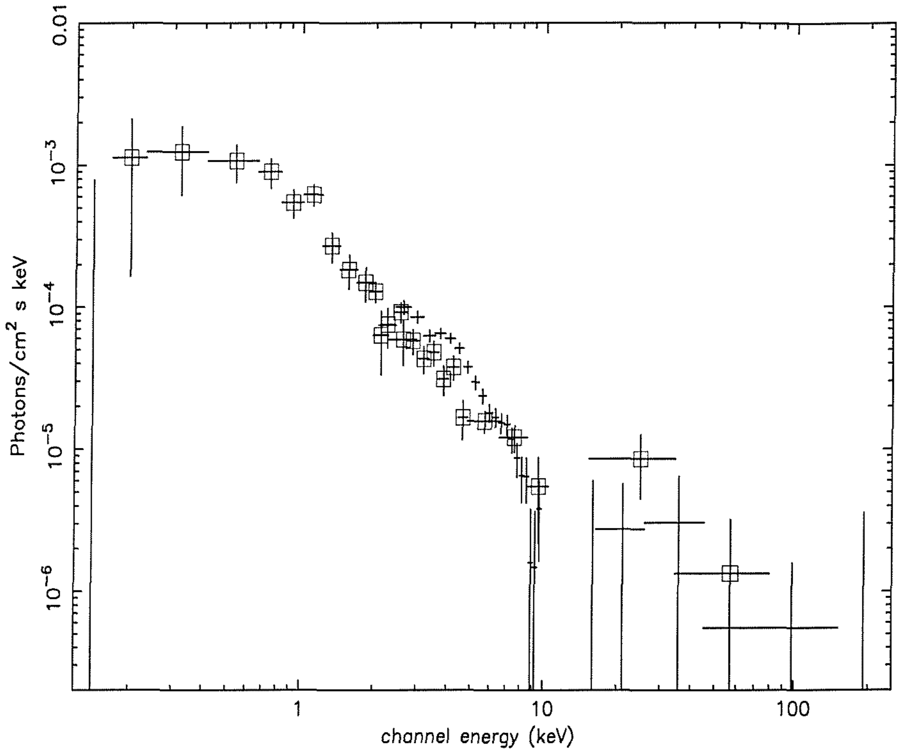

Figure 7.8: *BeppoSAX LECS, MECS and PDS spectra for 47 Tuc, compared with the RXTE PCA and HEXTE spectra adapted from Ferguson et al. (1999). The BeppoSAX data points are shown in boxes.*

	P(ms)	E_{min}(MeV)	E_{max}(MeV)
C	5.76	4.6×10^7	8.8×10^6
D	5.36	4.5×10^7	8.8×10^6
F	2.62	3.6×10^7	9.7×10^6
G	4.04	4.1×10^7	9.2×10^6
M	3.68	4×10^7	9.3×10^6
N	3.05	3.7×10^7	9.5×10^6

Table 7.8: *E_{min} and E_{max} calculated using the known period and an assumed magnetic field of* $10^8\,G$.

	P(ms)	E_{min}(MeV)	E_{max}(MeV)
C	5.76	2.7×10^7	1.3×10^7
D	5.36	2.6×10^7	1.32×10^7
F	2.62	2.1×10^7	1.45×10^7
G	4.04	2.4×10^7	1.37×10^7
M	3.68	2.3×10^7	1.39×10^7
N	3.05	2.2×10^7	1.42×10^7

Table 7.9: *E_{min} and E_{max} calculated using the known period and an assumed magnetic field of* $5 \times 10^8\,G$.

reasonable values of B the isolated millisecond pulsars in 47 Tuc would be "dead". This would make the expected luminosity of 47 Tuc 1.7×10^{34} erg/s due to the binary MSPs only. This is more compatible with the results, but is still higher than observed.

The estimated binary MSP luminosity could be reduced to match these observations in a number of ways. Firstly, the calculated flux in Ford et al. (1996) is for energies above 20 keV. The calculated photon flux above 120 keV is 1.2×10^{-6} photons cm^{-2} s^{-1}, giving a flux in the 20 - 120 keV band of 5.9×10^{-6} photons cm^{-2} s^{-1}. This would reduce the luminosity in 47 Tuc for each binary millisecond pulsar to $\sim 1 \times 10^{33}$ erg s^{-1}. More important is the assumption that the fraction of the total shock luminosity radiated in this band is close to one for an average ablating millisecond pulsar. In such a narrow band as 20 - 120 keV, the fraction of shock luminosity radiated may be significantly lower than this. A further assumption is that the spin-down power is $\sim 10^{34}$ erg/s. A smaller value,

	P(ms)	$E_{\rm min}$ (MeV)	$E_{\rm max}$(MeV)
C	5.76	2.15×10^7	1.56×10^7
D	5.36	2.1×10^7	1.57×10^7
F	2.62	1.65×10^7	1.72×10^7
G	4.04	1.9×10^7	1.63×10^7
M	3.68	1.85×10^7	1.65×10^7
N	3.05	1.74×10^7	1.69×10^7

Table 7.10: *$E_{\rm min}$ and $E_{\rm max}$ calculated using the known period and an assumed magnetic field of 10^9 G.*

$\sim 5 \times 10^{33}$ erg/s, would make the theoretical predictions of the binary millisecond pulsar model (Tavani 1993) compatible with the X-ray observations. The spin-down power is sensitive to age, and the old age of the 47 Tuc millisecond pulsars could result in a smaller spin-down power than assumed by Ford et al. (1996). In the model it is assumed that the pulsar is enshrouded in the material evaporated from the companion, if this were not the case then the emission would be less. Naturally if the efficiency of conversion of pulsar wind energy to X-/γ-rays is lower than expected then the emission would be lower.

Unsurprisingly, due to the large numbers of super-imposed periods in 47 Tuc and the weakness of the X-ray sources, no evidence of millisecond pulsations is seen. A limit on the amplitude of any pulsations in the 2 - 10 keV band of 3.21×10^{32} erg/s is set. This further suggests that the isolated millisecond pulsars are weak emitters.

Further observations with the next generation of X-/γ-ray satellites is necessary to resolve the high-energy emission of 47 Tuc. Emission above 10 keV has been detected at 1.4σ by HEXTE and at 2.1σ by the PDS. These have been used to place tighter constraints on emission models and suggest that MSPs are weak sources. A definitive result will only be obtained when a more sensitive, imaging, instrument is used to study 47 Tuc. The imaging capability is necessary to separate 47 Tuc from background sources, such as F1, and obtain its true luminosity.

Bibliography

Armstrong, T.W., Chandler K.C., Barish, J., 1973, *Journal of geophysical research*, 78, No. 16, 2715

Aurière M., Koch-Miramond L., Ortolani S., 1989, A&A 214, 113

Band, D., Matteson, J., Ford, L., Schaefer, B., Palmer, D., Teegarden, B., Cline, T., Briggs, M., Paciesas, W., Pendleton, G., Fishman, G., Kouveliotou, C., Meegan, C., Wilson, R., Lestrade, P., 1993, ApJ, 413, 281

Barret, D., Mandrou, P., Denis, M., Olive, J.F., Laurent, P., Claret, A., Lebrun, F., Paul, J., Sunyaev, R., Churazov, E., Gilfanov, M., Dyachkov, A., Khavenson, N., Novikov, B., Kremnev, R., & Sukhanov, A. 1993, ApJ, 405, L59

Barthelmy, S.D., Bartlett, L.M., Gehrels, N., Leventhal, M., Teegarden, B.J., Tueller, J., Belyaev, S., Lebedev, V., Klapdor-Kleingrothaus, H.V., 1994, ApJ, 427, 519

Bertsch, D.L., Dame, T.M., Fichtel, C.E., Hunter, S.D., Sreekumar, P., Stacy, J.G., Thaddeus, P., 1993, ApJ, 416, 587

Bhattacharya, D., & van den Heuvel, E.P.J. 1991, Phys. Rep., 203, 1

Bildsten, L., Chakrabarty, D., Chiu, J., Finger, M.H., Koh, D.T., Nelson, R.W., Prince, T.A., Rubin, B.C., Scott, D.M., Stollberg, M., Vaughan, B.A., Wilson, C.A., Wilson, R.B., 1997, ApJS, 113, 367

Bloemen, H., Wijnands, R., Bennett, K., Diehl, R., Hermsen, W., Lichti, G., Morris, D., Ryan, J., Schönfelder, V., Strong, A.W., Swanenburg, B.N., de Vries, C., Winkler, C., 1994, A&A, 281, L5

Bloemen, H., Bykov, A.M., Bozhokin, S.V., Diehl, R., Hermsen, W., van der Meulen, R.D., Oberlack, U., Ryan, J., Schönfelder, V., Strong, A.W., Winkler, C., 1997, ApJ, 475, L25

Bloemen, H., Morris, D., Knödlseder, J., Bennett, K., Diehl, R., Hermsen, W., Lichti, G., van der Meulen, R.D., Oberlack, U., Ryan, J., Schönfelder, V., Strong, A.W., de Vries, C., Winkler, C., 1999, Astrohysical Letters & Communications, 38, 349

Boella, G., Chiappetti, L., Conti, G., Del Sordo, S., La Rosa, G., Maccarone, M.C., Mineo, T., Molendi, S., Re, S., Sacco, B., & Tripiciano, M. 1997, A&AS, 122, 327

Bradt, H.V., Rothschild, R.E., Swank, J.H., 1993, A&AS, 97, 355

Briggs, M.S., Band, D.L., Preece, R.D., Paciesas, W.S., Pendleton, G.N., 1999, Astrophysical Letters and Communications, 39, 237

Camilo, F., Lorimer, D.R., Freire, P., Lyne, A.G., & Manchester, R.N. 2000, ApJ, 535, 975

Chan, K.-W., Lingenfelter, R.E., 1993, ApJ, 405, 614

Chen, K., 1991, Nat, 352, 695

Costa, E., Frontera, F., Heise, J., Feroci, M., In't Zand, J., Fiore, F., Cinti, M.N., Dal Fiume, D., Nicastro, L., Orlandini, M., Palazzi, E., Rapisarda, M., Zavattini, G., Jager, R., Parmar, A., Owens, A., Molendi, S., Cusumano, G., Maccarone, M.C., Giarrusso, S., Coletta, A., Antonelli, L.A., Giommi, P., Muller, J.M., Piro, L., Butler, R.C., 1997, Nature, 387, 783

Compton Observatory Science Support Centre, http://www.cossc.gsfc.nasa.gov/cossc

Dean, A.J., Lei, F., Knight, P.J., 1991, Space Science Reviews, 57, 109

Dermer, C.D., Bland-Hawthorn, J., Chiang, J., McNaron-Brown, K., 1997, ApJ, 484, L121

Dermer, C.D., Skibo, J.G., 1997, ApJ, 487, L57

Diehl, R., Dupraz, C., Bennett, K., Bloemen, H., Hermsen, W., Knödlseder, J., Lichti, G., Morris, D., Ryan, J., Schönfelder, V., Steinle, H., Strong, A., Swanenburg, B., Varendorff, M., Winkler, C., 1995, A&A, 298, 445

Esin, A.A., Narayan, R., Cui, W., Grove, J.E., Zhang, S.-N., 1998, ApJ, 505, 854

Ferguson, C., Lei, F., & Dean, A.J. 1999, A&A, 350, 847

Ferguson C., Lei F., Dean A.J., 2000, in prep.

Fiore, F., Guainazzi, M., & Grandi, P. 1999, Cookbook for BeppoSAX NFI SPectral Analysis, version 1.2

Firestone, R.B., Shirley, V.S., Baglin, C.M., Frank Chu, S.Y., Zipkin, J., 1996, Table Of Isotopes 8th Edition

Fishman, G.J., 1999, A&AS, 138, 395

Ford, E., Kaaret, P., Harmon, B.A., Tavani, M., & Zhang, S.N. 1996, ApJ, 467, 272

Frontera, F., Costa, E., Dal Fiume, D., Feroci, M., Nicastro, L., Orlandini, M., Palazzi, E., & Zavattini G. 1997, A&AS, 122, 357

Galama, T.J., Vreeswijk, P.M., van Paradijs, J., Kouveliotou, C., Augusteijn, T., Böhnhardt, H., Brewer, J.P., Doublier, V., Gonzalez, J.-F., Leibundgut, B., Lidman, C., Hainaut, O.R., Patat, F., Heise, J., in't Zand, J., Hurley, K., Groot, P.J., Strom, R.G., Mazzali, P.A., Iwamoto, K., Nomoto, K., Umeda, H., Nakamura, T., Young, T.R., Suzuki, T., Shigeyama, T., Koshut, T., Kippen, M., Robinson, C., de Wildt, P., Wijers, R.A.M.J., Tanvir, N., Greiner, J., Pian, E., Palazzi, E., Frontera, F., Masetti, N., Nicastro, L., Feroci, M., Costa, E., Piro, L., Peterson, B.A., Tinney, C., Boyle, B., Cannon, R., Stathakis, R., Sadler, E., Begam, M.C., Ianna, P., 1998, Nature, 395, 670

Geffert, M., Aurière, M., & Koch-Miramond, L. 1997, A&A, 327, 137

Gehrels, N., 1985, Instrumental background in balloon-borne gamma-ray spectrometers and techniques for its reduction, NASA Technical Memorandum 86162

Gehrels, N., Fichtel, C.E., Fishman, G.J., Kurfess, J.D., Schönfelder, V., 1993, Scientific American, 269, No. 6, 68

Giménez, A., Mas-Hesse, J.M., Jamar, C., McBreen, B., Culhane, J.L., Fabregat, J., Swings, J.P., Meurs, E., Torra, J., Hudec, R., 1999, Astrophysical Letters and Communications, 39, 347

Goldwurm, A., Goldoni, P., Laurent, P., Lebrun, F., Paul, J., 1998, Abstracts of the 19th Texas Symposium on Relativistic Astrophysics and Cosmology held in Paris, France, Dec. 14-18, 1998. Eds.: J. Paul, T. Montmerle, and E. Aubourg (CEA Saclay)

Gómez-Gomar, J., Isern, J., Jean, P., 1998, MNRAS, 295, No. 1, 1

Green, A.R., Lei, F., Bird, A.J., Dean, A.J., 1996, ESA Symposium Proceedings on "Environment Modelling for space-based applications", ESTEC, Noorwijk, NL

Grove, J.E., Johnson, W.N., Kroeger, R.A., McNaron-Brown, K., Skibo, J.G., Phlips, B.F., 1998, ApJ, 500, 899

Guessoum, N., Ramaty, R., Lingenfelter, R.E., 1991, ApJ, 378, 170

Guhathakurta, P., Yanny, B., Schneider, D., & Bahcall, J. 1992, AJ, 104, 1790

Harris, M.J., Naya, J.E., Teegarden, B.J., Cline, T.L., Gehrels, N., Palmer, D.M., Ramaty, R., Seifert, H., 1999, ApJ, 522, 424

Hasinger, G., Johnston, H.M., & Verbunt, F. 1994, A&A, 288, 466

Hernanz, M., José, J., Coc, A., Isern, J., 1996, ApJ, 465, L27

Hertz, P., & Grindlay, J.E. 1983, ApJ, 275, 105

Höflich, P., Wheeler, J.C., Khokhlov, A., 1998, ApJ, 492, 228

Hurley, K., 1998, Astrophysical Letters and Communications, 39, 225

Imhof, W.L., Nakano G.H., Reagan, J.B., 1976, Journal of geophysical research, 81, No 16, 2835

Iyudin, A.F., Bennett, K., Bloemen, H., Diehl, R., Hermsen, W., Lichti, G.G., Morris, D., Ryan, J., Schönfelder, V., Steinle, H., Strong, A., Varendorff, M., Winkler, C., 1995, A&A, 300, 422

Johnson, W.N., Kinzer, R.L., Kurfess, J.D., Strickman, M.S., Purcell, W.R., Grabelsky, D.A., Ulmer, M.P., Hillis, D.A., Jung, G.V., Cameron, R.A., 1993, ApJS, 86, 693

Kinzer, R.L., Purcell, W.R., Kurfess, J.D., 1999, ApJ, 515, 215

Kinzer, R.L., Jung, G.V., Gruber, D.E., Matteson, J.L., Peterson, L.E., 1997, ApJ, 475, 361

Kouveliotou, C., Dieters, S., Strohmayer, T., van Paradijs, J., Fishman, G.J., Meegan, C.A., Hurley, K., Kommers, J., Smith, I., Frail, D., Murakami, T., 1998, Nature, 393, 235

Kouveliotou, C., Strohmayer, T., Hurley, K., van Paradijs, J., Finger, M.H., Dieters, S., Woods, P., Thompson, C., Duncan, R.C., 1999, ApJ, 510, L115

Knödlseder, J., 1999, ApJ, 510, 915

Knoll, G.F., 1989, Radiation detection and measurement, 2nd edition

Krockenberger, M. & Grindlay, J.E. 1995, ApJ, 451, 200

Leahy D.A., Darbro W., Elsner R.F., Weisskopf M.C., Sutherland P.G., Kahn S., Grindlay J.E., 1983, ApJ 266, 160

Legacy download site,

ftp://legacy.gsfc.nasa.gov/xte/calib_data/

Lehoucq, R., Cassé, M., Cesarsky, C.J., 1989, A&A, 224, 117

Lei, F., Bird, A.J., Carter, A.J., Dean, A.J., Ferrero, J.L., Martinez, G., Reglero, V., Ruiz, J.A., Schutz, Y., 1993, Proc. SPIE, Vol 1948, 51

Lei, F., Green, A.R., Bird, A.J., Dean, A.J., 1996, ESA Symposium Proceedings on "Environment Modelling for space-based applications", ESTEC, Noorwijk, NL

Leising, M.D., Johnson, W.N., Kurfess, J.D., Clayton, D.D., Grabelsky, D.A., Jung, G.V., Kinzer, R.L., Purcell, W.R., Strickman, M.S., The, L.-S., Ulmer, M.P., 1995, ApJ, 450, 805

Leventhal, M., Barthelmy, S.D., Gehrels, N., Teegarden, B.J., Tueller, J., Bartlett, L.M., 1993, ApJ, 405, L25

Lingenfelter, R.E., Ramaty, R., 1989, ApJ, 343, 686

Lund, N., Budtz-Jørgensen, C., Westergaard, N.J., Hornstrup, A., Lundgaard Rasmussen, I., Laursen, S., Kristensen, R., Mogensen, P.B., Harbo Andersen, K., Rasmussen, I., Polny, J., Frederiksen, P., Lauridsen, B., Omø, K., Jonasson, P., Kämärinen, V., Andersson, T., Vilhu, O., Huovelin, J., Costa, E., Feroci, M., Rubini, A., Morelli, E., Morbidini, A., Frontera, F., Zavattini, G., Carassiti, V., Morawski, M., Juchnikowski, G., Reglero, V., Peris, J., Collado, V., Rodrigo, J.M., Perez, F., Requena, J.L., Larsson, S., Svensson, R., Zdziarski, A., Schnopper, H.W., 1999, Astrophysical Letters and Communications, 39, 339

Magdziarz, P., & Zdziarski, A. A. 1995, MNRAS, 273, 837

Macomb, D.J., Gehrels, N., 1999, ApJS, 120, 335

Mahoney, W.A., Ling, J.C., Wheaton, W.A., Jacobson, A.S., 1984, ApJ, 286, 578

Mallozzi, R.S., Paciesas, W.S., Pendleton, G.N., Briggs, M.S., Preece, R.D., Meegan, C.A., Fishman, G.J., 1995, ApJ, 454, 597

Manchester, R.N., Lyne, A.G., Robinson, C., D'Amico, N., Bailes, M., & Lim, J. 1991, Nat, 352, 219

Manzo, G., Giarrusso, S., Santangelo, A., Ciralli, F., Fazio, G., Piraino, S., & Segreto, A. 1997, A&AS, 122, 341

Marmier, P., Sheldon, E., 1970, Physics of nuclei and particles, volume 1

Matteson, J.L., 1978, The UCSD/MIT Hard X-ray and Low Energy Gamma Ray Experiment for HEAO-1: Design and Early Results. Presented at The AIAA 16th Aerospace Sciences Meeting

McDonald, F.B., Webber, W.R., 1959, Physical Review, vol 115, number 1, 194

Mereghetti, S., Jennings, D., Pedersen, H., Robert, A., Pellizzoni, A., Phol, M., Kretschmar, B., Walter, R., Courvoisier, T., 1999, Astrophysical Letters and Communications, 39, 301

Metzger, M.R., Djorgovski, S.G., Kulkarni, S.R., Steidel, C.C., Adelberger, K.L., Frail, D.A., Costa, E., Frontera, F., 1997, Nature, 387, 878

Michelson P.F., Bertsch D.L., Brazier K., Chiang J., Dingus B.L., Fichtel C.E., Fierro J., Hartman R.C., Hunter S.D., Kanbach G., Kniffen D.A., Lin Y.C., Mattox J.R., Mayer-Hasselwander H.A., von Montigny C., Nolan P.L., Schneid E., Sreekumar P., Thompson D.J., 1994, ApJ 435, 218

Mukherjee, S., Feigelson, E.D., Babu, G.J., Murtagh, F., Fraley, C., Raftery, A., 1998, ApJ, 508, 314

Naya, J.E., Barthelmy, S.D., Bartlett, L.M., Gehrels, N., Parsons, A., Teegarden, B.J., Tueller, J., Leventhal, M., 1998, ApJ, 499, L169

Naya, J.E., Barthelmy, S.D., Bartlett, L.M., Gehrels, N., Leventhal, M., Parsons, A., Teegarden, B.J., Tueller, J., 1996, Nature, 384, 44

O'Flaherty K.S., Bennett K., Diehl R., Hermsen W., McConnell M., Ryan J., Schonfelder V., Winkler C., 1995, A&A 297, 290

Paciesas, W.S., Harmon, B.A., Pendleton, G.N., Finger, M.H., Fishman, G.J., Meegan, C.A., Rubin, B.C., Wilson, R.B., 1993, A&AS, 97, 253

Paczyński, B., 1991, Acta Astronomica, 41, 257

Paczyński, B., 1998, ApJ, 494, L45

Parmar, A.N., Martin, D.D.E., Bavdaz, M., Favata, F., Kuulkers, E., Vacanti, G., Lammers, U., Peacock A., & Taylor, B.G. 1997, A&AS, 122, 309

Prantzos, N., & Diehl, R., 1996, Physics Reports, 267, 1

Purcell, W.R., Bouchet, L., Johnson, W.N., Jung, G., Kinzer, R.L., Kurfess, J.D., Mandrou, P., Roques, J.P., Skibo, J.G., Vedrenne, G., 1996, A&AS, 120, 389

Purcell, W.R., Cheng, L.-X., Dixon, D.D., Kinzer, R.L., Kurfess, J.D., Leventhal, M., Saunders, M.A., Skibo, J.G., Smith, D.M., Tueller, J., 1997, ApJ, 491, 725

Ramaty, R., Kozlovsky, B., Lingenfelter, R.E., 1979, ApJS, 40, 487

Ramaty, R., Leventhal, M., Chan, K.W., Lingenfelter, R.E., 1992, ApJ, 392, L63

Robinson, C., Lyne, A.G., Manchester, R.N., Bailes, M., D'Amico, N., & Johnston, S. 1995, MNRAS, 274, 547

Rudak, B., & Dyks, J. 1998, MNRAS, 295, 337

Ruiz, J.A., Porras, E., Ferrero, J.L., Reglero, V., Sanchez, F., Lei, F., Bird, A.J., Carter, T., Dean, A.J., 1994, ApJ Supplement Series, 92, 683

RXTE GOF web site, http://heasarc.gsfc.nasa.gov/docs/xte/xte_1st.html

Schönfelder, V., Aarts, H., Bennett, K., de Boer, H., Clear, J., Collmar, W., Connors, A., Deerenberg, A., Diehl, R., von Dordrecht, A., den Herder, J.W., Hermsen, W., Kippen, M., Kuiper, L., Lichti, G., Lockwood, J., Macri, J., McConnell, M., Morris, D., Much, R., Ryan, J., Simpson, G., Snelling, M., Stacy, G., Steinle, H., Strong, A., Swanenburg, B.N., Taylor, B., de Vries, C., Winkler, C., 1993, ApJS, 86, 657

Schönfelder, V., 1998, Proceedings of the LIBEB Workshop, Paris, Dec 1998

Share, G.H., Kinzer, R.L., Kurfess, J.D., Forrest, D.J., Chupp, E.L., Rieger, E., 1985, ApJ, 292, L61

Shaw, S.E., Westmore, M.J., Bird, A.J., Dean, A.J., Diallo, N., Ferguson, C., Lockley, J.J., Willis, D.R., Knödlseder, J., 2000, 4th INTEGRAL Workshop.

Strong, A.W., Bennett, K., Bloemen, H., Diehl, R., Hermsen, W., Purcell, W., Schönfelder, V., Stacy, J.G., Winkler, C., Youssefi, G., 1996, A&AS, 120, 381

Tavani, M. 1993, ApJ, 407, 135

Teegarden, B.J., Naya, J., Seifert, H., Sturner, S., Vedrenne, G., Mandrou, P., von Ballmoos, P., Roques, J.P., Jean, P., Albernhe, F., Borrel, V., Schönfelder, V., Lichti, G.G., Diehl, R., Georgii, R., Durouchoux, P., Cordier, B., Diallo, N., Matteson, J., Lin, R., Sanchez, F., Caraveo, P., Leleux, P., Skinner, G.K., Connell, P., 1998, Gamma-Ray Bursts : 4th Huntsville Symposium, Huntsville, AL September 1997. Edited by Charles A. Meegan, Robert D. Preece, and Thomas M. Koshut. Woodbury, New York : American Institute of Physics, 1998. (AIP conference proceedings ; 428)

Thompson, D.J., Bertsch, D.L., Fichtel, C.E., Hartman, R.C., Hofstadter, R., Hughes, E.B., Hunter, S.D., Hughlock, B.W., Kanbach, G., Kniffen, D.A., Lin, Y.C., Mattox, J.R., Mayer-Hasselwander, H.A., von Montigny, C., Nolan, P.L., Nel, H.I., Pinkau, K., Rothermel, H., Schneid, E.J., Sommer, M., Sreekumar, P., Tieger, D., Walker, A.H., 1993, ApJS, 86, 629

Tueller, J., Barthelmy, S., Gehrels, N., Teegarden, B.J., Leventhal, M., MacCallum, C.J., 1990, ApJ, 351, L41

Ubertini, P., 1998, Gamma-Ray Bursts : 4th Huntsville Symposium, Huntsville, AL September 1997. Edited by Charles A. Meegan, Robert D. Preece, and Thomas M. Koshut. Woodbury, New York : American Institute of Physics, 1998. (AIP conference proceedings ; 428)

Valinia, A., Kinzer, R.L., Marshall, F.E., 2000, ApJ, 534, 277

van Paradijs, J., Groot, P.J., Galama, T., Kouveliotou, C., Strom, R.G., Telting, J., Rutten, R.G.M., Fishman, G.J., Meegan, C.A., Pettini, M., Tanvir, N., Bloom, J., Pedersen, H., Nørdgaard-Nielsen, H.U., Linden-Vørnle, M., Melnick, J., van der Steene, G., Bremer, M., Naber, R., Heise, J., in't Zand, J., Costa, E., Feroci, M., Piro, L., Frontera, F., Zavattini, G., Nicastro, L., Palazzi, E., Bennet, K., Hanlon, L., Parmar, A., 1997, Nature, 386, 686

Vedrenne, G., Jean, P., Kandel, B., Albernhe, F., Borrel, V., Mandrou, P., Roques, J.P., von Ballmoos, P., Durouchoux, P., Cordier, B., Diallo, N., Schönfelder, V., Lichti, G.G., Diehl, R., Varendorff, M., Strong, A.W., Georgii, R., Teegarden, B.J., Naya, J., Seifert, H., Sturner, S., Matteson, J., Lin, R., Slassi, S., Sanchez, F., Caraveo, P., Leleux, P., Skinner, G.K., Connell, P., 1998, Multifrequency behaviour of high energy sources, Mem. S. A. lt., Vol 69, No. 4

Verbunt, F., & Hasinger, G. 1998, A&A, 336, 895

Watanbe, K., Hartmann, D.H., Leising, M.D., The, L.-S., 1999, ApJ, 516, 285

Winkler, C., 1998, Gamma-Ray Bursts : 4th Huntsville Symposium, Huntsville, AL September 1997. Edited by Charles A. Meegan, Robert D. Preece, and Thomas M. Koshut. Woodbury, New York : American Institute of Physics, 1998. (AIP conference proceedings ; 428)

Winkler, C., Gehrels, N., Lund, N., Schönfelder, V., Ubertini, P., 1999a, Astrophysical Letters and Communications, 39, 361

Winkler, C., 1999b, Astrophysical Letters and Communications, 39, 309

Zdziarski, A.A., 1996, MNRAS, 281, L9

Zhang, L., & Cheng, K.S. 1998, MNRAS, 294, 177